Damage Assessment for Composite Structures based on Individual Residual Strength Prediction

Von der Fakultät für Maschinenbau

der Technischen Universität Carolo-Wilhelmina zu Braunschweig

zur Erlangung der Würde

eines Doktor-Ingenieurs (Dr.-Ing.)

genehmigte Dissertation

von: Dipl.-Ing. Christoph Paul Dienel

aus (Geburtsort): Portimão, Portugal

eingereicht am: 5.9.2019

mündliche Prüfung am: 26.11.2019

Gutachter:

Prof. Dr.-Ing. Michael Sinapius

Prof. Dr.-Ing. Peter Horst

2019

Abstract

The current decision-making process for damage assessment and repair on composite structures is considered to be overly conservative. This is mainly due to the adopted empirical approach, which relies on heavy knock-down factors to cover the anticipated worst-case scenarios. In the present thesis, a novel decision-making process is proposed, based on predictions of the residual load carrying capability of an individually damaged structure, and on the strength recovery attainable for a particular repair configuration. The proposed procedure comprises of three independent modules. The first consists of a thorough characterization of the most influential damage features. In the second, a detailed individual model of the damaged structure is derived from these realistic defect representations. Structural behavior and residual load carrying ability are predicted using finite element analysis. Considering applicable design specifications, damage criticality is assessed and proper handling recommendations are derived. The third module is dedicated to assessing reparability of critically damaged structures. For that purpose, the attainable load carrying capacity of individually scarfed-bonded-repaired structures is also predicted through finite element analysis. Reparability is provided, if the repaired structure attains as-designed loading capability. Good agreement between experimental and simulation results at each module attests the proposed method's validity and highlights its potential contribution for future maintenance, repair, and overhaul processes.

Kurzfassung

Der herkömmliche Entscheidungsprozess zur Schadensbewertung und Reparatur an Faserverbund-Strukturen wird als "über-konservativ" eingeschätzt. Dafür ist der zugrunde liegende empirische Ansatz maßgeblich verantwortlich. Dazu werden hohe Abminderungsfaktoren benötigt, um die erwarteten Worst-Case-Szenarien abzudecken. In der vorliegenden Arbeit wird ein neuartiger Entscheidungsprozess vorgestellt, welcher auf der Berechnung der Resttragfähigkeit von individuell beschädigten Strukturen und der, für eine bestimmte Reparaturkonfiguration, erzielbaren Wiederherstellung der Tragfähigkeit basiert. Das empfohlene Verfahren umfasst drei unabhängige Module. Das erste besteht aus einer sorgfältigen Charakterisierung der wesentlichen Schlagschaden-Merkmale. Unter Berücksichtigung dieser ermittelten realistischen Schadensbilder wird im zweiten Modul ein detailliertes individuelles Modell der beschädigten Struktur abgeleitet. Mithilfe der Finite-Elemente-Analyse werden Strukturverhalten und Resttragfähigkeit ermittelt. Unter Hinzunahme der geltenden Auslegungslasten wird die Schwere des Schadens bewertet und geeignete Empfehlungen zur Handhabung vorgeschlagen. Das dritte Modul gilt der Bewertung der Reparaturfähigkeit kritisch beschädigter Strukturen. Dafür wird die erzielbare Tragfähigkeit von Strukturen mit individuell geschäfteten Klebereparaturen mittels der Finite-Elemente-Analyse berechnet. Reparaturfähigkeit ist dann gewährleistet, wenn die reparierte Struktur die entsprechend des Entwurfs vorgesehene Tragfähigkeit erreicht. Die gute Übereinstimmung zwischen experimentellen und Simulationsergebnissen in jedem Modul belegt die Gültigkeit der vorgeschlagenen Methode und unterstreicht ihren möglichen Beitrag für zukünftige Prozesse zur Instandhaltung, Reparatur und Überholung.

Acknowledgments

First of all, I praise God, the Creator of heaven and earth, for His creation that leaves us deeply amazed, as we try to grasp His perfectly balanced works in nature.

I'm gratefully indebted to you, Hanna, my faithful companion, and to our lovely children, Mira and Benjamin, for granting me the time and concentration needed to accomplish this goal. Without your support, this achievement would have been impossible.

I also express my gratitude for the effort employed by my parents in laying a good foundation for this achievement, and for the continuous support of my siblings. Thank you for all you've done!

This accomplishment is also owed to the efforts of the software engineering company Quazar GmbH in implementing my damage characterization vision, leading to the DaMapper tool. Thank you, Mr. Matthias Wild, for our many hours ~~fighting about~~ intensively discussing algorithms, implementation approaches, and bugs; you did a great job!

I also thank Dr.-Ing. Tobias Wille for granting me the opportunity of conducting this research. My appreciation goes to all my colleagues from the structure mechanics department for the many constructive discussions on this topic, in particular to Dr.-Ing. Dirk Wilckens and Dr.-Ing. Christian Willberg.

Special acknowledgment is owed to my supervising professor, Prof. Dr.-Ing. Michael Sinapius, for his advice and motivation throughout this endeavor.

Finally, I thank my teacher and friend, PhD John Wolf, for his continuous support and encouragement since elementary school. You are the true definition of a good teacher!

Contents

Abstract iii

Kurzfassung v

Acknowledgments vii

Nomenclature xiii
Abbreviations . . . xiii
List of Latin Symbols . . . xiv
List of Greek Symbols . . . xvi
List of Superscripts . . . xvi
List of Subscripts . . . xvii

1. Introduction 1

2. Decision-Making Process 5
2.1. Current Decision-Making Process . . . 5
2.2. Novel Decision-Making Process . . . 9
2.2.1. Literature Review . . . 10
2.2.2. Methodology . . . 11

3. Impact Damage Characterization 15
3.1. Motivation . . . 15
3.2. State of Knowledge . . . 16
3.2.1. Impact Damage Morphology . . . 16
3.2.2. Damage Detection Methods . . . 19
3.2.3. Analysis of NDI Images . . . 22
3.3. Experimental Procedure . . . 25
3.3.1. Specimen Manufacturing . . . 26
3.3.2. Damage Introduction . . . 26
3.3.3. Acquisition of NDI Images . . . 28
3.4. Damage Characterization Method . . . 29
3.4.1. Analysis of Ultrasonic Images . . . 29
3.4.2. Analysis of µCT Images . . . 34
3.4.3. Generic Fiber Crack Distribution . . . 40
3.5. Results and Validation . . . 43
3.5.1. Interlaminar Damage . . . 43
3.5.2. Intralaminar Damage . . . 44

3.6. Sensitivity Study on Defect Parameters . . . 47
3.6.1. Defect Shape . . . 47
3.6.2. Damage Feature Combination . . . 50
3.6.3. Defect Scaling . . . 51
3.7. Conclusion . . . 52

4. Impact Damage Assessment **55**
4.1. Motivation . . . 55
4.2. Review on Residual Strength Prediction . . . 55
4.3. Methodology . . . 59
4.3.1. Phenomenology of Impact-Damaged Laminates . . . 59
4.3.2. Structural Model Setup . . . 60
4.3.3. Simulation Result Analysis . . . 84
4.4. Results and Experimental Validation . . . 87
4.4.1. Virgin Coupons . . . 88
4.4.2. Impacted Coupons at 20 J . . . 89
4.4.3. Impacted Coupons at 30 J . . . 91
4.4.4. Impacted Coupons at 40 J . . . 93
4.4.5. Impacted Coupons at 50 J . . . 94
4.4.6. Artificially Delaminated Coupons: A- and B-Series . . . 96
4.4.7. Artificially Delaminated Coupons: C- and D-Series . . . 99
4.4.8. Artificially Delaminated Coupons: AC- and BD-Series . . . 101
4.5. Damage Assessment . . . 105
4.6. Conclusion . . . 106

5. Reparability Verification **109**
5.1. Motivation . . . 109
5.2. Review on Composite Repair . . . 110
5.3. Experimental Test Setup . . . 112
5.4. Methodology . . . 115
5.4.1. Phenomenology of Bonded-Repaired Laminates . . . 115
5.4.2. Structural Model Setup . . . 116
5.4.3. Reparability Criterion . . . 121
5.5. Results and Experimental Validation . . . 122
5.5.1. Virgin Coupons . . . 122
5.5.2. Repaired Coupons . . . 125
5.6. Reparability Verification . . . 137
5.7. Conclusion . . . 138

6. Summary **139**

A. Defect Verification **141**
A.1. Delamination Characterization Verification . . . 141
A.2. Experimental Fiber Fracture Characterization . . . 144

B. Interlaminar Matrix Properties **149**
B.1. DCB Test 149
B.2. MMB Tests 151

C. Adhesive Properties **157**
C.1. DCB Test 157
C.2. MMB Tests 158

D. Impact and Residual Strength Test Results **163**
D.1. Virgin Coupons 164
D.2. Impacted Coupons at 20 J 166
D.3. Impacted Coupons at 30 J 170
D.4. Impacted Coupons at 40 J 174
D.5. Impacted Coupons at 50 J 178

E. Artificial Damage and Residual Strength Test Results **183**
E.1. Artificially Delaminated Coupons: A-Series 183
E.2. Artificially Delaminated Coupons: B-Series 188
E.3. Artificially Delaminated Coupons: C-Series 192
E.4. Artificially Delaminated Coupons: D-Series 196
E.5. Artificially Delaminated Coupons: AC-Series 199
E.6. Artificially Delaminated Coupons: BD-Series 205

F. Tensile Repair Strength Test Results **209**
F.1. Virgin Coupons 209
F.2. Repaired Coupons 210

Bibliography **211**

Nomenclature

Abbreviations

1D	one-dimensional
2D	two-dimensional
3D	three-dimensional
ABR	Anti-buckling Rail
ADL	Allowable Damage Limit
ATR	Automatic Target Recognition
BK	Benzeggagh-Kenane
BVID	Barely Visible Impact Damage
CAI	Compression after Impact
CAIS	Compression after Impact Strength
CBT	Corrected Beam Theory
CDM	Continuum Damage Mechanics
CDT	Critical Damage Threshold
CFRP	Carbon-Fiber Reinforced Plastic
CL	Computer Laminography
CLT	Classical Laminate Theory
CO_2	Carbon Dioxide
CoV	Coefficient of Variation
CT	Computer Tomography
CZM	Cohesive Zone Model
DCB	Double-cantilever Beam
Dela	Delamination
DIC	Digital Image Correlation
DLL	Design Limit Load
DoF	Degrees of Freedom
DoH	Determinant of Hessian
DUL	Design Ultimate Load
ENF	End-notched Flexure
ET	Envelope Type
FC	Fiber Crack
FE	Finite Element

FPZ	Fracture Process Zone
GLARE	Glass Reinforced Aluminum
HW	Hot-Wet Condition
IGES	Initial Graphics Exchange Specification
LEFM	Linear-elastic Fracture Mechanics
LoG	Laplacian of Gaussian
LVI	Low-velocity Impact
MMB	Mixed-mode Bending
MRO	Maintenance, Repair and Overhaul
µCT	Micro-Computer Tomography
N/A	Not available, Not applicable
NDI	Non-destructive Inspection
NO_x	Nitrogen Oxide
OCR	Optical Character Recognition
OEM	Original Equipment Manufacturer
RDL	Repairable Damage Limit
ROI	Region of Interest
RS	Residual Strength
RSS	Residual Sum of Squares
RVE	Representative Volume Element
SB	Slender Bodies
SERR	Strain Energy Release Rate
SF	Safety Factor
SHM	Structural Health Monitoring
SI	Stress Intensity
SRM	Structural Repair Manual
STI	Stable Time Increment
TAI	Tension after Impact
ToF	Time-of-Flight
VCCT	Virtual Crack Closure Technique
XML	Extensible Markup Language

List of Latin Symbols

a	Crack length
A	Area, Coefficient
B	Coefficient
c	Constant
C	Compliance
d	Degradation variable
D	Diameter

$\mathbf{D}$	Second-order partial derivative of the Gaussian kernel
$\mathbf{d}$	Discrete second-order partial derivative operator
E	Young modulus
$\mathcal{E}$	Energy
f	Narrowing parameter
F	Force
$\boldsymbol{\mathcal{F}}$	Scalar field
g	Gaussian function
G	Shear modulus
$\mathbf{G}$	Gaussian kernel
$\mathcal{G}$	Fracture toughness
h	Beam half-thickness
$\boldsymbol{\mathcal{H}}$	Hessian matrix
I	Geometrical moment of inertia
$\mathbf{I}$	Identity matrix
$\boldsymbol{\mathcal{I}}$	Image
k	Kernel size
K	Interfacial stiffness
$\mathbf{K}$	Interfacial stiffness matrix
l	Length
n	Arbitrary spacial dimension
N	Number
P	Plateness measure
$\boldsymbol{\mathcal{P}}$	Plateness image
q	Stack
r	Ratio
R	Constant
s	Standard deviation
S	Shear strength, Structureness
$\mathbf{S}$	Stiffness matrix
t	Thickness, Traction
T	Time
$\mathbf{t}$	Traction vector
$\mathbf{v}$	Eigenvector
w	Width
x	First axis in the laminate coordinate system; Vector component (when used with index)
X	Strength in fiber direction
$\mathbf{x}$	Position vector
y	Second axis in the laminate coordinate system

Y	Strength transversely to the fiber
z	Third axis in the laminate coordinate system

List of Greek Symbols

α	Scarf ratio
β	Constant, Mixed-mode ratio
γ	Shear strain, Constant
Γ	Parameter
δ	Separation
Δ	Parameter, Displacement
$\boldsymbol{\delta}$	Separation vector
ε	Normal strain
ζ	Mode-mixity ratio
η	BK-exponent, Relative stack number
θ	Polar angle
$\boldsymbol{\Theta}$	Polar angle image
Λ	Parameter
λ	Eigenvalue
ν	Poisson's ratio
ξ	Relative control variable
ρ	Material density
σ	Normal stress
τ	Shear stress
ϕ	Azimuth angle
$\boldsymbol{\Phi}$	Azimuth angle image
χ	Correction parameter
ψ	Fracture angle

List of Superscripts

$+$	Tensile loading
$-$	Compressive loading
adh	Adhesive
c	Characteristic
CDM	Continuum Damage Mechanics
f	Fiber
F	Failure
L	Transversal shear
m	Matrix

M	Index
max	Maximum
N	Index
O	Onset
s	Shear
SB	Slender-body
T	Longitudinal shear

List of Subscripts

1	First axis in ply coordinate system, Along the fiber orientation
2	Second axis in ply coordinate system, Orthogonal to the fiber, mode I
3	Third axis in ply coordinate system, Through the thickness
6	Mode II
adh	Adhesive
AS	Artificial Strain
B	Bottom
BA	Bottom Adhesive
$butt$	Butt region
c	Critical, Center
d	Degradation
D	Damage-related dissipation
DCB	Double-cantilever Beam
e	Element
ENF	End-notched Flexure
eq	Equivalent
EW	External Work
F	Filler ply
FC	Fiber Crack
fin	Final, Last
FPZ	Fracture Process Zone
g	Gauge
hys	Hysteresis-filtered
i	Index
I	Mode I, Internal
II	Mode II
III	Mode III
i, j	Indices
in	Inner

ini	Initial, first
$inter$	Interlaminar
$intra$	Intralaminar
k	Index
K	Kinetic
L	Lever
max	Maximum
min	Minimum
mm	Mixed-mode
MMB	Mixed-mode Bending
MS	Mass Scaling
msk	Masked
out	Outer
PW	Penalty Work
s	Standard deviation (scale)
S	Shear, Strain
SA	Butt and scarf Adhesive bond-line
T	Total, Top
TA	Top Adhesive
VD	Viscous Dissipation

1 Introduction

The demand for air transportation has been growing continuously over the last decades. In 2015, passenger growth forecasts projected the passenger number to reach 7 billion by 2034, doubling the passenger number expected for 2015 [1]. Along with this prospective development comes the demand for environment friendly transportation, aiming at Carbon Dioxide (CO_2) and Nitrogen Oxide (NO_x) emission reductions by 75 % and 90 %, respectively, as formulated in the Flightpath 2050 goals [2]. Among others, one viable approach to cope with these apparently contradictory requirements consists in reducing aircraft structural weight, by applying light-weight materials such as Carbon-Fiber Reinforced Plastic (CFRP).

Since the 1970s, CFRP has been increasingly adopted for secondary, and later for primary aircraft structures, aiming at structural weight reduction. The composite share in modern commercial aircraft, such as the Boeing 787 Dreamliner and the Airbus A350, has now surpassed the 50 % mark [3]. The increasing interest in this material is owed to its high specific strength and stiffness along with other advantages, such as corrosion resistance, good formability, and the integral design suitability. However, reticence concerning the use of CFRP is mainly motivated by the experience advance in metal design, using aluminum alloys, as opposed to the numerous still open questions concerning composite design [4].

Among the many composite related open questions, much attention has been given to the subject of accidental impact damage on composite structures. This is because CFRP is considered insensitive to the conventional design drivers of metallic structures, like corrosion and fatigue, while being very responsive to accidental impact damage. Hail, runway debris, bird strike, tool drop during maintenance, and collision with ground vehicles are typical impact damage causes, that threaten different aircraft components (see figure 1.1). Damage inspection, assessment, and repair of the damaged structure result not only in additional maintenance costs but also in revenue losses, due to aircraft unavailability. For instance, the financial penalty to an airline, resulting from a grounded Airbus A350, is estimated to roughly 300 000 $[1]. A representative airline fleet is exposed to an impact probability of a few impact events per day [6]. This makes evident, how crucial condition-based damage assessment and demand-oriented repair is.

In order to prevent financial aspects from compromising flight operations' safety, civil aviation authorities demand that metallic and composite primary structures comply to damage tolerant design requirements. The main objective of this design policy is to ensure that, in case of fatigue, corrosion, or accidental damage, the remaining structure is able to withstand reasonable loads, without failing or experiencing excessive distortion, until the damage is detected [7]. Applying this

[1] A representative flight from Seattle to Shangai (4972 M), seating 319 passengers, is taken as a reference. An average ticket revenue for this flight of 1500 $ per passenger, and the corresponding total costs per available seat mile of 0.1196 $ are considered [5].

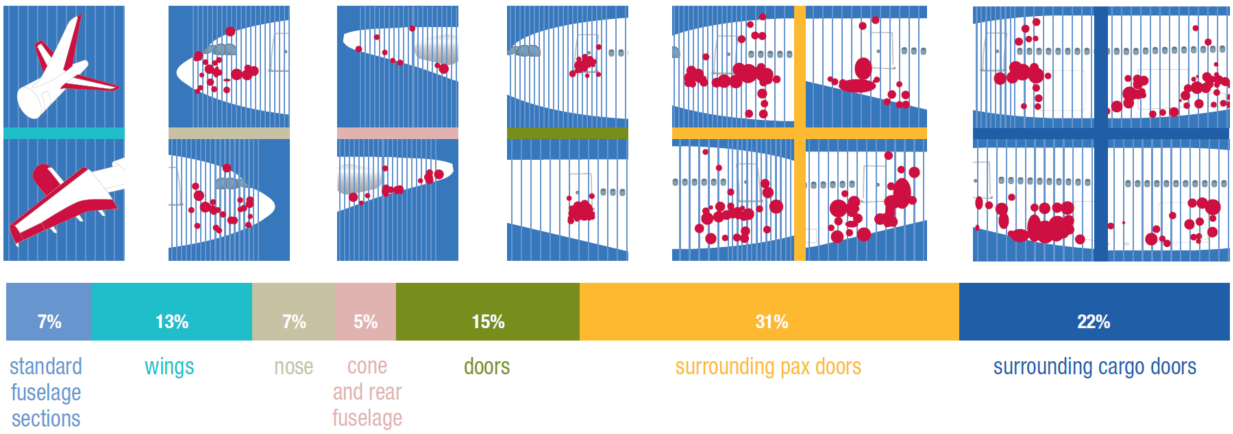

Figure 1.1.: Global percentage of impacts by zones on a typical single-aisle aircraft (courtesy of Airbus S.A.S.) [3].

requirement to the composite design, it demands that as long as the accidental impact damage remains undetected, it must not lead to substantial residual strength reductions, that may cause structural failure. This exigency raises basically two questions: one regarding the minimum damage size that can be reliably detected, and the other concerning the influence, this damage size may effectively exert on the structural residual strength.

By nature, the detection and characterization of impact damage on an aircraft is a challenging task due to limited access. This is even aggravated when dealing with composite structures, because low-velocity and low-energy impacts can cause sub-surface damage, not visible from the outside, that may result in significant residual strength reductions [8]. To cope with this challenge, the commonly adopted approach consists in identifying typical damage threats, and defining a damage size threshold that can be reliably detected, at an affordable inspection effort. This is commonly referred to as Barely Visible Impact Damage (BVID), inferring visual inspection to be the accepted damage detection method [9].

Determining the residual strength associated to a specific damage is a fundamental exercise on which both, structural aircraft design and repair procedures are based on. On the one hand, allowable loads are defined to satisfy the recommendation given by the civil aviation authorities in sizing the structure such, that it can "tolerate" damages below BVID. On the other hand, repair actions are requested, whenever the damage is beyond the visibility threshold (BVID). This demand is rooted in the assumption that the loading capacity is significantly degraded, due to accidental damage beyond BVID.

The relation between damage size and its residual strength can be determined with more or less accuracy by adopting different approaches [8], that distinguish by the model, describing that relationship. These are classified as experiment-based (empirical), probabilistic, and deterministic methods. Today, the empirical approach is well-established throughout aircraft industry. At Airbus, for instance, the empirical method consists in the collection of actual damage characteristics from real in-flight and ground impact events. Under test conditions, a series of impacts is inflicted to a representative structure, in order to reproduce the collected impact damages. From these

tests, a relation between the applied impact energy and the resulting damage size is obtained. Then, by evaluating in-service and test data, the impact threat is determined. This is defined as the mathematical description of the occurrence probability of an impact event at a specific energy. The severest impact threat within a particular zone, expected to occur once in the aircraft's lifetime, is a crucial factor determining the respective part's design. This energy level is finally considered for tests on composite structures, ranging from coupon to component level, in order to validate the sizing rules and design allowables, adopted for damage tolerant composite structures [3]. The results of this experiment-based approach determine not only the composite parts' design, but also the decision-making process for damage assessment and repair specifications, as usually reflected in the Structural Repair Manual (SRM), issued for each aircraft type.

How ever intuitive and confidence inspiring such an approach might be, it conceals the immense testing effort required, and the many simplifying assumptions made, to derive a robust damage assessment method. Due to the variety of parameters influencing the impact event and consequently the establishing damage, the conduction of an exhaustive testing program, accounting for all variables, is highly impractical. For this reason, it requires the identification of worst-case scenarios to be included in the test matrix. Based on such test results, analytical surrogate models are derived, as an attempt to correlate damage properties (e.g. the projected damage size) with the expected residual loading capacity. However, due to the modest damage description detail usually required by these simple models, the estimated residual strength poses a rather rough estimate, being associated with considerable conservatism, to cover the uncertainties.

In contrast to this approach, a novel decision-making process is proposed in this thesis, which has the potential of replacing over-conservative damage handling recommendations by demand-oriented procedures. This is achieved through individual residual strength predictions of the damaged structure, and by attainable load carrying capability estimation of tailored repair configurations. By comparing the individually determined strengths to the applicable design allowables, damage criticality and structural reparability can be assessed. By this means, demand-oriented damage handling recommendations can be issued. This however can only be achieved, if the validity of the following hypotheses is given.

- From a structural mechanics perspective, sufficiently detailed characterization of the most influential impact-damage features can be achieved.
- The residual strength of individual impact-damaged CFRP structures can be accurately predicted, to a relative error of less than 10 %, regarding the experimentally determined value.
- Attainable strength of repaired CFRP structures is predictable with sufficient accuracy (relative error below 10 %).

These hypotheses are discussed throughout this thesis. In chapter 2, the novel decision-making process based on residual strength estimations is introduced, and contrasted to the current statistical approach. The three above mentioned hypotheses are scrutinized in the subsequent chapters 3 to 5. A summary and concluding remarks are provided in chapter 6. Results to the conducted experiments are presented in the appendices A to F.

To delimit the scope of the present thesis, it is noted that the suggested approach is primarily demonstrated for monolithic CFRP structures, damaged by virtue of accidental Low-velocity Impact (LVI) in a supposed in-service scenario. Moreover, from the many damage removal techniques available, scarf-bonded repair is adopted. Although the employed repair model is designed to enable parameter variations, thus being suitable for repair configuration optimization, this step is deliberately left for follow-up research. It is also noted that the response of impact-damaged models is analyzed under static compression loading condition. In turn, repaired structures are subjected to static tension loads. These particular loading conditions are chosen for demonstration purposes and are regarded as most critical for the respective structural condition.

2 Decision-Making Process

Impact damage on airframe composite structures is handled according to a workflow, designed to evaluate the damage criticality and to ultimately determine, when and how a specific damage is to be resolved. This chain of steps, also designated as the decision-making process, is specified by the Original Equipment Manufacturer (OEM) and gives guidance to the Maintenance, Repair and Overhaul (MRO) service provider, on how to restore structural integrity and airframe airworthiness.

As described in chapter 1, an over-conservative experiment-based decision-making process is currently well established in the aircraft industry. In contrast, a novel decision-making process is suggested, based on residual strength estimations of both, damaged and repaired structures, and its comparison to applicable design allowables. Further action is ultimately determined by this comparison outcome.

2.1. Current Decision-Making Process

In pursuing the objective of maintaining aircraft airworthiness throughout its service life, OEMs issue SRMs, describing type-specific decision-making processes. These specify how damage is to be handled on the various aircraft components. Severity thresholds for damage classification and the respectively recommended repair methods are thus specified for each component [10]. An example of a current decision-making process for damage and reparability assessment is depicted in figure 2.1.

The first step of the decision-making process is the damage inspection. This examination is prescribed to scheduled checks, or may be required out of schedule, if damage is visible or suspected. For detected damages, a defect description as well as the identification of the affected structural part is required. Information is collected regarding the damage type, the respective size, its location on the component (also referred to as damage mapping), and the existence of previous repairs in its vicinity. Then, the damage is evaluated and classified regarding its characteristics and by taking into account the Allowable Damage Limit (ADL), specified for the different zones of the component. Allowable damage, although not compromising structural integrity of airframe parts, generally still requires surface protection restoration, to prevent further deterioration from occurring, until the damage is permanently repaired [10]. In contrast, any non-allowable damage is assumed to impair structural performance, therefore requiring repair action. Repairs covered by the SRM are classified as temporary and permanent repairs, depending on its severity. Any damage beyond the Repairable Damage Limit (RDL) is not covered by the SRM, thus requiring OEM support to restore airworthiness [11].

This decision-making flowchart (figure 2.1) can be clustered into three groups: damage char-

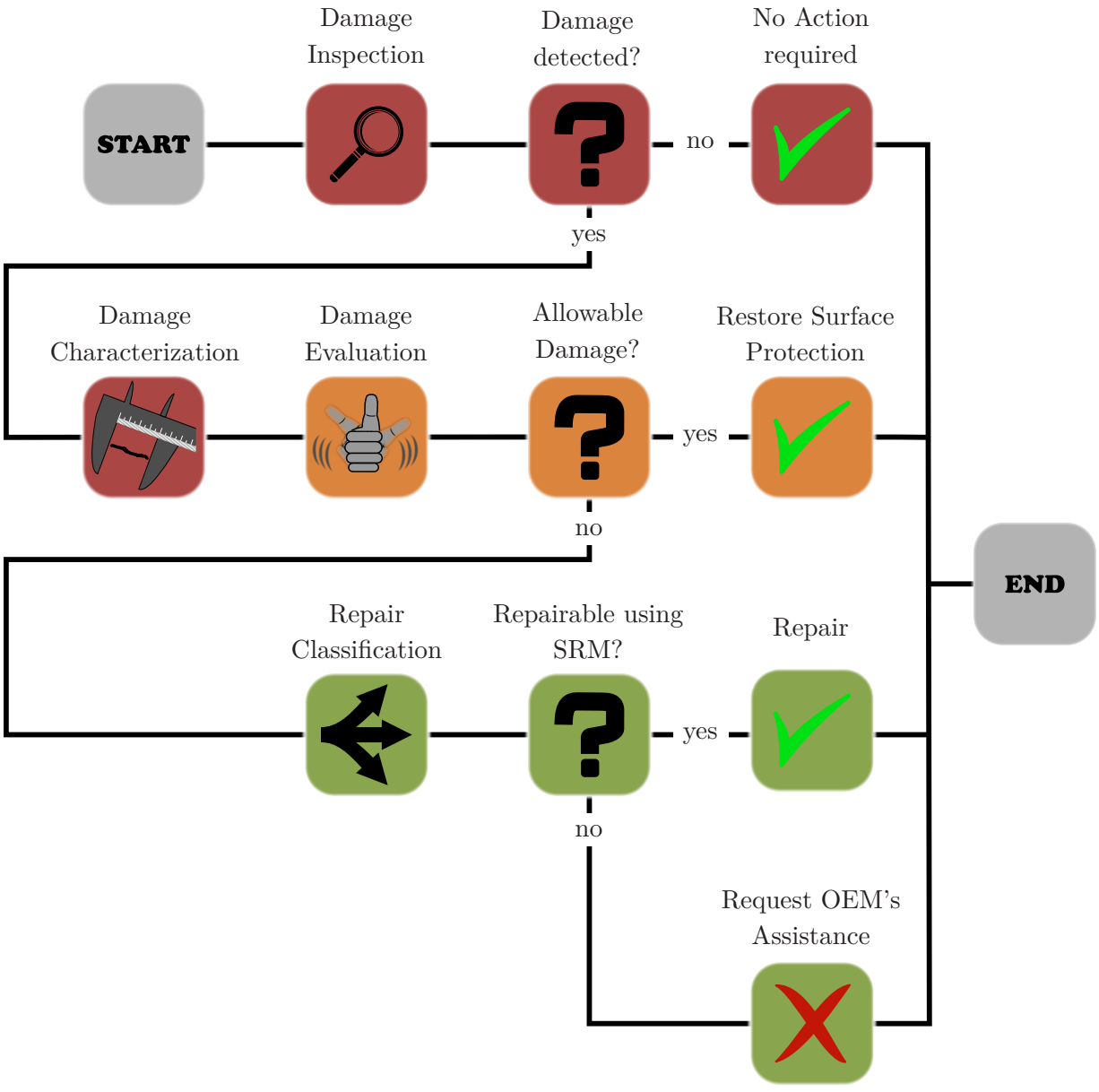

Figure 2.1.: Current decision-making process, synthesized from [11]. Damage size is the decisive parameter, determining the workflow at the decision nodes (represented by question marks).

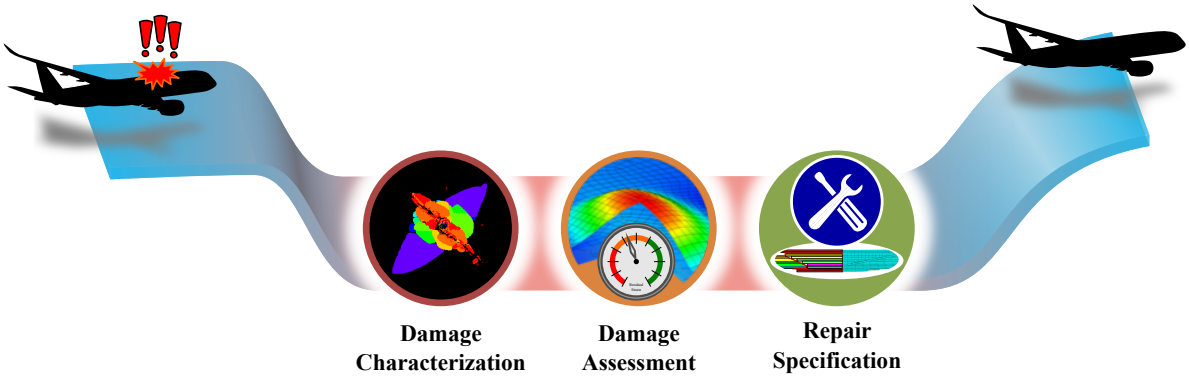

Figure 2.2.: Clustered view of the decision-making process.

acterization, damage assessment, and repair specification (figure 2.2). Any overly conservative assumptions made in any of these three modules leads to increased maintenance costs and unnecessary aircraft ground-time.

In the first module, adopted damage representations are generally too pessimistic. This is because impact damage morphology is very complex and of challenging characterization. Over-simplified enveloping contours are therefore adopted to cover potential undetected defects [11]. Considering the thresholds ADL and RDL, such overly conservative damage representations may exceed these limits, thus requiring repair action or even structural overhaul.

Regarding the second module, the damage assessment basis for the current decision-making process consists of an empirically determined relation between damage size and residual strength. This correlation is determined through a considerable experimental effort [3]. Among the many experiments, conducted to establish that relation, coupon tests cover the vast majority [9]. Especially Compression after Impact (CAI) tests have been regarded as a suitable standard to study the correlation between Compression after Impact Strength (CAIS) and damage size. This is attributed to the cautious reasoning that the compression strength in composite structures is of itself lower than tensile strength, and that the detrimental effect of impact damage is more significant under compressive loading [12]. Hence, CAI tests are adopted for damage tolerant design substantiation, and for derivation of the above mentioned thresholds for defect classification and assessment.

The experiment-based process of determining the design allowables and damage size thresholds is illustrated in figure 2.3. For the sake of argument, generic value pairs are considered. Each single data point symbolizes an individual CAI coupon, depicting its measured projected damage area and the respective residual strength. The average curve represents the least squares fit through these pairs of values. The crossing point between this curve and the ordinate represents the average strength of undamaged coupons. To reduce the probability of over-predicting the residual strength, a B-basis correction is applied, where 90 % of the data points are designed to lay above that curve, with a 95 % confidence [13]. To account for adverse environmental conditions and stress concentrations, establishing at potentially undetected defects, the virgin strength is further "knocked down" by respectively 10 % and 30 %. Thus, the resulting Design Ultimate Load (DUL) represents merely 50 % of the undamaged average loading capability [14, 15]. Considering the B-

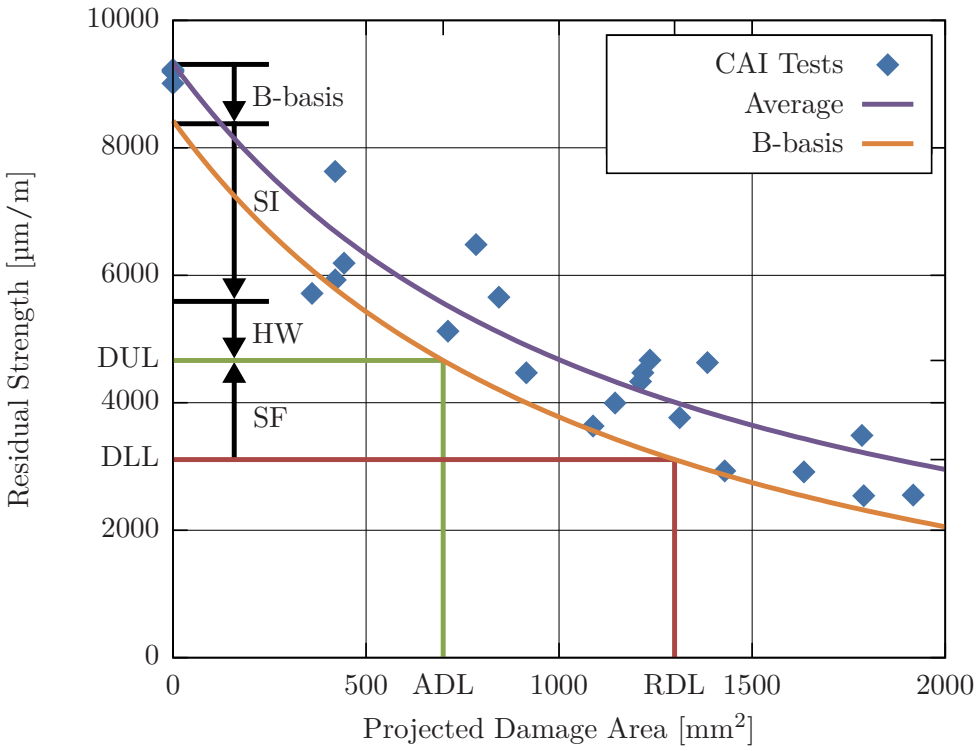

Figure 2.3.: Generic relation between damage size and compression after impact strength. Design load and damage threshold definition according to the current method. Average virgin strength is diminished by B-basis correction −10 % (B-basis), stress intensity at undetected defects −30 % (SI), and hot-wet conditions −10 % (HW). DUL is obtained by applying a 1.5 safety factor (SF) to DLL. ADL and RDL are determined from DUL and DLL, respectively, and from the B-basis curve.

basis curve, the damage size corresponding to DUL is denoted as ADL. Any defect below ADL is expected to withstand DUL, while damage beyond ADL is considered requiring structural repair. In turn, RDL is determined by the B-basis curve and the Design Limit Load (DLL). This is defined as the load, likely to occur once in the airframe's operational life. Given the adopted safety factor of 1.5 between DUL and DLL, the latter equates only 33 % of the average pristine strength.

Besides the conservative design allowables, resulting from the severe knock-down factors, applied to cover for the many uncertainties related to composite design [14–16], relying only on such a statistical instead of an individual approach for residual strength prediction adds further conservatism to the process. This is because roughly 90 % of the individual residual strengths, are underestimated by this analytical surrogate model [13]. As suggested by figure 2.3, the residual strengths of some coupons are found above DUL, in spite of presenting damage sizes beyond ADL.

The adoption of the CAI test standard as a means to derive the relation between residual strength and damage size is of itself very restrictive [12]. This is owed to a series of reasons associated to this test setup:

- The impact threat is obtained from surveying impact damages on real airframe structures

and replicating them on identical parts, in order to derive the impact energy, responsible for the in-service damage [3]. When impacting CAI coupons with the same impact energy as that, applied to realistic components, the resulting damage is generally more extensive. This is owed to the significantly higher bending stiffness of the first in comparison to the latter, which results from its tighter boundary conditions. In consequence, the detrimental effect of expected impact threats is considerably overestimated [12].

- The small coupon size leads to a high ratio of damaged to undamaged cross-section. This prevents the load from bypassing the damaged area, thus leading to overrated stress concentrations and consequently to residual strength reductions, that would never occur in larger realistic airframe structures [12].
- CAI coupons are single load path structures, without alternatives for load redistribution. In contrast, most composite airframe components present multiple load paths (e.g. via surrounding stiffeners and skin), thus being more tolerant to single defects.
- Not every impact damage influencing parameter (e.g. laminate thickness, layup, impactor shape, impact energy and velocity, etc. [8]) can be extensively tested, due to the associated exorbitant effort. Thus, only a few parameter sets are selected, at least covering the worst-case scenarios. Through interpolation, the residual strength of non-tested configurations is inferred from effectively conducted worst-case scenario tests. Due to the associated uncertainty, further knock-down factors are applied.
- Residual strength is plotted against a damage severity parameter, which is commonly expressed as one of many damage-related properties: projected damage area (short: damage size), dent depth, damage width, damage length, impact energy, etc. These are known to affect scatter in residual strength plots differently. Although the least scatter is observed when expressing damage severity in terms of impact energy, this is generally an unknown measure in in-service scenarios [13]. What ever of these damage severity measures is adopted, none of them represents the complex impact damage pattern (comprised by delaminations, fiber and matrix cracks, plastic deformation, etc.) in its entirety. Yet, these damage features are known for having significant influence on the residual strength [8, 17, 18].

Regarding the repair module, this also contributes to over-conservative damage assessment. On the one hand, this is because RDL definition is often too restrictive, as already discussed. On the other hand, because the attainable repair strength is generally underestimated. This occurs due to pessimistic analysis methods, based on two-dimensional (2D) stress analyses (c.f. chapter 5).

2.2. Novel Decision-Making Process

In this thesis, a novel decision-making process is proposed. Its aim consists in avoiding the causes, identified in the previous section, leading to restrictive damage assessments. At the same time, care is taken not to compromise aircraft safety. This is achieved by an individual deterministic assessment of impact damaged and repaired structures. This is to say, that strength is predicted by considering the actual properties of the damaged and repaired structures, and the main phenomena governing their structural behavior. Thus, condition-based damage assessments and demand-

oriented repairs can be attained.

2.2.1. Literature Review

Although the conventional decision-making process suggests strong dependencies between the modules damage characterization, damage assessment, and repair (c.f. figure 2.1), these are generally addressed independently throughout the literature. Most studies focus only on some aspects of the decision-making process (such as damage detection, impact damage prediction, residual strength estimation, repair, etc.), but not on the entire process with its inherent interdependencies. Yet, the combined consideration of (1) suitable Non-destructive Inspection (NDI) techniques, (2) accurate and reliable residual strength prediction methods, and (3) knowledge regarding design allowables for structural sizing, is considered a powerful and necessary approach for in-service damage assessment [19].

In an attempt to evaluate the criticality of impact damaged composite parts, many approaches have been proposed. Roughly, these can be classified as experiment-based (empirical), probabilistic, and deterministic methods, and hybrids thereof.

As described in the previous section, the widely accepted damage assessment approach is mainly of empirical nature. This means that the residual strength of a particular damaged part is derived from curve-fitting and interpolation through a-priori experimentally determined results. Hereby, the experimental basis covers mostly combinations of the anticipated worst-case conditions.

In an attempt to reduce conservatism, probabilistic damage tolerance analyses have been proposed [20–22]. For each influencing parameter, a function relating the parameter's severity to its probability of occurrence is defined, based on experimental data. By combining the diverse functions, design robustness can be calculated. Since the probability of all critical conditions (i.e. highest design load, largest damage considered for structural sizing, mechanical properties most degrading temperature, etc.) occurring simultaneously is by far lower than the highest occurrence probability of a single critical parameter, probabilistic designs promise better material exploitation than currently adopted approaches. Design and maintenance specifications based on such methods can lead to life-cycle cost reductions, while maintaining high safety and reliability standards. Although less conservative, experimental data for derivation of probabilistic functions is still subjected to the same issues discussed in the previous section, concerning experiment-based methods.

Deterministic methods have the potential of further reducing conservatism in damage assessment and repair specification processes. This presupposes that physically consistent models are available, which accurately represent the structural condition, thus ultimately enabling individual response predictions. The comparison of residual strengths predicted by this means with the applicable design allowables is considered a solid criterion for assessing the damaged structure's airworthiness and its necessity of repair.

Many studies dedicated to the deterministic residual strength after impact estimation comprise two distinct disciplines: damage resistance, where the damage extension is obtained from impact simulations; and damage tolerance, dedicated to the residual strength prediction [23–30] . It has

been viewed as convenient to combine these disciplines because the first is expected to provide a more or less realistic representation of the complex impact damage morphology, which ought to provide a reasonable residual strength estimation. This approach provides a good understanding of the relation between impact threat and residual strength, and has the potential of complementing the design process, while reducing the experimental effort [25, 31]. However, the cause of a particular damage occurring during the aircraft's operational life is not always known, much less the parameters that characterize the impact event. In order to still being capable of assessing in-service impact damage, it requires the characterization of damage from NDI images. For that purpose, it has been proposed to extract simplified delamination shapes from ultrasonic inspection images and to map them onto basic models for residual strength prediction [19, 32, 33].

Towards more realistic damage representations and more accurate residual strength predictions, de Moura et al. [34] coupled NDI image analysis to finite element modeling. By mapping more detailed single delamination shapes obtained from ultrasonic images onto meso-scale models, and by adopting cohesive elements to represent failure mechanisms in the inter-ply region, they achieved good agreement between experimentally and numerically determined residual strengths. Ellison and Kim [35] included also intralaminar defects in their representation of the impact-damaged structure, by considering Micro-Computer Tomography (µCT) inspection results.

2.2.2. Methodology

The novel decision-making process suggested in the present thesis (figure 2.4) is understood as an endorsement of the current workflow. It is intended to support MRO activities by providing a convenient tool for reliable impact damage assessment and repair specification of in-service structures. Its novelty consists mainly in detailed damage characterization, and in damage and repair assessments based on individual residual strength estimations.

Similarly to the current decision-making process, the suggested workflow is also initiated by damage inspection during scheduled or unscheduled checks, if damage is visible or suspected (figure 2.4). In a prospective scenario, this step could be supported by the implementation of Structural Health Monitoring (SHM) systems, in order to indicate the presence of damage and its rough location, thus triggering condition-based and demand-oriented, instead of scheduled maintenance [36, 37]. Either way, a detailed damage description must be provided, in order to accurately predict the residual strength. This is achieved by NDI methods capable of capturing the mechanically relevant damage features, and by sophisticated NDI image processing methods, enabling detailed defect characterization and accurate mapping (addressed in chapter 3). Residual strength is calculated by taking into account all relevant parameters regarding the structure (i.e. material parameters, geometry, layup, etc.) and the damage features from the preceding characterization step. For this purpose, a detailed meso-model is created, accounting for the particular structural condition and the anticipated phenomena. Through Finite Element (FE) analysis the residual loading capacity is ultimately determined (addressed in chapter 4). As opposed to the current workflow, the damage assessment criterion is rather expressed in terms of residual strength than of damage size. If predicted load carrying capacity exceeds DUL, a cosmetic repair — to be carried out at a convenient time — suffices. Conversely, a permanent repair is eventually

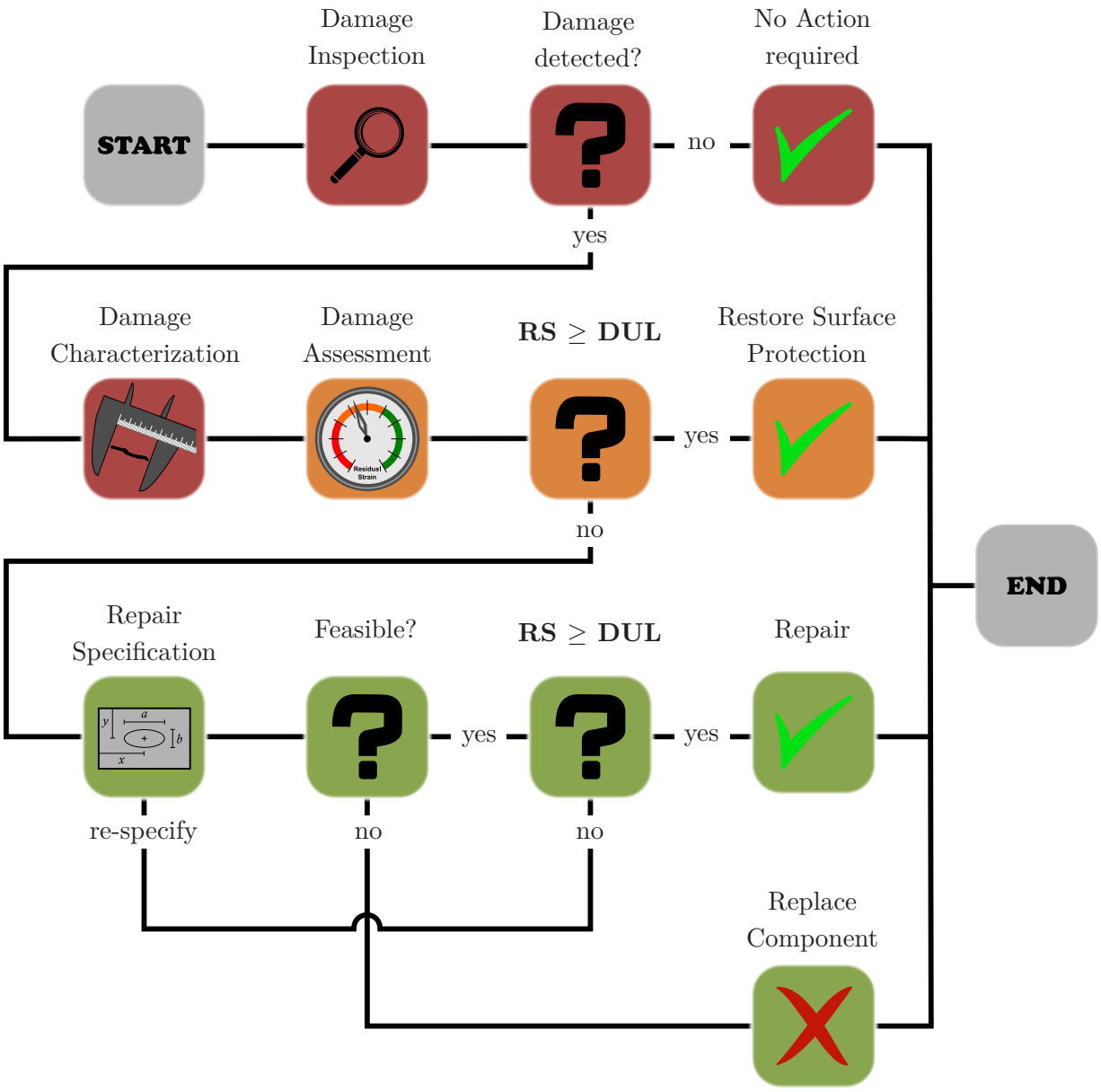

Figure 2.4.: Novel decision-making process. Residual strength determines the workflow at the decision nodes (question marks). Repair re-specification occurs manually and feasibility is currently specified by the available parameter space.

necessary. Therefore, the third row in figure 2.4 is dedicated to estimating the attainable repair strength of scarf-bonded repair configurations. In case the specified configuration attains DUL capability, the structure is considered reparable. However, if the predicted strength is still too low, repair parameters may be adjusted, until reaching an adequate configuration. If no parameter set, covered by the model parameter space, satisfies the feasibility criterion, replacement of the damaged part is recommended (addressed in chapter 5). In this context, it is noted that technical and economical feasibility aspects are disregarded in the present thesis. Regarding the repair optimization loop depicted in figure 2.4, it is not further explored in the present scope.

3 Impact Damage Characterization

This impact damage characterization module is designed to provide meaningful defect descriptions to the subsequent assessment module, as depicted in figures 2.2 and 2.4. In order to acquire the most influential damage features to the structural behavior, two NDI methods are regarded as appropriate. The results obtained from these complementary techniques are subjected to further image processing steps, yielding the effective damage contours and positions, crucial for residual strength predictions. Besides providing examples of realistic impact damage for the development of NDI image analysis methods, a few experimentally impacted coupons are further submitted to destructive testing, thus providing a solid validation basis for the present module. In addition, the influence of specific damage feature combinations on the structural behavior is discussed through parametric studies, regarding defect shape and size.

3.1. Motivation

The damage assessment module is designed to process images of the damaged structure, and to return the description of the most relevant damage features. Regarding the current damage assessment approach (c.f. section 2.1), this task is accomplished by the surrogate model, described in figure 2.3. This rather simple mathematical expression returns for each projected damage area an unequivocal residual strength. In practice, a specific damage is merely classified based on its size, and under consideration of two thresholds, which in turn are derived from that surrogate model. In an attempt to reduce over-conservatism associated to this approach, a sophisticated residual strength prediction model is proposed. In contrast to the former one, this approach requires a much more detailed impact damage representation as an input.

Considering the manifold causes of impact, damage morphology in composite structures can vary considerably. Hail, runway debris, turbine disc-burst, tire failure, bird strike, collision with ground-vehicles, equipment or structures, are only a few of the many threats, the airframe structure is exposed to [38]. This diversity implies a wide spectrum of parameters governing the impact event (such as laminate thickness, boundary conditions, kinetic energy, projectile velocity, and others), therefore influencing the damage morphology. Due to its heterogeneous nature, the composite constituents handle impact energy differently, giving rise to different defect features and extensions. Of the numerous elementary defects establishing, the most influential are fiber cracks, delaminations, and transversal matrix cracks, the latter however being mainly relevant as a starting point for delaminations [8, 39–41].

Before this background, proper NDI techniques must be identified, that enable the detection of such damage features. In addition, the development of adequate methods for extracting such features from NDI images, is essential for accurate structural behavior predictions and ultimately for robust damage assessments.

3.2. State of Knowledge

For more than 40 years, impact damage on composite structures is being studied. On the one hand, these studies focus on the influence of divers impact parameters on the establishing damage pattern, i.e. the study of impact resistance. On the other hand, the effects of the various damage features on the residual strength are addressed in the context of damage tolerance [8]. While the first identifies the establishing defects due to impact, the latter highlights the most influential features. From these two research fields, a set of requirements for the present damage characterization module can be derived.

3.2.1. Impact Damage Morphology

To date, special attention is given to the accidental LVI, as this poses a frequent threat to airframe structures. The formation of sub-surface damage is characteristic to such an impact scenario, which often goes undetected by routine visual inspection, in spite of compromising the structural performance. Although its definition is somewhat ambiguous regarding the impact velocity, LVI is better described as an event, where damage onset is rather caused by quasi-static plate-like deformation, than by impact-induced compressive, shear, and surface waves [8]. The main damage features resulting in such a scenario are summarized as matrix cracking, delamination, and fiber fracture [8, 39–41].

Matrix failure is the first establishing damage mode during the impact event. Its orientation is predominantly parallel to the fibers (figure 3.1a). In a cross-sectional view of the impacted laminate, matrix cracks establish under oblique angles to the specimens' surface, as a result of transverse shear stresses, especially in thicker structures. Matrix cracks are also found propagating in normal direction to the impacted surface. This is attributed to in-plane loads, caused by tensile bending stresses at the impact-averted surface. Such cracks are often found in thinner laminates (c.f. figure 3.1b) [41]. In addition, tensile matrix cracks can also result by virtue of high localized stresses, at the immediate impact vicinity [8].

Although matrix cracks can extend over wide regions in a complex pattern, they are often disregarded for quasi-static residual strength estimations, as their detrimental effect on mechanical properties is considered negligible. However, transversely growing matrix cracks are generally redirected at ply interfaces[1], giving rise to delaminations [40].

Impact-induced delaminations are typically found between layers of dissimilar orientation. They generally present a peanut-shaped extension, having their major axis aligned with the lower adjacent ply orientation (c.f. figure 3.2). Depending on the structure's bending stiffness, the delamination distribution through the multi-directional layup thickness may resemble a pine tree, reversed pine tree [8] or even a barrel [42] (figure 3.3). Interlaminar mode II shear stresses and bending stiffness mismatches are responsible for the onset and propagation of delaminations during the impact event [39, 42, 43]. Their emergence is further favored by the presence of transversal matrix cracks [40].

[1] Interface denotes the transition zone between two stacks of dissimilar orientation.

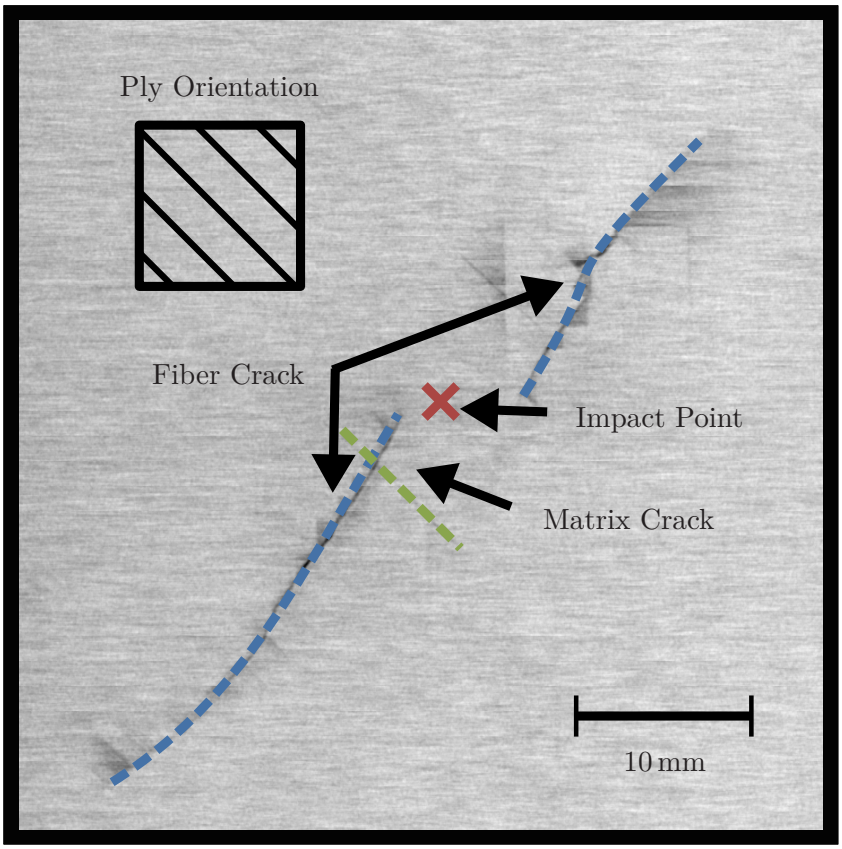

(a) top view

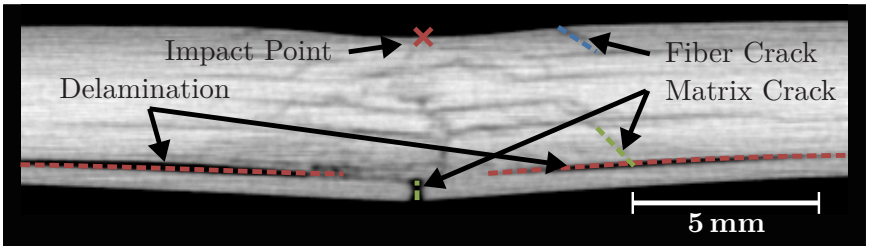

(b) sectional view

Figure 3.1.: Top and sectional view of a CAI specimen, impacted at 40 J. Intralaminar damage is confined to the immediate impact vicinity. Depicted images are obtained from µCT inspection.

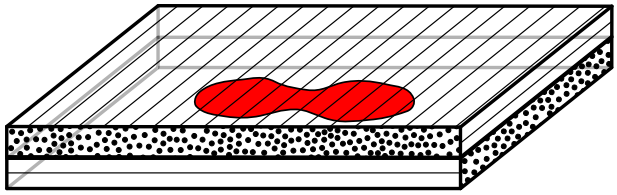

Figure 3.2.: Schematic peanut-shaped delamination in a 0°/90° interface.

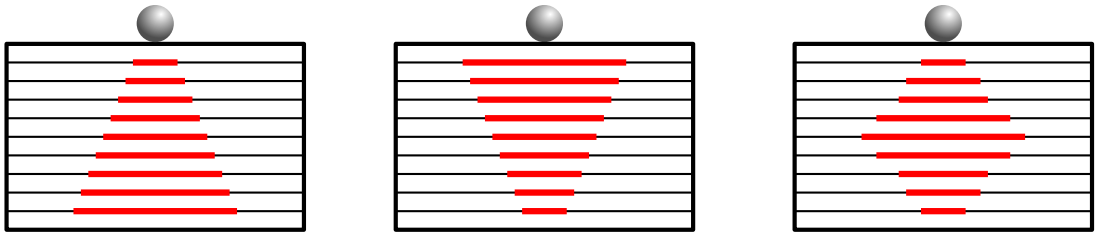

(a) pine tree (b) reverse pine tree (c) barrel

Figure 3.3.: Typical delamination patterns through the laminate thickness ss(sectional view)

Under loading conditions, other than tensile, delaminations can significantly reduce the residual strength, depending on their size, shape, and position in the laminate [42, 44]. Delaminations divide the layup locally into sub-laminates of lower than the undamaged layup's bending stiffness. Under loading conditions promoting stability failure, i.e. compression and shear, they can experience sub-laminate buckling. This mechanism, when occurring in sub-laminates of considerable thickness or in multiple sub-laminates simultaneously, can cause sudden delamination growth [43]. This is generally assumed to coincide with failure of the entire structure [8].

At higher impact energies, fiber failure occurs either due to local tensile stresses at the impact site, or at the impact-averted surface, as a consequence of bending-induced tensile stresses [45]. Its formation is favored by matrix cracks and delaminations [42]. These jagged fractures spread rather perpendicularly to the fiber orientation and can extend over multiple layers throughout the laminate thickness [46]. Fiber crack extension is rather confined to the impact axis vicinity [47] and its extension is often in the same order of magnitude, as the minor axis of the largest delamination enveloping ellipsis [46] (c.f. figure 3.1).

Depending on the loading condition, the detrimental effect of fiber cracks on the residual strength varies. Under tensile conditions, fiber failure alone is rather insignificant. However, in combination with delaminations, its influence is considerable. This is owed to the shear-lag effect. In absence of delaminations, the load path interruption caused by a fiber crack in a particular layer, promotes load redirection through adjacent plies. However, due to transversal shear load transfer, the damaged ply recovers its initial load carrying capacity, within a short distance from the crack. On the other hand, the presence of delaminations prevents this effect, hence further reducing the residual properties [42, 46]. However, under compression load, the residual strength sensitivity to the existence of fiber cracks is rather low.

3.2.2. Damage Detection Methods

Detection of the most influential defect types is a prerequisite for accurate condition-based damage assessment. For that purpose, many NDI techniques have been developed, each with its particular advantages and disadvantages [10, 48–51]. However, a comprehensive characterization of the complex impact damage, by means of a single NDI technique, is not possible yet. Thus, complementary methods are required, to achieve a sufficiently accurate damage characterization [52]. Relevant NDI techniques are reviewed in the following.

3.2.2.1. Visual Inspection

According to the current design philosophy, structures are designed to withstand non-visible damage. Visual examination poses the first inspection, which might by followed be other more sophisticated methods, if indication of damage exists. The required equipment is fairly inexpensive [10]. Characterization of inner damage by this method is at most of qualitative nature, merely indicating the existence of damage, rather than yielding any defect depth or extent information [51]. This however applies only to special composite materials, such as glass/epoxy and Kevlar/epoxy, where inner damage extent can be detected, using a strong back-light [48]. For opaque materials, such as CFRP, inner damage is yet undetectable by this method. Concerning superficial defects, visual inspection is sufficient for describing the length, orientation, and position of fiber and matrix cracks. Capabilities of this method are summarized in table 3.1.

3.2.2.2. Ultrasonic Inspection

Ultrasonic inspection is fairly mature for the detection of delamination damage in composite laminates. The principle consists in ultrasonic stress waves being excited at frequencies ranging from 1 MHz to 20 MHz [48]. At higher frequencies, small defects are more likely to be detected, whereas lower frequency waves can penetrate to greater depths. Besides signal frequency, damage detection also depends on the structure's material elasticity and damping properties [10]. Material discontinuities can cause wave reflection and transmission at reduced amplitudes, which are indicators of damage [49]. Due to mostly single-side access to airframe components, the pulse-echo is the preferred usage mode. Hereby, a single transducer excites pulses and receives echoes, resulting either from a defect or from the back-wall. At each sample point, the echo amplitude vs. Time-of-Flight (ToF) is recorded (A-scan). Plotting the maximum amplitudes exceeding a specified threshold at each sampling point, yields a 2D map of discontinuity locations (C-scan). In knowing the specific sound-speed and the echo's transit time, a depth map (D-scan) can be derived, enabling a three-dimensional (3D) damage localization [10]. Scanning a damaged structure at normal incidence, the pulse attenuation experienced at the first encountered defects is considerable, such that subjacent damage can hardly be detected. This is often referred to as the shielding [48] or shadowing effect [53]. Another limitation associated to the normal incidence pulse-echo technique, resides in its incapacity to detect fiber and matrix cracks, as they don't offer a wide enough reflecting surface [54]. To overcome these limitations, acoustic backscattering technique has been proposed. It consists in an oblique incidence pulse-echo method, enabling fiber and matrix crack detection, while reducing the shadowing effect [48, 54].

One major advantage of ultrasonic inspection methods is the 3D characterization of delaminations. On the other hand, the method's complexity, time consumption, and the requirement for experienced personnel are rather viewed as drawbacks [10]. The increased effort, associated to the acoustic backscattering technique, may be the reason for reticence regarding its implementation in aircraft maintenance procedures. As a consequence, normal incidence pulse-echo ultrasonic inspection is generally adopted, although not providing for the detection of intralaminar cracks (c.f. table 3.1).

3.2.2.3. Thermographic Inspection

Thermographic inspection is widely used in aircraft maintenance for the detection of large delamination and disbonds. Different modes are available, that enable the detection of both, near-surface and deep-lying defects [10]. Damage is responsible for thermal conductivity inhomogeneity, resulting in temperature gradients, detectable by infrared sensors [49]. The 2D images obtained by this means, indicate the presence of delamination-type damage, although not resolving its through-the-thickness position [54]. Especially regarding CFRP materials, the detection of flaws in greater depths is very challenging. This is owed to a much higher thermal in-plane conductivity than through-the-thickness, thus obscuring deep-lying defects [10].

Quick inspection of large structures is the main advantage of thermography. On the down-side however, result interpretation requires knowledge of the aircraft structure and systems, which may act as heat sources or sinks. In addition, the sensitivity to detect delamination is inferior to that, offered for instance by ultrasonic systems [10]. At best, this inspection method enables delamination extent acquisition (table 3.1).

3.2.2.4. X-Ray Inspection

X-ray-based methods are increasingly adopted to detect small defects in industrial applications, lending themselves also for the characterization of impact-induced damage in composite structures. Projectional radiography is the most simple X-ray-based method. All defects are projected onto a 2D image, thus revealing only the damage extent [48]. To determine the defect's through-the-thickness position, stereo-radiography is suggested. This approach resides in capturing two X-ray photographs from two distinct perspectives [48]. However, the interpretation of such results is difficult and the computed defect's depth is fairly inaccurate [54].

A more recent approach in overcoming the challenge of 3D defect positioning in composite materials, consists in recurring to Computer Tomography (CT). The approach involves capturing several X-ray pictures from different perspectives around the specimen, which are post-processed to yield a 3D representation of the scanned volume [48]. Focusing small Region of Interest (ROI) with high resolution, (also referred to as µCT), enables the detection of impact-induced intra- and interlaminar defects, as well as the characterization of micro-cracks, caused by fatigue [55, 56]. Although enabling quantitative volumetric representation and detailed damage positioning, CT and µCT methods require sophisticated image processing and analysis algorithms for accurate damage segmentation [35, 57]. Methods enabling automatic defect segmentation and recognition in CFRP structures are presently of low maturity. Instead, tedious and error-prone manual anal-

ysis of the obtained inspection results is required. In addition, high capital costs, the emergence of reconstruction artifacts, limited portability, safety protection requirements, and the need for 360° access to the inspected part, are factors hindering the method's acceptance [10, 48].

However, due to the high-quality results, further X-ray methods have been developed, targeting at some disadvantages identified in earlier studies. In an attempt to loosen the 360° access requirement, which can hardly be met for most airframe structures, Computer Laminography (CL) has been proposed. Contrary to CT , CL doesn't require a full rotation around the specimen to return a 3D image. This technique enables in-situ inspection under laboratory conditions, revealing damage onset and growth [58]. However, the attainable result quality is found somewhere between projectional radiography and CT [59].

Depending on the adopted X-ray method for impact damage inspection, the result quality ranges from rough defect extent estimations to 3D detailed shape and position descriptions. The X-ray inspection method rating, as summarized in table 3.1, refers to the µCT mode.

3.2.2.5. Eddy Current Inspection

The induction of eddy currents to conducting CFRP structures is a suitable method for damage identification. Conductivity disturbances in the inspected structure are mainly indicators of carbon fiber fractures. Although capable of detecting complex impact damage, defect characterization is rather of qualitative nature, except for fiber cracks. Their extent and through-the-thickness position can be determined quantitatively [10, 51, 60, 61]. Therefore, this method is mostly a complementary technique to the other methods [10] (table 3.1).

The method's up-side resides in being a low-cost and contactless procedure, requiring only single-side access to the subject of inspection. However, it also requires additional calibration effort for each material and layup, since varying fiber orientations affect conductivity.

A summary of relevant NDI methods currently available, and their ability in capturing the most relevant impact damage features, is given in table 3.1. Ultrasonic and µCT inspection are the most promising methods for the characterization of impact damage in small coupons. These techniques are therefore adopted throughout the present thesis.

Defect Mode	Inspection Methods				
	Visual	Ultrasonic	Thermography	X-Ray (µCT)	Eddy Current
Delamination	--	++	+	++	-
Fiber Crack	--	--	--	++	++
Matrix Crack	--	--	--	++	-

Table 3.1.: Capabilities of conventional NDI methods in detecting impact damage in CFRP structures. Legend: method returns defect extent and location (++), renders rough dimensions (+), indicates defect existence only (-), no detection possible (--)

.

3.2.2.6. Destructive Methods

Although being irrelevant for defect characterization in the context of impact damage assessment, destructive methods are very instructive regarding establishing damage patterns, and are considered excellent techniques for calibration of NDI methods and their respective image analysis algorithms. For these purposes, two methods are widely adopted: the de-ply technique and the cross-sectional fractography.

The de-ply technique is often used in combination with a gold chloride penetrant. Once the fluid penetrates internal cracks, the solution is vaporized at elevated temperature, leaving behind gold chloride crystals. At approximately 400 °C, partial matrix pyrolysis occurs, such that the plies can be carefully peeled off. Microscopical ply-by-ply analysis of the crystal residues distribution reveals the extent and position of delamination and matrix cracks. In return, fiber fractures are readily visible, thus dispensing contrast enhancing penetrants [48, 62].

Cross-sectional fractography consists in carefully cutting small slices at different locations and with different orientations from the subject of inspection. After meticulous preparation, the slice cross-sections can be analyzed under the microscope, revealing fiber and matrix cracks as well as delaminations [48]. This however, supports only damage characterization at the dissected surfaces.

3.2.3. Analysis of NDI Images

Generally, sought-for damage features do not present themselves readily in NDI images. Instead, the acquired images often require detailed analyses, to ultimately identify and describe the relevant defects. To reduce analysis errors, provide easily interpretable outputs, and finally enable operator-independent and reproducible damage assessments, automated image examination is recommended [51]. This coincides with the declared objective of computer vision. By following the example of human vision, this interdisciplinary field is dedicated to developing the automatic computer-based capability of perceiving imagery, by recovering specific object properties. A good introduction to the topic is for instance given by Szeliski [63].

Before this background, methods are developed to return the relevant damage contours from raw NDI images. These are discussed in section 3.4. However, a brief introduction to existing image processing methods is given in this sub-section. These methods are clustered according to the four processing steps, along the damage characterization workflow (figure 3.4).

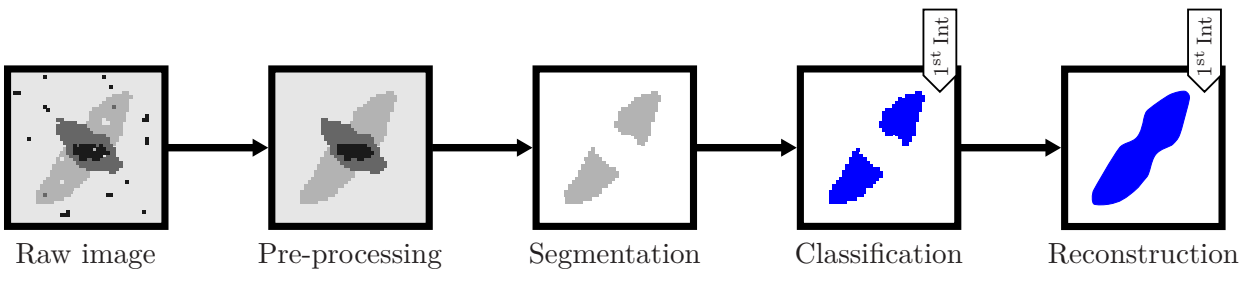

Figure 3.4.: Damage characterization workflow by the example of a generic ultrasonic D-scan image.

Image pre-processing refers to the first set of operations, conducted to convert the raw image into an intermediate result, suitable for further analysis. Such operations include image noise reduction and contrast enhancement [63].

The issue of noise is typical for NDI images, obtained from real structures. A commonly adopted approach for suppressing image noise is neighborhood filtering. Hereby, the new processed pixel value is obtained by considering the neighboring pixel values. The neighbors taken into account and the weight of their contribution to the new pixel value is determined by the kernel[2]. For the purpose of noise reduction, the Gaussian smoothing filter is widely adopted. It is understood as a weighted-average kernel, whose coefficients are obtained by discretization of the continuous Gaussian function. Its many advantageous properties have led to its preference over many other smoothing algorithms. On the one hand, the Gaussian is a low-pass filter, used for suppressing high-frequency noise. This is suitable for eliminating small-scale structures, unlikely to represent relevant damage. However, even large noisy pixel agglomerations can be suppressed, by the use of larger kernels. This scalability is another very convenient property, often explored in multi-scale filtering. A further advantage is the continuity and differentiability of the Gaussian function, which enables the combination of smoothing and feature enhancement operations in the same kernel, for better computational performance. Further efficiency increase is achieved by exploiting the Gaussian kernel's separability property, where costly multi-dimensional kernels are decomposed into one-dimensional (1D), and thus computationally lighter operators [63, 64].

Towards inter- and intralaminar damage segmentation, suppressing noise is a crucial pre-processing step. However, since segmentation consists in clustering similar pixels, based on their properties, enhancing contrast for better distinction and separation is also a critical pre-processing step. For that purpose, feature enhancement algorithms have been proposed. They highlight and suppress pixels, such that the longed for objects, or at least their delimitations, become more distinguishable.

Edge detection algorithms can be very effective in highlighting the boundaries of damage features, but identifying the effective defect might still be challenging, especially in images containing many defects, and thus many edges. Hence, blob[3] detection algorithms pose an adequate alternative.

For instance, the second derivative of Gaussian — Laplacian of Gaussian (LoG) — is such a method, that also enables the detection of defects of arbitrary size and shape. Due to its function characteristics, the LoG can highlight the area enclosed by two consecutive edges. However, the scale (i.e. the adopted standard deviation determining the kernel size) must match the size of the sought-for defects. Since real images may present very dissimilar damage sizes, finding the objects of interest requires convolution at multiple scales (multi-scale), covering the expected damage size spectrum [65].

Another, more powerful, blob detection algorithm is based on the Determinant of Hessian (DoH), where the coefficients of the Hessian matrix are the second-order partial derivatives in all image space directions. The eigenvalues obtained from the DoH describe the local second-order structure

[2]In the present thesis, as in computer vision literature, kernel, filter, mask, and operator can be used interchangeably.

[3]Blob refers to arbitrarily shaped objects.

of the image [66]. In 2D images, the ortho-normal eigenvectors span a local ellipsis (in 3D images an ellipsoid), where the vector lengths are a dimension of contrast. Besides identifying the defects (similarly to the LoG), this eigenvalue analysis returns the detected defect shape characteristic. This is particularly convenient not only for the subsequent image segmentation, but for the damage type classification. It enables defect distinction, based on their shape and their orientation. A similar approach is suggested by Frangi [66] for vessel detection in medical imaging applications and its generalization is proposed by Antiga for the detection of different object shapes in the n-dimensional space [67].

Once irrelevant pixels have been eliminated from the original image through several pre-processing operations, as those introduced above, image segmentation can be conducted (c.f. figure 3.4). This refers to the separation of different pixels from each other, resulting in pixel clusters of uniquely similar characteristics [68]. Strictly following this definition, it is admitted, that some of the operations introduced as pre-processing methods, could also be understood as segmentation (e.g. distinction between noise and relevant pixels). Therefore, the definition is sharpened to describe only the separation of relevant pixels.

For the present purpose of damage characterization, attention is drawn to two segmentation methods: histogram-based and neighborhood segmentation. The first is very efficient as it disregards the defect morphology and the pixel neighborhood. Pixels are separated in two or more groups, defined by one or more thresholds, regarding a particular pixel property (e.g. gray-scale, position, orientation, etc.) [68]. Image segmentation based on neighborhood analysis methods is especially recommended, when the pre-processor output is still very noisy. In that case, double-threshold (i.e. hysteresis thresholding) segmentation is capable of providing more realistic results. This concept consists in defining two thresholds (upper and lower) for pixel classification. Pixels above the upper threshold are labeled strong and are considered true damage pixels; pixels below the lower threshold are suppressed; and pixels, whose values lay between these two thresholds are considered weak. Weak pixels are only regarded as true damage, if the chain of weak pixels is somehow connected to a strong pixel [63, 69]. This approach leads to less fragmented and thus more realistic objects.

The classification step's main task consists in assigning the segmented pixel clusters to relevant classes, from the perspective of damage characterization. In practical terms, this means that relevant pixels are classified according to their damage type and their position in the layup architecture.

Reconstruction is the final step in the damage characterization workflow (figure 3.4). In computer vision, reconstruction is often used in the context of model creation of historic sites, heads and faces, etc. [63]. The concept consists in using effectively measured data, which tends to be fragmented, and completing it by some a priori knowledge, in order to achieve empirically consistent results. In the present context and considering the many operations required along the damage characterization workflow (figure 3.4), it is likely that the resulting defect shapes are fragmented and empirically inconsistent. Yet, physically significant defect representations can still be attained, when including empirical knowledge, regarding impact damage morphology (c.f. subsection 3.2.1). Here too, many sophisticated reconstruction algorithms exist, which are beyond

the present scope. In view of the detail level required for damaged structure modeling, discussed in section 3.6, simple contours suffice for representing the main damage features.

Recurring to the vast collection of existing methods and algorithms, several approaches have been suggested for damage characterization in composite structures. Early approaches to automatic damage characterization consist in evaluating ultrasonic C-scans, by determining the number of pixels exceeding a given threshold, and in deriving the corresponding delamination area. Accurate and reproducible defect area estimations are achievable by this means [53]. In an attempt to describe impact damage with more detail, by also taking intralaminar defects into account, other more recent approaches have been proposed. Hereby, damage characterization is conducted on µCT datasets, in order to classify both inter- and intralaminar defects. In adopting image pre-processing and segmentation methods, objects indicating damage are identified and labeled. In order to describe impact damage position and extent, and ascribing the detected objects to specific plies or interfaces, McCombe et al. [70] reconstruct the damage volumes by analyzing the µCT-image, pixel slice by pixel slice. Yet, inferring defect positions in the laminate architecture by evaluating the ortho-slice offset from the top surface, is a viable approach when considering nearly flat and lightly deformed structures. However, if those conditions are not fulfilled, other more sophisticated object positioning methods are required. By applying a distance transform method, based on the Euclidean distance between defect and the top surface, the impact-induced deformation can be compensated, enabling a ply-by-ply reconstruction and visualization of the damaged specimen [35, 71]. Instead of clustering the pixels representing damage, based on their gray-scales or position, approaches for image segmentation, based on the objects' morphology, have been proposed too. For instance, Stoessel et al. [57] pursue a plate-like structure enhancement filter in their damage detection method. This is based on the approach proposed by Frangi for vessel enhancement, in the medical imaging context [66]. As a result of this DoH-based approach, more relevant filter responses are obtained, highlighting objects of realistic defect shapes.

Many advances in image processing and segmentation offer the possibility of extending the many NDI methods from being merely defect detection tools, to becoming full damage characterization instruments.

3.3. Experimental Procedure

In this section, the experimental procedure adopted to introduce damage in CFRP specimens, and the employed methods for its detection are presented. Two objectives are mainly pursued by this experimental work. On the one hand, the damaged specimens provide specific use cases for developing and validating the damage characterization method. On the other hand, the same damaged coupons are subjected to mechanical testing, in order to determine their residual strength. These results, in turn, are used for the validation of the residual strength prediction method, introduced in the following chapter.

3.3.1. Specimen Manufacturing

All CAI coupons are extracted from CFRP plates of identical laminate architecture (figure 3.5). The manufacturing process is conducted in compliance with the prepreg manufacturer's specifications [72]. Different stack[4] thicknesses are included, in order to verify the proposed methods' applicability to realistic stack thickness ranges. The adopted laminate is comprised by a total of 22 plies, resulting in an average laminate thickness 4.15 mm. The stacking sequence includes typical ply orientations used in airframe structures. To avoid bending-extension coupling, a symmetric architecture is adopted.

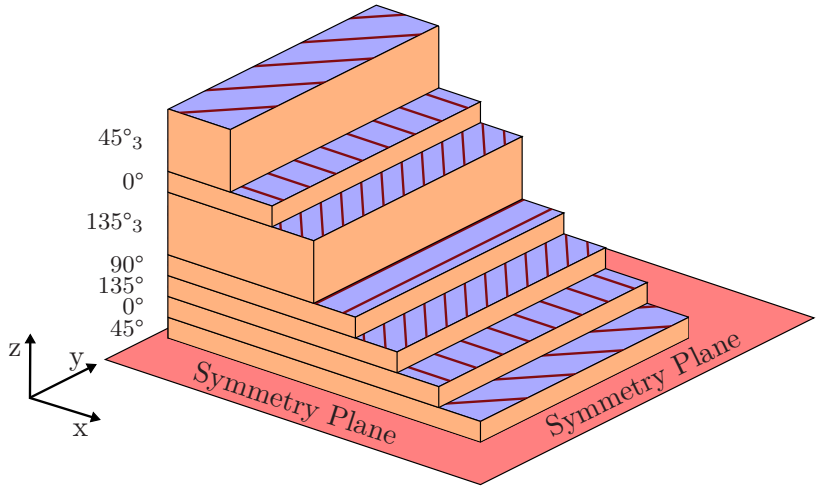

Figure 3.5.: Specimen symmetric layup adopted in the present thesis.

The CAI specimens are prepared in compliance with the geometrical requirements regarding dimension, and parallelism and orthogonality between edges. Coupon in-plane dimensions are set to a 150.0 mm length by 100.0 mm width. Further details on coupon geometrical specifications are provided in the applied test standards [73–75]. The effective geometrical parameters are summarized in the tables presented in appendices D and E.

3.3.2. Damage Introduction

Realistic impact damage is introduced to CAI coupons using a drop-weight tower and an impactor mounted with a hemispherical 16 mm-diameter steel striker. Impactor weight and drop-height are set to achieve different impact energies, ranging from 20 J to 50 J. The FractoVis Gravity Drop test equipment used to conduct the impact tests is equipped with an anti-bounce device, in order to avoid multiple consecutive impacts. Specimens are clamped onto a steel base with a window of 125 mm length by 75 mm width, inside which the specimen is allowed to experience transversal deflection. Coupon dimensions and boundary conditions are depicted in figure 3.6, where the hatched area denotes the specimen portion, experiencing contact with the base. Further details regarding the test setup are described in the respective test standards [73, 74]. Resulting damage parameters are provided in appendix D.

[4]Stack refers to a connected group of plies of same orientation.

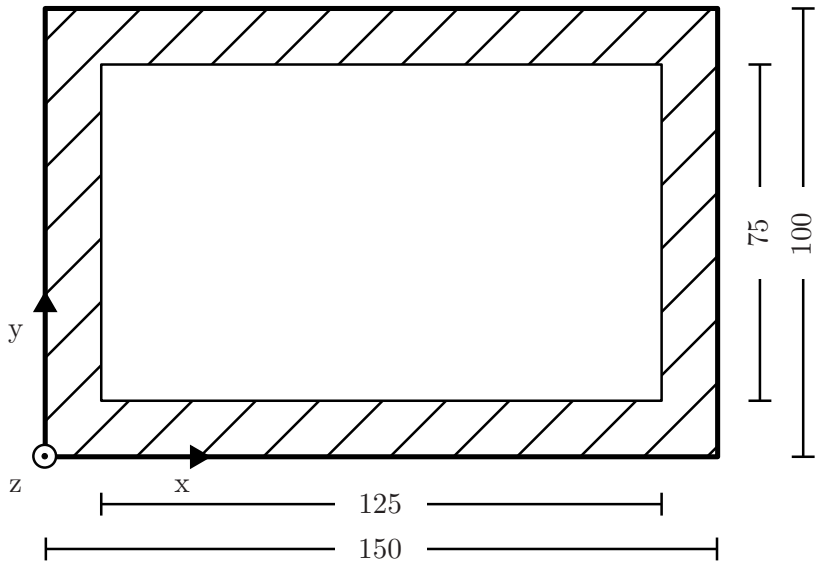

Figure 3.6.: CAI coupon dimensions (in mm) and boundary conditions during impact testing.

Apart from the impact damaged specimens, six further specimen series are considered. These contain different combinations of artificial defects. According to the technique adopted in [46], a 13 µm thin Teflon foil is included in the laminate, to obtain artificial delaminations. As depicted in figure 3.7, a 50 mm-diameter circular shape is introduced at the center at two different interfaces. Likewise, intralaminar cracks are artificially introduced by cutting through a specific number of stacks and integrating a Teflon strip, to prevent resin from filling the gap, during the autoclave process. The cut's length amounts 25 mm presenting the same 135° orientation through all affected stacks. These artificial defects are considered individually and in combination, as summarized by table 3.2. The respective residual strengths, obtained by mechanical testing, are discussed in subsections 4.4.6 to 4.4.8 and summarized in appendix E. It is noted, that all specimens containing artificial delaminations are also subjected to a 4 J blunt impact with a 25 mm by 25 mm rectangular contact surface. This is considered necessary to break any potential adhesion between the sublaminates and the Teflon foil. Ultrasonic inspection conducted on pre-impacted specimens suggests this particular condition.

Series	Delamination	Intralaminar Crack
A	1st Interface	None
B	3rd Interface	None
C	None	1st Stack
D	None	1st to 3rd Stacks
AC	1st Interface	1st Stack
BD	3rd Interface	1st to 3rd Stacks

Table 3.2.: Adopted defect configurations in artificial specimen series

.

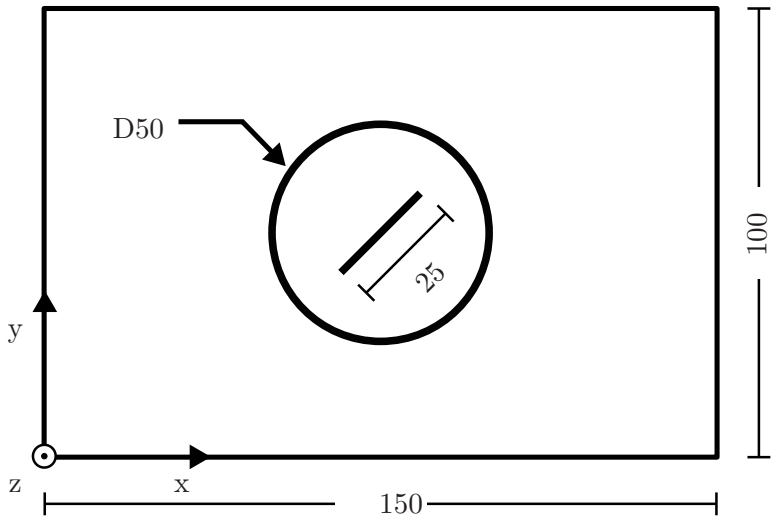

Figure 3.7.: Artificial CAI-like coupon dimensions in (mm). Schematic representation of the artificial delamination and intralaminar cracks.

3.3.3. Acquisition of NDI Images

As discussed before, pulse-echo ultrasound and µCT are viewed as appropriate inspection methods for the detection of impact damage-related defects. Visual inspection and the destructive de-ply technique are also considered.

By visual inspection, the impact-induced indentation is measured with a dial indicator. Superficial fiber and major matrix cracks are captured using a caliper. In addition, the specimens are subjected to ultrasonic pulse-echo inspection, at normal incidence. A Hillgus system equipped with an Olympus V309-2 transducer is employed. The sampling frequency is set to 5 MHz and the probe points are distributed along a 0.25 mm by 0.25 mm grid. These inspections are conducted for all impact-damaged and artificially damaged coupons.

In addition, µCT inspection is conducted on six specimens, impacted at 40 J. The tomograms are obtained from a GE phoenix v|tome|x L450 device. The applied tube voltage and current intensity are respectively 200 kV and 380 µA. In order to identify small defects, a spacial resolution (i.e. voxel size) of 51.81 µm is employed.

From the µCT inspected specimens, three are further submitted to destructive testing, using the de-ply technique. This method is adopted to determine the effective fiber crack distribution through the thickness. Experimentally obtained fiber crack orientations and lengths are presented in appendix A.2. These results pose an appropriate basis, for validating the fiber cracks, obtained from µCT image analysis.

3.4. Damage Characterization Method

Based on the advances in computer vision, introduced in sub-section 3.2.3, a method is proposed that supports NDI image analysis for impact damage characterization in CFRP structures. Different algorithms are adopted and developed to process the NDI results, acquired by ultrasonic and µCT inspection. The first is predominantly responsible for providing data for delamination characterization. Although the latter provides insight into both, inter- and intralaminar defects, deriving delamination contours from ultrasonic inspection images is more straight-forward.

In view of the subsequent damage assessment module, the present method's principal objectives consists in deriving sufficiently accurate damage contours, and in assigning them to their correct position in the layup architecture. A realistic representation of the damaged structure and its mechanical behavior can only be attained by considering these details.

Given the very distinct nature of ultrasonic and µCT images, the adopted image analysis approaches are presented and discussed separately in the following sub-sections.

3.4.1. Analysis of Ultrasonic Images

The analysis of ultrasonic datasets, as implemented in this damage characterization module, follows the general image processing workflow, presented in figure 3.4. This is initiated by a raw image (D-scan), depicting the 3D coordinates of features, reflecting the ultrasonic pulse (figure 3.8).

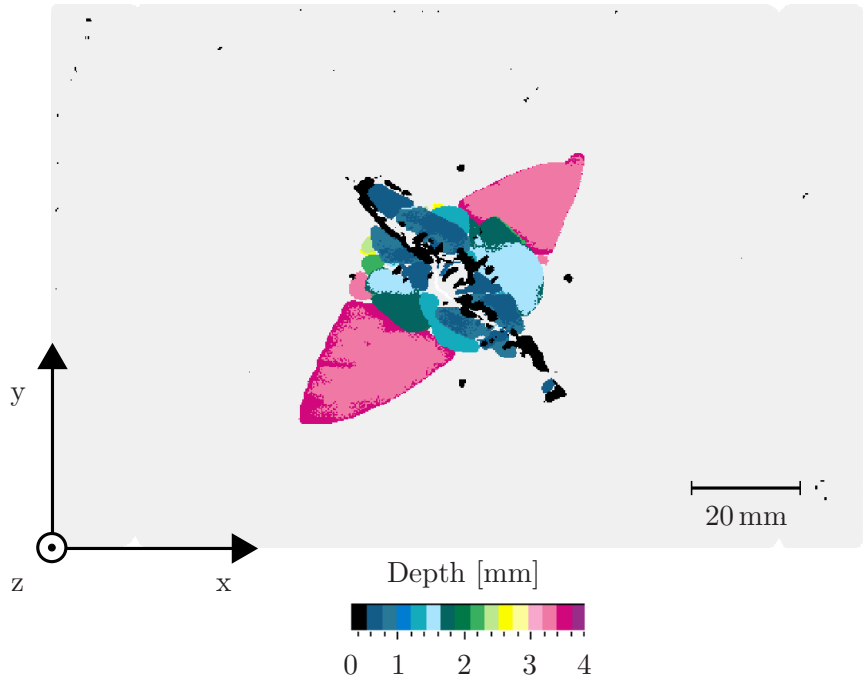

Figure 3.8.: Exemplary D-scan, obtained from a CAI coupon, impacted at 40 J.

Due to excellent contrast generally found in D-scan images, the pre-processing is confined to noise reduction. This occurs by means of two simple steps. First, by defining a rectangular ROI, enclosing the impact damage. This is an effective means of regarding only for relevant pixels,

based on their location. Then, small pixel agglomerations can be suppressed, based on their size.

D-scan results are commonly presented with a spectrum, indicating the depth of detected structures (figure 3.8). This offers a good perception of the defect's 3D position. However, that segmentation and classification is inappropriate for deriving defect contours.

Plotting the depth of relevant pixels in a histogram (figure 3.9), they are mostly found agglomerating at discrete depths, which correspond to the laminate interfaces. This particularity is the key to this new histogram-based image segmentation algorithm. Hereby, multiple thresholds are defined, based on the provided layup architecture (green scale in figure 3.9). By default, these thresholds are defined from one stack mid-plane to the next adjacent stack mid-plane, thus spanning over the nominal interface. Thresholds can be adjusted manually, if required. Pixels, whose depths are found between two consecutive thresholds, are projected onto a single plane. These are eventually classified as delaminations and are assigned to the nominal interface depth. This assignment is in agreement with the empirical findings, which point to impact-induced delaminations establishing only between stacks of different orientation.

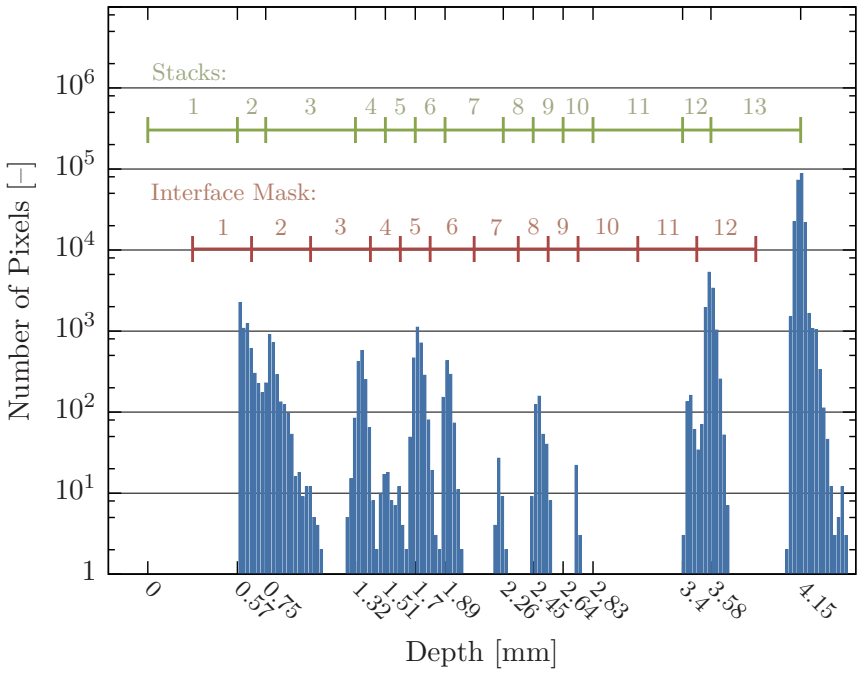

Figure 3.9.: D-Scan histogram of an impacted CAI specimen, depicting the number of defect pixels found at specific depths, measured from the inspected surface. The interface mask is derived from the layup and indicates the pixel segmentation scheme. Bars at roughly 4.15 mm represent the back-wall.

The presence of signal noise and the shielding effect lead to fragmented delamination areas, thus requiring image reconstruction. This occurs in several steps. In a first step, the segmented pixels are approximated by polygonal contours, in each interface. For that purpose, the algorithm proposed by Suzuki and Abe [76] is adopted, which returns the object borders from binary images. By evaluating the damage polygons, single, projected, and total delamination areas can be accurately

determined.

In a second step, a novel shielding compensation method is applied, to achieve empirically consistent defect contours. Through the long period of impact damage research, typical characteristics of impact-induced delamination damage have been identified (c.f. sub-section 3.2.1). For the present image reconstruction algorithm, typical delamination characteristics are considered as binding requirements. They are summarized as follows:

1. Delaminations establish between adjacent stacks of different orientation.
2. Interlaminar damage is found in each interface between the top-most and bottom-most delamination, typically presenting distribution patterns, as depicted in figure 3.3.
3. The major delamination axis direction matches the lower adjacent ply orientation.
4. Impact induced delaminations consist of single areas, resembling a peanut silhouette.

As discussed in the context of segmentation and classification, the first requirement is satisfied by the adopted histogram-based thresholding algorithm, which assigns relevant pixels to the discrete layup interfaces.

Although interlaminar damage is expected to establish at each interface, some delamination may go fully undetected. This occurs, when a particular delamination does not exceed the above-lying shield[5] (figure 3.10a). To satisfy the second requirement, this limitation is overcome, by defining an ellipsis under the shield, as depicted in figure 3.10b. Its center is set in congruency with the estimated impact point, which in turn is assumed to coincide with the centroid of all projected delaminations.

In compliance with the third requirement, the ellipsis major axis is aligned with the lower adjacent stack orientation. Major and minor axis lengths are determined by the shield's periphery (indicated by the blue points in figure 3.10b). Finally, only effectively shielded portions of the ellipsis are regarded as potential defects, while fragments exceeding its extension are suppressed (figure 3.10c).

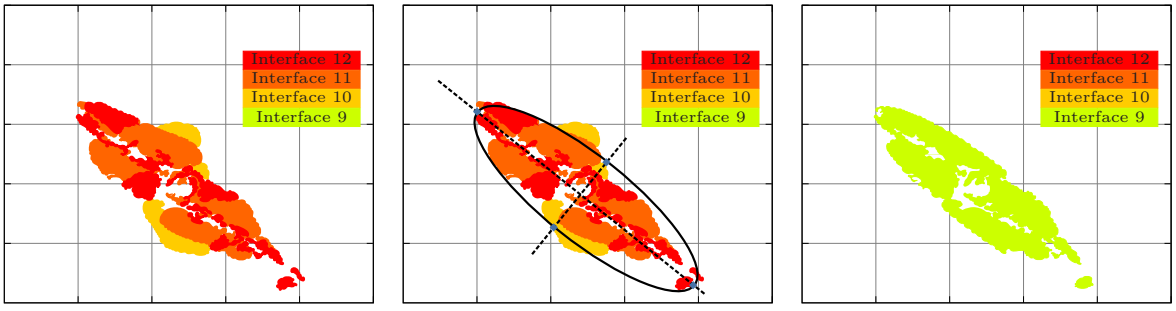

(a) Shield (b) Ellipse construction (c) Potential delamination extension

Figure 3.10.: Shield compensation steps at the 9th interface.

While some delaminations are obscured by the shield in their totality, others are only partially

[5]Shield designates the combined projection of defect features within a determined region.

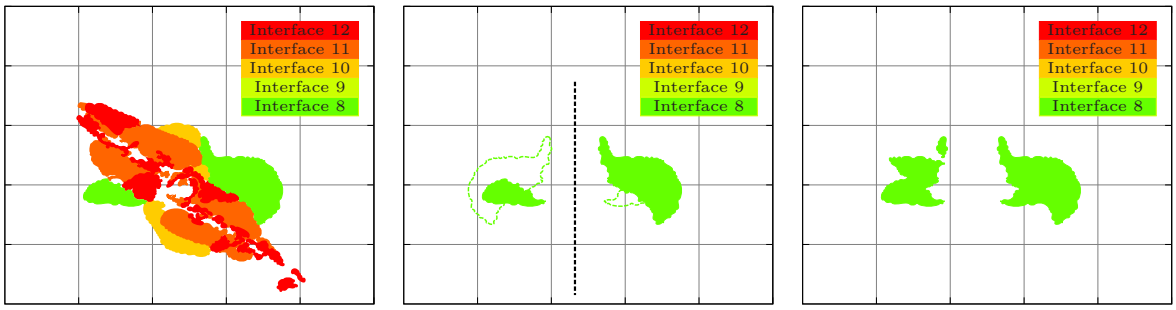

(a) Shield and 8th interface (b) Defect mirroring (c) Potential delamination extension

Figure 3.11.: Shield compensation steps an the 8th interface.

shielded, as depicted in figure 3.11a for the 8th interface. However, the most part of the delamination is likely to be covered by the shield. For such fragmented delaminations, another shield compensation algorithm is suggested. It consists in mirroring the detected portions about a symmetry axis. This is defined as running through the computed impact point, while being orthogonal to the lower adjacent stack orientation (figure 3.11b). Then, similarly to the previous shadowing compensation algorithm, the shield is applied as mask, to return a more realistic delamination extension (figure 3.11c).

The final reconstruction step following shield compensation is the derivation of realistic delamination contours, in compliance with the fourth requirement mentioned above. For that purpose, an enveloping hull is defined around the assumed delamination fragments, in each interface. Different envelope types are implemented, and their influence on the predicted residual strength is discussed in sub-section 3.6.1.

Figure 3.12 depicts the delamination fragments at the first interface, along with the implemented envelope types. The convex hull algorithm returns a convex envelope, which coincides with the delamination fragment borders, wherever they are convex. Apart from that, this contour bridges over gaps and concave regions. Two elliptical hull types are also implemented, which can be readily described by a 2D mathematical function. This delamination description is especially preferred by analytical damage assessment methods [26–30]. Hereby, the best fit ellipsis represents a least-square fit to the provided delamination fragments. On the other hand, the aligned ellipsis is derived from a defect enveloping rectangle, presenting the same orientation as the lower adjacent ply. Both, polygon- and star-based envelopes, represent the most realistic delamination contours, as they enable peanut-silhouette representation. The difference between the two is depicted in figure 3.13.

As suggested by figure 3.13a, the final delamination envelope (solid thick line) is obtained based on a polygon (dashed thin lines), connecting the fragment centroids, represented by orange circles. The segment narrowing between the fragments is controlled by the parameter f, that scales the distance between envelope segment and inner polygonal chord. Regarding the star-based hull (figure 3.13b), the center structure (thin dashed lines) results from each defect centroid being connected to the image centroid. The same narrowing algorithm is also applied to the star-

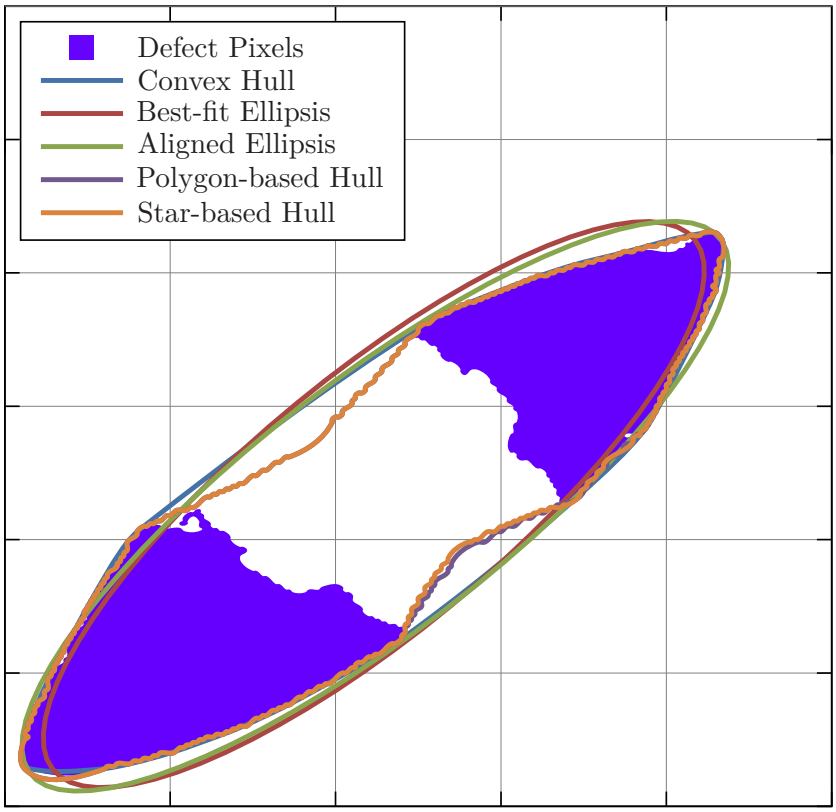

Figure 3.12.: Delamination envelope derivation using different approaches.

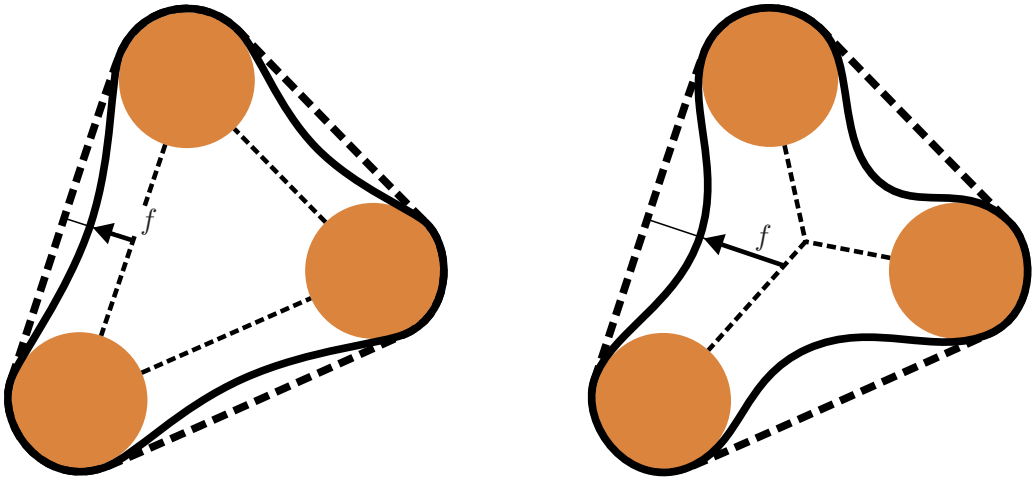

(a) Polygon-based Hull

(b) Star-based Hull

Figure 3.13.: Envelope construction for a generic image, using polygon- and star-based hulls.

based hull. Due to the different chord shapes, applying the same scaling factor yields distinct results, whenever more than two non-collinear delamination fragments are considered. The default narrowing parameter f is set to 25 %.

The output of this ultrasonic image analysis method consists, on the one hand, of a detailed delamination size analysis, for each interface and in total. On the other hand, the resulting contours are provided as common industry formats (Extensible Markup Language (XML) and Initial Graphics Exchange Specification (IGES)), for further consideration in the subsequent damage assessment module.

3.4.2. Analysis of µCT Images

In order to return defect contours from µCT images, the raw dataset is submitted to a series of steps, according to figure 3.4. While this generic workflow applies in principle to both, ultrasonic and µCT image analysis, the implemented algorithms for processing µCT datasets are much more demanding. On the one hand, this is attributed to the 3D nature of the image, and the associated necessity, of extending existing image processing algorithms to the third dimension. On the other hand, contrast between very small defects and the intact structure is fairly low, often being hardly distinguishable. Although the radiation absorption coefficients of air (i.e. the gap) and carbon (i.e. the main constituent of CFRP structures) are very dissimilar, thus suggesting excellent distinctiveness, contrast is also affected by image resolution. This, however, is limited by the adopted inspection equipment. As a rule of thumb, the volumetric pixel (voxel) size should be at least half the sought-for defect extension. This inevitably leads to very small features being either undetectable, or of poor contrast.

The process for obtaining intralaminar defect contours from µCT images, requires many processing steps at two different levels. First, image pre-processing, segmentation and classification is conducted on 3D µCT images. These processing steps result in two new images (for intra- and interlaminar defects), where the impact-induced deformation is reversed. In doing so, defect identification, classification, and assignment to its correct position in the layup architecture is enabled. At the second level, 2D ortho-slices (i.e. offsets from the top surface) of these intermediate images are submitted to segmentation, classification, and reconstruction (c.f. figure 3.4). The principal output of the second level consists in the provision of relevant intra- and interlaminar defect idealizations, assigned to their respective position in the laminate.

At the beginning of this method's development, µCT image analysis methods, proposed by other authors, supported merely the segmentation of damage, yet disregarding their assignment to the layup, which however is considered crucial for deriving meaningful damage assessment models. In the meantime, new methods have recently been proposed [35, 71], describing similar approaches, to the one being presented in this sub-section.

[6] In the present context, standard deviation is often referred to as scale space constant or simply scale.

3.4.2.1. Analysis of 3D µCT Images

The pre-processing of µCT images consists of reducing signal noise and highlighting the sought-for defects. As discussed before, the many advantages associated to the Gaussian blur filter commend it to the present application. For the n-dimensional space and considering a standard deviation[6], s, the Gaussian function $g(\mathbf{x}, s)$ is defined by equation (3.1), where $\mathbf{x}$ is the pixel position vector and $\|\mathbf{x}\|_2$ is its Euclidean norm.

$$g(\mathbf{x}, s) = \frac{1}{\sqrt{2\pi \cdot s^2{}^n}} \cdot e^{-\frac{\|\mathbf{x}\|_2^2}{2s^2}} \tag{3.1}$$

Gaussian blur kernels, $\mathbf{G}_s$, for arbitrary scales, s, are obtained by discretization of the bell-shaped function, $g(x, s)$. The recommended convolution filter size depends on the chosen scale, s. A good approximation is achieved, when the kernel size equals the first odd integer greater than $6s$ [64]. The respective kernel coefficients are obtained by numerical integration of the Gaussian function.

Besides high-frequency noise reduction with a Gaussian blur filter, an object enhancement algorithm is implemented, based on the previously introduced DoH method. The Hessian matrix, $\boldsymbol{\mathcal{H}}_s$, is defined by equation (3.2). Matrix coefficients are determined by second-order partial derivation of the field, $\boldsymbol{\mathcal{F}}$, which represents the raw image, $\boldsymbol{\mathcal{I}}$, blurred by the Gaussian kernel, $\mathbf{G}_s$. For that purpose, a discrete second-order partial derivative operator, $\mathbf{d}_{s,\mathrm{ij}}$, is employed (left-hand side of equation (3.3)). Due to the convolution[7] operation's associative property and taking advantage of the Gaussian function's differentiability, this can be reduced to a single convolution (right-hand side of equation (3.3)), for higher computational efficiency. This is defined by the convolution between kernel $\mathbf{D}_{s,\mathrm{ij}}$, representing the discretized continuous second-order partial derivative of the Gaussian function, $g(x, s)$, and the raw image, $\boldsymbol{\mathcal{I}}$. Contrary to the recommended kernel size for Gaussian function approximation, an appropriate size for sampling the Gaussian function's second-order partial derivative is now given by the next odd integer greater than $7s$ [64]. Factor s^2 in equation (3.3) is introduced for scale-normalization, thus ensuring the response compatibility, obtained at different scales.

$$\boldsymbol{\mathcal{H}} = \begin{bmatrix} \frac{\partial^2 \boldsymbol{\mathcal{F}}}{\partial x_1^2} & \frac{\partial^2 \boldsymbol{\mathcal{F}}}{\partial x_1 \partial x_2} & \frac{\partial^2 \boldsymbol{\mathcal{F}}}{\partial x_1 \partial x_3} \\ \frac{\partial^2 \boldsymbol{\mathcal{F}}}{\partial x_2 \partial x_1} & \frac{\partial^2 \boldsymbol{\mathcal{F}}}{\partial x_2^2} & \frac{\partial^2 \boldsymbol{\mathcal{F}}}{\partial x_2 \partial x_3} \\ \frac{\partial^2 \boldsymbol{\mathcal{F}}}{\partial x_3 \partial x_1} & \frac{\partial^2 \boldsymbol{\mathcal{F}}}{\partial x_3 \partial x_2} & \frac{\partial^2 \boldsymbol{\mathcal{F}}}{\partial x_3^2} \end{bmatrix} \tag{3.2}$$

$$s^2 \cdot \mathbf{d}_{s,\mathrm{ij}} * \underbrace{(\mathbf{G}_s * \boldsymbol{\mathcal{I}})}_{\boldsymbol{\mathcal{F}}} = s^2 \cdot \mathbf{D}_{s,\mathrm{ij}} * \boldsymbol{\mathcal{I}} \tag{3.3}$$

Considering the symmetry about the Hessian matrix main diagonal, six distinct images, $\mathbf{D}_{s,\mathrm{ij}} * \boldsymbol{\mathcal{I}}$, are computed, according to the Hessian coefficients. The respective eigenvalues, λ_k, and eigenvectors, $\mathbf{v}_k$, are obtained from equations (3.4) and (3.5), respectively, where $\mathbf{I}$ is the identity matrix.

[7] The mathematical symbol for convolution is $*$.

$$det\left(\boldsymbol{\mathcal{H}} - \lambda \mathbf{I}\right) = 0, \tag{3.4}$$

$$\left(\boldsymbol{\mathcal{H}} - \lambda_k \mathbf{I}\right) \mathbf{v}_k = 0. \tag{3.5}$$

In the 3D space, three eigenvalues and three eigenvectors are obtained for each voxel. The ortho-normal eigenvectors are the axes of the characteristic ellipsoid, which describes the voxel's local second-order structure. In turn, the eigenvalues correspond to the lengths of the ellipsoid semi-axes (i.e. the eigenvector's magnitudes), and are a measure of contrast [66]. In other words, each voxel's characteristic ellipsoid not only describes the contrast with respect to its neighborhood, but also the shape and orientation of the object it belongs to.

Referring to figure 3.14, the gray cube represents a single voxel, pertaining to a flat object (flat ellipsoid in blue color). Due to its proximity to the object boundary, the contrast along the vertical axis (i.e. the eigenvalue, λ_3) is much higher than in the other ortho-normal directions (λ_1 and λ_2). The elongated shape of the orange-colored characteristic ellipsoid is consistent with the conditions $\lambda_3 \gg \lambda_2$ and $\lambda_2 \approx \lambda_1$, which characterize voxels, belonging to plate-like objects. More generally, analyzing the Hessian eigenvalues sorted according to their magnitudes ($|\lambda_1| \leq |\lambda_2| \leq |\lambda_3|$), the object shape is classified according to table 3.3 [66].

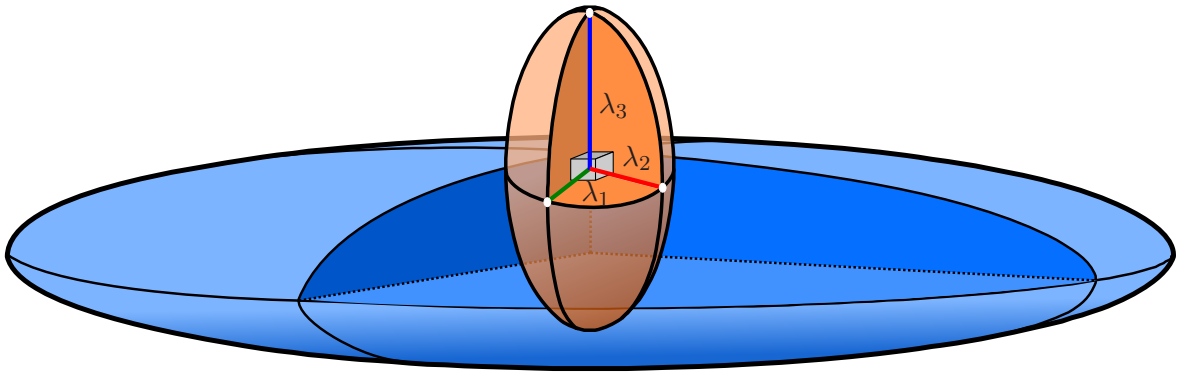

Figure 3.14.: Generic representation of the characteristic ellipsoid (orange shape), at an edge voxel, inside a flat object (blue ellipsoid).

Structure Shape	λ_1	λ_2	λ_3
Noise	L	L	L
Blob-like	H	H	H
Tubular	L	H	H
Plate-like	L	L	H

Table 3.3.: Object shapes in 3D images (L: low, H: high).

Considering the blurred image's ($\mathbf{G}_s * \boldsymbol{\mathcal{I}}$) eigenvalues, the *objectness* at each voxel can be determined [67]. Contrary to the raw image, which visualizes the radiation absorption, the *objectness*

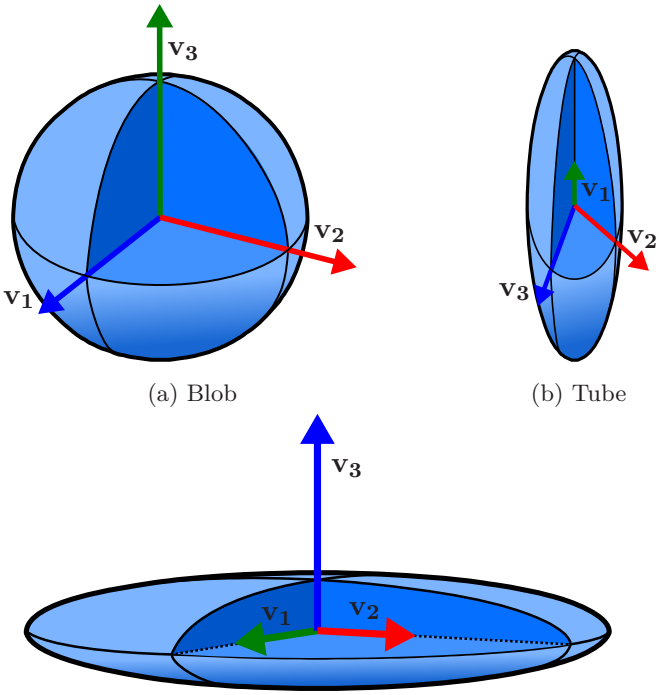

(a) Blob (b) Tube

(c) Plate

Figure 3.15.: Characteristic structures for object classification.

image depicts the degree of resemblance of a particular detected object, with respect to a determined characteristic structure: blob, tube, or plate (figure 3.15).

Since inter- and intralaminar impact-induced defects are described as line-cracks, extruded in a certain direction, the sought-for objects in µCT images are of plate-like shape. For the purpose of highlighting such objects, the *plateness* measure, P, is defined by equation (3.6) [67].

$$P = e^{-\frac{r^2}{2\beta^2}} \cdot \left(1 - e^{-\frac{S^2}{2\gamma^2}}\right), \tag{3.6}$$

The ratio, r, between the two largest eigenvalues (equation (3.7)) indicates, whether the object is rather tubular ($r \to 1$) or plate-like ($r \to 0$).

$$r = \frac{|\lambda_2|}{|\lambda_3|} \tag{3.7}$$

The *structureness*, S, is the Frobenius norm of the Hessian matrix and is defined in equation (3.8). The term in equation (3.6) containing S is used to control the sensitivity of the *plateness*, P, to background noise [67]. The constants β and γ are user-defined parameters, which have been set as defaults to 0.2 and 1.68×10^7, respectively.

$$S = \sqrt{\lambda_1^2 + \lambda_2^2 + \lambda_3^2} \tag{3.8}$$

Impact-induced defects cover a wide range from narrow to open-wide cracks. Since the DoH algorithm only highlights objects of similar size of the applied kernel, a multi-scale approach is highly recommended. Hereby, the raw image, $\boldsymbol{\mathcal{I}}$, is convolved with $\mathbf{D}_{s,\mathrm{ij}}$-filters at different scales, s, covering the full spectrum of expected crack sizes. The multi-scale *plateness* image, $\boldsymbol{\mathcal{P}}_{max}$, ultimately results from keeping the maximum response at each voxel position, $\mathbf{x}$, through all the *plateness* images obtained at different scales, $\boldsymbol{\mathcal{P}}_s$ (equation (3.9)). The implemented workflow for 3D image processing is summarized in figure 3.18, on page 41.

$$\boldsymbol{\mathcal{P}}_{max}(x) = \max_{s\in[s_{min},\ldots,s_{max}]} \{\boldsymbol{\mathcal{P}}\in_s(x)\}. \tag{3.9}$$

Besides returning the *plateness* images, $\boldsymbol{\mathcal{P}}_s$, two further images are generated at each scale, s, describing the major eigenvector polar and azimuth angles, $\boldsymbol{\Theta}_s$ and $\boldsymbol{\Phi}_s$, at each pixel (figure 3.16). The voxel values of the merged multi-scale images, $\boldsymbol{\Theta}_{max}$ and $\boldsymbol{\Phi}_{max}$, are collected from the single-scale polar and azimuth images, according to a mask. This mask is derived from the previous *plateness* merging step, which indicates each voxel's source image. By applying this mask, the polar and azimuth angles corresponding to the $\boldsymbol{\mathcal{P}}_{max}$ voxels are obtained (c.f. figure 3.18).

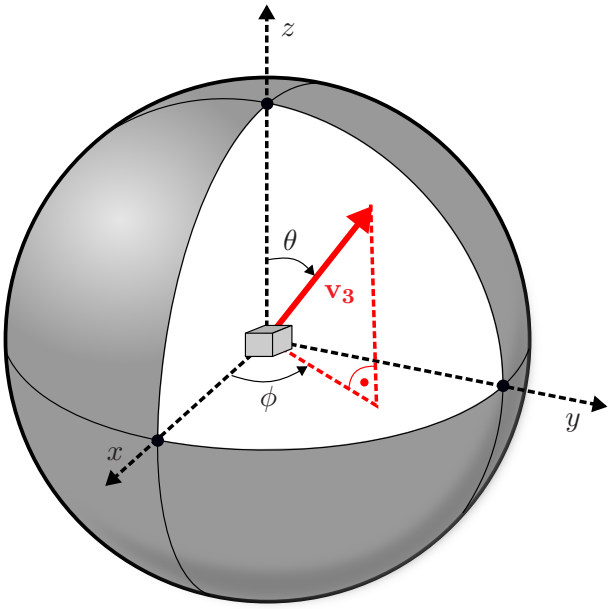

Figure 3.16.: Definition of polar θ and azimuth ϕ angles.

After increasing the raw image contrast, by exploring its second-order structure, a first segmentation step is conducted on the multi-scale *plateness* image, P_{max}. Inspired by the edge detection algorithm proposed by Canny [69], segmentation by hysteresis thresholding is implemented for 3D images, in order to suppress objects of weak *plateness* value. This provides more realistic and less fragmented candidate defect features (c.f. figure 3.18).

As depicted in figure 3.18, applying the hysteresis filtered *plateness* image, $\boldsymbol{\mathcal{P}}_{hys}$, as a mask on the polar and azimuth angle images, $\boldsymbol{\Theta}_{max}$ and $\boldsymbol{\Phi}_{max}$, is an effective means of suppressing irrelevant

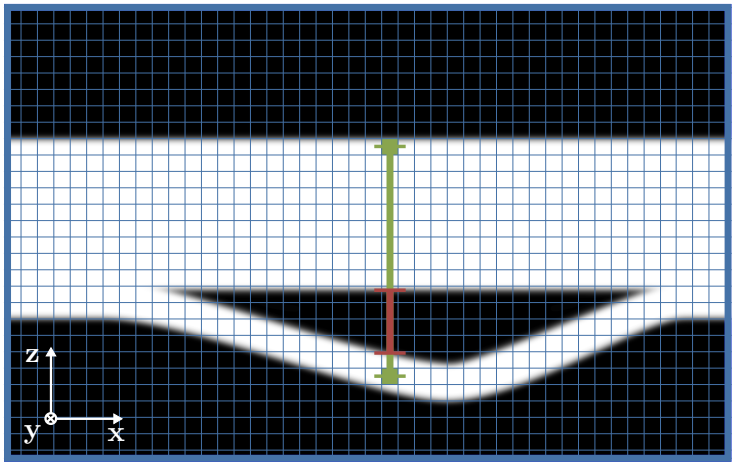

Figure 3.17.: Generic representation of a sectional view through a region with delamination damage. Effective euclidean distance between an arbitrary pixel and the closest top surface pixel is the sum of all segments, highlighted in green color.

voxels from these images. Since interlaminar damage is roughly orthogonal to the part's through-the-thickness direction, whereas intralaminar cracks are rather parallel or oblique to it, pixels can be separated based on their polar angles. For this purpose, hysteresis thresholding is applied to $\mathbf{\Theta}_{msk}$, resulting in two intermediate volumetric images: one comprising mainly interlaminar, $\mathbf{\Theta}_{inter}$, and another predominantly consisting of intralaminar defects, $\mathbf{\Theta}_{intra}$.

In order to counteract impact-induced deformation, relevant voxels are relocated, based on their effective Euclidean distance to the specimen's top surface. This is the shortest straight segment of a specific voxel to the top surface, subtracted by segment lengths, running through candidate delaminations (figure 3.17). The result of this compressing algorithm is an undeformed volume, aligned with the image axes. This is applied to the inter- and intralaminar volumes ($\mathbf{\Theta}_{inter}$ and $\mathbf{\Theta}_{intra}$), thus enabling the correct assignment of individual damage pixels to their true positions in the laminate (c.f. figure 3.18).

Similarly to the segmentation and classification of ultrasonic images (c.f. figure 3.9), a multi-threshold approach is applied to the compressed interlaminar damage volume, $\mathbf{\Theta}_{inter}$, (c.f. figure 3.18). This enables the separation of delamination voxels, based on their distance to the top-surface, and their classification according to the layup interfaces. The respective thresholds are located at the stack mid-planes, such that defects in ortho-slices between two consecutive thresholds are projected onto one plane, representing an interface. The resulting volumetric image is finally comprised by a number of ortho-slices, equivalent to the amount of layup interfaces.

In order to distinguish intralaminar damage modes, the intralaminar damage volume $\mathbf{\Theta}_{intra}$ is submitted to the same compressing algorithm. However, relocated voxel values are adopted from their position equivalent voxels in the azimuth angle volume, $\mathbf{\Phi}_{msk}$, resulting in a compressed version of this image. A multi-threshold segmentation approach is also employed to distinguish the intralaminar defects, and to classify them by stack number (c.f. figure 3.18). For that purpose, the thresholds are defined according to the stack boundaries. All damage voxels within two consecutive thresholds are assigned to the respective stack. In this volume, ortho-slices and layup

stacks are of equivalent number.

Figure 3.18 summarizes the workflow, implemented for deriving intra- and interlaminar damage volumes, for further analysis of the respective 2D ortho-slice images.

3.4.2.2. Analysis of 2D µCT Images

To finally determine the defect contours, the compressed volumes, resulting from the 3D image analysis, are submitted to further image processing steps. For this purpose, 2D ortho-slices are separated and analyzed. Although, in the context of µCT image analysis, the focus is on the extraction of intralaminar defects, delamination damage is also addressed in the following.

Regarding the ortho-slices of the compressed intralaminar damage volume, they entail the azimuth angles, ϕ, of both, fiber and matrix cracks. To distinguish both defect types, the stacking sequence and part orientation is required. The basis for the implemented histogram-based segmentation are the assumptions that matrix cracks are aligned with the stack's fiber orientation, and that fiber fractures assume orientations other than the stack direction. Considering the azimuth angles, ϕ, and the fiber orientation in each stack, defect voxels are separated and classified as fiber or matrix cracks (figure 3.19). Currently, the reconstruction of realistic fiber cracks is conducted manually. These defects are idealized as straight lines, spanning over the extension of all voxels, classified as fiber fracture. This simplification is in good agreement with the crack morphology, found through destructive de-ply tests.

As discussed in sub-section 3.2.1, small matrix cracks are of minor importance, regarding their influence on the residual strength. However, large splits, typically installing at the impact-averted stack, may exert a noticeable influence. Thus, these cracks are also characterized by a straight line.

Regarding the interlaminar damage volume, segmentation and classification are dispensed, because the image only contains delamination damage (figure 3.18). The obtained voxel agglomerations for each ortho-slice can be evaluated by the same methods employed for ultrasonic image analysis.

3.4.3. Generic Fiber Crack Distribution

Although fiber crack distribution in impact-damaged laminates can be characterized from µCT images, such proper datasets are rarely available. Before this background, an additional method is implemented, which estimates the through-the-thickness distribution of fiber cracks, by extrapolation of superficial fractures. A parametric function (equation (3.10)) is implemented for predicting the fiber crack length, l_{FC}, in each stack, q_i, between the initial stack, where the crack is measurable (generally at the impacted side), q_{ini}, and an the last stack, with the smallest extrapolated crack, q_{fin}. The respective crack lengths are the measured extension, $l_{FC,ini}$, and an arbitrary crack length at the final stack, $l_{FC,ini}$. A proper parameter choice is given by table 3.4. Their agreement with results, obtained from destructive inspection, is depicted in figure 3.20. It is noted, that the crack orientation is by default orthogonal to the respective stack direction. The residual strength sensitivity to the adopted function parameters is discussed in sub-section 3.6.1.

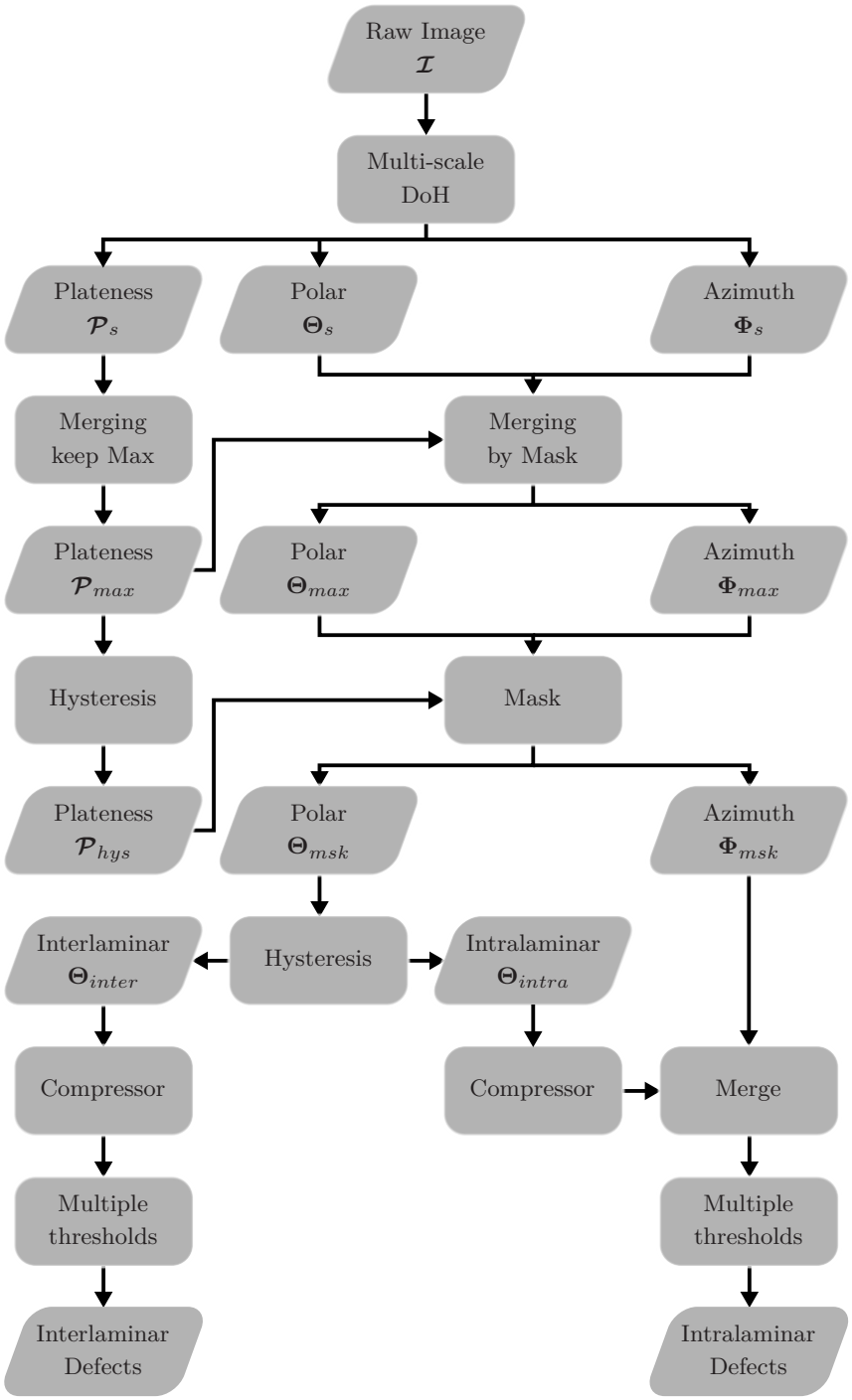

Figure 3.18.: Implemented workflow for processing 3D images, obtained from µCT. Trapezoids represent volumetric images, while rectangles denote processing steps.

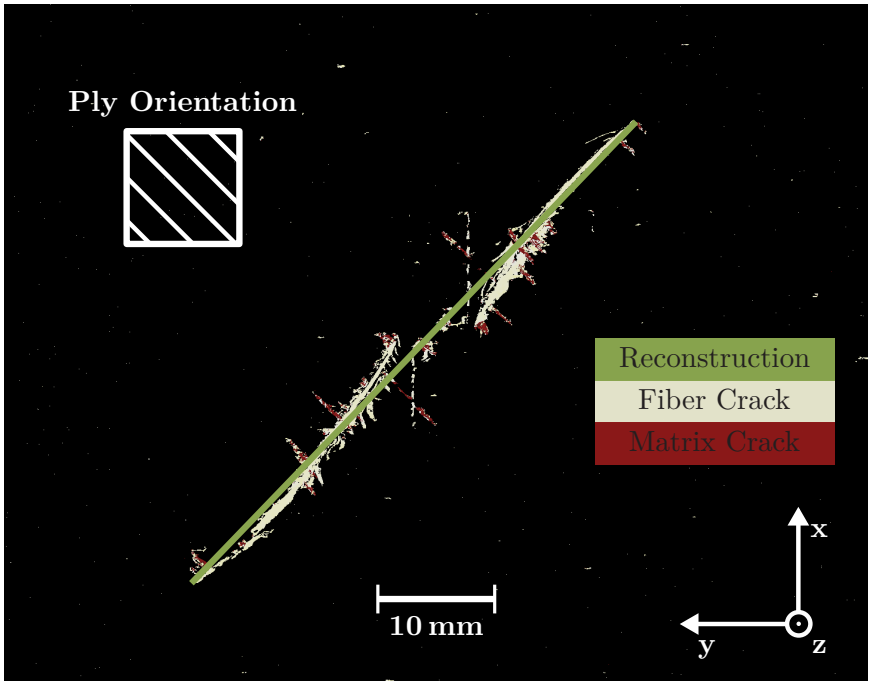

Figure 3.19.: 2D image analysis of the top-most stack. Defects are segmented and classified as fiber and matrix cracks, according to the ply orientation. Fiber crack is reconstructed as a straight segment.

$$l_{FC}(q_i) = l_{FC,fin} + (l_{FC,fin} - l_{FC,ini}) \cdot \left(c_1 + c_2 \cdot \eta_i + c_3 \cdot \eta_i^2 + c_4 \cdot \eta_i^3\right), \tag{3.10}$$

with

$$\eta_i = \frac{q_i - q_{ini}}{q_{fin} - q_{ini}}. \tag{3.11}$$

Function Type	Constants			
	c_1	c_2	c_3	c_4
Constant	1	0	0	0
Linear	0	1	0	0
Quadratic	0	$0 \leq c_2 < 1$	$1 - c_2$	0
Cubic	0	> 0	< 0	$c_4 = 1 - c_3 - c_2$

Table 3.4.: Coefficients for fiber crack length extrapolation function (equation (3.10)).

.

Analysis results, obtained from µCT images are also exported as IGES or XML files, for further consideration in the subsequent damage assessment module.

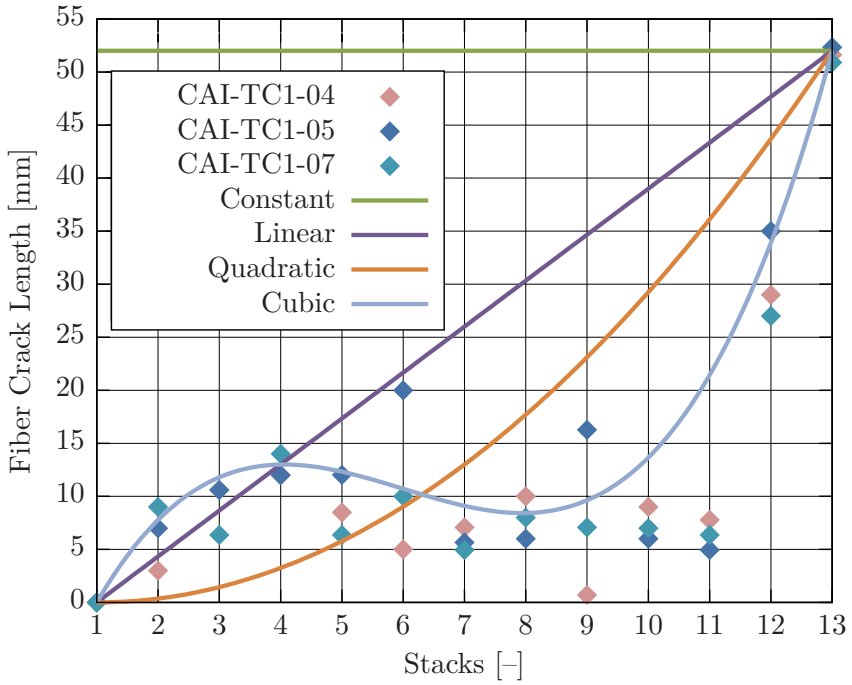

Figure 3.20.: Projected fiber crack lengths, determined experimentally and through extrapolation. Coefficient specifications for quadratic: $c_2 = 0$, and cubic functions: $c_2 = 2.3$, $c_3 = -6.5$.

3.5. Results and Validation

In this section, the results obtained from the aforementioned algorithms are discussed, regarding their conformity with effectively measured defects. These are obtained from three specimens, impacted at 40 J and submitted to destructive testing (c.f. table D.4).

3.5.1. Interlaminar Damage

Ultrasonic inspection is the appointed technique for delamination detection. Owing to the technique's nature, delaminations in impact damaged laminates present themselves either plainly or fragmented, the latter being attributed to the shielding effect. Thus, two main aspects regarding the adopted image analysis approach are discussed.

First, the methods capability in accurately returning the true defect extension is discussed. For that purpose, specimens with single artificial delaminations pose a proper validation basis, because the defect shape is known a priori and the image is free from shielding effects. The nominal delamination area is 1963 mm^2, for specimens from the series A, B, AC, and BC, which results from the inclusion of a circular Teflon foil (50 mm in diameter). Delamination areas, derived for each specimen by the present method, are listed in tables E.1, E.2, E.5 and E.6, in appendix E. Measured delamination areas are found slightly exceeding the nominal area by an average of 3 % and by 5 % at most. This is a rather moderate error, which may result from the employed manufacturing tolerances.

The second aspect being discussed, is the method's ability in representing shielded delaminations,

considering the implemented shielding compensation algorithms. Currently, available inspection methods (both, destructive and non-destructive) are inappropriate to determine the effective extensions of shielded delaminations. Even the method proposed by Freeman [62], who suggests the use of penetrants (e.g. gold chloride in diethyl ether), to display the damage extension during de-ply inspection, is found insufficient. This is because such a method requires a connection of all inner defects, to enable the penetrant reaching each cavity. This condition is not naturally given for an arbitrary impacted structure, thus causing reticence regarding its use. In spite of its poor resolution and the challenge of correctly assigning delamination voxels to their respective layup position, µCT images are considered the currently best available method. Delamination distributions, as resulting from the µCT image analysis proposed above, are regarded here as the baseline, for discussing the ultrasonic image analysis results. It is noted though, that this comparison is more viewed as a hint, rather than as a final algorithm validation.

Delamination contours, derived from ultrasonic image analysis, are qualitatively compared to µCT images, by superposing the respective results. Figure 3.21 depicts the overlapping images for each interface of specimen CAI-TC1-05. Two further comparisons are presented in appendix A.1. In general, results obtained by shield compensation are in good agreement with the interlaminar damage volume, obtained from a µCT image. They are mostly found enveloping relevant defect voxel. However, the automatic thresholds, applied to dissect the interlaminar volume, $\mathbf{\Theta}_{intra}$, into single interfaces, are in part found inappropriate. For instance, the threshold distinguishing the first two interfaces (figures 3.21a and 3.21b) is shown separating pixels, that evidently should be attributed to the first interface. Therefore, when considering the respective and adjacent µCT images, the estimated delamination contours are found fairly plausible. The estimated shape in figure 3.21f poses an exception. Even considering the adjacent images brings no harmony between the two results. However, excellent agreement is attained at the top interfaces (figures 3.21j to 3.21l). These findings are consistent with the observations regarding coupons CAI-TC1-04 and CAI-TC1-07 (c.f. figures A.1 and A.2).

3.5.2. Intralaminar Damage

The primary motivation for considering the µCT inspection technique is the offered detectability of intralaminar defects. Hereby, fiber crack characterization is of special interest. Defect characteristics, derived by the introduced image processing method, are compared to those, obtained from de-ply tests on three specimens. The results of specimen CAI-TC1-04 are discussed here, while the remaining results for coupons CAI-TC1-05 and CAI-TC1-07 are presented in appendix A.2, due to their similarity.

Figure 3.22 depicts the measured fiber crack lengths in each laminate stack. Fiber defect extensions derived from the µCT volume are also plotted along with the extrapolated fiber crack length, based on the cubic function of equation (3.10) ($c_2 = 2.3$, $c_3 = -6.5$). In a few stacks (4, 7, 8, and 13) the image analysis method suggests shorter cracks than those effectively measured. However, the error is rather low (less than 5 mm). In general, good coincidence between the results is attained. It is noteworthy, that the cubic extrapolation of the crack length at stack 13 renders a remarkably accurate approximation of the fiber crack length distribution. This also applies for the remaining

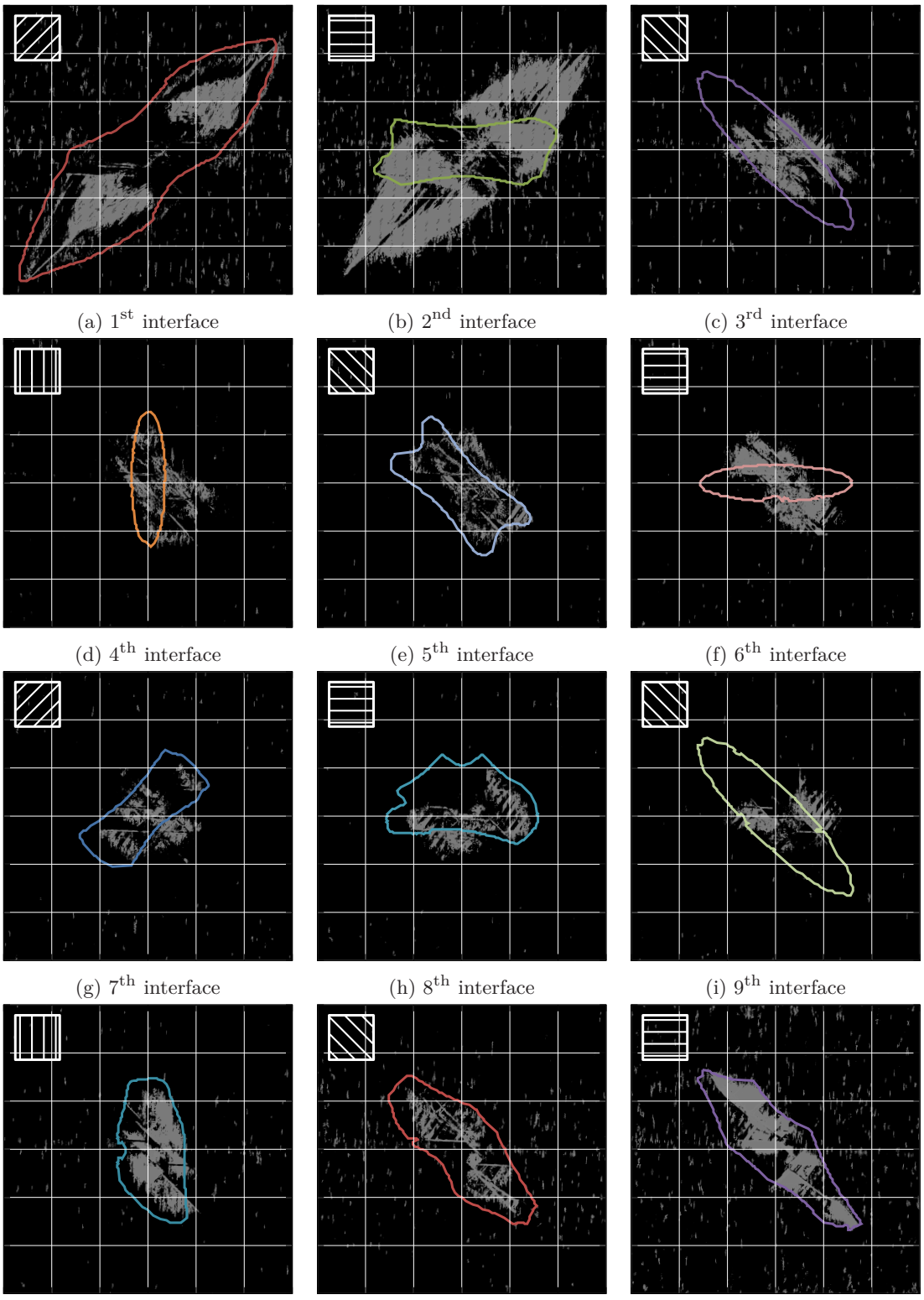

(a) 1st interface (b) 2nd interface (c) 3rd interface

(d) 4th interface (e) 5th interface (f) 6th interface

(g) 7th interface (h) 8th interface (i) 9th interface

(j) 10th interface (k) 11th interface (l) 12th interface

Figure 3.21.: Superposition of delamination contours from ultrasonic image analysis (polygons), with interlaminar damage pictures from µCT image processing (gray-scale figure), for specimen CAI-TC1-05. Grid line spacing is 10 mm. Adopted thresholds cause inappropriate voxel segmentation. However, considering the images of adjacent interfaces provides a good perception of the delamination extent.

two specimens (c.f. figures A.3 and A.6).

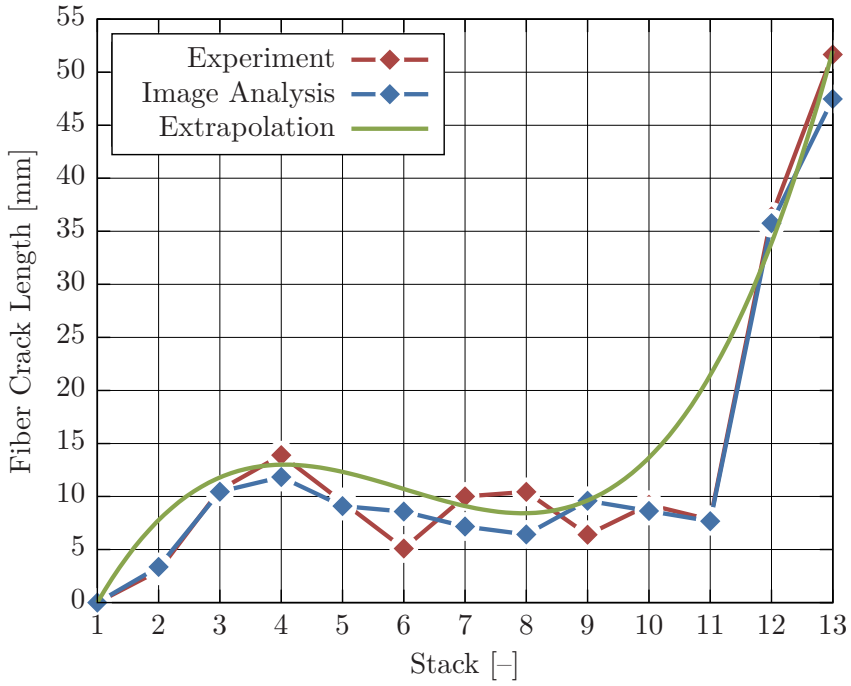

Figure 3.22.: Measured crack lengths derived from de-ply test, image analysis, and from the cubic extrapolation ($c_2 = 2.3$, $c_3 = -6.5$), for coupon CAI-TC1-04. Good agreement among the applied methods.

Regarding crack orientation (figure 3.23), good agreement is mostly attained, except for stacks 4, 5, 7, and 9, where the mismatch is between 30° and 90°. In these stacks, the experimentally determined crack direction is in conflict with the theoretically expected value.

From the perspective of damage assessment, the projected crack length is of special interest. This denotes the projection of the effective crack segment onto the axis, orthogonal to the stack direction. As such, it is a good indicator of loading capacity loss. The results plotted in figure 3.24 also point to very good agreement between all three methods.

Although matrix cracks are expected to exert a negligible effect on the residual stress, the major split at the impact-averted surface is also considered. It is shown that the split length of 104 mm is consistently found in all three specimens, as measured by visual inspection. However, µCT image analysis suggest a much shorter matrix crack length (80 mm in average). This is attributed to the applied thresholds for hysteresis filtering, adopted to suppress signal noise. Given the poor contrast due to the crack gap closing towards its ends, in combination with the rough image resolution, the split extremities have been suppressed, by the adopted filter settings. More generous thresholds may prevent this error from occurring, which however comes at the expense of higher signal noise in the images.

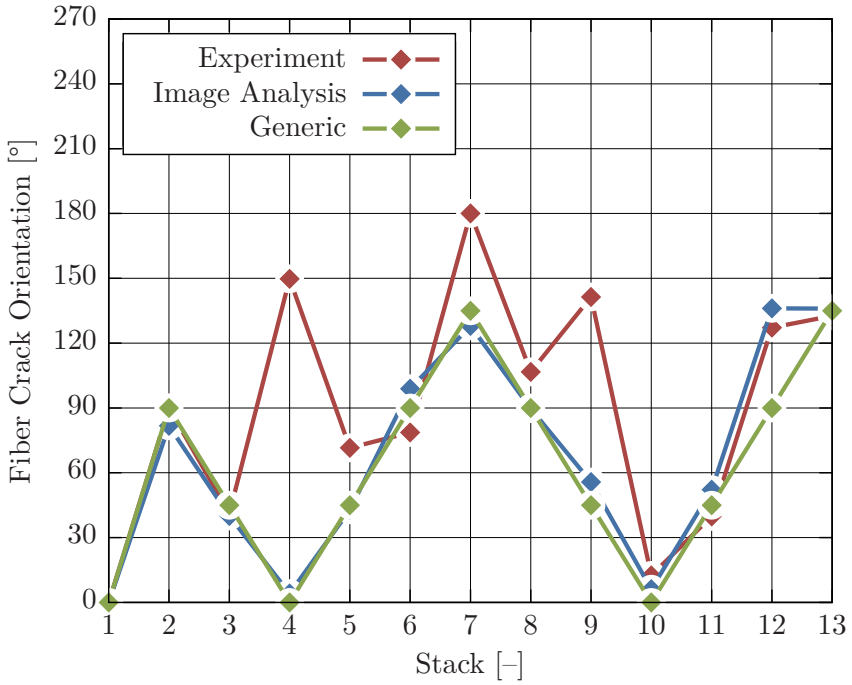

Figure 3.23.: Fiber crack orientations derived from de-ply test, image analysis, and from the generic method, for coupon CAI-TC1-04.

3.6. Sensitivity Study on Defect Parameters

As shown by the previous section, some discrepancies are found between the experimentally determined results, and those obtained by NDI image analysis. To assess the importance of these errors, a sensitivity study is conducted on specimen CAI-TC1-02 and on artificially damaged coupons (series B and D), under CAI test conditions. Three aspects are investigated: defect shape, combination of damage features, and damage scaling. Therefore, the detailed residual strength prediction model (introduced in the next chapter) is adopted, which — for now — be considered physically consistent.

3.6.1. Defect Shape

This study addresses different methods, implemented for reconstructing defect shapes, and their influence on the predicted residual strength.

3.6.1.1. Delamination Damage

Different shapes are proposed to represent delamination extension, as discussed in sub-section 3.4.1 and shown by example in figure 3.12. While varying the delamination shapes, the remaining intralaminar defects are fixed to one configuration.

In figure 3.25, the predicted CAISs are presented in relation to their corresponding values, determined through experimental testing. These results are presented along with the total delamination area, understood as the sum through all interfaces. It is noted, that the reference total delamina-

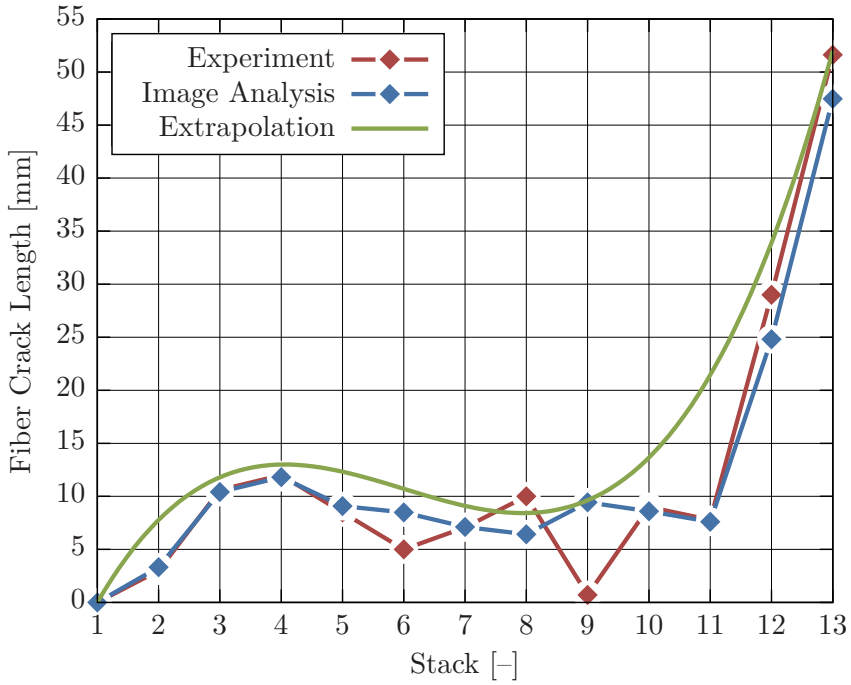

Figure 3.24.: Projected crack lengths derived from de-ply test, image analysis, and from the cubic extrapolation ($c_2 = 2.3$, $c_3 = -6.5$), for coupon CAI-TC1-04. Good agreement among the applied methods.

tion area is not available, due to a lack of proper methods for determining it.

Figure 3.25 depicts a realistic relation between total delamination area and residual strength, in as much as increasing defect areas are associated with residual strength reductions. In other words, the more generous the delamination shape representation is, the more conservative the predicted failure strength. By considering the implemented Envelope Types (ETs) as introduced in the context of figure 3.12, the predicted strengths range from 87 % to 96 % of the experimentally obtained value, thus suggesting an acceptable degree of conservatism associated to any of these representations[8]. Considering specimen CAI-TC1-02 is also shown, that the most realistic delamination representation, i.e. the star-based polygon (ET5), yields the most accurate residual strength approximation. Therefore, this representation is adopted throughout this thesis.

3.6.1.2. Fiber Crack Distribution

Regarding the through-the-thickness distribution of fiber cracks, this is either acquired from µCT images, or derived by extrapolation, based on the crack length, measured at the surface. In addition, the effectively determined distribution, resulting from the de-ply test on specimen CAI-TC1-04 is attributed to coupon CAI-TC1-02, considered in this study. Delamination envelope is set to star-based polygon and the major matrix split at the impact-averted surface is also considered. Figure 3.26 depicts the predicted CAIS and the sum of all fiber crack lengths through

[8] Referring to figure 3.12, the implemented delamination shape idealizations are abbreviated as ET1: convex hull, ET2: best-fit ellipsis, ET3: aligned ellipsis, ET4: polygon-based hull, and ET5: star-based hull.

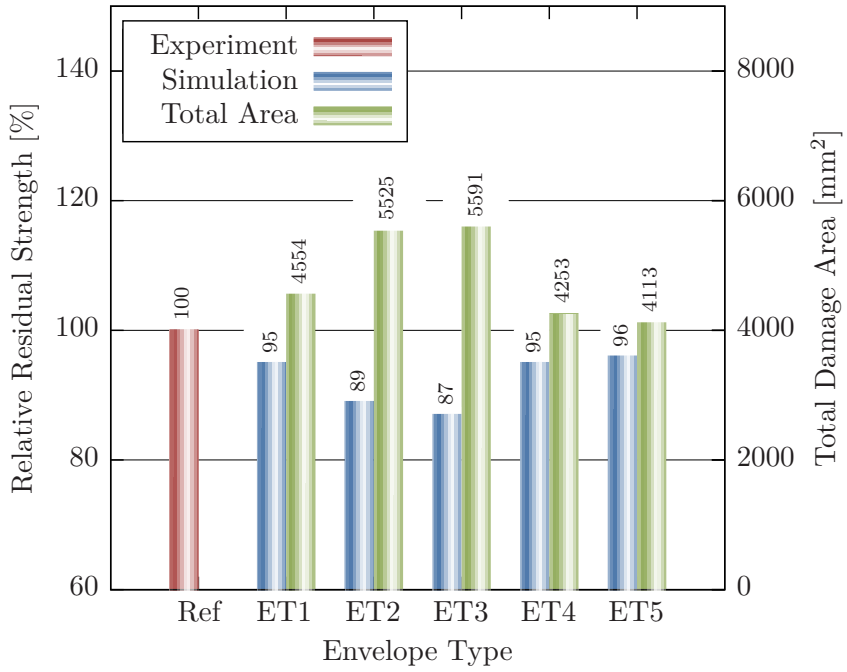

Figure 3.25.: Residual strength and total damage size, obtained from different delamination representations. Ref: experiment, ET1: convex hull, ET2: best-fit ellipsis, ET3: aligned ellipsis, ET4: polygon-based hull, and ET5: star-based hull.

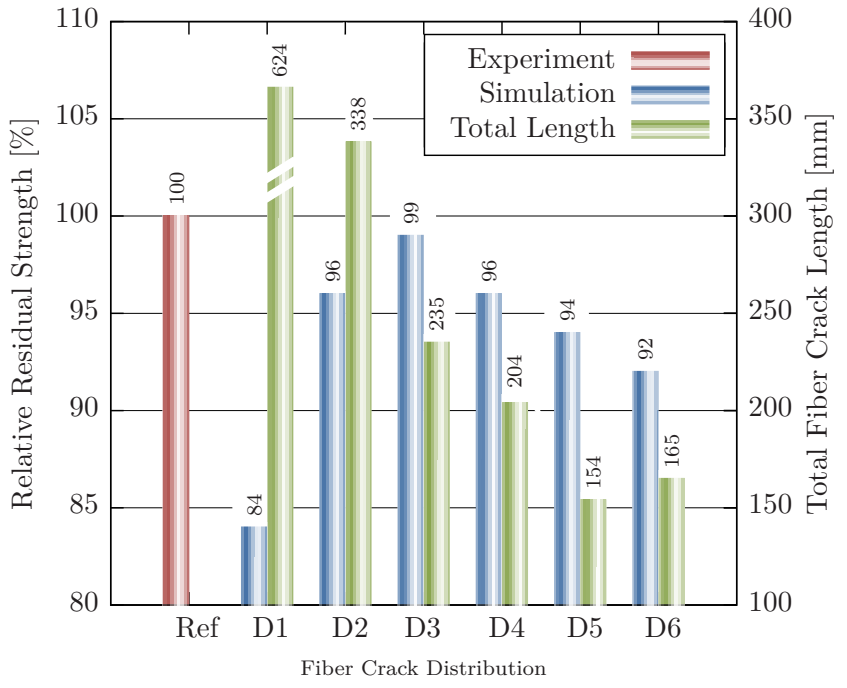

Figure 3.26.: Residual strength sensitivity to different fiber crack distributions and their respective total fiber crack lengths. Ref: experiment on CAI-TC1-02, D1: constant extrapolation, D2: linear extrapolation, D3: quadratic extrapolation, D4: cubic extrapolation, D5: fiber crack distribution from de-ply inspection on coupon TC1-CAI-04, D6: µCT image reconstruction for specimen CAI-TC1-02.

all stacks, as obtained from the different fiber crack distributions.

The results indicate a moderate residual strength variation caused by the applied fiber crack distributions, except for the constant distribution function (D1). The serious damage introduced by this function leads to a considerable CAIS underestimation. However, the remaining extrapolated distributions provide more realistic results, with an error less than 4 %, regarding the experimentally determined strength. This low distinction among the linear, quadratic, and cubic functions must not be generalized, since a more accentuated difference may result for other layups, presenting for instance more main load carrying plies near the impacted surface. More realistic damage distributions, as resulting from de-ply inspection on identical specimens (D5), or by µCT image analysis (D6), result in slightly more conservative results. Yet, in absence of µCT images, the cubic extrapolation function commends itself for its good experimental data approximation, and is adopted throughout this thesis. However, its general applicability to other laminates and impact energies requires further verification. It is also noted, that no correlation establishes between residual strength and total fiber crack length. Total fiber damage extent per se, is suggested having only moderate influence on the results. The variation among the residual strengths is rather owed to the interaction between defect types. In turn, this commends the consideration of the individual damage pattern for the structural assessment.

3.6.2. Damage Feature Combination

As discussed in sub-section 3.2.1, different defect types have distinct influence on the structural behavior. In this particular study, different detected damage features in coupon CAI-TC1-02 are combined. Considering the three most relevant damage types, all permutations are considered. The respective results are depicted in figure 3.27.

As figure 3.27 implies, multiple delaminations induced by a 40 J impact, exert the most significant influence on the compressive failure strength. This damage mode alone is responsible for reducing the virgin failure strength by 58 %, achieving good agreement with the experimentally determined CAIS. In fact, disregarding fiber and matrix cracks in the damaged structure model, still provides accurate estimates, although slightly overestimating the experimental result. The effect of including the major matrix split at the impact-averted surface (D,M) is negligible. This is supported by the residual strength predicted by model M, which estimates the pristine loading capacity reduction to 2 %. In combination with other defect types, its contribution to the failure strength reduction does not exceed 1 %. In contrast, fiber cracks are more influential. When regarded alone, fiber fracture causes a loading capability drop of 38 %, yet still overestimating the CAIS by 21 %. When combined with impact-induced delaminations, the influence of fiber cracks is only moderate (4 % further CAIS reduction). The trends indicated by this study are in compliance to the findings of Pavier and Clarke [46].

The relevance of one damage mode over another should not be quantified based on this study. The interaction of different damage modes and their contribution to the residual strength depends on numerous parameters, such as loading type, layup, and damage size. However, this trend indicates a qualitative ranking, and underlines the importance of enclosing all defect types in the damage assessment model.

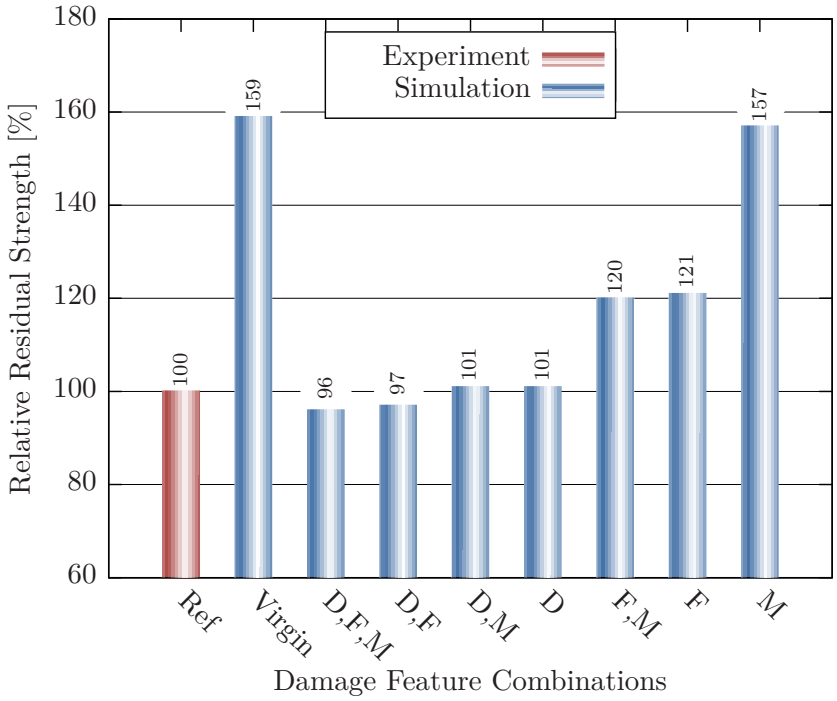

Figure 3.27.: Residual strength obtained from different defect combinations. Ref: experimental result for specimen CAI-TC1-02, D: star-based delamination envelopes, F: fiber crack distribution obtained by cubic extrapolation, M: matrix split at the impact-averted surface, as obtained from visual inspection.

3.6.3. Defect Scaling

In damage characterization, faulty defect extensions can be derived due to insufficient image resolution, poor contrasts between defects and the sound structure, shield compensation, and due to fiber crack length extrapolation. In this study, the residual strength sensitivity on such defect size misrepresentations is discussed. First, the study is conducted for delamination damage and intralaminar defects individually, based on the results from the B- and D-series. Then, the study extends to the effects associated to scaling all impact-induced defects simultaneously. Experimentally tested coupons are considered as references. Regarding single delamination damage, the average residual strength of the B-series is regarded as the baseline (c.f. table E.2). Concerning intralaminar defects, the reference is given by the D-series average residual strength (c.f. table E.4). Finally, the experimentally determined CAIS for specimen TC1-CAI-02 is regarded as the reference for studying scale effects on realistic impact-damaged coupons.

The respective results are depicted in figure 3.28. It is noted that up- and down-scaling consists of increasing or reducing the initial defect size by a specific fraction. Specimens with artificial defects are scaled by $\pm 20\,\%$, while the impact damage is scaled by $\pm 10\,\%$.

The results suggest that increasing the size of a single delamination by $20\,\%$ causes only a slight residual strength reduction by $2\,\%$, regarding the originally predicted value. On the other hand, down-scaling the delamination by the same ratio, causes a residual strength increase by $5\,\%$.

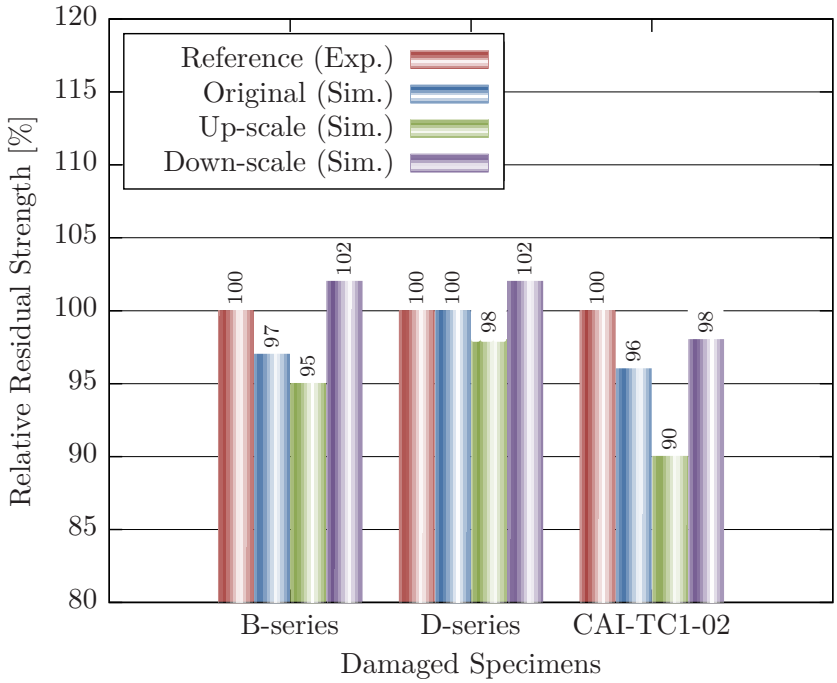

Figure 3.28.: Residual strength sensitivity to defect scaling by ±20 % on single delamination coupons (B-series) and on specimens with artificial intralaminar defects (D-series). Defects in coupons, impacted at 40 J, are scaled by ±10 %. Residual strength sensitivity to scaling is more pronounced in impact-damaged specimens.

With regards to intralaminar defects, a crack size amplification by 20 % leads to a 2 % residual strength reduction; decreasing its size by 20 % results in a 2 % residual strength increase. When considering a realistic impact damage, the implication of consistent defect size misrepresentations is more pronounced. Amplifying all defects by 10 % causes a residual strength reduction by 6 %, while down-scaling the defects by 10 % leads to a slight CAIS increase by 2 %.

The presented results point to a moderate residual strength sensitivity to modest damage size misrepresentations, in lightly damaged structures. However, the presence of multiple defects of different types tends to increase the influence of such errors. To secure conservative residual strength estimations, image analysis parameters should be defined as to rather overestimating the defect, than underestimating it.

3.7. Conclusion

Impact-induced damage on composite structures is comprised by diverse defect types of different influence on the structural behavior. To determine the residual strength of a particular damaged structure, it requires the consideration of many relevant structural parameters. For attaining accurate residual strength estimations, a detailed description of the most influential damage features is considered indispensable. Thus, a novel approach for impact damage characterization is proposed, based on NDI images, as resulting from ultrasonic and µCT inspection. Although many image processing methods are available, capable of highlighting defects in NDI images, de-

tailed damage characterization in the context of composite laminates is barely supported. The proposed method's novelty consists, on the one hand, in defect classification with respect to the layup architecture, which is crucial for deriving realistic structural models. On the other hand, image reconstruction based on empirical damage morphology knowledge, poses another innovative feature, contributing to more physically consistent model setups. The introduced algorithms are implemented in a damage mapping tool, labeled DaMapper.

Adopting µCT image analysis results to validate delamination contours, derived from ultrasonic images, is found a complicated and error-prone approach. Yet, the comparison of both images hints at a fairly accurate delamination shape estimation. By this means and in spite of the shielding effect, realistic damage descriptions can be achieved. Intralaminar defect characterization is validated against de-ply test results and good agreement is attained. However, even more accurate results can be obtained from images with higher resolution and less restrictive filter settings. The proposed cubic extrapolation function for inferring inner fiber crack distributions, based on superficial cracks, agrees remarkably well with the experimental results. However, its general applicability requires further study.

The residual strength sensitivity on various parameters describing the damage shape, defect combination, and scaling is studied. The considered range of values suggests a rather moderate impact on the residual strength. A more accentuated influence is exerted by defect scaling, especially on realistic impact-damaged structures. However, assuming a $\pm 10\,\%$ damage size error, resulting from image analysis, a marginal impact on residual strength prediction is found.

To ultimately assess the proposed method's reliability in returning accurate defect representations, more validation tests are required. A deeper study on the influence of damage misrepresentations on the residual strength should be conducted, by also considering other loading conditions.

Referring to the first hypothesis presented on page 3, it is shown that the most influential damage features can be derived from NDI images, in good agreement with the effective defect morphology. The attainable accuracy of damage representations is shown being sufficient to enable physically consistent structural behavior predictions of damaged parts.

4 Impact Damage Assessment

In this chapter, the implemented damage assessment module is introduced. Its role in the novel decision-making process consists in evaluating the damage criticality, based on which further structural part handling specifications are triggered. According to the proposed workflow presented in figure 2.4, this element processes the damage features, synthesized by the preceding characterization step, and returns the individual residual strength of the damaged structure. By comparing this value with the adopted design load, the damage is assessed.

The following sections introduce the adopted model setup for residual strength prediction and its experimental validation. Further models, representing the Double-cantilever Beam (DCB) and Mixed-mode Bending (MMB) tests, are also introduced and discussed with regards to their agreement between numerical and experimental results. These two models are used in parametric studies for parameter set calibration, which enables efficient and sufficiently accurate cohesive behavior representations. This parameter set is ultimately assigned to the more complex CAI model, and can be extended to virtually any composite part.

4.1. Motivation

Crucial to the damage assessment is the adopted model for relating measurable features of the damaged structure to a priori unknown residual properties. As discussed in chapter 2, a widely adopted approach consists in deriving such a model from structural test data. Due to its many conservative assumptions, the analytical model poses only a rough estimate of the effective residual strength. In contrast, more accurate results are expected from this proposed approach, which relies on the individual detailed representation of the damaged structure and its behavior, through FE modeling and analysis. Hereby, the employed model covers for the main phenomena, that determine the structural behavior of impact-damaged structures. The more accurate the simulation results, the more uncertainty-driven conservatism can be reduced. Such condition-based damage assessments contribute to demand-oriented damage removal, and increased aircraft availability. On the one hand, such an approach is enabled by advanced NDI techniques and image analysis tools; on the other hand, state-of-the-art hardware and software allow individual residual strength predictions to be conducted in a matter of minutes or a few hours, thus making the suggested approach affordable in the context of in-service damage assessment.

4.2. Review on Residual Strength Prediction

In order to guarantee safe aircraft operation, most CFRP primary airframe structures are designed to comply to the damage tolerance criterion [37]. This determines that barely detectable damage, i.e. any defect below ADL, must not degrade the residual static strength below DUL. At the same

time, this criterion requires that structures with defects larger than ADL, sustain at least DLL, until being detected [9]. To ensure that airframe design and its maintenance schedule are compliant to these requirements, static and fatigue behavior of impact-damaged composite structures is being studied, and different approaches are suggested to predict the respective residual loading capacity.

In chapter 2, different residual strength prediction approaches for impact damage assessment are introduced. The spectrum of proposed approaches is classified into the categories empirical, probabilistic, and deterministic. From deterministic models, physically consistent representations can be expected, of the main phenomena governing the structural behavior. Hence, the more relevant details are covered by the model, the more accurate residual strength predictions can be awaited. Before this background, deterministic residual strength estimation approaches have been suggested over the last decades.

Since the detrimental effect of impact damage is more pronounced under compressive loading, due to sub-laminate buckling phenomena, most attention has been given to the study of delamination damage and its effect on the CAIS. Xiong et al. [77] propose an analytical method, where the delaminations obtained from ultrasonic C-scans are approximated by elliptical shapes. Their detrimental effect on the residual compressive strength is determined by sub-laminate buckling analysis, based on the Rayleigh-Ritz method. This procedure is rooted on the assumption, that significant stiffness loss establishes, once the sub-laminates experience stability failure under compression load. The damaged area is represented by a soft region, embedded in the structure. Its residual stiffness is derived from the modulus retention ratio, which is defined as the buckling load to failure strength ratio. Stress concentrations establishing at the soft-inclusion edges are obtained by Lekhnitskii's complex variable method and by finite width corrections. Finally, the failure load is evaluated at a characteristic distance from the soft-inclusion. In spite of the good results obtained, the authors find this characteristic distance being a material parameter, thus requiring curve fitting through extensive experimental data. A similar approach is suggested by Gottesman and Girshovich [19], where delaminations are approximated by the smallest enclosing rectangle. Once a sub-laminate buckles, the residual stiffness is set to zero, and the respective ply is excluded from the load carrying section. Final failure is assumed, once all sub-laminates present either stability or strength failure.

The strategy of representing the impact-induced delaminations by soft-inclusions, whose residual stiffness is determined by analytical sub-laminate buckling analysis, has been adopted by many other authors. This is mainly owed to the method's simplicity. However, the simplifying assumptions may either lead to significant inaccuracies, or to a very limited number of applicable use cases, or even both. Therefore, regarding the calculation of stress concentrations in the soft-inclusion's vicinity, FE analysis is preferred to simulate the mechanical response of more realistic damaged structures. Some authors [26, 27] propose evaluating the effective failure load at a specific distance, which is determined by the damage influence criterion. In their research, Yang et al. [33] also consider soft-inclusions to represent the damage region. However, to determine the CAIS, they adopt an Continuum Damage Mechanics (CDM) approach in combination with Hashin's criterion, using FE analysis.

To account for contact phenomena, occurring in the context of sub-laminate buckling, Sekine et

al. [78] propose a numerical model to predict the effective buckling load of composite structures, containing elliptical delaminations. The first step in their iterative method consists in determining the eigenmodes of each sub-laminate, using FE analysis. Then, their inter-penetrations are resolved by a penalty method to counteract over-closures. Considering this new stiffness added to the model, the eigenmodes are re-computed in the next iteration. The method is re-iterated until all over-closures are eliminated, thus providing the final buckling load in each sub-laminate, and eventually the structural failure load. This model enables the study of the effect of different layup and delamination parameters on the buckling load.

Other authors suggest, that the residual compressive strength should rather be determined in the fatigue context. For metallic structures, damage propagation rate is generally slow, stable and predictable. Therefore, the damage tolerance criterion can be approached by the slow-growth strategy [9]. However, this behavior is generally not found in composite structures. Although many models have been proposed, their accuracy in predicting damage growth as a function of load cycles is rather poor, when viewed in relation to the immense testing effort, required to derive such models [79]. Because of that, the so-called no-growth approach is widely applied today for damage tolerant composite airframe structures. This implies that defect propagation under real service loads is not allowed, until being detected through maintenance [9]. This approach takes advantage of the residual strength invariance up to large numbers of load cycles at rather low load levels, characteristic to CFRP structures [80]. It ultimately requires full-scale tests for substantiation, that defects with a specific extension and loaded under such conditions will not grow [9].

As reviewed by Nettles and Jackson [81], a simple method to obtain residual fatigue strengths consists in applying knock-down factors to the residual static strength. However, this has been regarded as a highly conservative estimate. They report that for 10^6 compressive load cycles with peak amplitudes as low as 60 % of the static CAIS, no significant detrimental effect on the structural loading capability is observed. Similarly, no deleterious effect is found for 10^4 cycles at 80 % of the static CAIS. Hinged on the no-growth requirement, various authors suggest that the critical load for delamination growth due to sub-laminate buckling is equivalent to the residual fatigue strength. Rhead and Buttler [82–84] propose an analytical method to estimate the load at delamination growth, based on the critical sub-laminate buckling load, the laminate membrane stiffness, and the material toughness. Baaran et al. [85] predict delamination growth and hence fatigue strength using FE analysis to determine the Strain Energy Release Rate (SERR) at each increment. Delaminations are assumed to grow, once the SERR exceeds the respective material toughness.

The aforementioned approaches address only the detrimental effect of interlaminar damage on the CAIS. Although intralaminar damage features are less influential on the residual compressive strength, they also contribute to loading capacity reductions, especially when interacting with delaminations. To account for the complex impact damage pattern, different representation methods have been presented. It has been proposed to derive the modulus retention ratios from the analysis of existing experimental results [32, 86] and assigning them to the damaged areas, identified by ultrasonic C-scans. Other inverse methods have also been suggested, where the reduced stiffness properties are inferred from strain field measurements on the damaged specimen [87, 88]. Similar

inverse approaches are pursued, where generic defect distributions are defined and assigned to a structural part. A detailed FE meso-model representing the damaged region is virtually tested and its stress-strain behavior stored as a non-linear material model. Then, a computationally more efficient model of the damaged part is created, onto which the homogenized soft-inclusion is finally mapped to. It is reported that the simulation results underestimate the experimentally obtained results [89, 90]. Borelli et al. [25] derive their realistic damage extent through impact simulations, using detailed meso-models. After homogenizing the complex damage, they transfer the soft-inclusion to a macro-model of the CAI specimen, in order to predict its residual strength. Still another strategy of representing impact-induced damage in its completeness consists in the specification of an equivalent open-hole. Hawyes et al. [91] propose that the hole diameter can be derived from the area presenting extensive damage, as implied by 2D projectional X-ray images. Kannan et al. [92] achieve good results by such an approach for perforated structures. For partially penetrated laminates, the equivalent hole diameter is determined by an empirical method. Common to all these methods is the evaluation of critical stresses, establishing due to stress concentrations in the soft-inclusion vicinity, and FE analysis is the established tool, for predicting those stress distributions, with sufficient accuracy.

With increasing capabilities offered by software and hardware, simple approaches based on the integration of soft-inclusions or open-holes in finite shell element based models have been replaced by more sophisticated approaches. Using FE methods and 3D stacked shell element models, the interaction between delaminating ply stacks and the mechanisms associated to delamination growth are expected to be adequately represented [85, 93]. Using such a 3D meso-model, De Moura et al. [34] predict the CAIS in good agreement with experimental results for structures with a single delamination. In their FE model, the interlaminar damage is simulated by applying cohesive elements to the interface region and solid elements to the sub-laminates. A similar approach is proposed by Short et al. [17], who predict the behavior of artificially delaminated structures. Delaminations are represented by disconnecting the element nodes of adjacent sub-laminates. Contact conditions are applied to the sub-laminate surfaces, to prevent node inter-penetration. A maximum stress criterion in fiber direction is adopted to determine the critical load. The achieved results are in acceptable agreement with those obtained from experiments. This model, initially developed for structures containing single delamination, is later extended to study the effect of multiple artificial delaminations on the compressive failure strength [94].

Adopting a multi-scale computational method, Yan et al. [95] account for the main impact-induced defect features and their interaction in woven fiber composites. The Cohesive Zone Model (CZM) is adopted to reproduce the mechanisms associated to interlaminar failure, while the intralaminar behavior is described by a Representative Volume Element (RVE). Impact-induced delamination is represented by circular shapes, distributed in a pine-tree pattern throughout the thickness. Likewise, the intralaminar loading capacity of fiber and matrix within the damage cone is assumed being fully degraded. Their results suggest that sub-laminate buckling and delamination growth ultimately lead to intralaminar damage propagation immediately before final failure.

In order to obtain more realistic impact damage representations, comprised by inter- and intralaminar features, many researchers suggest the conduction of impact simulation as a first step. The resulting 3D meso-models, containing the predicted impact damage, are then submitted to virtual

CAI testing [23, 31, 96–98]. To simulate delamination onset and growth, the CZM is assigned to the interface regions. Intralaminar damage onset and propagation is predicted using CDM, while considering different constitutive material models. Instead of CDM, Rivallant et al. [96, 97] include a cohesive element pattern throughout the ply stacks' thickness. In doing so, they succeed in predicting intralaminar matrix crack propagation and impact-induced permanent indentation.

Examining the research work conducted over the past decades regarding residual strength prediction, the proposed approaches are found predicting the residual strength with sufficient accuracy. Yet, many approaches are of very limited applicability due to their simplifying assumptions. In contrast, other modeling approaches cover for detailed damage features and phenomena, thus enabling reasonable structural behavior estimations, while being more versatile regarding the representation of realistic impact damaged structures. However, such complicated damage patterns are mainly derived by impact simulation. Since impact event parameters are mostly unknown, such approaches are inadequate to acquire the impact damage of a specific structure. As an alternative, the method proposed in the present thesis takes the effective damage into account, as measured by NDI. Proposed methods by other authors are combined to develop a parametric model, capable of evaluating individual impact-damaged structures.

4.3. Methodology

The proposed procedure for damage assessment consists of proper model setup and evaluation of the simulated structural behavior, with regards to design allowables.

In the first step (section 4.3.2), a model is defined to represent the damaged structure, while considering the most influential defect features, provided by the preceding damage characterization module. The FE model is defined such that several phenomena, known to affect the structural response, are taken into account. Appropriate model parameters, representing the cohesive behavior, are derived through the proposed calibration procedure.

In the second step (section 4.3.3), simulation results are first assessed regarding their physical consistency. Then, the predicted residual strength is compared to governing design allowables, by which the damage is ultimately assessed. From this comparison, further handling recommendations can be derived.

4.3.1. Phenomenology of Impact-Damaged Laminates

As described in sub-section 3.2.1, the establishing impact damage morphology in composite laminates depends on many parameters, resulting in complicated combinations of damage features. These lead to different interacting mechanisms, that ultimately determine the structural response. In view of the CAI test, adopted for validation of the proposed method, the focus is on phenomena associated to compressive loading.

In delaminated structures loaded in compression, sub-laminates experience out-of-plane deflections, leading to interactions between adjacent stacks. This may lead to two relevant mechanisms, occurring in the transition zone (interface) between two neighboring stacks: contact pressure and cohesive behavior. The first occurs when two adjacent sub-laminates would experience different

out-of-plane deflections, thus hindering each other. At this, the more compliant sub-laminate is supported by the adjacent stiffer stack, thus retaining considerable loading capability. While contact pressure occurs at crack closure due to nodal displacements in surface normal direction (mode I), cohesive phenomena occur under crack opening (mode I), sliding (mode II), and tearing conditions (mode III) (c.f. figure 4.5). Provided the respective displacements are sufficiently large, cohesive failure, i.e. delamination onset and eventually propagation, establishes.

Initial impact-induced intralaminar defects are often found propagating, as the load increases. This is owed to stress concentrations, establishing at the crack ends. However, new intralaminar defects may also occur at boundary condition hot-spots and in intact stacks, adjacent to damaged plies. Due to the heterogeneous nature of composite laminates, fiber and matrix can experience failure at different loads. Single load-path structures, as the CAI coupon, experience catastrophic failure, once fiber breakage sets in. In contrast, structures can generally take up further loads, even beyond intralaminar matrix failure onset.

4.3.2. Structural Model Setup

In view of the physical phenomena expected to occur in impact-damaged laminates, a proper FE model setup is adopted. It basically consists of a detailed meso-model with stacked 3D shell elements to represent the individual ply stacks, and surface-based contact properties acting between them, based on CZM and the penalty method. Thus, the representation of inter- and intralaminar failure mechanisms is enabled. The adopted settings apply primarily to the simulation of CAI tests. However, by changing boundary conditions and geometrical properties, other tests and structures can also be represented.

4.3.2.1. Simulation Details

The structural behavior and the ultimate failure load is predicted by transient analysis, using an explicit time integration (central difference) scheme[1]. Although often adopted for dynamic analyses, this method is also appropriate for solving quasi-static problems. Given that the next increment displacement vector is computed based on the equation of motion at the current increment, costly stiffness matrix decompositions and inversions are dispensable [99]. However, small time increments are required to keep the associated error low. Considering the detail and the enormous number of Degrees of Freedom (DoF) associated to the proposed model, and accounting for the expected multiple non-linear phenomena (geometric, contact and material non-linearities) governing the structural response, the explicit solver commends itself.

However, the adopted explicit integration scheme is conditionally stable. In other words, stability is given as long as the employed time increment is below the Stable Time Increment (STI), ΔT_c [99]. This is defined as the smallest transient time of a dilatation wave, running across any mesh element [100]. For solid materials it is given by equation (4.1), where l^c is the characteristic finite element length, E_{ii} the Young's modulus along the wave propagation direction, and ρ the material density.

[1] For the sake of reproducibility, it is referred that all CAIS analyses have been submitted to the Abaqus/Explicit solver, version 2017.

$$\Delta T_c = l^c \sqrt{\frac{\rho}{E_{ii}}} \tag{4.1}$$

Taking into account the highly refined meshes, required to capture failure progression, STIs about 5×10^{-8} s establish, which are highly impractical due to the exorbitant computation time. Therefore, computational efficiency is increased by the adoption of mass scaling. The material density, ρ, assigned to the finite elements is scaled such, that the least STI exceeds the specified value of 1×10^{-7} s. This mass scaling factor is sufficiently low to ensure quasi-static conditions, where the kinetic energy remains a small fraction of the internal energy (less than 5 %) [101], and the artificial work, resulting from propelling mass added by mass scaling, is negligible [100]. The residual strength is merely reduced by 2 % due to mass scaling, while the computation time reduction is roughly 60 %, when compared to unscaled material density models.

4.3.2.2. Boundary Conditions

The geometric parameters of all CAI specimens considered in this thesis are presented in section 3.3. As specified by the test standards [73, 75] and depicted in figure 4.1, the CAI specimens are clamped over a length of 10 mm at the left and right edges, while being constrained by Anti-buckling Rails (ABRs) at the top and bottom surfaces, in order to prevent Euler-buckling from occurring. The ABRs' length is 114 mm and their positions are at an offset of 5 mm from the respective lateral edges. Quasi-static displacement is enforced to the left edge.

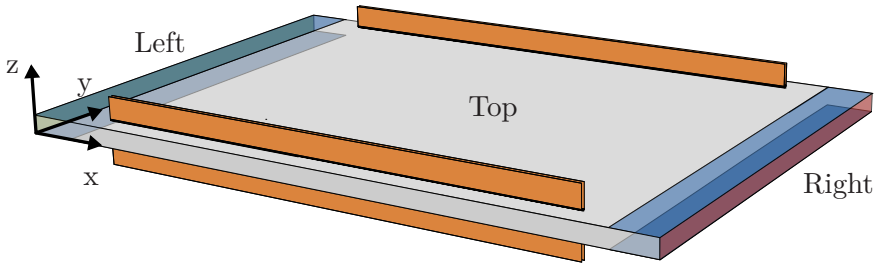

Figure 4.1.: Boundary conditions applied to the CAI coupon model: clamped over a 10 mm length at the left and right edges; displacement enforced to the left edge; ABRs at the top and bottom surface (length:114 mm, offset from edges: 5 mm).

The same boundary conditions are implemented in the model. Referring to figure 4.1, all top and bottom surface nodes highlighted in blue at the left and right edges are constrained in z-direction, to mimic clamped conditions. The nodes at the right end-plane (highlighted in red) are constrained solely in x-direction. Equal displacement along the x-axis is prescribed to all nodes of the left end-plane, highlighted in green. Quasi-static behavior is secured by the prescription of smooth displacement profiles, as depicted in figure 4.2. In order to reduce computation time, two intervals are defined to simulate different average velocities (875 mm/s and 250 mm/s). In doing so, lower displacement rates are applied in the loading segment, where most displacement rate sensitive phenomena are expected to occur.

The ABRs are represented as rigid bodies, initially in contact with the specimen top and bottom surfaces. In order to avoid over-closures between specimen and ABRs, contact conditions based

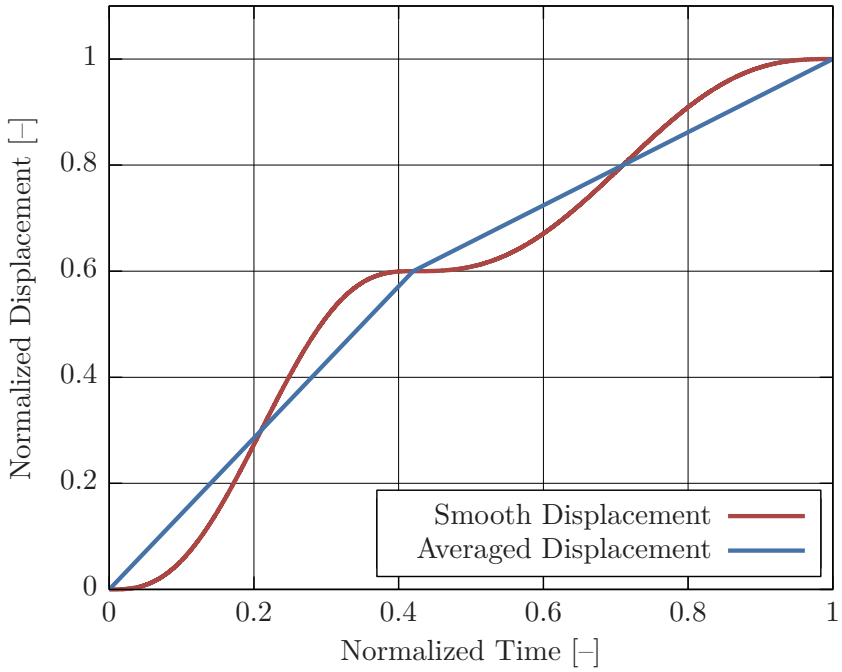

Figure 4.2.: Displacement profile with smooth transitions. Average displacement rates are set to 875 mm/s and 250 mm/s.

on the penalty method are adopted. In the first step, this technique examines the model for over-closures at each increment. In case impermissible penetrations are found, virtual spring forces are applied upon the slave nodes penetrating a master volume. Hereby, the spring forces are defined as a function of over-closure depth and penalty stiffness [101]. Since the penalty method introduces additional stiffness to the model, it may affect the STI [100, 101]. Therefore, the default penalty stiffness is adopted, which is slightly higher than the representative transverse stiffness of the deformable elements, experiencing contact [100].

4.3.2.3. Intralaminar Behavior of Ply Stacks

4.3.2.3.1 Adopted Element Type

A meso-scale modeling approach is adopted to reproduce the interactions between sub-laminates as well as intralaminar failure mechanisms. The thin-walled stacks are represented by plane-stress continuum shell elements with reduced integration[2], one element per stack thickness. This approach enables the reproduction of many relevant mechanisms associated to the CAI test [85, 93]. For instance, delamination onset and propagation, as well as contact pressure between sub-laminates can hardly be represented using conventional shell elements. Continuum shell elements, however, are specifically recommended for such purposes, especially when considered in combination with interlaminar cohesive behavior [100]. In contrast, common solid elements are often computationally too expensive, particularly when using linear solid elements to represent bending

[2]In Abaqus, the label for linear continuum shell elements with reduced integration is SC8R or SC6R for 8-node hexahedrons or 6-node triangular wedges, respectively.

phenomena. To achieve accurate responses, this element type requires six elements through the thickness, thus resulting in an immense number of DoF. Although other efficient solid elements are available in Abaqus (such as the linear, full integration solid element with incompatible modes C3D8I), the continuum shell element is the most accurate and most efficient type in reproducing the behavior of thin-walled structures [102, 103]. Like conventional shell elements, the kinematic and constitutive behavior of continuum shell elements is described by plane-stress formulation, extended by internal DoF for the representation of linear through-the-thickness strain field variation [104]. Hence, thickness changes and first-order transverse shear deformation in each composite layer can be determined [100], thus providing a fairly comprehensive laminate response.

4.3.2.3.2 Hourglass Control

Although preventing shear locking, the adopted element type is prone to hourglassing phenomena [101]. This is known as the faulty mesh distortion, suggesting no strains at the integration points, while the element nodes experience significant deformations, with no resisting stresses acting upon them [23]. To counter this spurious effect, enhanced hourglass control is applied, which represents a refinement of the pure stiffness method. Hereby, the stiffness coefficients are based on the enhanced assumed strain method [100].

4.3.2.3.3 Elastic Material Behavior

The constitutive behavior assigned to the adopted finite elements is given by equation (4.2), where in-plane normal and shear stresses (σ and τ) are obtained from the stiffness matrix and the in-plane normal and shear strains (ε and γ). The stiffness matrix is defined by the Young's moduli, E_{ij}, shear moduli, G_{ij}, and the in-plane Poisson's ratios, ν_{ij}. Indices indicate the respective directions (1: in fiber direction, 2: orthogonal to the fiber). Fibers and matrix are regarded as homogeneous and transverse isotropy is assumed throughout the unidirectional stacks.

$$\begin{bmatrix}\sigma_{11}\\ \sigma_{22}\\ \tau_{12}\end{bmatrix} = \frac{1}{(1-\nu_{12}\nu_{21})}\begin{bmatrix}E_{11} & \nu_{21}E_{11} & 0\\ \nu_{12}E_{22} & E_{22} & 0\\ 0 & 0 & (1-\nu_{12}\nu_{21})G_{12}\end{bmatrix}\begin{bmatrix}\varepsilon_{11}\\ \varepsilon_{22}\\ \gamma_{12}\end{bmatrix} \tag{4.2}$$

Elastic material properties considered in equation (4.2) and throughout this thesis are experimentally determined for a high performance unidirectional prepreg system, known by the label HexPly®M91/IM7. This material combines an intermediate modulus carbon fiber with a toughened epoxy matrix for better impact resistance, thus being appropriate for aerospace primary structures and engine housing [72]. All material characterization tests are conducted at 23 °C and 50 % relative humidity, according to test standards. The bulk material elastic properties are listed in table 4.1, where the superscripts + and − distinguish between parameters respectively obtained from tensile and compressive loading conditions. A total of 6 to 10 specimens per test setup is tested. Average value, Coefficient of Variation (CoV), and the applied test standard are provided. As for the elastic parameters in equation (4.2), the mean value between tensile and

Property	Average	CoV [%]	Test Standard
E_{11}^{+}	173.8 GPa	0.5	DIN EN 2561 [106]
E_{11}^{-}	146.2 GPa	1.3	DIN EN ISO 14126 [107]
E_{22}^{+}	8.5 GPa	0.7	DIN EN 2597 [108]
E_{22}^{-}	8.6 GPa	0.7	DIN EN ISO 14126 [107]
$G_{12} = G_{13}$	5.6 GPa	1.4	ASTM D5379 [109]
G_{23}	3.3 GPa	–	Equation (4.3)
ν_{12}^{+}	0.30	2.8	DIN EN 2561 [106]
ν_{12}^{-}	0.33	4.4	DIN EN ISO 14126 [107]

Table 4.1.: Experimentally and analytically determined unidirectional elastic properties of the bulk material (HexPly®M91/IM7).

compressive properties is assigned to the constitutive equation. Although not being considered in equation (4.2), transverse shear moduli, G_{13} and G_{23}, are required to determine the first-order transverse shear deformations. Hereby, G_{13} and G_{12} are assumed being identical, while the transverse shear modulus in the isotropic plane, G_{23}, is obtained from equation (4.3) [105]. To solve this equation, it is assumed that all Poisson's ratios are identical ($\nu_{12} = \nu_{13} = \nu_{23}$). This is readily applicable for the first two Poisson's ratios ($\nu_{12} = \nu_{13}$). Yet, the equivalence $\nu_{12} = \nu_{23}$ is a simplification, employed due to the lack of experimental data. However, the resulting error caused by this simplification is considered negligible for two reasons: on the one hand, stacks are not expected to experience significant strains in the transverse isotropic 2,3-plane; on the other hand, the difference between these Poisson's ratios is generally accepted as being rather low [31].

$$G_{23} = \frac{E_{22}}{2(1+\nu_{23})} \tag{4.3}$$

4.3.2.3.4 Damage Initiation Criteria

To determine damage onset in composite structures, many criteria have been suggested. These are presented as phenomenological and physically-based criteria, which have been widely discussed regarding their predictive capabilities in the scope of the world-wide failure exercises [110]. Phenomenological criteria describe methods of predicting failure onset, however without distinguishing between the damage modes that may establish in composite laminae, as, for instance, the Tsai-Wu criterion. On the contrary, physically-based criteria discern the stress state and failure mechanisms in the composite constituents, thus enabling a selective material property degradation. One widely accepted continuum-based criterion for plane-stress conditions is proposed by Hashin [111, 112]. His criterion regards for fiber and matrix failure, due to tension and compression loads. Although this criterion is developed for purely unidirectional laminates, it has also been successfully applied to progressive failure analyses of multi-directional laminates, by considering in-situ unidirectional strengths, to account for the constraining interactions between adjacent stacks [113]. In spite of its known deficiencies regarding matrix and fiber compressive failure [113], and although being

Property	Average [MPa]	CoV [%]	Test Standard
X^+	3012.0	2.1	DIN EN 2561 [106]
X^-	1288.5	4.5	DIN EN ISO 14126 [107]
Y^+	67.4	9.7	DIN EN 2597 [108]
Y^-	237.0	2.2	DIN EN ISO 14126 [107]
S^L	88.5	2.5	ASTM D5379 [109]
S^T	89.3	–	Equation (4.8)

Table 4.2.: Experimentally and analytically determined unidirectional ply strengths of the bulk material (Hexcel®M91/IM7).

aware of the existence of more sophisticated failure criteria, Hashin's criterion is still employed in the present model. This is because the inaccuracies are rather slight and the required test effort for material characterization is moderate [104].

Hashin's criterion distinguishes four different failure mechanisms, thus being comprised by four individual failure criteria, one for each mode. Fiber rupture in tension is expected to establish, once the tensile stress, σ_{11}^+, equates the respective strength, X^+ (equation (4.4)). Similarly, the condition for fiber buckling and kinking in compression is assumed to be fulfilled, once the ratio between the stress in fiber direction and the respective compressive strength, X^-, reaches unity (equation (4.5)) [100, 111, 112, 114].

$$\frac{\sigma_{11}^+}{X^+} = 1 \tag{4.4}$$

$$\frac{\sigma_{11}^-}{X^-} = 1 \tag{4.5}$$

Regarding matrix failure in tension and compression, the contribution of shear stresses is also considered. Matrix cracking under transverse tension, σ_{22}^+, and in-plane shear stresses, τ_{12}, occurs if equation (4.6) is fulfilled. Matrix crushing under transverse compression, σ_{22}^-, and shear stresses is expected to establish, if the criterion in equation (4.7) is satisfied. Hereby, Y^+ and Y^- are the transverse tension and compression strengths, while S^T and S^L are the in-plane longitudinal and transverse shear strengths, respectively [100, 111, 112, 114]. Experimentally determined unidirectional strengths are listed in table 4.2.

$$\left(\frac{\sigma_{22}^+}{Y^+}\right)^2 + \left(\frac{\tau_{12}}{S^L}\right)^2 = 1 \tag{4.6}$$

$$\left(\frac{\sigma_{22}^-}{2S^T}\right)^2 + \frac{\sigma_{22}^-}{Y^-}\left[\left(\frac{Y^-}{2S^T}\right)^2 - 1\right] + \left(\frac{\tau_{12}}{S^L}\right)^2 = 1 \tag{4.7}$$

It is noted, that the experimental determination of the transverse shear strength, S^T, (acting in

the 2,3-plane) is fairly complicated. To circumvent the associated difficulties, S^T is determined analytically from the transverse compressive strength, while assuming a typical fracture angle, ψ, of 53°, according to Davila et al. [113]. This relation is given by equation (4.8).

$$S^T = Y^- cos\,\psi \left(sin\,\psi + \frac{cos\,\psi}{tan\,2\psi} \right) \tag{4.8}$$

According to Parvizi et al. [115], matrix-dominated strengths in constrained plies, i.e. layers within or at the surface of multi-directional laminates, are found failing at higher loads, when comparing to unidirectional laminae. They suggest this effect becoming more evident, the thinner the constrained ply thickness. To account for this phenomenon, in-situ strengths are also considered in the present model, distinguishing between fully-embedded stacks, and such partially constrained due to their position at the top- and bottom-most surfaces. Hereby, the transverse shear strength, S^T, is assumed to remain unaffected by in-situ effects, while in-plane shear, S^L, and transverse tensile strengths, Y^+, assume different values, depending on their position in the multi-directional laminate [116–118]. The in-situ transverse tension and in-plane shear strengths of fully embedded thin layers are calculated by the equations (4.9) and (4.10), respectively. These strengths depend on the matrix fracture toughnesses under mode I, $\mathcal{G}^m_{2+}$, and mode II loading conditions, $\mathcal{G}^m_6$ (table 4.3), the individual stack's thickness, and the elasticity parameters (table 4.1). Since according to experimental findings, matrix cracks in typical airframe composite layups generally extent over the stack's thickness, the equations for the thin embedded ply assumption apply [117]. The parameter Λ_{22} is defined by equation (4.11).

$$Y^+_{emb} = \sqrt{\frac{8\mathcal{G}^m_{2+}}{\pi t \Lambda_{22}}} \tag{4.9}$$

$$S^L_{emb} = \sqrt{\frac{8\mathcal{G}^m_6 G_{12}}{\pi t}} \tag{4.10}$$

$$\Lambda_{22} = 2\left(\frac{1}{E^+_{22}} - \frac{{\nu^+_{21}}^2}{E^+_{11}} \right). \tag{4.11}$$

Thin stacks located at the outer laminate's faces, are constrained at one surface, resulting in less pronounced in-situ effects. The in-situ transverse tension and in-plane shear strengths under such conditions are accordingly defined by equations (4.12) and (4.13).

$$Y^+_{out} = 1.79\sqrt{\frac{\mathcal{G}^m_{2+}}{\pi t \Lambda_{22}}} \tag{4.12}$$

$$S^L_{out} = 2\sqrt{\frac{\mathcal{G}^m_6 G_{12}}{\pi t}} \tag{4.13}$$

4.3.2.3.5 Damage Evolution

For proper structural response prediction, the consideration of damage propagation mechanisms is required. An effective method consists in defining constitutive models, that addresses the degradation associated to micro-cracks, establishing once the material strength is reached. For this purpose, different material degradation formulations have been suggested that can be categorized as i) heuristic models, based on a ply-discounting material degradation approach and ii) progressive failure models, using internal state variables based on CDM. Ply-discounting methods impose instantaneous (or recursive) stiffness degradation, once the damage initiation criterion is met, regardless of the new establishing stress field. In contrast to this fairly pessimistic approach, stress redistributions caused by local material degradation are considered in progressive damage modeling approaches. Hereby, the inner micro-cracks are homogenized over the element and described by internal state variables for the various damage modes. The evolution of these state variables is determined by the respective stress-displacement behavior, often assumed as a bi-linear relation [119, 120].

Figure 4.3 presents a generic bi-linear constitutive behavior, generally adopted in progressive failure analysis of composite structures, being assigned to each single failure mode. It depicts a constant stiffness up to damage onset, where the equivalent stress, σ_{eq}^{O}, reaches the respective failure strength, at the equivalent displacement, δ_{eq}^{O}. Upon further loading, the equivalent stress decreases as a consequence of irreversible stiffness degradation, until reaching zero. At this point, the equivalent displacement is δ_{eq}^{F} and the damage variable reaches unity, i.e. full stiffness degradation. On the one hand, prior to damage onset, the slope is determined by the pristine material stiffness. On the other hand, the softening slope results from the fracture toughness associated to the specific fracture mode. Once the strain energy (i.e. the integral of the stress-displacement relation) equates the mode-specific fracture toughness, failure establishes [100, 121].

At a microscopical level, micro-cracks resulting from overload would become wider, as the applied load increases. From a macroscopic perspective, the strain experienced by the material is not distinguishable from crack-opening, thus being together regarded as an effective strain, and being perceived as a softer material. Matzenmiller et al. [122] suggests accounting for this softening by including state variables in the original stiffness matrix, as introduced in equation (4.2). This new stiffness matrix, $\mathbf{S}_d$, accounts for the influence of micro-cracks (equation (4.14)), where $\Delta = 1 - (1 - d^f)(1 - d^m)\nu_{12}\nu_{21}$. The state variables d^N, $N \in \{f, m, s\}$ range from zero (pristine) to unity (fully degraded), and represent respectively a measure of fiber (f), matrix (m) and shear (s) stiffness degradation. The shear state variable results from the mode-dependent degradation variables and is defined as $d^s = 1 - (1 - d^{f+})(1 - d^{f-})(1 - d^{m+})(1 - d^{m-})$.

$$\mathbf{S}_d = \frac{1}{\Delta}\begin{bmatrix} (1-d^f)E_{11} & (1-d^f)(1-d^m)\nu_{21}E_{11} & 0 \\ (1-d^f)(1-d^m)\nu_{12}E_{22} & (1-d^m)E_{22} & 0 \\ 0 & 0 & (1-d^s)(1-\nu_{12}\nu_{21})G_{12} \end{bmatrix} \tag{4.14}$$

According to the crack band model proposed by Bažant and Oh [121], this degradation caused by micro-crack propagation is expected to be confined to a narrow crack band. They point out

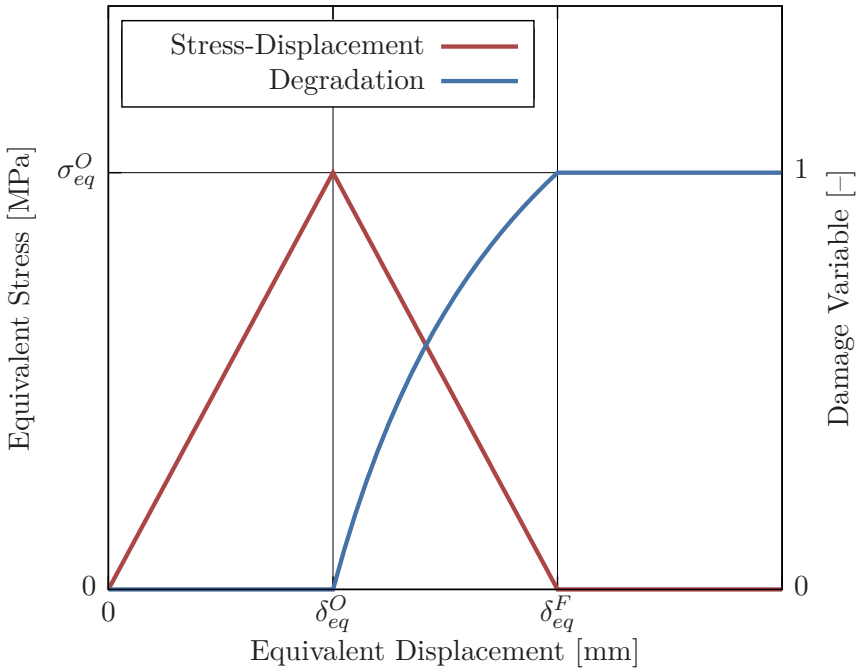

Figure 4.3.: Generic bi-linear constitutive law for pure mode I loading. Equivalent stress and damage variable are functions of the equivalent displacement. Superscript O denotes damage onset, while F indicates failure.

that applying crack growth criteria expressed in terms of stress, would lead to mesh-dependent results, because the establishing stress depends on the chosen element size. The same applies to strain based criteria, that also suggest failure loads converging to zero for increasing mesh refinement. To counter this unphysical behavior, they proposed employing damage propagation criteria, based on the fracture toughness in conjunction with a characteristic length, representing the crack band width. In a FE mesh, the crack band establishes along a one-element-wide path, such that the characteristic length results from the element size[3]. By regularizing the computed dissipated energy in an element through its conjunction with the characteristic element length l^c, mesh size independency is favored. Under these circumstances, crack propagation occurs, once the regularized dissipated energy equates the material fracture toughness.

In accounting for the crack band theory, the constitutive behavior depicted in figure 4.3 is expressed as a stress-displacement relation, where the equivalent stresses and displacements are calculated from equations (4.15) to (4.22), for each failure mode. For fibers loaded in tension ($\sigma_{11} > 0$), the following equations apply[4] [100, 114]:

$$\delta_{eq}^{f+} = l^c \langle \varepsilon_{11} \rangle \tag{4.15}$$

and

[3]For (continuum) shell elements, the characteristic element length is defined as $l^c = \sqrt{A_e}$, with A_e representing the element reference surface [100, 121].

[4]The Macaulay operator $\langle\rangle$ is defined as $\langle x \rangle = (x + |x|)/2$.

$$\sigma_{eq}^{f+} = \langle \sigma_{11} \rangle \,. \tag{4.16}$$

For the fiber compression mode ($\sigma_{11} < 0$), the equivalent stress and displacement read

$$\delta_{eq}^{f-} = l^c \langle -\varepsilon_{11} \rangle \tag{4.17}$$

and

$$\sigma_{eq}^{f-} = \langle -\sigma_{11} \rangle \,. \tag{4.18}$$

Regarding the matrix tension mode ($\sigma_{22} > 0$), the equations below apply

$$\delta_{eq}^{m+} = l^c \sqrt{\langle \varepsilon_{22} \rangle^2 + \gamma_{12}^2} \tag{4.19}$$

and

$$\sigma_{eq}^{m+} = \frac{l^c \left(\langle \sigma_{22} \rangle \langle \varepsilon_{22} \rangle + \tau_{12}\gamma_{12} \right)}{\delta_{eq}^{m+}}. \tag{4.20}$$

Finally, the equivalent stress and displacement for the matrix compression mode ($\sigma_{22} < 0$) is defined by

$$\delta_{eq}^{m-} = l^c \sqrt{\langle -\varepsilon_{22} \rangle^2 + \gamma_{12}^2} \tag{4.21}$$

and

$$\sigma_{eq}^{m-} = \frac{l^c \left(\langle -\sigma_{22} \rangle \langle -\varepsilon_{22} \rangle + \tau_{12}\gamma_{12} \right)}{\delta_{eq}^{m-}}. \tag{4.22}$$

It is based on these equivalent stresses σ_{eq}^{M} and displacements δ_{eq}^{M}, $M \in \{f+, f-, m+, m-\}$, that the mode-dependent degradation variables, d^M, are computed (equation (4.23)). The effective damage variables, d^N, considered in the damaged stiffness matrix, $\mathbf{S}_d$ (equation (4.14)), are finally derived from the damage variables, d^M, according to the effective loading condition (equation (4.23)) [100, 114].

$$d^M = \frac{\delta_{eq}^{M,F} \left(\delta_{eq}^{M} - \delta_{eq}^{M,O} \right)}{\delta_{eq}^{M} \left(\delta_{eq}^{M,F} - \delta_{eq}^{M,O} \right)} \tag{4.23}$$

The intralaminar fracture toughnesses, required to determine the in-situ strengths and the softening behavior for each damage mode, are provided in table 4.3. Fiber fracture toughnesses concerning longitudinal tension, $\mathcal{G}_{1+}$, and compression, $\mathcal{G}_{1-}$, are adopted from literature [123], for

Property	Average Value	CoV [%]	Test Standard
$\mathcal{G}_{1+}^{f}$	81.5 N/mm	7.6	From literature [123]
$\mathcal{G}_{1-}^{f}$	106.3 N/mm	2.1	From literature [123]
$\mathcal{G}_{2+}^{m}$	0.44 N/mm	2.3	ASTM 5528 [125]
$\mathcal{G}_{2-}^{m}$	6.85 N/mm	–	Equation (4.24)
$\mathcal{G}_{6}^{m}$	4.12 N/mm	6.3	ASTM 6671 [126]
η^{m}	1.31	–	ASTM 6671 [126]

Table 4.3.: Experimentally and analytically determined fracture toughnesses for the bulk material (Hexcel®M91/IM7).

a similar material system as the one, considered in this thesis. Matrix fracture toughness due to transverse tensile loading, $\mathcal{G}_{2+}^{m}$, is determined by DCB tests (appendix B.1), and the respective parameter for compressive loading, $\mathcal{G}_{2-}^{m}$, results from equation (4.24) [124]. Herein, $\psi = 53°$ is the assumed fracture angle, and $\mathcal{G}_{6}^{m}$ is obtained from MMB tests (appendix B.2), conducted at different mode-mixtures. The parameter η^{m} is the exponent of the Benzeggagh-Kenane (BK) law, determined by curve fitting.

$$\mathcal{G}_{2-}^{m} = \frac{\mathcal{G}_{6}^{m}}{cos\,\psi} \tag{4.24}$$

4.3.2.3.6 Mesh Settings

Although Bažant's crack band model is intended to provide mesh-independent results, the authors refer that the element size should not exceed a specific value, which is determined by the material properties [121]. This recommendation has been extended to other than tensile fracture modes [23, 104], and can be written as equation (4.25). According to this recommendation and considering the bulk material parameters introduced above, the minimum proposed element edge length, l_e^{CDM}, for obtaining mesh-independent results is 0.84 mm.

$$l_e^{CDM} \leq min\left\{2 \cdot \frac{E_{11}^{+}\mathcal{G}_{1+}^{f}}{(X^{+})^2}, 2 \cdot \frac{E_{11}^{-}\mathcal{G}_{1-}^{f}}{(X^{-})^2}, 2 \cdot \frac{E_{22}^{+}\mathcal{G}_{2+}^{m}}{(Y^{+})^2}, 2 \cdot \frac{E_{22}^{-}\mathcal{G}_{2-}^{m}}{(Y^{-})^2}\right\} \tag{4.25}$$

Besides adopting an adequate mesh size, mesh orientation mismatch with respect to the natural crack propagation direction is also reported to affect the structural response [127–129]. This is owed to the CDM implementation as a local model, where the damage variables are determined by evaluating the element's stress state, but disregarding the degradation state of neighboring finite elements. Thus, crack paths may establish, that are unphysical for composite laminates. Assuming that the main loading direction is known a priori, and that the crack band establishes transversely to it, the proposed model generator is designed to automatically align the mesh, to reduce spurious effects.

Regarding the chosen continuum shell element type, the default settings promote unphysical

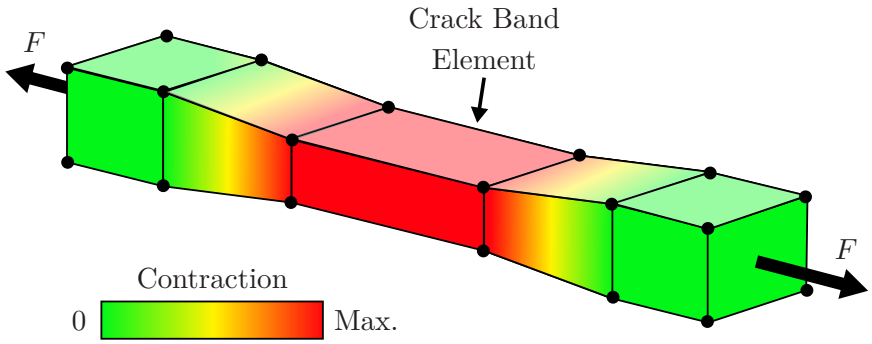

Figure 4.4.: Spurious thickness change and elongation of adjacent finite elements, due to tensile stiffness degradation in the crack band element.

structural responses, once the crack band element starts degrading. Against the argumentation presented above, this particular element type presents mesh-dependent behavior, even when complying to the maximum element edge length recommendation, discussed above [129]. This is attributed to internally computed thickness changes, resulting from the default transverse Poisson's ratios, ν_{13} and ν_{23} [100]. Since the degrading crack band elements experience significant strains in loading direction, considerable thickness changes establish. Contrary to conventional shell elements, where the element thickness is defined by the section property, the continuum shell element thickness is determined from the nodal positions [100]. Since adjacent finite elements share the same nodes, their thickness is also affected by the contraction (or expansion), experienced by the crack band elements. In consequence, the spurious thickness change in the adjacent elements induces additional in-plane strains, due to the Poisson's ratios, thus suggesting a more compliant material behavior. This phenomenon is depicted in figure 4.4 for a generic finite element row, loaded in tension.

In fact, this phenomenon is even aggravated for smaller element lengths. This is owed to the crack band model regularization, which enforces constant equivalent separations at failure, δ_{eq}^{F} (c.f. figure 4.3), regardless of the element length. Since the equivalent separation is generically defined as the failure strain, scaled by the characteristic element length, $\delta_{eq}^{F} = l^{c}\varepsilon_{eq}^{F} = constant$, element size reduction (l^{c}) inevitably leads to failure strain (ε_{eq}^{F}) increase.

In the present model, this unphysical behavior is prevented by nullifying the transversal Poisson's ratios ($\nu_{13} = \nu_{23} = 0$). Given that these parameters are disregarded by the constitutive equation for plain-stress conditions, this definition does not alter the model's in-plane response.

As the material stiffness degrades towards zero due to damage evolution, it is recommended to delete highly degraded elements, in order to avoid sudden excessive element distortions that can cause premature simulation abortion [23]. This is achieved by imposing a maximum degradation threshold, above which elements are excluded from the equation. This threshold is set to $d_{max}^{f} = 0.99$, which implies that, once the fiber degradation variable of an arbitrary element reaches this value, it ceases offering resistance to further deformation [100].

As discussed in chapter 3, intralaminar defects are represented by straight line segments. The use of identical coordinate systems allows unequivocal defect mapping, from NDI images to the

damage assessment model. By projecting the intralaminar crack onto the finite element mesh of the respective stack, defect elements are identified and deleted. This is the equivalent to degrading the stiffness properties of the concerning finite elements, yet this approach is more efficient. These initial defects lead to stress singularities, which are responsible for further crack propagation.

Mesh settings, employed to achieve mesh-independent and physically consistent responses, are summarized in table 4.4.

Property	Value	Specification
l_e^{CDM}	0.84 mm	Equation (4.25)
$\nu_{13} = \nu_{23}$	0.00	Specified
d_{max}^f	0.99	Specified

Table 4.4.: Adopted mesh settings for proper intralaminar response prediction.

4.3.2.4. Interlaminar Behavior between Ply Stacks

4.3.2.4.1 Interaction Properties

As introduced on page 61, the behavior between two adjacent sub-laminates may be determined by contact pressure, as the crack closes. To prevent unphysical over-closures, the penalty method, introduced on page 61, is assigned to both, delaminated and non-delaminated regions. The interlaminar behavior in non-delaminated regions is additionally described by the CZM. This formulation is understood as a combination of stress-based and fracture mechanics approaches. It accounts for delamination onset and (non-similar) propagation, mixed-mode conditions, and nonlinear material behavior [130].

Two CZM formulations are available: cohesive elements with traction-separation response and surface-based cohesive behavior. Although very similar, some decisive differences exist that determine the preference of one over the other. While the first is adequate to represent the structural behavior of non-zero thickness components such as adhesives, the latter is designed for interfaces of negligible thickness, such as the resin-rich transition zone in composite laminates. Due to its formulation as a node-to-surface interaction, no further DoF are added to the model [100], thus posing a good compromise between computational efficiency and response accuracy [131].

4.3.2.4.2 Elastic CZM Behavior

The constitutive law assigned to the present CZM is represented as a linear-elastic and linear-softening (short: bi-linear) traction-separation relation [132]. Hereby, separations denote the relative displacement experienced by slave nodes with respect to their master surface. In 3D structures, as those exemplarily depicted in figure 4.5, separations along the three fracture mode directions are considered: normal opening (mode I), δ_I, sliding (mode II), δ_{II}, and tearing (mode III), δ_{III}. The respective tractions, t_i, $i \in \{I, II, III\}$, are defined as the cohesive forces, divided by the current area at each point [100].

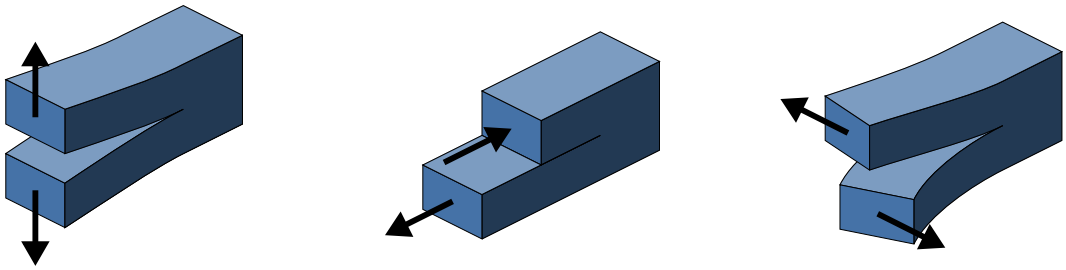

(a) Mode I: Opening (b) Mode II: Sliding (c) Mode III: Tearing

Figure 4.5.: Fracture modes in 3D space.

In figure 4.6, a typical bi-linear traction-separation relation is exemplarily depicted for pure mode I loading conditions. Individual states along the traction-separation law are highlighted and respectively shown in a schematic representation of the cohesive zone. Linear-elastic behavior is assumed in the crack front (1-3), where any prescribed separation is fully reversible. At the cohesive crack tip (3), the traction equates the interfacial strength, thus fulfilling the damage initiation criterion. Further separation along the linear softening branch, which determines the cohesive behavior in the Fracture Process Zone (FPZ) (3-5), causes irreversible cohesive stiffness degradation. At the physical crack tip (5), the cohesive stiffness is fully degraded and the contact condition is released. Beyond this point, for instance at point 6, no cohesive constraints apply to the slave nodes [133].

The cohesive behavior is governed by the 3D constitutive law given by equation (4.26). Hereby, an uncoupled cohesive stiffness matrix, $\mathbf{K}$, is adopted, indicating that neither normal separations give raise to tangential tractions, nor tangential separations cause normal tractions. Mode-specific interfacial stiffness is denoted by K_i, $i \in \{I, II, III\}$. Once the damage initiation criterion is fulfilled, the degradation variable, d, evolves monotonically from null (original stiffness) to unity (full stiffness degradation). As opposed to the intralaminar damage evolution formulation introduced earlier, a single degradation variable is employed to describe the cohesive contact damage state, without mode distinction.

$$\mathbf{t} = \begin{bmatrix} t_I \\ t_{II} \\ t_{III} \end{bmatrix} = (1-d) \begin{bmatrix} K_I & 0 & 0 \\ 0 & K_{II} & 0 \\ 0 & 0 & K_{III} \end{bmatrix} \begin{bmatrix} \delta_I \\ \delta_{II} \\ \delta_{III} \end{bmatrix} = \mathbf{K}\boldsymbol{\delta} \tag{4.26}$$

Most composite structures in real application scenarios are subjected to complex loading conditions, which give raise to a combination of different fracture modes, acting simultaneously upon the cohesive zone. To account for this circumstance, mixed-mode bi-linear traction-separation behavior is assumed, which is understood as a function of the mixed-mode ratio, $\mathcal{G}_I/\mathcal{G}_S$, relating normal to shear work, $\mathcal{G}_S = \mathcal{G}_{II} + \mathcal{G}_{III}$. Figure 4.7 illustrates the variation of damage onset and final failure, according to the mode-mixture. The traction-separation behavior for a particular mixed-mode ratio (red triangle) results from sweeping, say, the light-green triangle from the pure mode I plane, towards the pure shear mode plane, about the vertical axis. Tractions and separations for any mixed-mode condition are thus limited by the damage onset and the failure

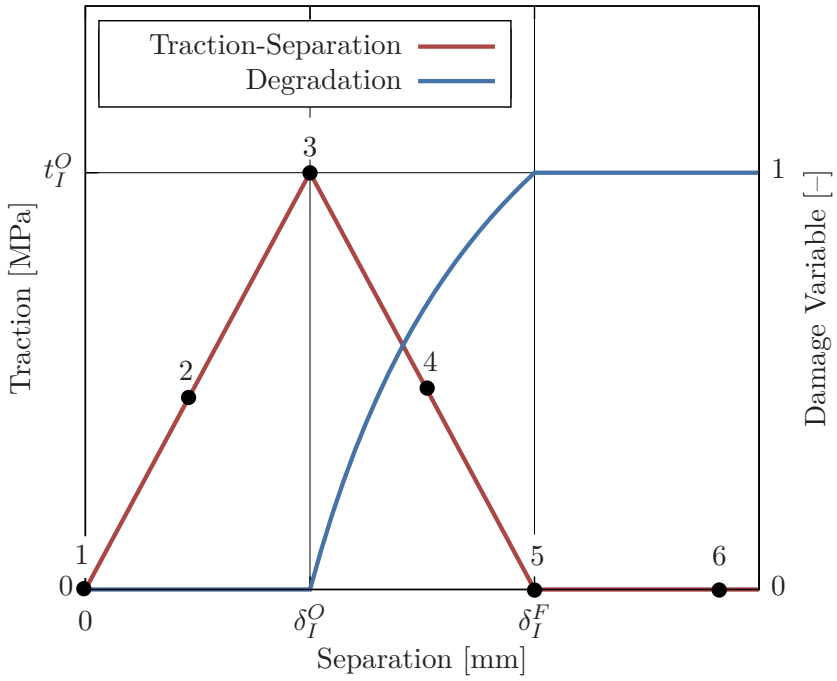

(a) Generic bi-linear traction-separation relation for pure mode I loading.

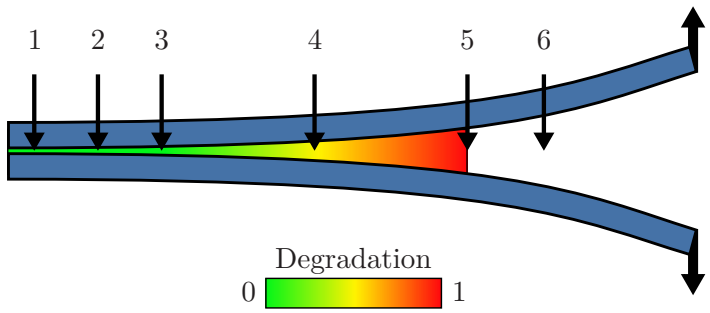

(b) Schematic representation of the cohesive zone.

Figure 4.6.: Cohesive zone model: bi-linear constitutive law and degradation states in the cohesive zone.

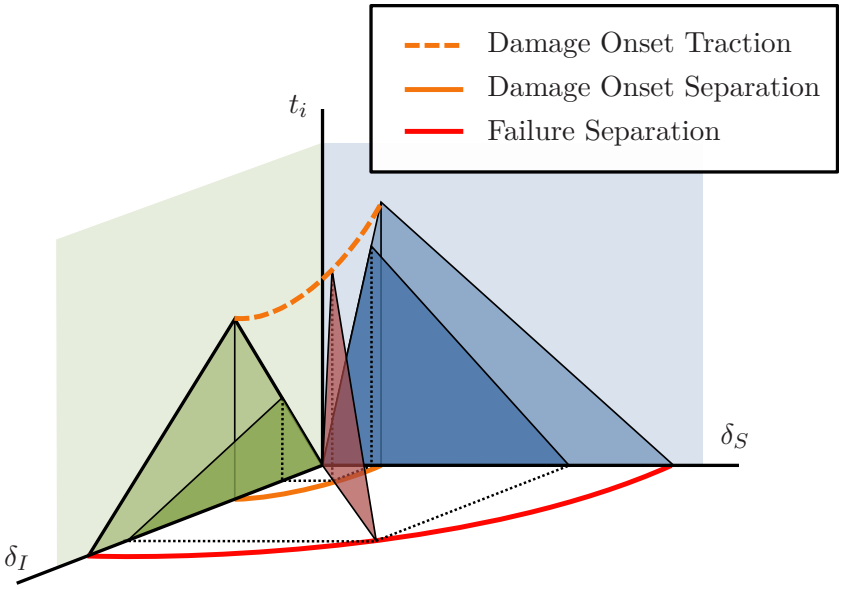

Figure 4.7.: Mixed-mode bi-linear traction-separation law. Mixed-mode behavior is described by the red triangle, which is spanned by the origin, failure separation, and damage onset traction loci. Dark-green and -blue triangles represent the normal and shear contributions. Light triangles denote the pure normal and shear bi-linear relations.

separation curves.

Both, the effective mixed-mode traction, t_{mm}, and separation, δ_{mm}, are defined as the Euclidean norm of the respective vectors, as $\|\mathbf{t}\|_2$ and $\|\boldsymbol{\delta}\|_2$, accordingly. Herein, the component in mode I direction is only regarded if positive, otherwise it is set to null.

4.3.2.4.3 Damage Initiation Criterion

Damage onset is determined by a quadratic stress criterion (equation (4.27)), that accounts for mixed-mode conditions, and is represented by the dashed orange curve in figure 4.7 [132, 134]. This criterion suggests that damage onset may occur, even before attaining any mode-specific interfacial strength, t_i^O, $i \in \{I, II, III\}$. The Macaulay operator in the first term indicates that the criterion disregards any mode I crack closing tractions.

$$\left(\frac{\langle t_I \rangle}{t_I^O}\right)^2 + \left(\frac{t_{II}}{t_{II}^O}\right)^2 + \left(\frac{t_{III}}{t_{III}^O}\right)^2 = 1 \tag{4.27}$$

4.3.2.4.4 Damage Evolution

Accounting for progressive cohesive stiffness degradation and ultimately cohesive failure, the energy-based criterion proposed by Benzeggagh and Kenane [135] is employed (equation (4.28)). The BK-law expresses an equivalent critical toughness for mixed-mode conditions, $\mathcal{G}_{mm,c}$, based on the mode-specific critical toughnesses, $\mathcal{G}_{Ic}$ and $\mathcal{G}_{IIc}$, and under consideration of the mode-mixture,

$\mathcal{G}_S/\mathcal{G}_T$, where the total cohesive work, $\mathcal{G}_T$, is comprised by normal, $\mathcal{G}_I$, and shear work, $\mathcal{G}_S$. Critical interlaminar toughnesses are consistent with those presented in table 4.3, i.e. $\mathcal{G}_{Ic} = \mathcal{G}_{2+}^m$ and $\mathcal{G}_{IIc} = \mathcal{G}_6^m$. The exponent η is a constant determined through curve-fitting.

$$\mathcal{G}_{mm,c} = \mathcal{G}_{Ic} + (\mathcal{G}_{IIc} - \mathcal{G}_{Ic}) \left(\frac{\mathcal{G}_S}{\mathcal{G}_T} \right)^{\eta} \tag{4.28}$$

Cohesive failure establishes, once the current SERR equates the critical mixed-mode toughness, $\mathcal{G}_{mm,c}$. The BK-criterion is found especially appropriate, whenever the tangential fracture toughnesses are identical, $\mathcal{G}_{IIc} = \mathcal{G}_{IIIc}$, which is commonly assumed in delamination propagation problems [23, 100, 131, 136].

Considering the employed bi-linear traction-separation behavior, the degradation variable, d, is defined as a function of the maximum experienced mixed-mode separation, δ_{mm}^{max}, and the separations at degradation onset, δ_{mm}^O, and failure, δ_{mm}^F (equation (4.29)).

$$d = \frac{\delta_{mm}^F \left(\delta_{mm}^{max} - \delta_{mm}^O \right)}{\delta_{mm}^{max} \left(\delta_{mm}^F - \delta_{mm}^O \right)} \tag{4.29}$$

Under the assumption of identical interfacial stiffness, $K_I = K_{II} = K_{III} = K$, and similar tangential fracture toughnesses, $\mathcal{G}_{II} = \mathcal{G}_{III}$, the mixed-mode separation at degradation onset is given by equation (4.30). Mode mixity ratio, ζ, is defined by δ_S/δ_I, and $\delta_S^2 = \delta_{II}^2 + \delta_{III}^2$ applies [132].

$$\delta_{mm}^O = \begin{cases} \delta_I^O \delta_S^O \sqrt{\frac{1+\zeta^2}{\left(\delta_S^O\right)^2 + \left(\zeta \delta_I^O\right)^2}}, & \text{if } \delta_I > 0 \\ \delta_S^O, & \text{if } \delta_I \leq 0 \end{cases} \tag{4.30}$$

Mixed-mode separation at failure is described by equation (4.31) [132].

$$\delta_{mm}^F = \begin{cases} \frac{2\mathcal{G}_c}{K \delta_{mm}^O}, & \text{if } \delta_I > 0 \\ \delta_S^F, & \text{if } \delta_I \leq 0 \end{cases} \tag{4.31}$$

4.3.2.4.5 Calibration of Mode I Parameters

The cohesive behavior, as introduced above, is governed by a few parameters, to which the structure responds differently. Defining a suitable parameter set, to reproduce the cohesive behavior of a particular material system, is associated to two challenges. On the one hand, determining the cohesive properties of composite materials is either fairly complicated, or it lacks test procedures for an extensive characterization. On the other hand, the FPZ in typical carbon epoxy materials is very small, thus requiring very refined discretization, to resolve failure mechanisms, occurring at the crack tip. To cope with these challenges, different approaches have been proposed to determine pseudo cohesive properties, such that high mesh density requirements can be relaxed. It

is postulated that such a parameter set, calibrated by experimentally or analytically determined responses of simpler coupons, can be applied to other layups, part geometries, and loading conditions, for cohesive failure prediction. Final CZM parameter calibration results are summarized on page 84.

The parameter set calibration for pure mode I conditions is discussed in the following. Experimental DCB tests are conducted to determine the fracture toughness, $\mathcal{G}_{Ic}^{m}$. Five specimens are tested in compliance to the respective test standard [125]. At the same time, the experimental load-displacement curves are regarded as the calibration baseline. Results are presented in appendix B.1. An analytical solution, based on the Corrected Beam Theory (CBT), is also plotted along with the experimental and simulation results, to highlight scatter. The derivation of the analytical load-displacement functions is also given in Appendix B.1.

Experimental and analytical results for specimen TC2-DCB-03 are regarded as the baseline. The properties addressed in this parametric study comprise: cohesive stiffness, K_I, interfacial strength, t_I^O, and laminate half-thickness, h, which ultimately lead up to a finite element edge length recommendation.

- **Cohesive stiffness:** Across the literature, a wide range of cohesive stiffnesses is regarded as appropriate. In their study, Turon et al. [137] propose a new guideline for determining appropriate interfacial stiffnesses, based on mechanical aspects, as opposed to empirical considerations only. They conclude that good results are achievable for values beyond $50\frac{E_{33}}{h}$, which is in the order of $10^5\,\mathrm{N/mm^3}$ for most carbon-epoxy DCB specimens. Applied to the present test setup, the resulting minimum interfacial stiffness recommendation is roughly $2.9 \times 10^5\,\mathrm{N/mm^3}$.

  In view of the damage assessment model and the adopted explicit time integration method, STI should be kept as high as possible, to enable efficient simulations. Since the STI behaves inversely proportional to the cohesive stiffness [100], there is a clear interest in reducing the cohesive stiffness to a minimum.

  Figure 4.8 depicts the load-displacement curves for specimen TC2-DCB-03, regarding cohesive stiffnesses in the range from $10^2\,\mathrm{N/mm^3}$ to $10^6\,\mathrm{N/mm^3}$. The curves clearly attest to excellent agreement between experimental and simulated results, achieved for stiffnesses beyond $10^3\,\mathrm{N/mm^3}$. No added value is attained by increasing the cohesive stiffness further than $10^4\,\mathrm{N/mm^3}$.

  The influence of interfacial stiffness on the FPZ length and the STI is depicted in figure 4.9. FPZ length converges to a constant value as the stiffness increases. Recalling the traction-separation law depicted in figure 4.6, decreasing the interfacial stiffness, while maintaining fracture toughness and cohesive strength, causes the separation at damage onset, δ_I^O, to shift towards the separation at failure, δ_I^F. At the limit, $\delta_I^O = \delta_I^F$, the cohesive stiffness would degrade instantaneously, once the damage onset criterion is fulfilled. In consequence, the FPZ length, extending between points 3 and 5 in figure 4.6, would be null. By the same reasoning, increasing the stiffness causes the FPZ length to expand. Considering, that the CZM requires the element size to be consistent with the FPZ length [131], extending

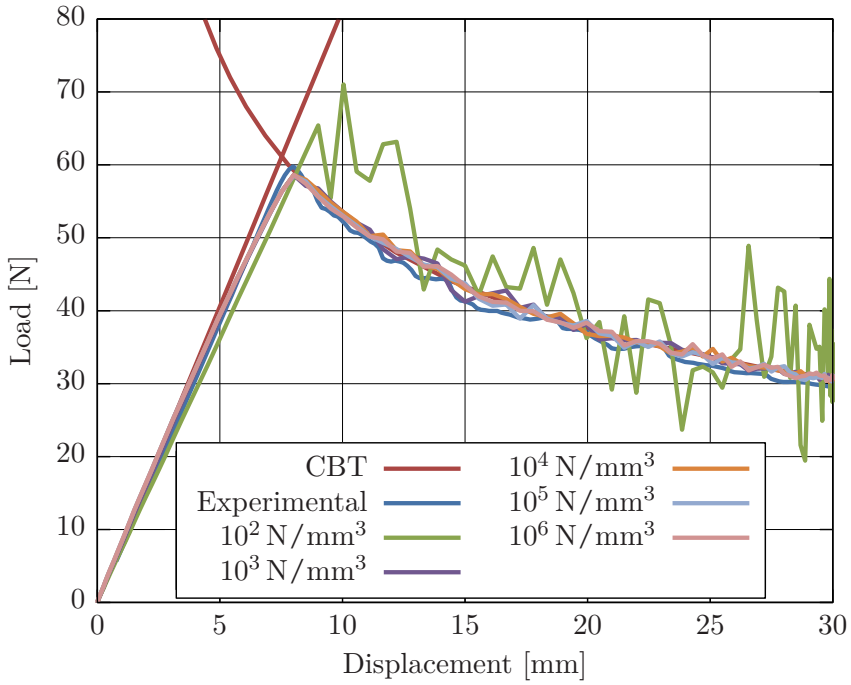

Figure 4.8.: Load-displacement curves under mode I conditions, considering different cohesive stiffness values, K_I. Excellent results are attained for cohesive stiffnesses beyond $10^3\,N/mm^3$.

this region by a reasonable interfacial stiffness choice, could enable the adoption of coarser meshes, ultimately leading to computationally lighter models.

However, the relation between cohesive stiffness and STI is inversely proportional, as suggested by figure 4.9. Until approximately $10^4\,N/mm^3$, STI is determined by the employed penalty stiffness, which is higher than the assigned cohesive stiffness[5]. Beyond this value, the critical time increment is determined by the cohesive stiffness.

These results suggest, that regarding the result accuracy, any cohesive stiffness beyond $10^4\,N/mm^3$ is adequate. However, bearing in mind that halving the STI roughly means doubling the computation time, and considering the complexity of CAI models, to which this parameter set is ultimately assigned, it is favored employing parameters that promote efficient computation at an acceptable accuracy. Thus, the adopted mode I cohesive stiffness is set to $10^4\,N/mm^3$.

- **Interfacial strength:** Although experimental methods are available to characterize the interlaminar properties of composite materials [138], such a test campaign is dispensed in the present thesis. This is because very low FPZ lengths, associated to the effective interfacial strength are anticipated, thus requiring prohibitively refined FE meshes [131, 139]. This

[5] In Abaqus, adopting the default cohesive stiffness, which is equivalent to the default penalty stiffness, also provides accurate results. This however, applies only to the 2019 version. In previous versions (e.g. 2016 and 2017), the default stiffness parameters led to faulty results. For the sake of consistency between results obtained from different Abaqus versions, and in view of extending the model generator to other numerical tools, it is recommended to define the cohesive stiffnesses manually.

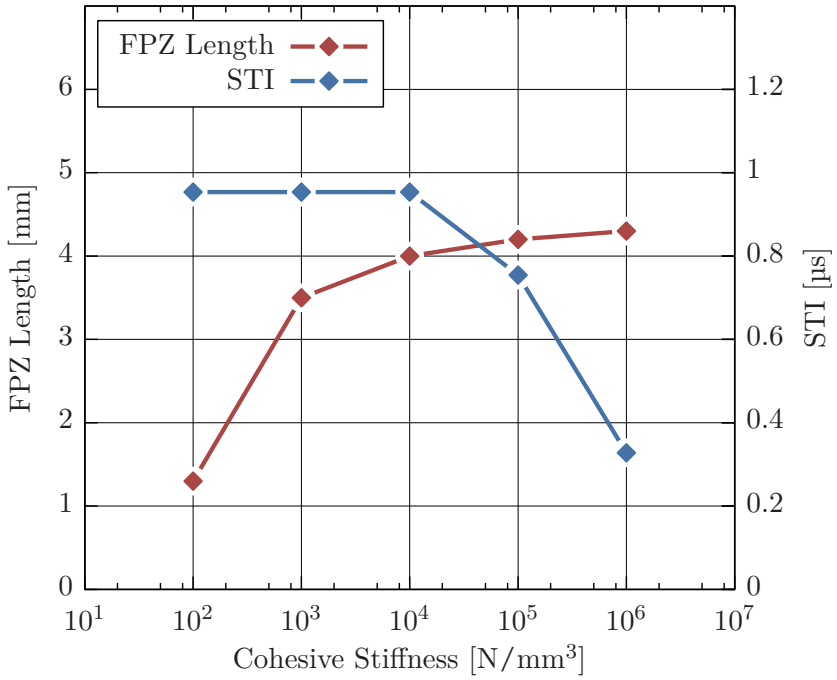

Figure 4.9.: Sensitivity of FPZ length and STI to the cohesive stiffness. A good compromise between FPZ length and STI is found at $K_I = 10^4\,\mathrm{N/mm^3}$. Results are obtained models with a 0.5 mm element edge length.

issue is circumvented by the adoption of non-physical strengths adjustments, causing the FPZ to expand artificially [137]. Although this promotes inaccurate stress concentrations at the crack tip, the energy dissipation, and thus the crack propagation is properly predicted. The implications of this approach on the estimated load-displacement response accuracy is widely discussed throughout literature [102, 131, 137, 139–141].

Interfacial strengths between 1 MPa to 15 MPa are considered, and the respective results are depicted in figure 4.10. It is shown that too low cohesive strengths promote early degradation, which is responsible for a pronounced misrepresentation of the structural behavior. As the adopted strength increases, closer agreement with the experimental result is attained. In the crack-growth domain (i.e. beyond the peak load), the response is predominantly controlled by the fracture toughness, which explains the response similarity, in spite of the distinct interfacial strengths. The figure also shows increasing oscillations in the load-displacement response for higher cohesive strengths. This points to the adopted element edge length fixed at 0.5 mm becoming insufficient to resolve the decreasing FPZ length.

Figure 4.11 illustrates the predicted response quality degrading for a decreasing number of elements, N_e, spanning the FPZ. For this analysis, an interfacial strength of 10 MPa is adopted for which the FPZ length is 4.0 mm. The results imply that, although oscillations caused by snap-back effects take place, two elements are sufficient to represent the FPZ, leading to accurate load-displacement responses. This is in agreement with findings reported elsewhere [140], whereby a number of three elements is generally preferred [23, 31, 137].

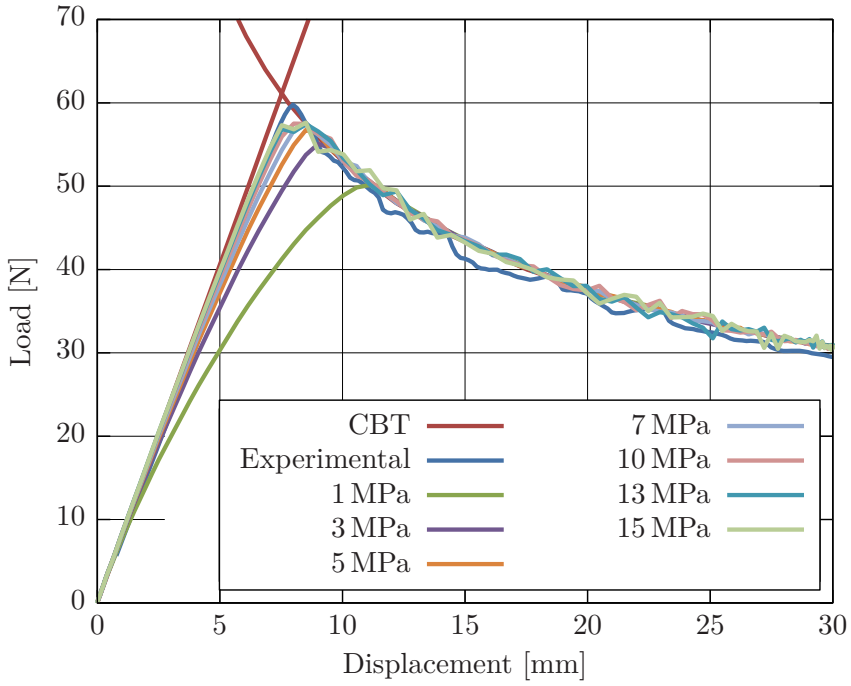

Figure 4.10.: Load-displacement curves for different interfacial strength values, t_I^O. Good agreement between analytical, experimental and simulation responses, for strengths beyond 5 MPa.

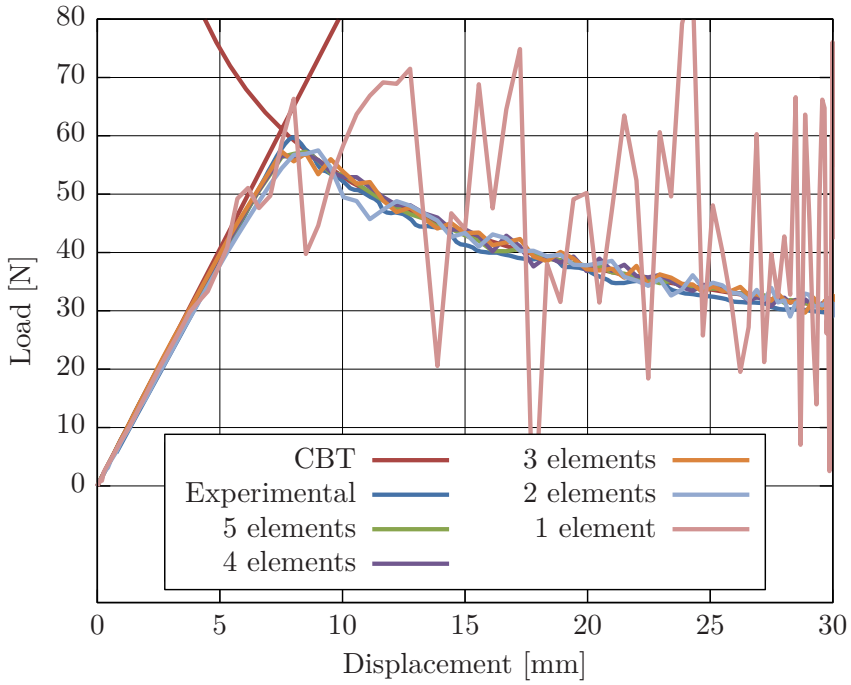

Figure 4.11.: Load-displacement curves for different numbers of elements per FPZ length. Satisfactorily results are obtained for two and more elements per FPZ length.

In figure 4.12, the effectively measured FPZ lengths, l_{FPZ}, are plotted over the respective interfacial strengths. For this analysis, a 0.2 mm element edge length is employed in the DCB model. This curve suggests an intimate inverse proportional relation between both measures, and many authors have attempted to describe it in a mathematical expression for different materials [137]. Their equations only vary with regards to the parameter R (c.f. equation (4.32)), which ranges from 0.21 to 1 [137]. These models are respectively proposed by Hui et al. [142] and Hillerborg et al. [143], and are extended to Slender Bodies (SB) formulation in equation (4.33), as proposed by Yang and Cox [131].

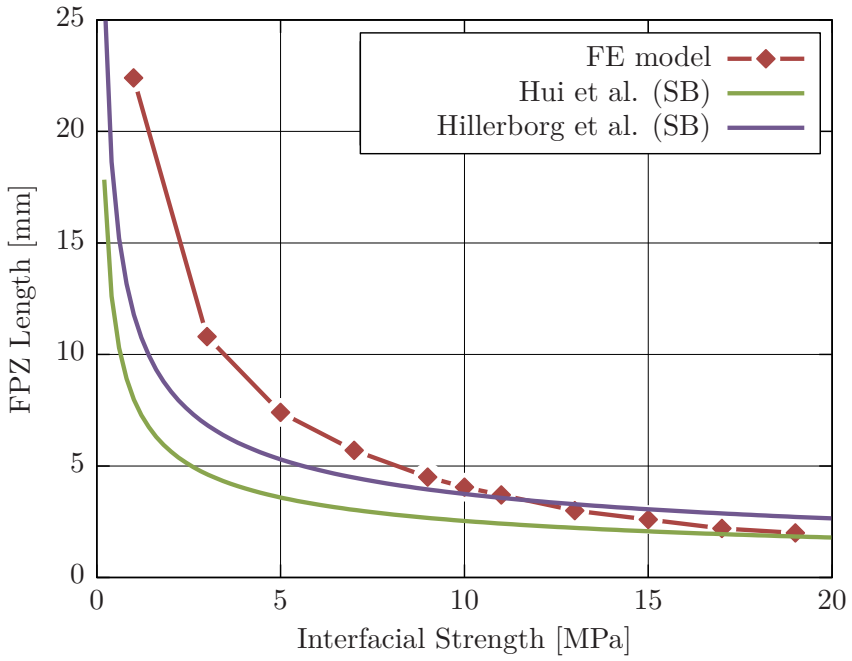

Figure 4.12.: FPZ length over interfacial strength: analytical predictions and numerical results. The range of proposed mathematical expressions provides poor agreement with the numerically obtained results.

$$l_{FPZ} = R\frac{E_{x,eq}\mathcal{G}_{Ic}}{(t_I^0)^2} \tag{4.32}$$

$$l_{FPZ}^{SB} = \sqrt[4]{l_{FPZ}\cdot h^3} \tag{4.33}$$

The parameter $E_{x,eq}$ in equations (4.32) and (4.33) denotes the equivalent Young's modulus for orthotropic materials, which is obtained from the laminate engineering constants and is given by equation (4.34) [131, 140].

$$\frac{1}{E_{x,eq}} = \sqrt{\frac{1}{2E_xE_z}}\sqrt{\sqrt{\frac{E_x}{E_z}} - \frac{\nu_{zx}E_x}{E_z} + \frac{E_x}{2G_{zx}}} \tag{4.34}$$

The reason for the special interest in the prediction of FPZ lengths consists in the potential reduction, or even avoidance, of mesh convergence studies on costly models. Considering the number of elements per FPZ length recommendations, the required FE edge length can be determined analytically, by equation (4.35).

$$l_e^{CZM} \leq \frac{l_{FPZ}}{N_e} \tag{4.35}$$

However, none of the proposed models is found approximating the relation between interfacial strength and FPZ length with sufficient accuracy. Therefore, a FE-based procedure is proposed, consisting instead of a series of DCB tests, with the objective of determining an adequate pair of values, (t_I^O, l_e). It is comprised by the following steps:

1. Determine the FPZ lengths, establishing for a specific range of cohesive strengths, using a FE model of the DCB specimen;
2. Compare the obtained load-displacement curves to analytically or experimentally determined responses, to identify the lowest strength, still providing accurate responses;
3. Consider the resulting FPZ length and derive the recommended element edge length, l_e from equation (4.35).

- **Adherent thickness:** Figure 4.13 visualizes the FPZ length dependence on cohesive strength and adherent thickness. The chosen thicknesses represent the nominal ply thickness (0.184 mm), the DCB half-beam height (1.515 mm), and an intermediate value (1 mm). It is shown that FPZ length decreases towards thinner adherents. Thus, the introduced procedure for determining interfacial strengths and corresponding element edge lengths should be conducted for the anticipated adherent thicknesses.

4.3.2.4.6 Calibration of Mixed-Mode Parameters

The parameter set calibration is extended to mixed-mode conditions. For that purpose, three sets of tests are conducted at different mode-mixtures (0.23, 0.49 and 0.92), in compliance with test standard ASTM 6671 [126], providing the mode II fracture toughness, $\mathcal{G}_{IIc}^m$, and the mixed-mode interaction parameter, η^m. The experimental results are provided in the appendix B.2. The following discussion is confined to cohesive stiffness and strength.

- **Cohesive stiffness:** As shown by the mode I calibration results, the structural response accuracy deteriorates for too low cohesive stiffnesses. In contrast, high interfacial stiffness reduces the STI, while having negligible effects on the structural response. Given that the STI is also determined by the default penalty stiffness, which is in the same order of magnitude as the transversal adherent stiffness, cohesive stiffness reductions below this value are of no added value.

  In general, interfacial shear stiffnesses, K_{II} and K_{III}, can be inferred from the transversal adherent stiffness. Considering that the interfacial stiffnesses are proportional to the respec-

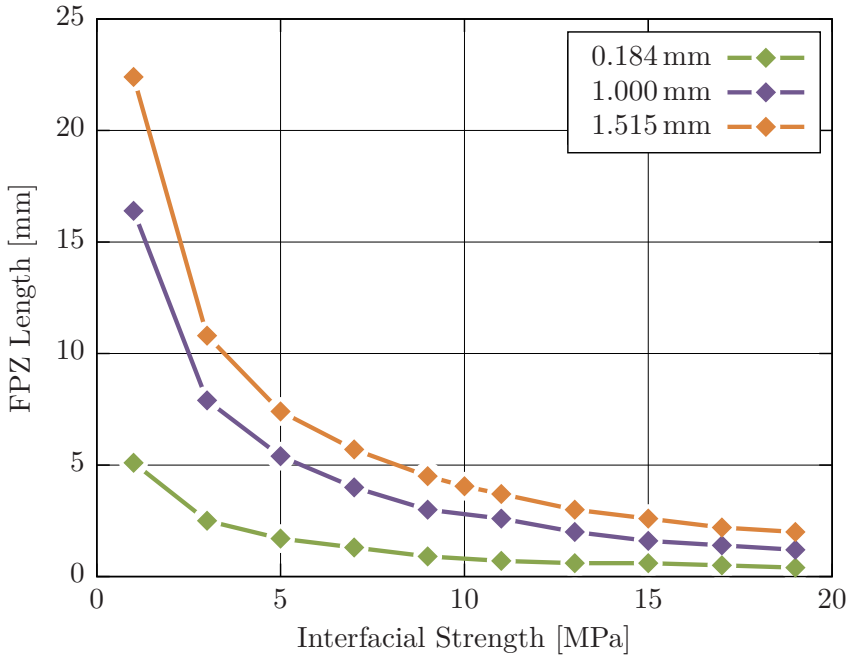

Figure 4.13.: Sensitivity of FPZ length to adherent thickness and interfacial strength. FPZ length decreases towards thinner adherents.

tive bulk material elasticity moduli, and assuming $E_{33} > G_{13} > G_{23}$ (which holds true for most carbon-epoxy materials), the conservative and pragmatic assignment $K_I = K_{II} = K_{III}$ is adopted.

- **Interfacial strength:** Also referring to the argumentation regarding mode I loading, the load-displacement response for pure mode conditions is found being virtually independent of the assigned strength, if chosen above the critical threshold. This, however, is not applicable for mixed-mode conditions, when varying normal and shear strengths independently. To still guarantee the same energy dissipation, especially for scaled strengths, Turon et al. propose a fixed proportion between normal and shear strengths, based on the respective fracture toughnesses (equation (4.36)). Hereby, $t_{II}^O = t_{III}^O = t_S^O$ is presupposed. The obtained simulation results are found being in excellent agreement with the analytical Linear-elastic Fracture Mechanics (LEFM) solution [141].

$$t_S^O = t_I^O \sqrt{\frac{\mathcal{G}_{IIc}}{\mathcal{G}_{Ic}}} \tag{4.36}$$

To date, no reliable methods have been proposed, relating FPZ length to the cohesive strengths, under mixed-mode conditions [139]. However, many parametric studies have been put forward, which consistently attest, that the FPZ lengths for any mode-mixture $G_S/G_T \leq 0$ are always larger than the FPZ length, establishing under pure mode I conditions. Therefore, it poses a conservative approach to derive the recommended mesh density, by considering pure mode I conditions [131, 139, 140]. This is considered appropriate, especially

in the context of impact-damaged structures, where the actual mode-mixture is unknown and subjected to significant variation throughout the loading history.

4.3.2.4.7 Interlaminar Parameter Summary

Taking all the considerations into account, regarding CZM parameter calibration, the finally adopted set is summarized in table 4.5. This set of values provides accurate and efficient response simulation of DCB tests, and is therefore assigned to impact-damaged and repaired structural models, for representation of interlaminar phenomena. The presented parameters refer to the matrix material of the adopted prepreg HexPly®M91/IM7.

Property	Value	Specification
K_I^m, K_{II}^m, K_{III}^m	$10^4\,\mathrm{N/mm^3}$	Derived from bulk material properties[6]
$t_I^{O,m}$	7.0 MPa	Derived from parametric studies.
$t_{II}^{O,m}$, $t_{III}^{O,m}$	21.3 MPa	Equation (4.36)
l_{FPZ}^m	1.3 mm	Determined from simulation[7]
l_e^m	0.6 mm	Equation (4.35)[8]

Table 4.5.: Calibrated CZM parameter set for prepreg matrix (Hexcel®M91/IM7).

Considering the finite element edge length, required to accurately predict intralaminar failure (0.84 mm, c.f. table 4.4), and the recommended element size, necessary for proper representation of interlaminar failure mechanisms (0.6 mm c.f. table 4.5), the least of these values is adopted throughout this thesis.

4.3.2.4.8 Impact-induced Damage Mapping

Interlaminar defect contours, provided by the damage characterization module (section 3.4), are invoked and mapped onto the surfaces of the respective ply stack meshes. By this means, finite element surfaces are classified into delaminated and non-delaminated regions, and the discussed surface properties are respectively assigned.

4.3.3. Simulation Result Analysis

Simulation result analysis is conducted in two steps: i) evaluating the physical consistency of simulated responses, based on engineering judgment, and ii) ultimately assessing the impact-damaged structure, based on the predicted residual loading capability.

In view of real-life damage assessment applications, effective experimental results for the individ-

[6] Value equates the adherents' transverse stiffness, rounded by order of magnitude.
[7] Under consideration of $t_I^{O,m} = 7\,\mathrm{MPa}$ and $t_{min} = 0.184\,\mathrm{mm}$.
[8] Considering $N_e = 2$.

ually damaged structure are evidently unavailable. Thus, it requires other means of evaluating the simulation result trustworthiness. Different complementary criteria are suggested for that purpose. Presupposing an impact-damaged structure is modeled in compliance with the rules and recommendations extensively discussed above, following simulation results are thoroughly examined.

- **Energy balance:** The analysis of the different energies over the loading history is a simple but effective method of evaluating the solution's plausibility. Equation (4.37) shows the total energy balance, ($\mathcal{E}_T$), which in the present model ought to be nearly null, over the entire loading history. Since quasi-static loading conditions are assumed, both the kinetic energy, ($\mathcal{E}_K$), and the work associated to propelling scaled masses, ($\mathcal{E}_{MS}$), ought to be negligible too (i.e. somewhat below 5 % of the internal energy, ($\mathcal{E}_I$)) [101]. Likewise, energy dissipated by viscous effects, ($\mathcal{E}_{VD}$), and the penalty work done to resolve over-closures, ($\mathcal{E}_{PW}$), should also represent a negligible portion when compared to the internal energy. Thus, the magnitude of both, the external work, ($\mathcal{E}_{EW}$), applied to the model and the internal energy should be close to identical over the most part of the loading history [100].

$$\mathcal{E}_T = \mathcal{E}_K + \mathcal{E}_I + \mathcal{E}_{VD} - \mathcal{E}_{EW} - \mathcal{E}_{PW} - \mathcal{E}_{MS} \tag{4.37}$$

  Regarding the internal energy, $\mathcal{E}_I$ (equation (4.38)), this is comprised by the reversible strain energy, $\mathcal{E}_S$, the artificial strain energy, associated to constraints to remove singular modes, such as hourglass control, $\mathcal{E}_{AS}$, and the irreversible energy dissipation due to damage propagation, $\mathcal{E}_D$. The internal energy is expected being equivalent to the strain energy up to the emergence of damage, where $\mathcal{E}_D$ is found increasing. Artificial strain energy, $\mathcal{E}_{AS}$, ought to be negligible, at least prior to failure [100].

$$\mathcal{E}_I = \mathcal{E}_S + \mathcal{E}_{AS} + \mathcal{E}_D \tag{4.38}$$

- **Load-displacement response:** Hints regarding the response plausibility are given by load-displacement curves. Especially with regards to CAI models, where ABRs prevent global Euler buckling, and damage onset and propagation is rather expected immediately prior to failure, the obtained response is mostly quasi-linear. Early non-linear behavior or severe oscillations may be indicators of inadequate loading rates, inappropriate mesh densities or excessively down-scaled cohesive strengths.
- **Failure mechanisms and damage distribution:** A physically consistent damage distribution also suggests the result's plausibility. The establishing damage disposition must be consistent with the applied boundary conditions and the initial impact-induced defects. More specifically, intra- and interlaminar damage is expected to propagate from the initial defects. Moreover, interlaminar degradation due to transversal shear may establish, which occurs especially under bending deflections. Edge delamination is also awaited in multi-directional laminates, due to dissimilar in-plane Poisson's ratios among the laminae [144].

Provided, the simulation result is found plausible with respect to the above mentioned characteristics, the residual performance of the damaged structure is evaluated. For this purpose, different criteria may be considered, depending on the properties regarded as most relevant. A few examples are named:

- **Residual strength:** It is interpreted as the remaining loading capacity prior to structural failure, and is derived from the attained peak load [73, 75].
- **Residual stiffness:** For some lightly loaded structures, the residual stiffness might be of greater interest than its actual strength. Hence, significant stiffness loss resulting from impact damage may become critical.
- **Buckling onset:** Another criterion to describe structural failure is associated to stability phenomena. Besides global buckling, sub-laminate buckling is regarded as an important criterion for the residual performance assessment of impact damaged structures (c.f. section 4.2).
- **Delamination growth:** In the context of the no-growth design approach, the load at which delaminations begin to grow is considered equivalent to the static fatigue strength (c.f. section 4.2). Thus, special interest in determining this structural performance property is given.

Although many properties are suitable to describe and assess the residual performance of impact-damaged structures, the present focus is on the residual strength property.

Since the coupon geometrical parameters may vary, it is common to express residual strength in terms of maximum attained load F_{max} per initial cross-section $(w \times t)$, for the sake of comparability. Residual nominal stress is then given by equation (4.39) [73, 75]. It is noted, that compression loads are considered positive in the present chapter.

$$\sigma_{max} = \frac{F_{max}}{w \cdot t} \tag{4.39}$$

However, equation (4.39) is somewhat misleading in multi-directional laminates, since different stresses establish in each stack, according to their orientation and stiffness. Therefore, it is preferred to express the residual strength in terms of strain, which under compression loading is mostly uniform throughout the thickness. The residual nominal strain is obtained from Hook's law (equation (4.40)). Hereby, the laminate Young's modulus in loading direction, E_x can be either obtained for each specimen individually, by evaluating the initial slope of the experimentally acquired stress-strain curve [75], or by adopting a theoretical value, based on the Classical Laminate Theory (CLT).

$$\varepsilon_{max} = \frac{\sigma_{max}}{E_x} \tag{4.40}$$

Regarding the test campaign conducted in the present scope, the displacement acquired by the hydraulic machine accounts for divers compliances along the load path, thus suggesting unrealistically high specimen strains. For most specimens, strain gauges are employed at distinct positions

to monitor bending effects. These however, are also found inappropriate to derive the nominal strain, due to strain field variations in the vicinity of damage and at the clamped regions. Given these uncertainties, the CLT approach is adopted, where E_x is derived from the membrane stiffness matrix. Considering the elastic properties listed in table 4.1 and the layup consistently adopted for all CAI specimens (c.f. figure 3.5), this engineering constant amounts to 50.39 GPa. It is noted, that this value is considered to determine the residual nominal strains listed in appendices D and E.

To ultimately assess impact damage, based on the structure's residual strength, specific thresholds must be specified. However, such margins are generally handled as confidential OEM knowledge. Thus, for the purpose of method demonstration, two thresholds are specified, according to figure 2.3. In deed, any other threshold set could be adopted instead.

According to the current damage assessment criteria, the lower threshold, below which repair feasibility must be evaluated by the OEM, is determined by DLL. Above DUL, the loading capability is considered unimpaired. For residual strengths between DLL and DUL, the damage is considered repairable and its repair can be postponed for a certain number of flight cycles, depending on its severity [9]. This simplistic classification is regarded as the baseline in the present thesis.

For the purpose of assigning absolute values to these thresholds, figure 2.3 is taken into account. It suggests, that DLL and DUL correspond to approximately 33 % and 50 % of the average loading capability, respectively. Considering the average failure strain of 9161 µm/m, determined by experiments on undamaged CAI coupons (table D.1), design limit and ultimate strains are rounded off to 3000 µm/m and 4500 µm/m, respectively. The adopted damage assessment criterion is illustrated by figure 4.14.

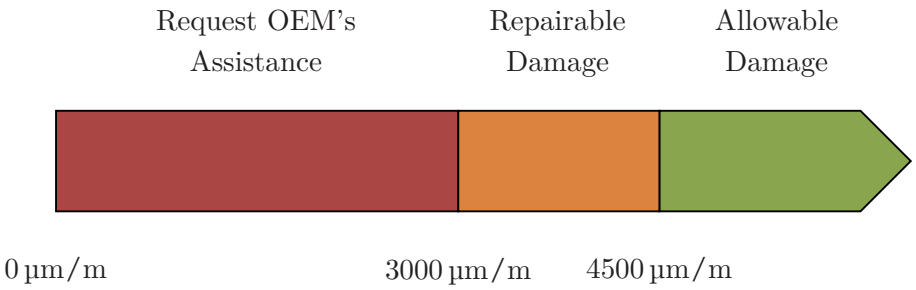

Figure 4.14.: Reference criterion for impact damage assessment. Thresholds are derived from virgin CAI test results as DLL: 3000 µm/m and DUL: 4500 µm/m.

4.4. Results and Experimental Validation

A variety of tests is conducted in order to determine the residual compressive strength of virgin, impacted, and artificially damaged specimens. Hereby, four different impact energies (20 J, 30 J, 40 J and 50 J) and six distinct combinations of artificial intralaminar cracks and delaminations (c.f. table 3.2) are considered. The respective experimental results are presented in the appendices D and E.

All specimens are tested in an universal electro-mechanic testing machine for test loads up to

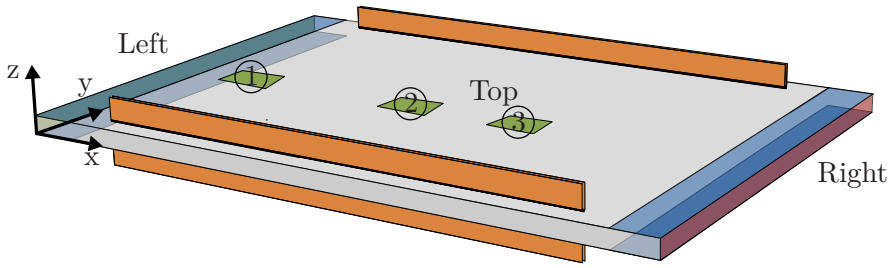

Figure 4.15.: Strain gauge in-plane positions (x,y) at top and bottom surfaces in millimeters: position 1 (15,50), position 2 (60,50), and position 3 (90,50).

200 kN. Loading is applied under displacement control conditions at a constant displacement rate of 0.5 mm/min. The remaining boundary conditions prescribed by the CAI test rig are described in the respective standards [73, 75] and are virtually consistent with those adopted in the numerical model, as described in the previous section. The specimen's behavior throughout its loading history is monitored by a load cell and the machine-own displacement transducer. As mentioned before, the signal acquired by the latter is useless, since it accounts for the testing machine compliance. Given that the associated error is significant at the applied load levels, this value is disregarded from the present discussion. Furthermore, all specimens are either equipped with strain gauges or monitored by two Digital Image Correlation (DIC) systems, to capture strains and displacements at the specimen surfaces. Six strain gauges are applied back-to-back at three different in-plane positions, to capture strains in loading direction. Three are placed at the top (i.e. impacted surface), and three at the bottom (impact-averted surface), as depicted in figure 4.15. Instead of strain gauges, DIC is applied to a few specimens, with a low resolution system (3.25 mm by 3.25 mm) applied to the impacted surface and a high resolution system (1 mm by 1 mm) applied to the impact-averted surface. The acquisition rate is set to 0.2 Hz. It is noted though, that due to limited access, only the center portion between the ABRs and the clamps is captured.

As discussed before, multiple phenomena govern the structural response, thus influencing the residual strength. The agreement between experimental and simulation results, regarding the representation of relevant mechanisms, is discussed in the following. Since all simulation results are found in compliance with the plausibility criteria, presented in sub-section 4.3.3, no further details are provided in the following. Also, for the sake of minimizing line of argument interruptions, result plots discussed in the following sub-sections, are presented in the appendices D and E.

4.4.1. Virgin Coupons

Experimental and simulation results obtained from virgin coupons are presented in appendix D.1. Result validity is discussed for a representative coupon (TC1-CAI-16), since the structural behavior is similar among all virgin coupons.

Strain gauge readings from virgin specimens (figure D.1) reveal non-uniform strains at the monitored positions, which is against the expectations. The curves suggest higher compliance at the specimen's center and similarity between local and nominal strains at position 1. Besides that,

the experimental readings point to a slight compliance increase, as the nominal strain increases. In contrast, the corresponding numerical local strains indicate strain field uniformity and linearity up to buckling onset (figure D.2). To investigate the cause of this discrepancy, the nodal DoF at the clamped surfaces (c.f. figure 4.1) are additionally constrained in width direction, to simulate ideal friction. The respective strain curves are presented in figure D.3.

The local strain analysis puts forward that friction phenomena at the clamped surfaces are responsible for the strain field non-uniformity. However, fully constraining the DoF in width direction is found being too restrictive, predicting the residual strength at roughly 7 % below the value obtained for the boundary conditions, otherwise adopted (c.f. figure 4.1). The results also suggest a much higher stiffness than that indicated by the experimental results. As for the non-linearity in the experimental strain gauge readings, this is attributed to varying friction conditions at the clamps. Although disregarding this effect might suggest a misrepresentation of the experimental setup, this simplification is still considered valid, as supported by the agreement between experimental and simulation results, regarding residual strength, mechanisms leading to failure, and establishing damage patterns. As a matter of fact, the friction effect becomes even less influential, as the damage severity increases. This is because impact-induced defects represent a more significant stress singularity than that, establishing due to friction at the clamps.

Regarding the acquired strains of coupon TC1-CAI-16 (figure D.1), divergence of the back-to-back strain readings begins at approximately 6300 µm/m, being an indicator of through-the-thickness deflection onset. The sudden strain change in all monitored positions at approximately 8700 µm/m is characteristic of buckling onset. Final failure establishes eventually at 9212 µm/m.

The simulation results depicted in figures D.2 and D.4, suggest slight transversal deflections, commencing at a nominal strain of 6200 µm/m, and buckling initiating at 8600 µm/m, which is immediately before the estimated failure (8860 µm/m). This value is only 5 % below the experimentally determined residual strength. Remarkable consistency between experimental and simulation results is also attained, regarding transversal deflection and buckling onset.

Residual strengths obtained from real and virtual CAI tests are depicted in figure 4.16. The results are expressed in relation to the average over experimentally determined failure strains, achieved by virgin specimens (9161 µm/m as reported in table D.1). As indicated by the bar chart, excellent agreement between experimental and simulated results is attained for all coupons, where the residual strength is underestimated by only 4 %, in average.

4.4.2. Impacted Coupons at 20 J

The structural behavior of CAI coupons impacted at 20 J is discussed for two representative specimens. For coupon TC2-CAI-02, local strains are acquired by the use of strain gauges. The transversal deflection throughout the loading history of specimen TC1-CAI-21 is captured by two DIC systems. The respective experimental and simulation results are provided in appendix D.2.

Both, the experimentally determined transversal deflection field (figure 4.17) as well as the local deflections, evaluated at the top and bottom surface center points (figure D.9), suggest slight transversal deflections, establishing right from the beginning along a quasi-linearly path through-

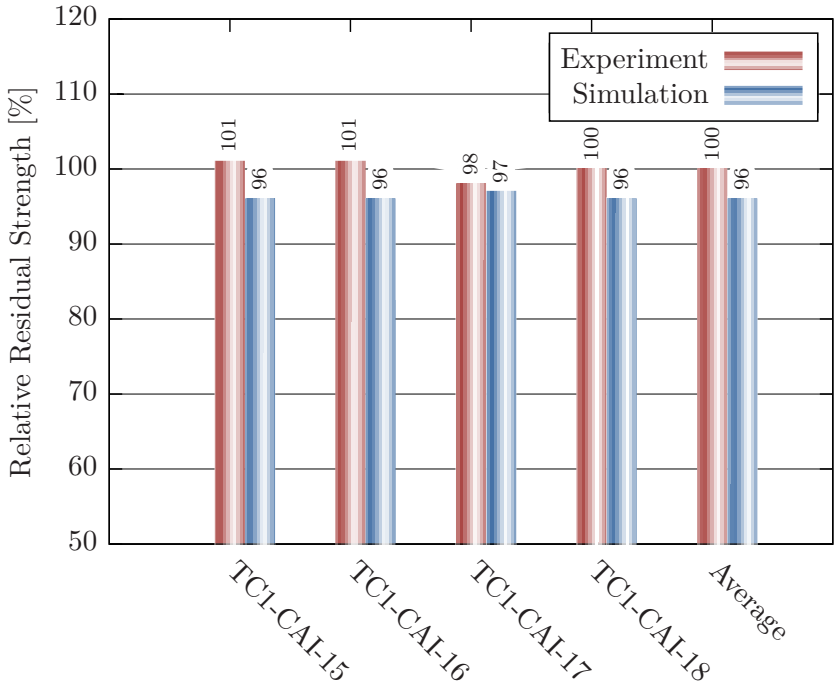

Figure 4.16.: Residual strengths obtained from experiments and simulation for virgin specimens. Excellent agreement with an average error of 4 %. Absolute average value (reference): 9161 µm/m.

out the loading history. In fact, these initial linear deflections are shown for all DIC monitored specimens, regardless of their damaged condition, thus pointing to a systematic peculiarity. Given that the deflections at the top (stack 13) and bottom surfaces (stack 1) are roughly identical[9], sub-laminate buckling can be excluded from the list of possible causes. Before the background that all 20 J impacted specimens exhibit similar behavior, a further hint is provided by the experimental strain gauge readings, obtained from TC2-CAI-02, as depicted in figure D.5. This plot attests the absence of bending phenomena up to sub-laminate buckling onset at approximately 5000 µm/m. Hence, the cause for the measured behavior is narrowed down to a rigid body rotation about the y-axis (c.f. figure 4.17), which can be either real or virtual. Virtual rigid body motion could be caused by a faulty calibration of the DIC systems, thus suggesting out-of-plane deflection, when the actual displacements are purely in-plane. This, however, would imply the occurrence of the same calibration error for both systems simultaneously, for two different testing campaigns, with a time interval of two years — which is highly improbable. It is viable though, that the whole CAI testing apparatus undergoes such a slight rigid body rotation, caused by machine compliances, transversely to the loading axis. Although the absolute DIC transversal deflection readings are therefore found inaccurate, through-the-thickness deflections can still be discussed qualitatively. Slight continuous transversal deflections are characterized by non-linear deflection curves, while sudden deflection jumps point to buckling phenomena.

Strain gauge signals obtained from specimen TC2-CAI-02 (figure D.5) point to sub-laminate buckling, occurring at 5000 µm/m, as indicated by the modest strain jumps, measured at the

[9]Discrepancies are attributed to mismatching sampling positions at the top and bottom surfaces and to distinct DIC system resolutions.

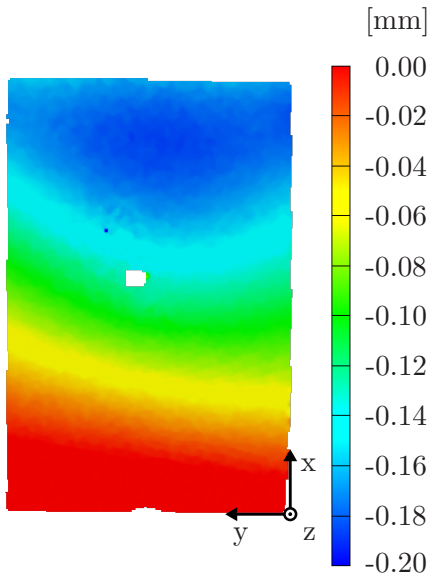

Figure 4.17.: Transversal deflection field at approximately 2000 µm/m nominal strain, obtained from the DIC system at the center region of the impact-averted surface (TC1-CAI-21). Deflection field suggests specimen rotation about the y-axis.

specimen center (sampling points 2 and 3). At a nominal strain of 5700 µm/m, all sampling positions indicate sudden strain jumps, thus implying buckling. Ultimate failure is at 6640 µm/m. Simulation results provided in figures D.6 and D.7 give evidence of sudden deflections of the two bottom-most sub-laminates at 5200 µm/m. At 5500 µm/m, the three top-most sub-laminates deflect in one direction, while the remaining stacks buckle in the opposite direction. Failure is predicted at 6254 µm/m.

Regarding the transversal deflections at the center of coupon TC1-CAI-21, obtained from DIC (figure D.9), no evidence of buckling phenomena is given for the entire loading history. This may be owed to the through-the-thickness deflection jumps being too small, thus going undetected by the DIC system. In contrast, the respective numerical model predicts sub-laminate buckling of two stacks at 4300 µm/m, and of all stacks at 6300 µm/m (figures D.8 and D.10). Failure is predicted at 6651 µm/m, which 1 % below the experimental result (6730 µm/m).

The results suggest that phenomena, occurring along the loading history, are well represented by the FE model. Residual strengths obtained from tests and simulation also attest to excellent prediction capability for lightly impact-damaged specimens at 20 J. The most inaccurate result underestimates the residual strength by 6 %, while the average error is −3 %. Hereby, the considered reference is the mean value of all experimentally determined residual strengths at 20 J, as presented in table D.2.

4.4.3. Impacted Coupons at 30 J

Specimens TC2-CAI-05 and TC2-CAI-07 are selected from among the coupons impacted at 30 J for closer discussion. The respective results are provided in appendix D.3.

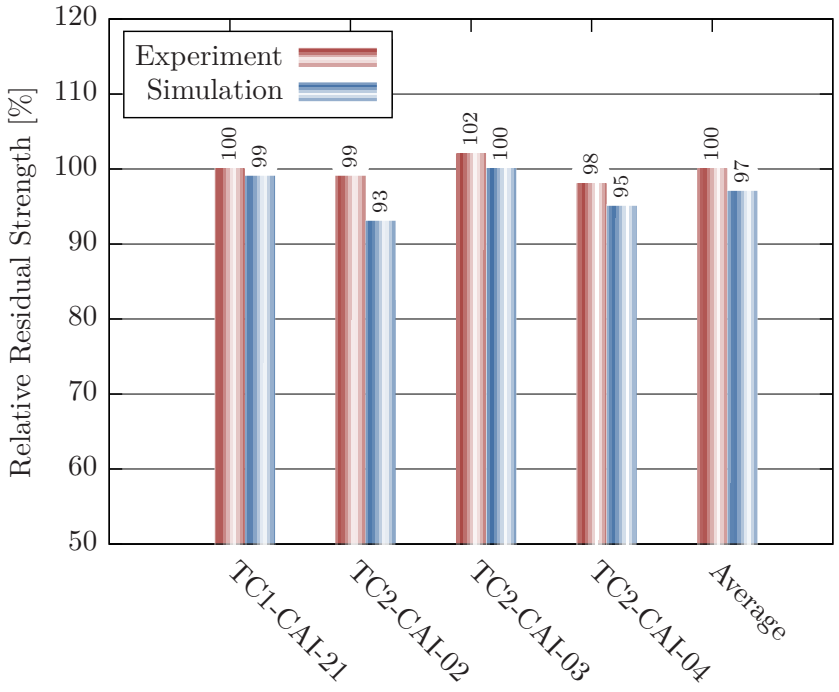

Figure 4.18.: Residual strengths obtained from experiments and simulation for specimens impacted at 20 J. Excellent agreement between experimentally and numerically determined residual strengths. Absolute average value (reference): 6704 µm/m.

As depicted by figure D.11 for coupon TC2-CAI-05, bending phenomena are absent until 2700 µm/m, where the bottom surface experiences strain alleviation. This is caused by the superposed tensile strains, establishing due to sub-laminate transverse deflection at the center. A pronounced strain jump is measured at 4100 µm/m, and divergence at sampling point 1 is detected at 5300 µm/m. The first is an indicator of sub-laminate buckling of a few stacks, while the latter indicates buckling of the entire coupon. Failure is measured at 6063 µm/m. Simulation results, presented in figures D.12 and D.13, provide similar findings. The first sub-laminates deflect at 2500 µm/m. At 4200 µm/m, most stacks experience sudden deflection, and finally all stacks undergo buckling at 5300 µm/m. The predicted failure strain is 5849 µm/m, which is 4 % below the experimentally determined residual strength.

Regarding specimen TC2-CAI-07, transversal deflections acquired by DIC (figure D.15) indicate non-linearity and curve divergence virtually from the very beginning. At roughly 3800 µm/m, the deflection rate seams to increase. The specimen fails at 5499 µm/m. Very low strains are predicted at the top surface center region (figure D.14). Upon bending, the top surface assumes a concave shape, and a compressive strain increase is expected, as a result of in-plane and bending strain superposition. However, these local strains suggest the contrary. As opposed to coupon TC2-CAI-05, this specimen presents a major impact-induced fiber crack at the top-most stack (c.f. table D.3). The observed lower strains are thus attributed to this major fiber crack, which interrupts the load carrying path. Figure D.16 implies all sub-laminates deflecting right from the beginning, and a sudden deflection jump is noticed at 3900 µm/m. Failure establishes ultimately at 5344 µm/m.

The relative residual strengths of the specimen set impacted at 30 J are depicted in figure 4.19. In average, the simulation is found underestimating the experimental results by 3 %, while the most pronounced underestimation amounts 4 %. It is noted, that this coupon set presents higher residual strength scatter, when compared to other coupon sets. The cause for this resides in the significant scatter, regarding the impact-induced damage extension, especially with respect to the measured fiber crack length, at the top surface (c.f. table D.3). The fact that experimental and simulation results still present excellent agreement, in spite of such dissimilar impact-damage patterns, underlines the proposed method's robustness.

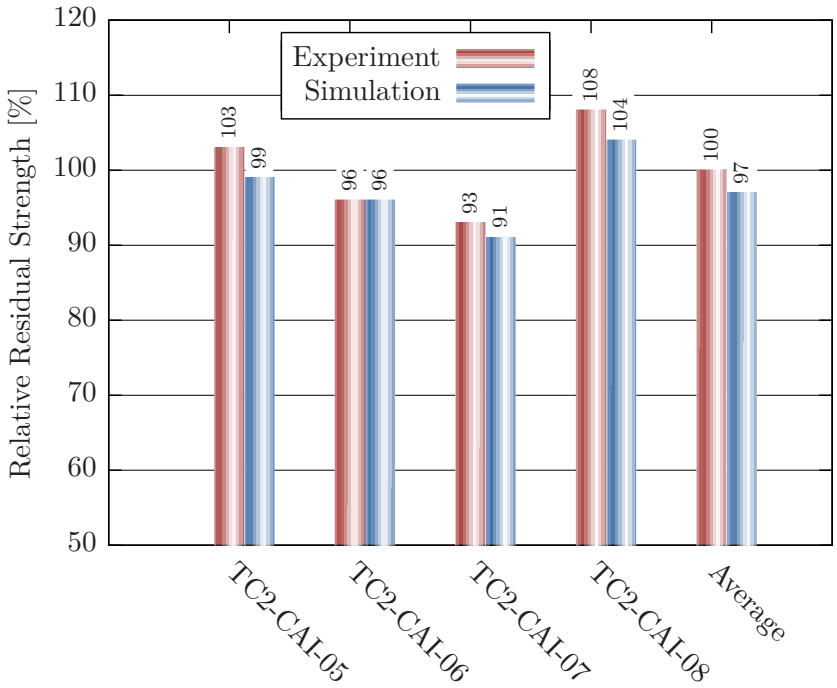

Figure 4.19.: Residual strengths obtained from experiments and simulation for specimens impacted at 30 J. Considerable scatter among experimentally determined residual strengths, due to varying damage extent. The proposed approach copes well with such variations. Absolute average value (reference): 5894 µm/m.

4.4.4. Impacted Coupons at 40 J

Specimens TC1-CAI-03 and TC1-CAI-08 are selected from among the coupons impacted at 40 J for closer discussion. The respective results are provided in appendix D.4 and the corresponding residual strengths are summarized in figure 4.20.

Strain gauge readings obtained from coupon TC1-CAI-08 indicate higher compliance in the bottom surface center region (figure D.17). This is attributed to the large delamination, the major intralaminar matrix crack at the bottom, and impact-induced deformation, which together inhibit load transfer in the bottom center region. At the top surface, strain decreases in the impact vicinity, beginning at 2200 µm/m. This is possibly caused by crest formation at the impact-induced fiber crack. As a consequence, load transfer capability is reduced at the top surface center region. Judging by the strain divergence at the sampling point 1, global buckling occurs roughly at

3400 µm/m. Failure is determined at 5503 µm/m. Simulated results (figures D.18 and D.19) indicate transversal deflection over the entire loading history and buckling of all stacks at 4300 µm/m. In contrast to the experimental results, lower strains establish at the top center region, caused by the fiber crack in the top-most stack and the large delamination beneath. The predicted failure strain amounts 5282 µm/m. Experimental and simulation results suggest some contradiction, mainly caused by two modeling simplifications. On the one hand, impact-induced permanent deformation is disregarded, causing transversal deflection to be less pronounced. On the other hand, the initial intralaminar cracks are modeled as one-element-wide gaps. This prevents entanglement effects from occurring at the intralaminar cracks, thus effectively hindering load transfer from one to the other crack side. This is a rather conservative assumption, since under compression loads, fiber cracks still enable some load transfer due to contacting and entangled laminate portions.

Results acquired by DIC for coupon TC1-CAI-03, imply increasing transversal deflections over the entire loading history (figure D.21). No distinct events are detected until failure, which establishes at 5174 µm/m. Simulated local strains at the top sampling points 2 and 3 are fairly low, due to the presence of a major fiber crack (figure D.20). At roughly 1900 µm/m the two bottom-most stacks separate from the remaining laminate (figure D.22). At 3500 µm/m, deflection rate increases, and the specimen is ultimately found failing at 5111 µm/m.

Regarding the sequence of events and the respective loads, coincidence between experimental and numerical results is rather modest. This is owed to measurement system limitations, but mostly to very individual mechanisms, occurring at the damage features, whose morphology is subjected to considerable variance. This scatter is ultimately responsible for the residual strength variation depicted in figure 4.20. Yet, accurate loading capability estimations are still attained, at an average error of −3 %.

4.4.5. Impacted Coupons at 50 J

The response of CAI specimens impacted at 50 J is representatively discussed for coupons TC2-CAI-09 and TC1-CAI-12. While the first specimen is monitored with strain gauges, the behavior of the second is screened by two DIC systems. The respective result plots are presented in appendix D.5, along with a summary table for all four tested coupons.

In figure D.23, the experimentally determined strains at the top and bottom surfaces diverge over the entire loading history. Divergence is found increasing at 1400 µm/m, as a possible sign of sub-laminate buckling. Pronounced strain jumps at the center sampling points at 4500 µm/m point to considerable sub-laminate buckling. Failure installs at 5046 µm/m. This is in good agreement with the predicted results (figures D.24 and D.25), which also point to increasing deflections over the entire loading history. Sub-laminate buckling is predicted somewhat later at 2100 µm/m, while severe buckling of all stacks is simulated at 3900 µm/m. The estimated failure strain is 4848 µm/m.

Regarding coupon TC2-CAI-12, the DIC readings depicted in figure D.27 indicate only slight non-linearity in the transversal deflection curve, until roughly 2000 µm/m, hinting at moderate effective deflections. However, explicit evidence of sub-laminate buckling is not found before

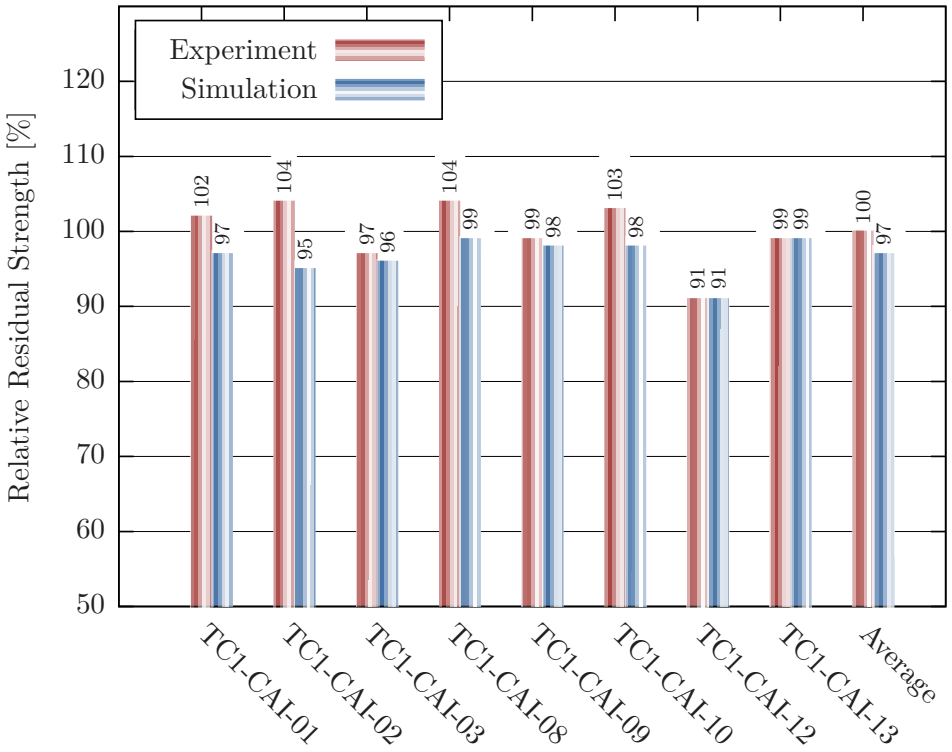

Figure 4.20.: Residual strengths obtained from experiments and simulation for specimens impacted at 40 J. Accurate residual strength prediction, in spite of considerable scatter. Absolute average value (reference): 5315 µm/m.

4100 µm/m. Final failure establishes at 4816 µm/m. The simulated results hint at sub-laminates separating at roughly 2000 µm/m (figures D.26 and D.28). From this point on, deflections become more pronounced, until buckling occurs at 3400 µm/m. A different buckling mode establishes at roughly 4200 µm/m, before coupon failure at 4818 µm/m.

Considering the complex damage state in these heavily impacted coupons, the establishing mechanisms are satisfactorily predicted. Figure 4.21 summarizes the obtained relative residual strengths from tests and simulations, suggesting excellent agreement between them. Average and maximum error are respectively $-2\,\%$ and $-4\,\%$.

From the comparison of virtual and real results obtained for coupons impacted at different energies, a few observations are highlighted. It is noted that the sequence of events leading to final failure is well predicted by the adopted models. However, the nominal strain at which they occur is partly found slightly deviating from the experimental results. Also strain and deflection magnitudes are found rather in qualitative than in quantitative agreement. On the one hand, this is owed to the limitations of the adopted measurement systems, which are insufficient to fully characterize the occurring mechanisms in the experimental setup. On the other hand, modeling-related simplifications are also accountable for such discrepancies. For instance, initial deformation, entanglement and friction phenomena, and partial load transfer across intralaminar cracks are disregarded in the present model. Yet, in spite of these mismatches, the simulated residual strengths are consis-

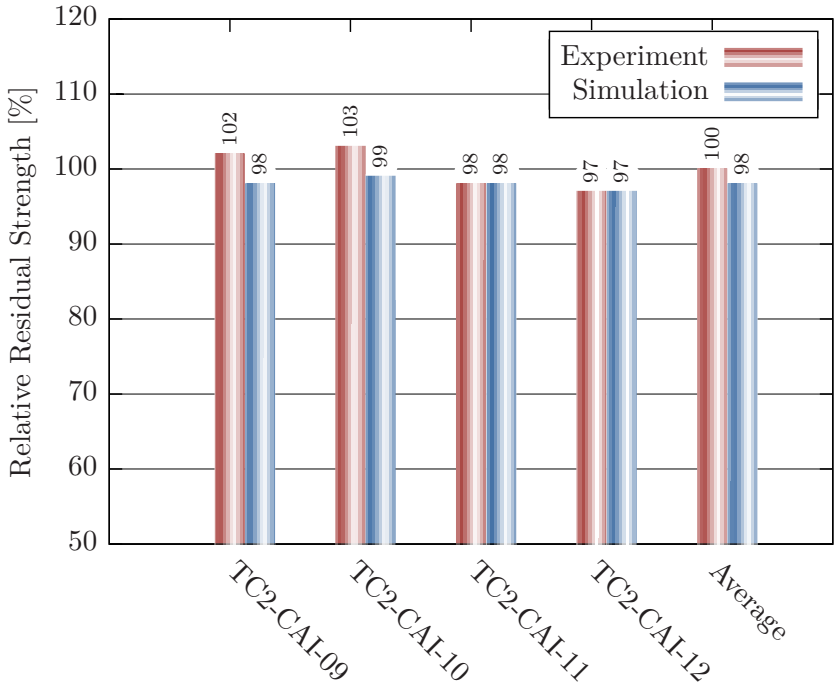

Figure 4.21.: Residual strengths obtained from experiments and simulation for specimens impacted at 50 J. Remarkable agreement is attained for heavily impacted coupons. Absolute average value (reference): 4960 µm/m.

tently found in excellent agreement with the experimentally obtained results, as summarized by figure 4.22.

4.4.6. Artificially Delaminated Coupons: A- and B-Series

In the following, the real and simulated structural behaviors of artificially delaminated coupons are discussed. As introduced in section 3.3, different coupon sets are considered, presenting distinct artificial defects. A-series specimens are characterized by a circular delamination of 50 mm diameter, located at the first interface (bottom), while an identical delamination shape is assigned to the third interface in the B-series. Here too, strain gauge and DIC records are alternately available.

From the A-series, specimens TC2-CAI-A1 and TC2-CAI-A3 are selected as representatives; DIC and strain gauge results are respectively analyzed. The respective graphics and the summary table E.1 are presented in appendix E.1.

Strain gauge records of coupon TC2-CAI-A3 imply buckling of the bottom-most sub-laminate and of the remaining laminate to occur nearly simultaneously at roughly 5000 µm/m (figure E.1). Structural failure is attained at 8856 µm/m. Similar response is obtained from the virtual test, where sub-laminate buckling onset is also suggested at 5000 µm/m, followed by main laminate buckling at about 5300 µm/m (figures E.2 and E.3). However, the model suggests sub-laminate deflections in opposite directions, while the experiment implies them deflecting upwards. The peak load attained by the artificially delaminated specimen is 7727 µm/m, which is 9 % below the

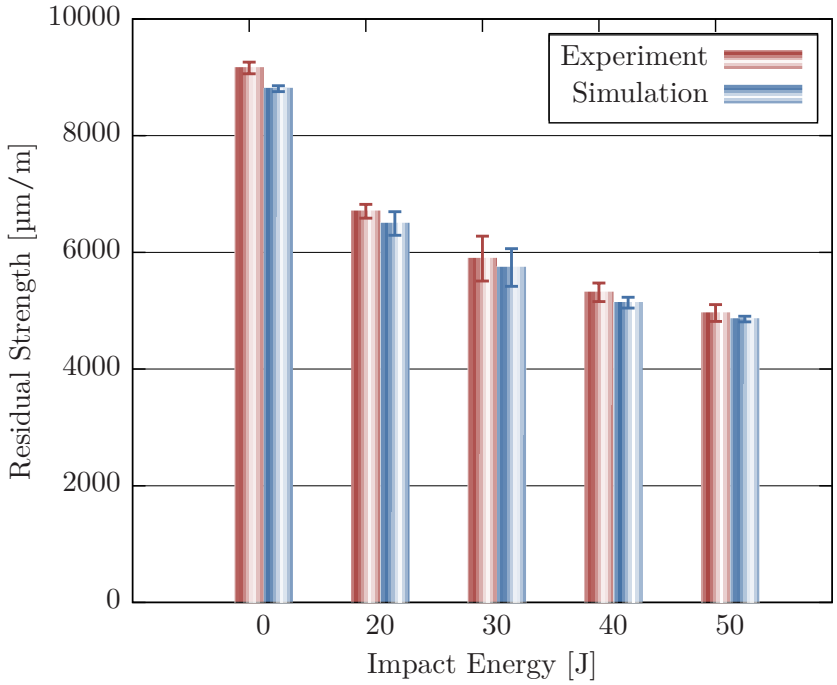

Figure 4.22.: Average residual strengths and respective standard deviations obtained from experiments and simulation for impact-damaged coupons.

experimental value.

Given the similarity between the two coupons, the virtual test responses obtained for coupons TC2-CAI-A1 and TC2-CAI-A3 are approximately identical (figures E.4 and E.6). The DIC readings obtained for TC2-CAI-A1 in figure E.5 confirm the upward deflection of both sub-laminates as opposed to the simulated behavior. As discussed before, the linearly increasing deflection is considered being of spurious nature, while the transition to non-linear deflection progression at roughly 5000 µm/m indicates buckling onset. Here too, the residual strength is fairly underestimated by 13 % of the test result 8478 µm/m.

The residual strengths of all A-series specimens are depicted in figure 4.23. The chart shows moderate scatter among the experimental results, as expected from artificially damaged specimens. Scatter among the predicted residual strengths is also low. The severest underestimation amounts 14 %, while the average error is −11 %. This systematic error is assumed being related to the different establishing buckling modes. The experimentally observed upward deflection of both sub-laminates contributes less to delamination growth, since peel loads are rather negligible. In addition, both contacting surfaces constrain themselves in normal and tangential directions, offering the specimen increased bending resistance. Many causes are conceivable for predicting buckling modes other than those establishing in the real test. Although all specimens with artificial delaminations are submitted to a blunt 4 J impact, in order to break up any potential adhesion between the sub-laminates and the Teflon foil, residual adhesion can not be fully ruled out. However, it is more likely that imperfections related to the experimental setup, such as geometric deviations, imperfect boundary conditions, and issues related to the load introduction are

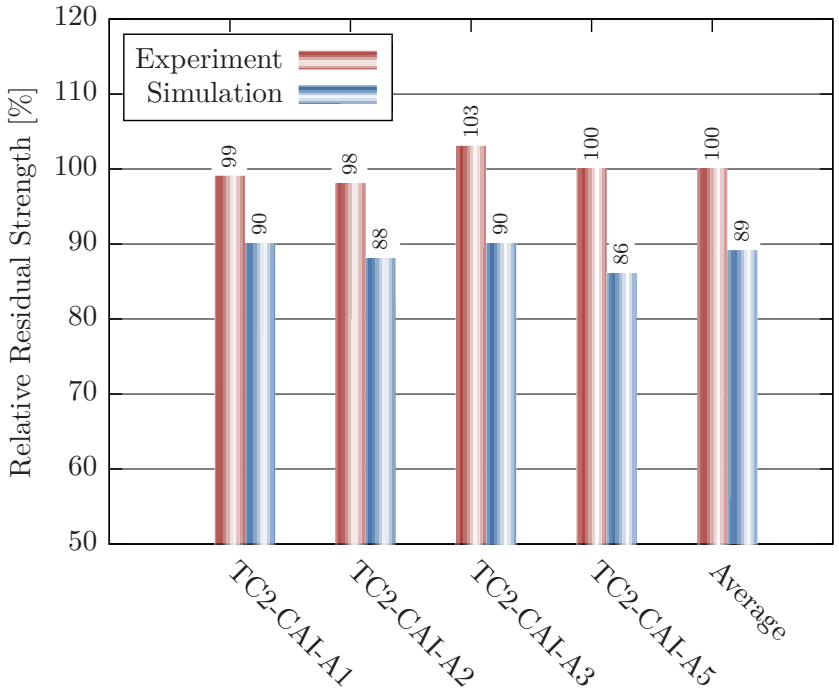

Figure 4.23.: Residual strengths obtained from experiments and simulation for artificially delaminated coupons (A-series). Absolute average value (reference): 8583 µm/m. Significant residual strength underestimation by an average of 11 %.

responsible for triggering another than the predicted buckling mode. As suggested by the results obtained for the other series, this particular artificial damage configuration is found responding very sensitively to such imperfections.

From the B-series, specimens TC2-CAI-B1 and TC2-CAI-B5 are discussed in the following. The respective results are shown in appendix E.2.

Strain gauge signals for coupon TC2-CAI-B1 give evidence of slight through-the-thickness motion at the center, beginning at roughly 3300 µm/m and leading up to buckling of both sub-laminates at 4500 µm/m and another two strain jumps at 4900 µm/m and 5200 µm/m, possibly associated to mode-shifts (figure E.7). This is in reasonable agreement with the simulation results (figures E.8 and E.9), where slight bottom surface deflections begin at 4400 µm/m and buckling of both laminate occurs at 4600 µm/m. At roughly 5000 µm/m and 5400 µm/m mode-shifts are suggested at the thinner sub-laminate. Failure is ultimately predicted at 5644 µm/m, which is 4 % above the test result.

Due to the likeness between all B-series specimens, the obtained simulation results are fairly identical among each other (compare figures E.8 and E.9 with figures E.10 and E.12). Experimentally determined transversal deflections, depicted in figure E.11, hint at both sub-laminates buckling simultaneously at 5200 µm/m, thus coinciding with the last predicted mode-shift. Buckling in opposite directions observed in the real test is also predicted by simulation. Failure strain is measured at 5789 µm/m and predicted at 5647 µm/m.

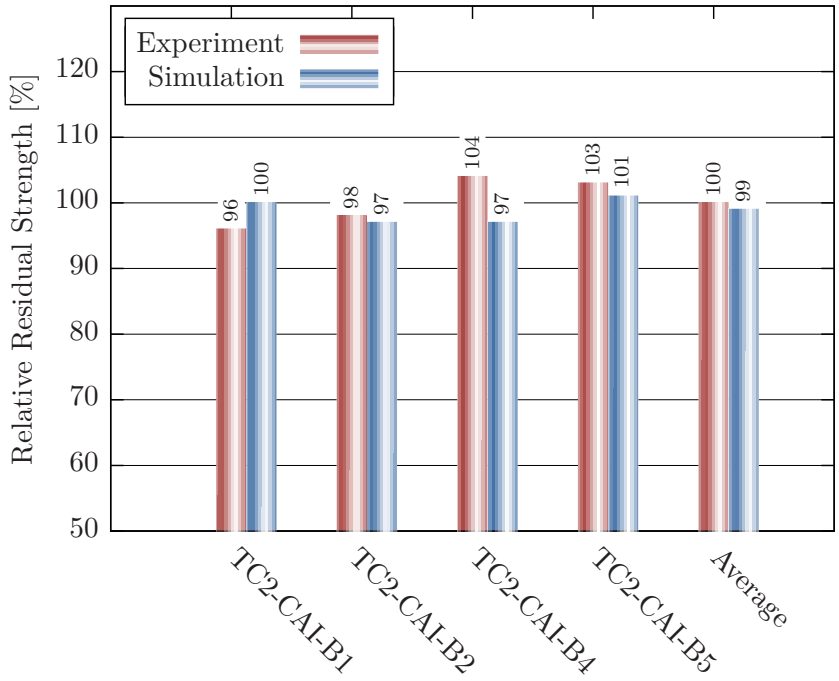

Figure 4.24.: Residual strengths obtained from experiments and simulation for artificially delaminated coupons (B-series). Absolute average value (reference): 5618 µm/m. Considerable scatter among experimental results. Good residual strength prediction.

The evaluation of all B-series responses, as summarized in figure 4.24, indicates a 8 % scatter among the experimental results, which is fairly high considering the coupons' similarity. In contrast, the variation amongst simulated residual strengths is less than 4 % and is caused by slight variations regarding the specimen geometry and damage size (c.f. table E.2). The mismatch between experimental and simulated residual strengths is less than −7 % (−1 % in average).

4.4.7. Artificially Delaminated Coupons: C- and D-Series

In this subsection, the effect of artificial intralaminar cracks through the first (C-series) and the first three stacks (D-series) is studied. Intralaminar crack length is 25 mm and its orientation is consistently 135°.

The behavior of CAI coupons with an artificial fiber crack through the first stack is discussed for specimens TC2-CAI-C3 and TC2-CAI-C5. The respective plots and summary table are given in appendix E.3.

Figure E.13 depicts the experimentally determined local strains. Although slightly diverging over the entire loading history, more accentuated divergence is observed at approximately 5000 µm/m. This smooth strain variation points rather to continuous transversal deflections than to sudden buckling. Such a strain jump is only observed at 7500 µm/m, immediately prior to failure (7754 µm/m). Similar results are predicted through simulation. Simulated strains are also found diverging over the entire loading history (figure E.14). A slight strain jump is noticed at 6000 µm/m, representing a sign of buckling. At 7500 µm/m, strain divergence increases and fail-

ure establishes at 8022 µm/m. Simulated transversal deflections at the coupon center (figure E.15) indicate slight through-the-thickness motion over the entire loading history, and confirm the occurrence of first buckling at 6000 µm/m. Deflection rate increases at 7500 µm/m. All stacks experience the same deflection, due to the absence of delaminations.

Regarding specimen TC2-CAI-C5, experimentally determined transversal deflections suggest buckling onset at the transition from linear to non-linear curve shape (5000 µm/m), and failure establishing at 7735 µm/m (figure E.17). Simulation results are similar to those presented for TC2-CAI-C3. However, buckling onset occurs at a slightly lower nominal strain of 5100 µm/m (figures E.16 and E.18). Increased deflection rate is found at 7500 µm/m and failure is eventually predicted at 8071 µm/m, which is 4 % above the test result.

Owing to their likeness, identical residual strengths are predicted among the C-series coupons (figure 4.25). Scatter among the experimental results is rather low and the simulated residual strengths overestimate the effective loading capabilities by less than 8 % (6 % in average). Insufficient experimental data is available to determine the exact cause for the systematic error associated to this test series. However, one plausible explanation is that the implemented intralaminar crack favors the formation of undulation in neighboring layers. Given that the crack is implemented by cutting through the uncured first stack, the neighboring stacks are likely to fill the gap, thus undergoing undulation during the curring process. The present layup design is comprised by four plies in loading direction, one of them being adjacent to the artificial crack. Reduced loading capacity due to undulation in this ply is expected to affect the coupon's residual strength. In fact, the simulation model does not account for the degrading effect of undulation, which may explain the obtained residual strength discrepancy. Although this hypothesis is plausible, further experimental investigation is required to prove its validity.

Experimental and simulation results obtained for specimens TC2-CAI-D3 and TC2-CAI-D5 are presented in appendix E.4 and discussed below. It is noted that due to the constant artificial crack orientation in the first three stacks, obviously a 25 mm fiber crack length results in the first stack. However, given their fiber orientation, this artificial crack yields a roughly 18 mm effective fiber crack length in the second 0°-oriented stack. Since the fiber orientation in the third stack is equivalent to the artificial crack direction, the resulting damage is viewed as a pure matrix crack of 25 mm length.

The experimental local strain plot presented in figure E.19 for specimen TC2-CAI-D3 hints at slight through-the-thickness motion over the entire loading history. Strains at the bottom surface center are slightly lower than the corresponding readings at the top surface gauges. It is assumed that slight bending deformation and load path interruption, caused by the artificial crack, are responsible for this behavior. At roughly 7500 µm/m, the strain curve slopes change, indicating buckling. The specimen fails at 7811 µm/m. Simulation results (figures E.20 and E.21) support the assumption made to explain the lower strains in the artificial crack vicinity. Indeed, transversal deflections are predicted over the entire loading history. The congruency among all simulated local strains, except for those close to the crack, implies reduced loading capacity at the bottom surface. A distinct buckling event is accused by local strains and transversal deflection plots at 6000 µm/m. The deflection rate increases at approximately 7100 µm/m and failure installs at 7657 µm/m.

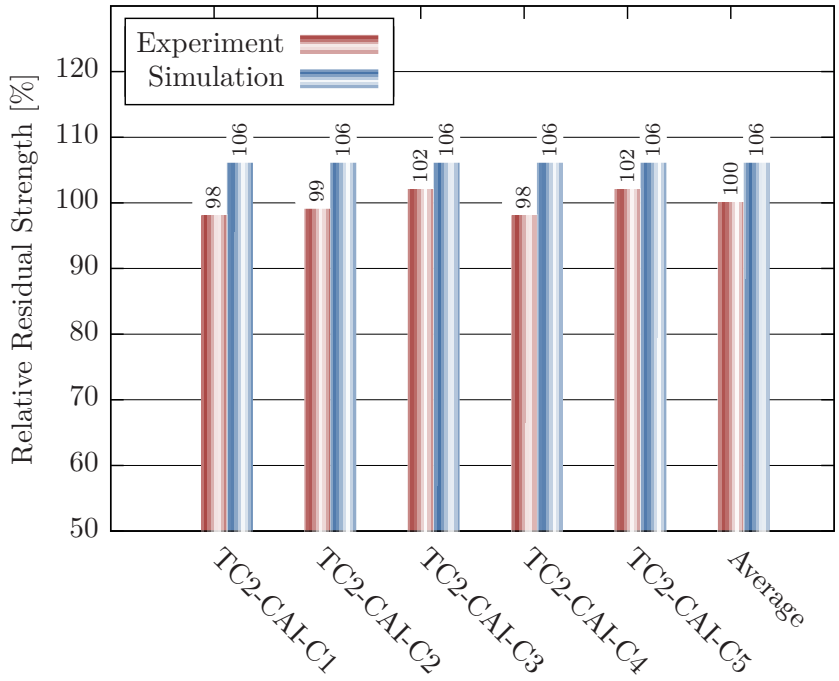

Figure 4.25.: Residual strengths obtained from experiments and simulation for coupons with artificial fiber cracks (C-series). Absolute average value (reference): 7583 µm/m. Overestimation of the experimental results is attributed to undulation effects in the tested specimens.

DIC results obtained for coupon TC2-CAI-D5 depict a deflection curve shape transition at roughly 5000 µm/m, which indicates buckling. The measured failure strain is 7666 µm/m. It is noted that the displayed divergence between top and bottom surface deflections suggests unphysical interpenetration, whose cause is attributed to mismatching sampling points and dissimilar resolution between the DIC systems. Simulation results indicate local strain and transversal deflection jumps at 5100 µm/m, which is characteristic of buckling phenomena. Higher deflection rate establishes at 6700 µm/m, and failure is predicted at 7678 µm/m.

Good agreement between test and simulation results, regarding the predicted mechanisms and their respective loads, is attained. As summarized by figure 4.26, scatter among experiments and simulation results is very low. The predicted residual strengths are also found in excellent agreement with those obtained by real testing. The maximum error amounts −2 %; in average 0 %. Although undulation is also expected to occur for this specimen set, its effect on the residual strength is negligible. This is because the neighboring stack is comprised by a single 90° ply and the next undamaged 0° ply is three plies apart. It can be safely assumed, that the farer the gap, the more the undulation amplitude dissipates.

4.4.8. Artificially Delaminated Coupons: AC- and BD-Series

The AC-series comprises the combination of a circular 50 mm diameter delamination in the first interface and a fiber crack, 25 mm long, through the first stack. Similarly, the BD-series represents the combination of a delamination introduced in the third interface and a intralaminar crack of

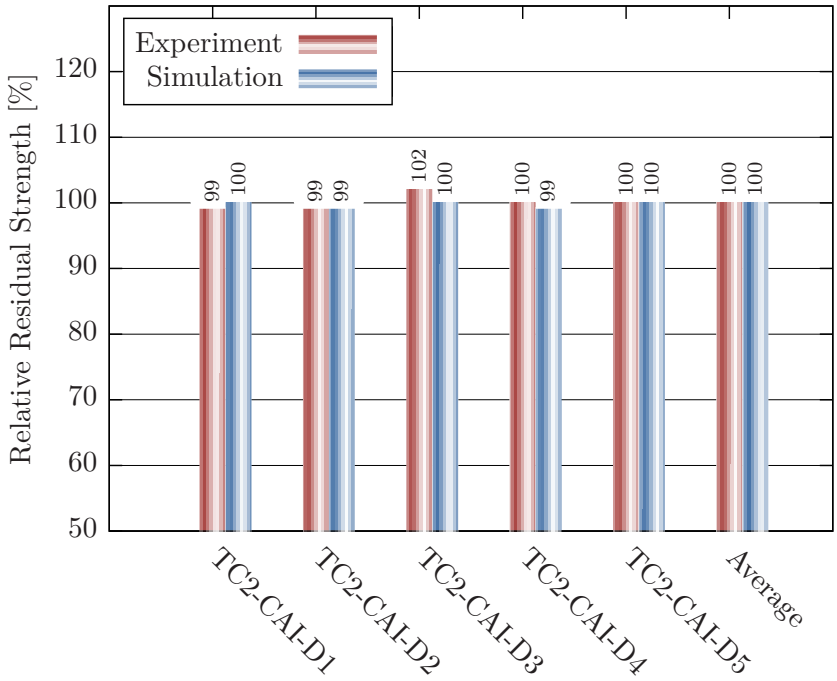

Figure 4.26.: Residual strengths obtained from experiments and simulation for coupons with artificial fiber cracks (D-series). Absolute average value (reference): 7678 µm/m. Low residual strength scatter and excellent agreement between test and simulation results.

constant orientation through the first three stacks (c.f. section 3.3). The respective test and simulation results are discussed below.

The AC-series results are discussed for specimens TC2-CAI-AC3 and TC2-CAI-AC5. The respective real and virtual test results are presented in appendix E.5.

Measured local strains (figure E.25) depict a sudden strain drop at all sampling points, which however is more pronounced in the damage vicinity (3300 µm/m). This implies buckling in both sub-laminates, with larger deflections at the bottom stack. At roughly 5000 µm/m increasing divergence indicates higher deflection rate at the thicker sub-laminate. The strain jump at 7000 µm/m is an indicator of buckling. Failure establishes at 7642 µm/m. The simulated behavior is somewhat different (c.f. figures E.26 and E.27). Both sub-laminates experience slight transversal deflection in the same direction. At 5900 µm/m, both sub-laminates buckle in opposite directions, and the bottom stack snaps back soon after. A mode-shift occurs at 6500 µm/m, where the first stack deflects again in the opposite direction. The simulated failure strain is 7489 µm/m. It is noted that predicted strains at the bottom surface are significantly lower than those measured during the experiment. The strain drop, acquired by the strain gauges, suggests a sudden break-up of the initially resin-filled intralaminar crack. This effect is not reproduced by the simulation, because the crack is modeled by a one-element-wide gap.

With respect to specimen TC2-CAI-AC5, the DIC results suggest the first stack buckling at 2200 µm/m (figure E.29). From this point on non-linear deflection progression is observed for the remaining stacks. At roughly 5000 µm/m these stacks undergo increasing continuous deflections.

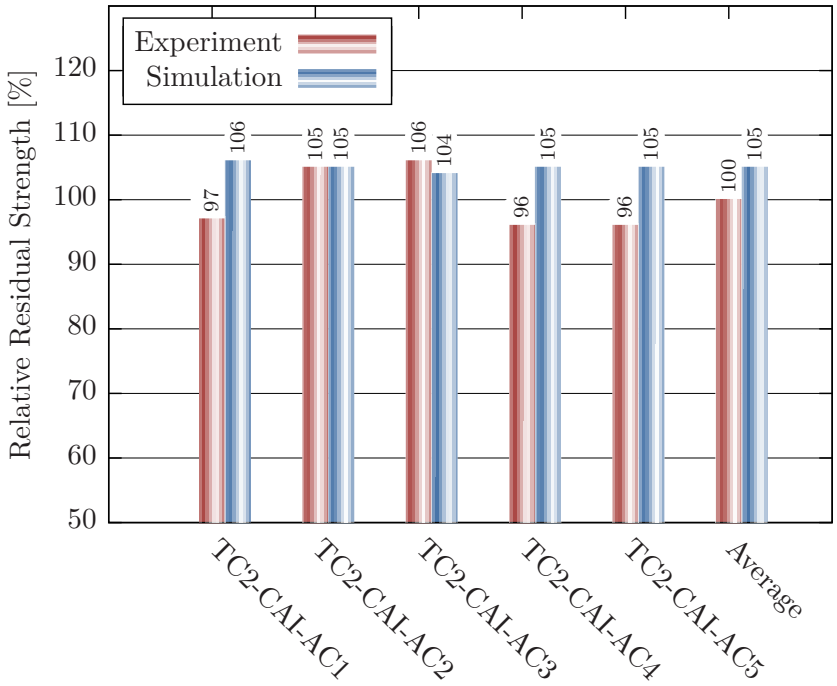

Figure 4.27.: Residual strengths obtained from experiments and simulation for coupons with artificial delaminations and fiber cracks (AC-series). Absolute average value (reference): 7189 µm/m. Failure strain overestimation is attributed to undulation effects.

At this load, the first stack experiences a buckling mode-shift. Failure strain is 6896 µm/m. Simulation results indicate slight transversal deflections beginning at 3000 µm/m (figures E.28 and E.30). Sub-laminates are found buckling in opposite directions at 5100 µm/m, where the bottom stack snaps-back immediately. At 6300 µm/m the bottom stack buckles again, separating from the main sub-laminate. The estimated residual strength is 6896 µm/m.

Although some predicted events differ from the monitored coupon behavior, similar conditions establish just prior to failure. The predicted residual strengths present very low scatter (figure 4.27), while the variation among experimental results is 10 %. This value is very high considering the supposed reproducibility of artificial defects and the negligible coupon thickness variation. As depicted in the bar chart, excellent agreement between real and virtual residual strengths is attained for specimens TC2-CAI-AC2 and TC2-CAI-AC3. However, the error associated to the remaining coupons of this series is similar to that observed for C-series specimens. Thus, the undulation establishing in the second stack is viewed as the cause for these discrepancies. In average, the residual strength is overestimated by 5 %, while the maximum overestimation amounts 9 %.

Experimental and simulation results obtained for the BD-series are presented in the appendix E.6. The behavior of specimens TC2-CAI-BD3 and TC2-CAI-BD5 is examined below.

Strain gauge readings for specimen TC2-CAI-BD3 imply both sub-laminates experiencing buckling at roughly 3800 µm/m (figure E.31). At 5000 µm/m, a snap-through event occurs and the specimen takes up load again, until failing at 5791 µm/m. This response is well predicted by the adopted model (figures E.32 and E.33). Results suggest both sub-laminates deflecting in opposite

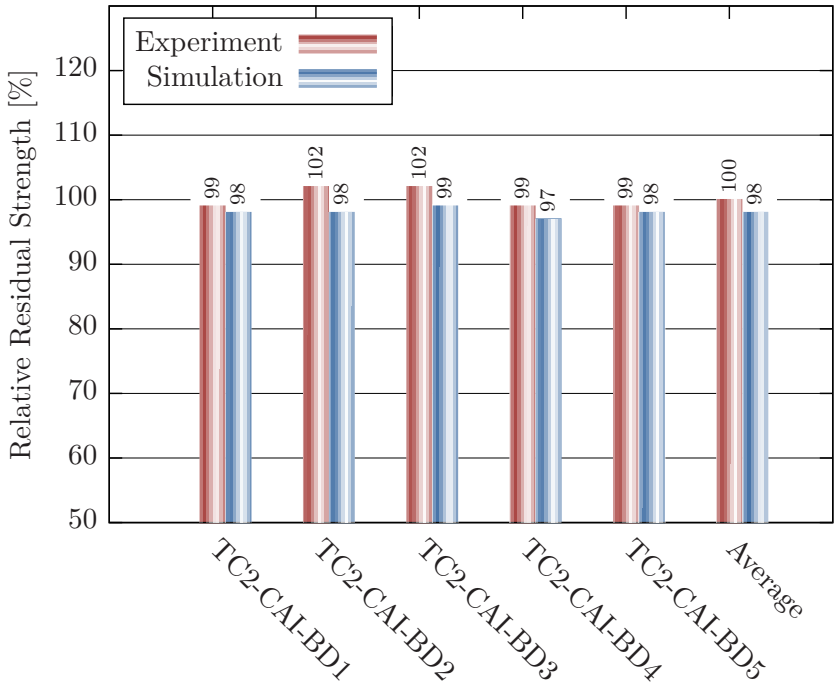

Figure 4.28.: Residual strengths obtained from experiments and simulation for coupons with artificial delaminations and fiber cracks (BD-series). Absolute average value (reference): 5698 µm/m. Experimentally determined residual strengths are well predicted.

directions, right from the beginning. At 5000 µm/m, the structure snaps-through and takes up load again, eventually failing at 5618 µm/m.

A slightly different behavior is acquired by the DIC systems for TC2-CAI-BD5 (figure E.35). First buckling of both sub-laminates in opposite directions occurs at 4400 µm/m and slight snap-through buckling is detected at 4800 µm/m. The experimentally determined residual strength is 5626 µm/m. The simulated behavior describes buckling of both sub-laminates at 4300 µm/m and failure at 5560 µm/m. The comparison of figures E.35 and E.36 underlines the excellent agreement between simulation and test results.

The residual strengths of all BD-coupons are depicted in figure 4.28. Scatter in experimental and simulation results is very low and excellent agreement is found between real and virtual residual strengths. Maximum and average underestimations amount 4 % and 2 %, respectively.

Figure 4.29 summarizes the residual strengths, obtained from coupons with distinct artificial damage. It is noted that the experimental residual loading capacity of A-series specimens is only slightly below the average virgin strength (9161 µm/m). However, the simulated behavior suggests that the near-surface delamination might lead to a more significant weakening, if a different buckling mode establishes, due to other boundary conditions. Although the mismatch between real and virtual results is considerable, the calculated strength poses a reasonably conservative estimate. The results also imply that a single deep-lying B-type delamination can cause considerable strength reductions, and that the contribution of additional intralaminar D-type defects is rather negligible. Similarly, comparing A- and AC-series results, the contribution of a C-type fiber

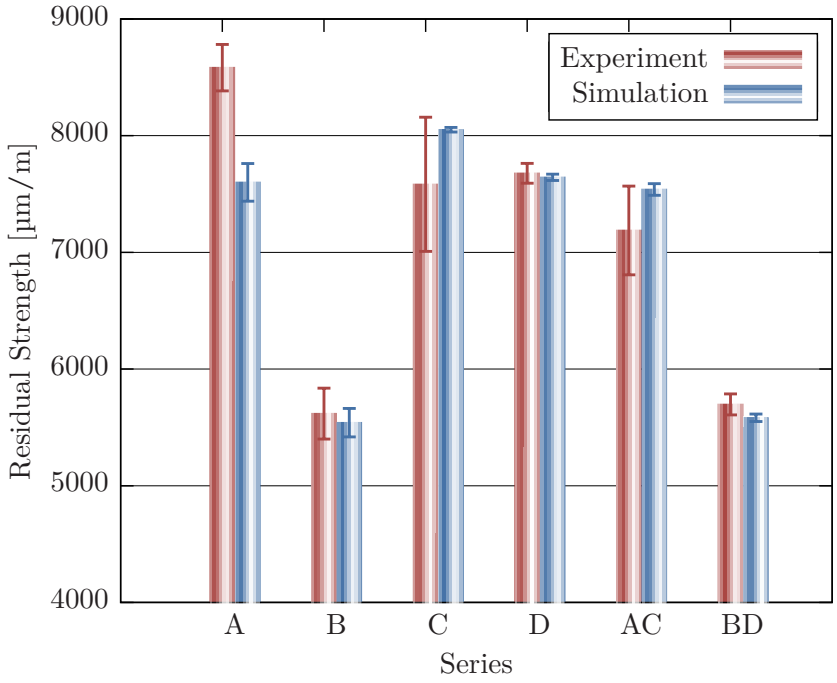

Figure 4.29.: Average residual strengths and respective standard deviations obtained from experiments and simulation for artificially damaged coupons. Good agreement especially for series B, D, and BD.

crack is predicted as being rather negligible. Residual strengths experimentally obtained from the C- and D-series are fairly similar. However, by undulation avoidance, higher strength can be expected for C- and AC-coupons. Except for the series A, C, and AC whose experimental results are questionable, the adopted modeling approach is found providing excellent residual strength predictions. Thus, it commends itself not only for the assessment of impact damaged structures, but also for the evaluation of parts with single delamination defects, as for instance occurring during composite part manufacturing.

4.5. Damage Assessment

The present thesis proposes the assessment of damage in composite structures, based on the predicted residual strength. The previous section attests the adopted approach an excellent capability in representing the structural behavior of damaged structures with high accuracy. This poses a solid foundation for a trustworthy damage assessment. However, criteria are required to effectively evaluate the structural condition. As depicted in figure 4.14, a simple criterion is introduced for the purpose of demonstration. This can evidently be replaced by any other criterion, defined in terms of residual strength.

In figure 4.30, the relation between projected damage area and determined residual strength is plotted for the experimentally tested coupons. Applying the residual strength thresholds to these results, implies that the residual static strengths of all impact-damaged coupons — even those impacted at 50 J — are above DUL, thus being tolerable. Similarly, referring to figure 4.29,

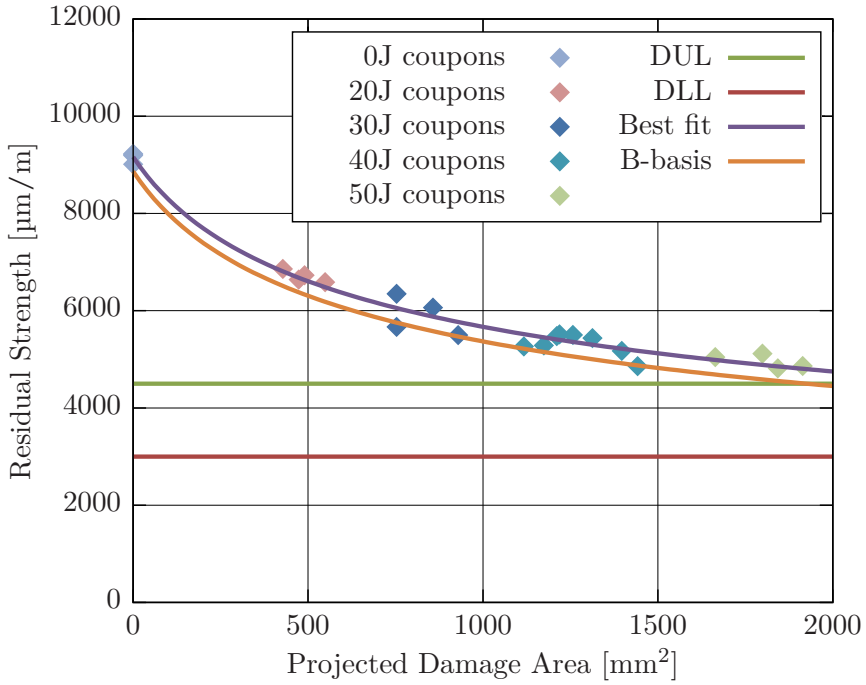

Figure 4.30.: Relation between projected delamination area and residual strength for impact damaged CAI coupons. All impact-induced defects are considered tolerable, when applying the proposed residual strength based damage assessment method.

none of the artificial defects considered in the present study causes a loading capability reduction below DUL. Hence, from a structural mechanics perspective, all these defects are regarded as uncritical, thus dispensing structural repair. In contrast, current assessment methods based on the damage detectability by visual inspection, demand repair action for projected damage areas beyond 600 mm^2 [37]. This implies all specimens, impacted at energies beyond 30 J, requiring structural repair.

4.6. Conclusion

In the context of decision-making regarding damage handling, assessing damage criticality is fundamental. In this chapter, a different approach than the currently established is proposed. It consists in the creation of an individual FE model, representing the actual condition of the damaged structure. This enables mechanical behavior simulation and ultimately the determination of the residual strength. Damage handling recommendations are then derived by the application of assessment criteria, expressed in terms of residual strength.

For that purpose, a sophisticated model is defined, which enables the representation of the main physical phenomena, determining the structural response of impact-damaged coupons loaded in compression. Modeling peculiarities are addressed and strategies for obtaining a physically and numerically consistent model are given. Special attention is given to modeling the cohesive zone. DCB and MMB tests are conducted, to ultimately determine a parameter set, that enables the efficient simulation of cohesive-zone-related mechanisms. A new procedure for deriving such a

consistent CZM parameter set through analytical and numerical methods is put forward, thus dispensing costly experimental parametric studies. Contrary to recommendations of other authors [137], lower interfacial stiffness (close to the adherents' transversal stiffness) is found contributing to higher computational efficiency, when adopting explicit time integration schemes, however without compromising result accuracy. The present study also suggests that the approach of artificially reducing the interface strength to increase FPZ length, as often discussed for virtual DCB and MMB tests, also provides reasonable results, when extended to more complex loading conditions and damage distributions, as establishing, for instance, in CAI specimens.

Through the analysis of different simulation outputs, such as load-displacement curves, energy balance over the loading history, and damage distribution, the physical consistency of the obtained solution can be evaluated. However, the method's ultimate validity and accuracy is discussed under consideration of several experimental test results, obtained from coupons with impact-induced and artificial damage, loaded in compression. This validation study attests the modeling approach an outstanding capability in predicting residual strengths and also the mechanisms leading up to final failure. Thus, the second hypothesis postulated in chapter 1 is substantiated.

Examining the experimental and numerical results gained from impact-damaged coupons, it is found that the residual strengths are slightly underestimated (by less than 6 %). It is also shown, that the simulated mechanical response before failure is also found in good agreement with the experimental behavior. In view of the complicated interaction of defects and the complex interplay of the associated physical phenomena, the prediction capability is found remarkable. Besides being owed to the detailed modeling approach, this is also attributed to the consideration of realistic damage features, as obtained from the characterization module, described in chapter 3. Given that µCT results are unavailable for most tested specimens, the generic cubic function describing the through-the-thickness fiber length distribution, as introduced in chapter 3, is found contributing to these accurate results.

Regarding the method validation against artificially damaged structures, excellent agreement is also achieved. Besides serving the purpose of validation, the results also underline the importance of considering each damage feature for accurate residual strength predictions. Although the studied intralaminar crack configurations are found being less influential than delaminations, they also contribute to significant residual strength reductions. The results also point out that some configurations are more sensitive to test setup imperfections (A-series), and that unintentional undulations, introduced during coupon manufacturing may lead to erroneous results, if not explicitly covered for in the model (C- and AC-series). To circumvent the formation of undulations in future intralaminar damage tests, it is recommended introducing intralaminar cracks after curring.

Defects considered in this thesis are eventually assessed with regards to a two-threshold criterion, established for the purpose of demonstration. According to the reasoning leading up to this criterion, none of the damaged structures considered in this thesis actually requires structural repair, since the predicted residual strengths are consistently above DUL. However, all specimens with impact energies beyond 30 J are considered exceeding the ADL, thus requiring repair, according to the currently adopted approach. This comparison hints at the great potential of the proposed method. Furthermore, more refined assessment criteria and associated handling recommendations

may contribute to even more efficient maintenance schedules and repairs. In addition, results obtained for artificially damaged coupons suggest the method's capability in assessing, for instance, structures containing single-delamination, as sometimes occurring during manufacturing.

With regards to fatigue assessment, the present method offers an excellent basis for its implementation. As discussed in 4.2, an often proposed approach consists in equating fatigue strength with the load, at which delaminations propagate. Given that the present method also predicts this phenomenon, returning the load of first delamination growth (i.e. the fatigue strength) is easily implemented.

5 Reparability Verification

The present chapter addresses the final module in the decision-making process for the assessment of damaged composite structures. This module is dedicated to verifying the ability of individual repair configurations, in restoring as-designed loading capability.

In the following sections, the method employed for reparability verification is introduced. Its relevance is discussed by comparing experimentally and numerically obtained results. Since the adopted modeling approach is very similar to that, introduced in the previous chapter, many references to chapter 4 are made, especially in section 5.4, to avoid repetition.

5.1. Motivation

As introduced in chapter 2 and depicted in figures 2.1 and 2.4, determining proper handling of damaged composite structures relies on a series of steps. Once the damage is found substantially impairing the structural performance, permanent repair or even replacement of the damaged structure is inevitable, to restore structural airworthiness. However, deciding which specific action is more appropriate, can be approached differently. The proposed method is intended to support that decision-making by providing a means of analyzing the structure's reparability, based on repair strength prediction.

The currently adopted approach consists in the specification of reparability thresholds in terms of damage size. As discussed in chapter 2, defects are considered critical when their extension exceeds ADL. This poses the boundary beyond which repair is required. Likewise, the RDL represents the other boundary, up to which structural repair is permitted, and beyond which additional substantiation data is required, to determine the damaged part's reparability [9]. On the one hand, this boundary is defined based on the supposed residual strength, anticipated for a specific damage size. The empirical methods generally adopted for that purpose are considered over-conservative for a variety of reasons, as discussed in the context of figure 2.3. On the other hand, RDL is defined based on the repair strength, considered attainable for a given damage size and repair configuration. This too is considered fairly restrictive. First, because a priori strength estimations are conservative by definition. Then, because repair analysis is currently conducted based on conservative analytical 2D methods, especially for bonded repairs [52, 145].

In contrast to the established method, this thesis suggests that reparability should be verified based on the individually attainable repair strength. For that purpose, the FE method is employed as a means of predicting repair strength in arbitrarily complex structures, accounting for relevant physical phenomena. More accurate and less conservative load capability predictions can be expected by taking the effective boundary conditions and individual repaired part properties into account. In addition, the method enables the derivation of tailored repairs, with higher repair

strengths and increased weight efficiency. Finally, equipping MRO service providers with such validated methods, that also support the definition of repairs beyond the scope covered by current SRMs, can contribute to cost-efficient repairs and to ground-time reductions.

5.2. Review on Composite Repair

Along with the increase of composite primary and secondary airframe structures comes the demand for high-performance composite repair. This has led to many research activities by the involved industry and academia, ranging from damage detection to automated repair techniques [52]. Those studies have led aviation authorities to stipulate standards for the substantiation of acceptable and airworthy repairs [9].

It is the primary aim of structural repair to restore mechanical performance, especially regarding strength and stiffness [146]. In pursuing that goal, bonded and bolted repair techniques are widely adopted [10]. Mechanically fastened repairs can experience high stress concentrations at the bolt holes and are therefore avoided in thin structures. Techniques, such as doubler and scarf-bonded repairs as well as resin-injection are typical to composite structures. Yet, enhanced load transfer, higher residual strength, and better aerodynamic performance is best attained by scarf-bonded repairs. However, extensive sound material removal due to scarf angles between 1:20 and 1:60 makes this technique more appropriate for thin structures, as in fact presenting in most airframe parts [52, 145, 147].

In the past decades, experimental, analytical, and numerical studies have been conducted to investigate the phenomena associated to bonded joints, and to identify the key-parameters determining the behavior of bonded repairs. Through numerous experiments and analytical considerations, Hart-Smith [148] introduces to the different failure mechanisms, establishing for each joint type. He also discusses, how these are influenced by parameters such as adherent thickness and applied load level. Due to the shear and peel stress non-uniformity, establishing under external patches, constructive measures are suggested. Namely chamfering adherent edges contributes to stress reductions at this critical region, thus contributing to enhanced joint strength. Also the avoidance of eccentricity, for instance by choosing scarfed repairs, is shown contributing to higher strengths [149]. Based on these analytical methods and associated design recommendations, different tools have been proposed to determine adequate joint designs and to predict the respective joint strengths [146, 150]. Further developments thereof have enabled the consideration of manufacturing defects and the elasto-plastic behavior, typical for adhesive materials [151, 152]. Other authors applied some of these principles to entire composite repair programs, ranging from NDI to repair manufacturing [146].

The pioneering work performed by Hart-Smith and other researchers is later extended to numerical analysis by Soutis and Hu [153]. Given the possibilities offered by new FE tools and powerful personal computers, they discuss the behavior of double-lap-bonded repairs under compressive load, both experimentally and numerically. As opposed to the still well-established analytical 2D methods, the 3D behavior of patch-repairs is thoroughly analyzed, using appropriate FE models. By this means, various patch-repair parameters are adjusted in order to determine efficient external patch-repairs. They conclude, that 2D analyses pose over-conservative estimates of the repair

strength, because the residual loading capability of the parent structure — which can be regarded as a notched plate — is ignored. Failure strength is thus under-estimated by more than 40 % [154]. In contrast, the response obtained from the 3D models is found being in good agreement with experimentally determined results. It is also reported that 80 % of the pristine loading capability is attained for bonded patch-repairs. In another study, the authors predict the strength of scarf-repairs based on similar 3D stress analysis. An average stress criterion is adopted, where the characteristic distance specification requires calibration in order to achieve a good match between simulation and test results.

Wang and Gunnion [145, 155] also point to the conservatism associated to the widely established 2D analysis methods, as these fail to represent load bypass, occurring once the adhesive undergoes plastic yielding. As opposed to previous studies, strain-based failure criteria are adopted and the non-uniform stress distribution installing in the scarf of multi-axial composite laminates is also considered. Comparison with experimental results attests the proposed method good capability of predicting repair efficiency.

Campilho et al. [156] discuss the dependency of scarf-bonded joint strength on the stacking sequence and scarf angle using FE analysis and cohesive elements to simulate the adhesive behavior. Since the scarf joint spanned the entire width, thus depriving the structure from alternative load paths, the effect of adhesive toughness on the joint strength is found being weaker than expected in 3D repaired structures. By assigning a mixed-mode damage model to the cohesive elements, adhesive damage onset and propagation is well predicted in single-strap tensile specimens [157]. Extension of the modeling approach to single- and double-patch 3D repair models enables detailed analysis of stress distributions as well as the simulation of damage onset and propagation, establishing due to the implementation and combination of different design features, such as adherent chamfering and the use of fillets and fillers. Such a model is considered an appropriate tool for deriving design guidelines for efficient repairs [158]. The adhesive material model is described by a quadratic traction criterion to determine damage onset. Crack propagation in the bond-line is predicted by a linear energy fracture criterion. While the fracture toughnesses are determined by experiments, the remaining parameters characterizing the cohesive behavior are obtained by calibration of the numerical model, to simulate the experimental response [159]. Pinto et al. [160] extended this modeling approach to 3D scarf repairs to study the influence of repair width, scarf angle, and the use of cover plies on the overall behavior and the ultimate strength. The achieved results commend the reported approach for supporting repair design specification.

Cheng et al. [161] investigated the tensile behavior of external patch-repaired specimens. An isotropic elastic-perfectly plastic behavior is ascribed to the adhesive. Stress concentrations establishing at the circular patch longitudinal and at the hole's transversal edges are found responsible for initiating parent adherent failure. By optimization of the repair parameters, strength recovery beyond 90 % is predicted.

Xiaoquan et al. [162] studied failure mechanisms in scarf-bonded repairs using 3D models. Adhesive behavior is linear elastic up to damage onset, which is determined by a maximum shear stress criterion, thus ignoring peel effects. Elastic properties are suddenly degraded, once this criterion is fulfilled. To account for the structural behavior beyond adhesive failure, the Hashin and Chang

criteria are assigned to the parent laminate. Adhesive failure is shown commencing close to the 0° plies and propagating in circumferential direction along the scarf bond-line. Ultimately, intralaminar crack onset and propagation establishes between the scarf region and specimen lateral edges. In spite of the many simplifications associated to the adopted adhesive material model, good agreement between experimental and simulation results is achieved.

From the many studies conducted on the subject of repair strength prediction it is concluded that numerical models pose an appropriate means of determining the complex stress states and resulting failure mechanisms, establishing in real repaired airframe structures. Non-linear methods based on fracture mechanics and cohesive zone modeling enable accurate predictions of the fracture behavior and repair strength. Such sophisticated and validated analysis methods are consistently viewed as appropriate means for the specification of efficient repairs.

In the present context of individual damage assessment, it requires a reliable method for reparability verification. For that purpose, some of the proposed approaches are extended to obtain a parametric 3D model, that enables repaired strength predictions of different configurations. This poses an important basis for iterative repair optimization processes, yet disregarded in the present thesis. While most prediction models addressed in this review focus solely on adhesive-related failure mechanisms, it is considered appropriate to account also for intralaminar failure and delamination of the adherents. This is because, under certain circumstances (e.g. the use of thick doublers), such failure mechanisms might become crucial with respect to repair strength. Hence, the proposed model is designed to account not only for adhesive-related, but for all relevant failure mechanisms, expected to occur in composite laminates.

5.3. Experimental Test Setup

To validate the numerical results, obtained from detailed repair models, large flat coupons are submitted to uni-axial tensile loading. Although many other specimen types and loading conditions could be applied, the tensile test is preferred for mainly two reasons. On the one hand, test setup is rather simple thus minimizing experiment-related uncertainties, which may difficult the result interpretation. On the other hand, repair-induced stress concentrations can be better studied, due to the absence of stress superpositions, caused by other effects, such as buckling for instance.

A total of ten large tension specimens is considered for experimental testing. All large coupons are manufactured from the same prepreg material as the CAI specimens. However, a different stacking sequence is adopted, yet presenting the same degree of orthotropy and thus the same in-plane laminate Young moduli as the CAI layup (figure 5.1).

Specimen are 600 mm long and 300 mm wide (figure 5.2). The effectively measured laminate thickness amounts in average 2.11 mm. A circular scarf-bonded repair is introduced at the center of seven specimens in a co-bonding process[1], while the remaining three are tested in their pristine condition, as a reference. At both longitudinal ends, 2 mm thick glass fiber reinforced polymer tabs are adhesively-bonded onto the coupon surfaces for load introduction. Tabs length is 100 mm

[1] Cytec FM®300 epoxy adhesive film is employed for all bonded repairs [163].

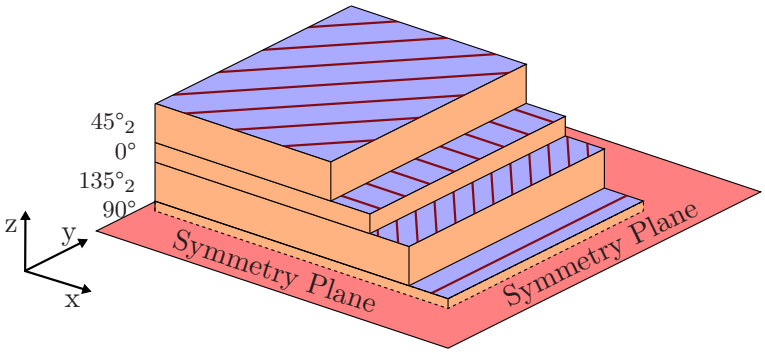

Figure 5.1.: Stacking sequence of large repair coupons.

and the width matches that of the parent laminate. A total of 23 holes of 11 mm diameter is equidistantly drilled through the tabs and parent laminate, in three parallel rows. Each side is clamped between two steel plates, which are fastened by 23 M10-screws, at a tightening torque of 80 Nm.

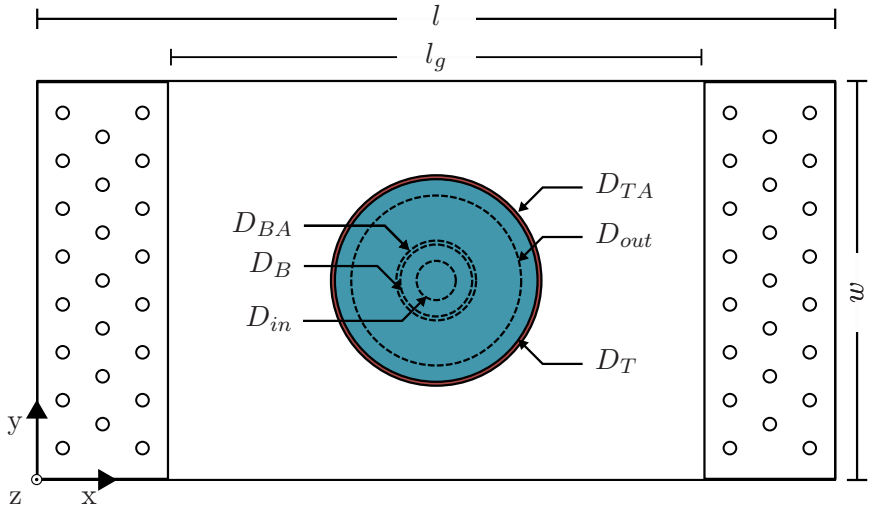

Figure 5.2.: Sketch of the main large tension coupon measurements.

As depicted in figures 5.2 and 5.3, a 30 mm diameter hole, D_{in}, is machined through the laminate thickness. A 1:30 scarf angle is introduced such as to form a butt edge at the bottom stack, to avoid fraying (figure 5.3). Patch and parent stacking sequences are identical, except for the additional 45° filler ply, introduced between the first and second patch-stacks. In addition, single 45° cover plies are included at the top and bottom surfaces, exceeding the cutout diameters D_{in} and D_{out} by respectively 25 mm (D_B and D_T). The cover adhesives' diameters are 6 mm larger than their respective cover plies (D_{BA} and D_{TA}). The adopted parameters are summarized in table 5.1.

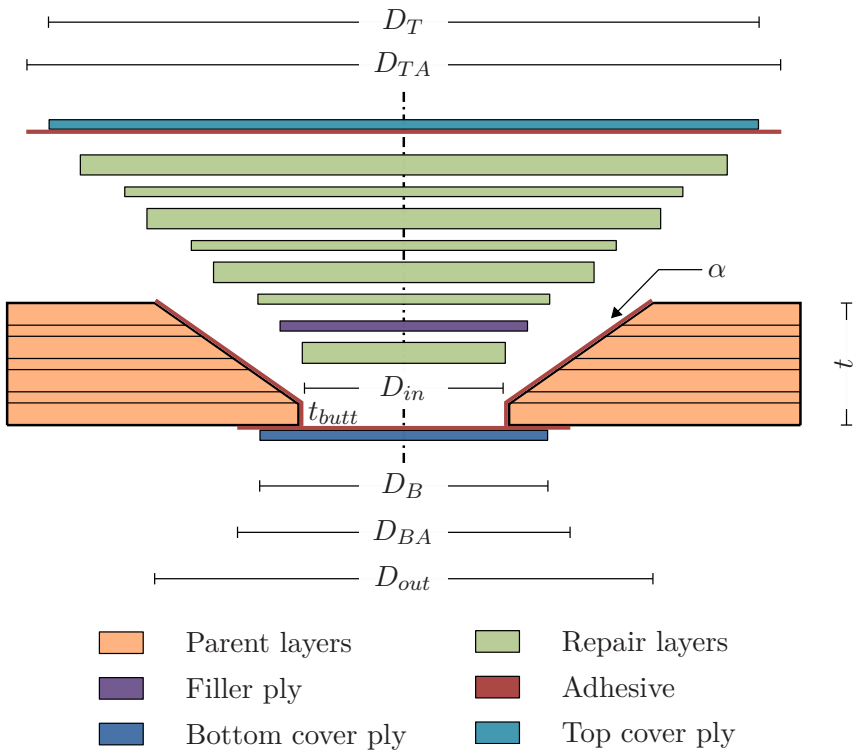

Figure 5.3.: Schematic representation of the repair cross-section.

Parameter	Symbol	Value
Specimen length	l	600 mm
Gauge length	l_g	400 mm
Specimen width	w	300 mm
Specimen thickness	t	2.11 mm
Scarf ratio	α	1:30
Butt thickness	t_{butt}	0.38 mm
Cutout diameter (bottom)	D_{in}	15 mm
Filler ply thickness	t_F	0.19 mm
Top cover thickness	t_T	0.19 mm
Bottom cover thickness	t_B	0.19 mm
Top cover diameter	D_T	155 mm
Bottom cover diameter	D_B	55 mm
Top cover adhesive diameter	D_{TA}	161 mm
Bottom cover diameter	D_{BA}	61 mm
Adhesive thickness	t_{adh}	0.2 mm

Table 5.1.: Geometric parameters of large tensile repair coupons (c.f. figures 5.2 and 5.3).

Most specimens are equipped with five strain gauges, respectively at the top and bottom surfaces. Referring to the coordinate system depicted in figure 5.2, the strain gauge in-plane positions are

listed in table 5.2. Identical locations at both surfaces are chosen to monitor eventual bending deformations. For three specimens, strains and motions at the top surface are monitored using a DIC system. An universal hydraulic testing machine for test loads up to 400 kN is adopted. Quasi-static displacement controlled loading at a rate of 0.5 mm/min is chosen. Load and displacement are respectively acquired by a load cell and the machine-own displacement transducer. Similarly to the results obtained form the CAI tests, the acquired displacement also accounts for compliances along the entire loading path and is therefore considered inappropriate for further analysis.

Strain gauge	In-plane coordinates (x,y) [mm]
1	(400,150)
2	(300,150)
3	(200,150)
4	(300,270)
5	(300,30)

Table 5.2.: Strain gauge in-plane positions (x,y) at the top and bottom coupon surfaces, according to the coordinate system depicted in figure 5.2.

5.4. Methodology

In this thesis, it is proposed that the decision — whether or not a damaged part can be repaired — be made, based on attainable repair strength, instead of projected damage extent. For that purpose, a detailed parametric FE model is developed, capable of predicting the repaired structure's response. Simulation results obtained thereof are first examined regarding their physical consistency. Then, the actual reparability is verified through the comparison of estimated repair strength and as-designed loading capability.

5.4.1. Phenomenology of Bonded-Repaired Laminates

Before introducing the adopted structural model setup, a brief description of the main failure mechanisms in scarf-bonded repairs is given. Like the behavior of impact-damaged structures, many interacting mechanisms determine the response of bonded repaired composite laminates.

From a macroscopic perspective, transverse deflections can occur in spite of the plane-stress condition. These are for instance caused by buckling phenomena, secondary bending due to asymmetric repairs, and counteraction of initial warpage.

At meso-scale, intralaminar matrix and fiber failure can occur at particular stress hot-spots, in sequence of the ultimate strength being attained. Delaminations may occur at free edges due to transversal shear and peel stresses, caused by dissimilar stiffnesses and Poisson's ratios of adjacent plies. At the free edges of stiff doublers, significant shear and peel stresses may install in the adhesive. These are known to promote near surface delamination in the parent adherent and eventually intralaminar failure at the doubler run-out [148, 149]. Given the non-uniform through-the-thickness stiffness distribution in multi-directional laminates, non-uniform shear and

peel stresses establish in the adhesive, along the scarf. Peak loads are especially found at the run-outs of 0° layers [159], which can cause adhesive yielding and eventually failure initiation [162]. Since machined repair hole edges can be considered free edges too, the stiffness and Poisson's ratio mismatches between adjacent plies also favor delamination onset, both in the parent and patch adherents. Due to their elastic-plastic material behavior, adhesives can experience high strains before failing. This causes loads to be bypassed through the parent adherent, where intralaminar failure ultimately occurs [155].

In summary, the expected failure modes in bonded-repaired laminates are inter- and intralaminar failure of parent and patch adherents, and cohesive failure of the film adhesives, employed for repair.

5.4.2. Structural Model Setup

The parametric repair model generator developed in the scope of this thesis supports the simulation of flat and curved monolithic panels, loaded in tension and compression. In addition, individual definitions of the parameters listed in table 5.1 and beyond are supported. However, in view of the model validation against experimental tension tests, only details regarding the actually tested tension-loaded coupons are provided in the following.

Regarding model setup details, it is noted that the mechanisms, determining the intralaminar behavior of ply stacks and the interlaminar response at their interfaces, is identical to what is described in section 4.3. Since the same prepreg material is also considered in the study presented in this chapter, material and mesh parameters determined for the CAI model are readily applicable. However, special attention is given here to the adhesive material parameter set, which is also obtained by calibration.

5.4.2.1. Boundary Conditions

A combination of boundary conditions is assigned to the model, in order to simulate the experimental setup described in the previous sub-section. For the sake of computational efficiency, the specimen's gauge length is considered along with dummy tabs. These are intended to introduce load to the gauge region and to provide realistic boundary conditions at its edges. For that purpose, an isotropic material definition is assigned to the tabs, with elastic properties similar to those of the parent laminate (Young modulus: 50.39 GPa, in-plane Poisson's ratio: 0.45, transversal Poisson's ratios are set to null as discussed in section 4.3.2.3). At the fixed and moving tab edges, DoF of all top and bottom surface nodes are constrained in thickness and width direction, to simulate clamping conditions.

A displacement-time profile is imposed to the moving edge, composed by two consecutive smooth steps, similarly to the profile introduced in the previous chapter (figure 4.2). An average loading velocity of 1000 mm/s is adopted, whereas the velocity ratio between the first and second segments is 3.5. Although the velocity is rather high, a quasi-static behavior is still secured.

Like the CAI model, the repaired models are also submitted to transient analysis using an explicit time integration method. The parameters are chosen such as to ensure quasi-static loading, thus

keeping dynamic effects negligible until failure. In compliance to this requirement, the elements' mass is scaled to achieve a target STI of 2×10^{-7} s, to reduce computation time.

5.4.2.2. Adhesive Behavior

Given that a CZM is also attributed to the film adhesive, the same considerations presented in section 4.3.2.4 also apply with regards to the initial traction-separation response, the initiation of damage, and its propagation. However, instead of being considered as a contact condition, this behavior is assigned to special cohesive elements[2]. Similarly to the CZM attributed to stacks interfaces, separation experienced by cohesive elements is also described by three components in 3D-models, according to the three fracture modes depicted in figure 4.5. The adhesive material behavior is governed by a mixed-mode bi-linear traction-separation law, according to figure 4.7 and equation (4.26). A stress-based quadratic damage initiation criterion is employed (equation (4.27)). Stiffness degradation and ultimate failure are described by the BK-law (equation (4.28)).

A parameter set to properly describe the adhesive behavior is determined, according to the calibration procedure introduced in section 4.3.2.4. From experimental DCB and MMB tests, the fracture toughness parameters are determined and listed in table 5.3. These tests are regarded as the calibration baseline and the respective results are presented in appendices C.1 and C.2.

Property	Average Value	CoV [%]	Test Standard
$\mathcal{G}_{Ic}^{adh}$	1.28 N/mm	8.3	ASTM 5528 [125]
$\mathcal{G}_{IIc}^{adh}$	11.04 N/mm	6.2	ASTM 6671 [126]
η^{adh}	2.06	–	ASTM 6671 [126]

Table 5.3.: Experimentally determined fracture toughnesses and BK-exponent (Cytec FM®300).

Mode I Properties

A parametric DCB model is defined to replicate the experimental results obtained for specimen TC2-DCB-CO-06. For that purpose, the respective geometrical parameters and fracture toughness are considered (c.f. table C.1). Element edge length in crack propagation direction is chosen as low as 0.2 mm in order to enable more accurate FPZ length measurements. The influence of cohesive stiffness and strength as well as adherent thickness is studied with respect to result accuracy and computational efficiency. It is referred to appendix C.1 for the remaining experimental results.

- **Cohesive stiffness:** Usually, high cohesive stiffnesses are recommended to minimize unrealistic adherent separations [137]. However, too high stiffness causes the STI to drop, which, in explicit time-integration analyses, leads to an increased number of iterations and consequently higher computation effort. In order to determine an adequate cohesive stiffness,

[2] In Abaqus, cohesive elements are referred to as COH3D8 and COH3D6 for hexahedral and wedge elements, respectively.

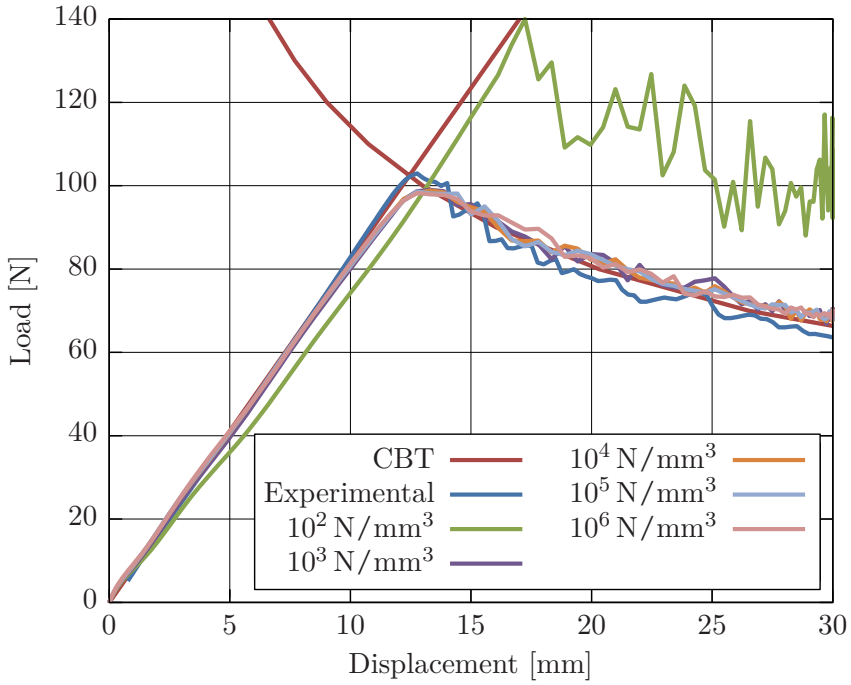

Figure 5.4.: Load-displacement curves of a DCB test, considering different cohesive stiffness values, K_I, for the adhesive material FM®300.

enabling the efficient computation of sufficiently accurate results, values between $10^2\,\mathrm{N/mm^3}$ and $10^6\,\mathrm{N/mm^3}$ are considered.

As depicted in figure 5.4, values beyond $10^2\,\mathrm{N/mm^3}$ provide an accurate load-displacement response, which is in agreement with both experimental and analytical (CBT) results .

Figure 5.5 depicts the dependency of the FPZ length and STI on the cohesive stiffness. It evidences, that the STI decreases for increasing cohesive stiffnesses. At the same time, FPZ length increases, which in turn enables the use of larger and thus computationally more efficient elements. Yet, the STI reduction has a much more significant impact on the simulation runtime. Thus, in view of the result accuracy (c.f. figure 5.4) and considering the target time increment, the value $10^4\,\mathrm{N/mm^3}$ is found appropriate.

- **Cohesive strength:** Typical adhesive materials present rather short FPZ lengths, thus requiring very refined meshes. Artificial strength adjustments, while keeping the physical fracture toughness unchanged, have shown providing good result accuracy at acceptable computational expense [102, 131, 137, 139–141]. The influence of strengths between 10 MPa and 40 MPa is studied. Figure 5.6 suggests that any strength in the studied range provides sufficiently accurate results, judging by the agreement between simulated, experimental and analytical load-displacement relations. However, the adopted cohesive strength strongly influences the FPZ length and consequently the required mesh density (figure 5.7).
- **Adherent thickness:** Although experimental data is available for adherent thicknesses of approximately 1.51 mm, deriving appropriate mesh densities from the respective simulation

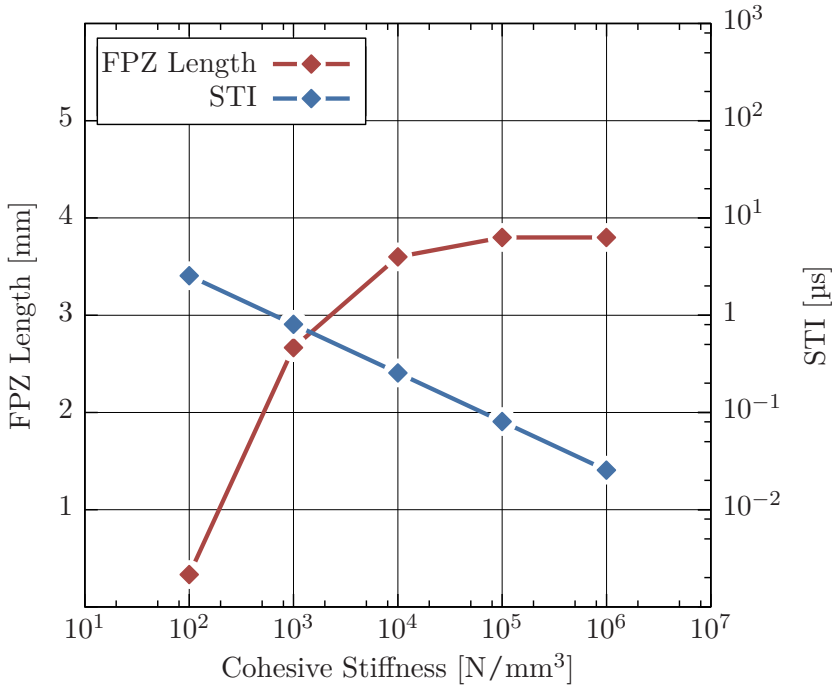

Figure 5.5.: Sensitivity of FPZ length and STI to the adhesive FM®300 cohesive stiffness, under pure mode I conditions.

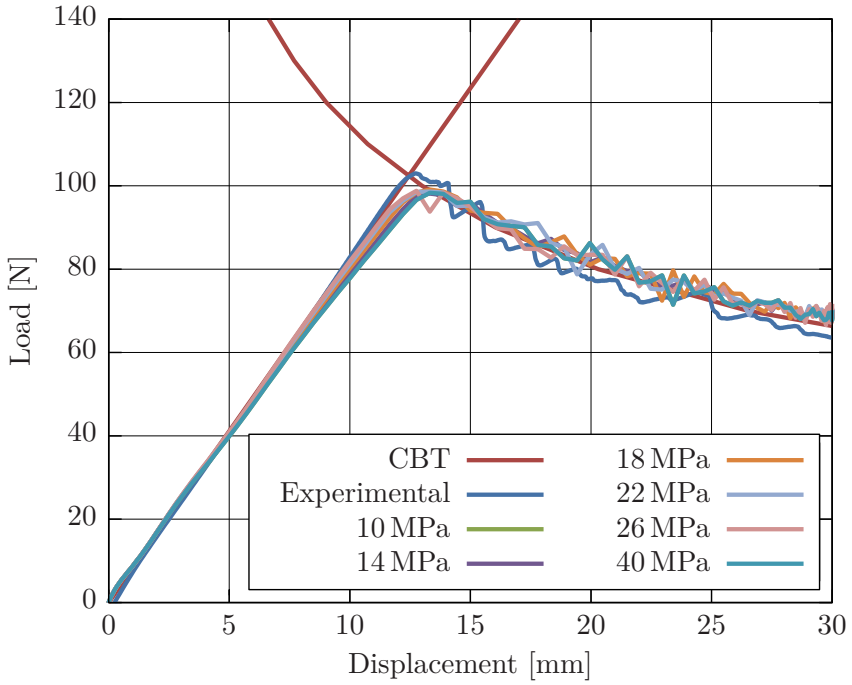

Figure 5.6.: Load-displacement curves for a DCB test, regarding different cohesive strength values, t_I^O, for the adhesive material FM®300.

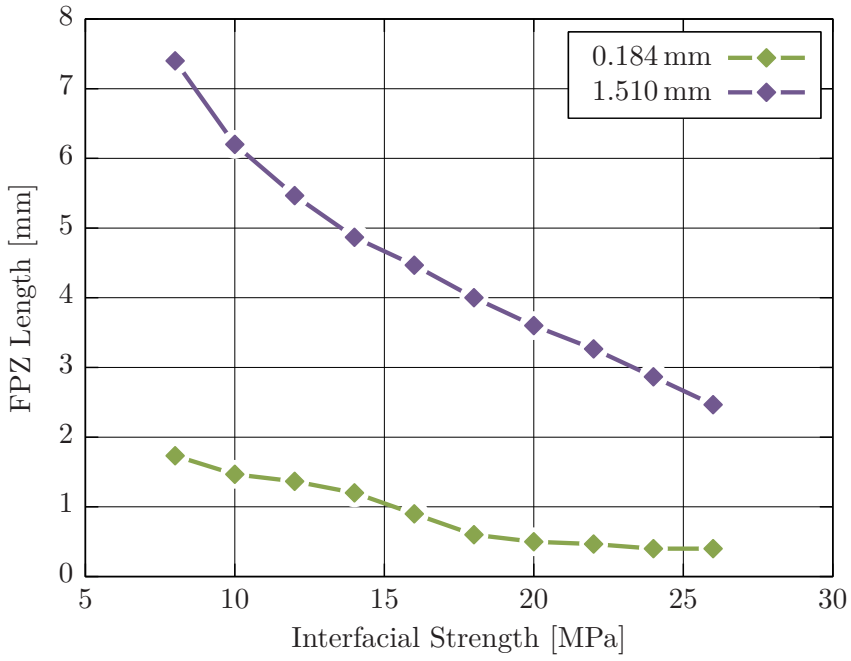

Figure 5.7.: Sensitivity of FPZ length to adherent's thickness and interfacial strength.

and assigning them to the repair models is inadmissible. This is especially owed to the fact that FPZ length and therefore the recommended element edge length depends on the adherent thickness. For that reason, the relation between interface strengths ranging from 7 MPa to 26 MPa and the respective FPZ length is studied for the thinnest anticipated adherent thickness. Regarding the repair specimen under study, the cover plies are the thinnest adherent, with a 0.184 mm nominal thickness.

Results depicted in figure 5.7 suggest a FPZ length of 1.47 mm for a 10 MPa cohesive strength. Considering the recommendation of at least two elements per FPZ length, a maximum element edge length of 0.74 mm is proposed.

Mode II Properties

Regarding mode II and mixed-mode conditions, property calibration is found by simple considerations, thus dispensing extensive parametric studies. This is because mode II (and mixed-mode) properties are less exigent regarding mesh density than mode I properties. In other words, fulfilling the mesh requirements for pure mode I condition, automatically satisfies the requisites associated to the mode II condition [131, 140].

- **Cohesive Stiffness:** As discussed before for mode I, the effect of stiffness on the predicted cohesive behavior is rather insignificant for values in the same order of magnitude as the adherents transversal stiffness and beyond. Thus, assuming similarity between the cohesive and the transversal adherent stiffness, and considering the relation $E_{33} > G_{13} > G_{23}$, the frequently adopted simplification $K_I = K_{II} = K_{III}$ is considered a safe assumption [23].

- **Cohesive Strength:** The aim of adjusting cohesive strengths resides in increasing the recommended element size for affordable computation, while attaining physically consistent results. To do so, Turon et al. [141] recommend deriving the mode II strength based on the mode I strength and the respective fracture toughnesses, according to equation (4.36).

  With respect to mode II loading, the resulting FPZ length is generally found being much larger than that establishing for pure mode I loading [131, 139, 140]. Thus, in models where different mode-mixtures are expected, adopting the highest mesh density required by pure mode I condition, is recommended.

Calibrated Parameter Set

In summary, the calibrated adhesive parameters employed in the present model are synthesized in table 5.4.

Property	Value	Specification
K_I^{adh}, K_{II}^{adh}, K_{III}^{adh}	$10^4\,\mathrm{N/mm^3}$	Derived from bulk material properties[3]
$t_I^{O,adh}$	10.0 MPa	Derived from parametric studies
$t_{II}^{O,adh}$, $t_{III}^{O,adh}$	29.3 MPa	Equation (4.36)
l_{FPZ}^{adh}	1.47 mm	Derived from simulation[4]
l_e^{adh}	0.7 mm	Equation (4.35)[5]

Table 5.4.: Calibrated CZM parameter set for the adhesive material (Cytec FM®300).

5.4.3. Reparability Criterion

Given the repair model's complexity and the large number of parameters editable by the user, physically inconsistent results may be obtained through improper parameter choice. In a first step, the solution's physical consistency is thus verified, by examining the results with respect to some relevant criteria. Especial consideration of the energy balance, load-displacement response, and predicted failure mechanisms and damage distribution is recommended for this purpose, as also described in sub-section 4.3.3. Although being only hints, these analyses may be helpful in narrowing down potential causes of erroneous simulation results.

If found physically consistent, the attainable repair strength is determined and assessed with respect to the as-designed strength. As discussed in sub-section 4.3.3, it is convenient expressing the repair strength in terms of nominal strain, by considering the predicted peak load, cross-section, and the structural in-plane stiffness. It is noted, that tension loads are considered positive in the present chapter.

[3] Value equates the adherents' transverse stiffness, rounded by order of magnitude.
[4] Determined for $t_I^{O,adh} = 10\,\mathrm{MPa}$ and $t_{min} = 0.184\,\mathrm{mm}$.
[5] Considering $N_e = 2$.

To assess the repair configuration's fitness in restoring structural airworthiness, insight into the specified loading capability is required. Considering that design allowables vary among structural parts, and taking the generic character of the studied specimens into account, a representative reparability threshold is stipulated, for the sake of argument. This is defined in reference to figure 2.3, where the design ultimate load is assumed being 50 % below the experimentally determined average strength. Accounting for the results obtained for virgin large coupons, tested under tension load (table F.1), the derived DUL capability is roughly 5900 µm/m. This means that any damaged part, whose predicted repair strength exceeds this threshold, is considered repairable and the respective repaired structure is regarded as airworthy.

5.5. Results and Experimental Validation

Tension tests of large virgin (i.e. without repair) and repaired structures are appointed here for validation of the simulation-based repair strength prediction methodology. Hereby, the experimentally determined response is compared to the behavior, estimated by simulation. Results are presented and discussed below.

5.5.1. Virgin Coupons

The scatter among the three tested virgin specimens is moderate, regarding the attained nominal failure strain (3.1 %, as indicated by table F.1). Therefore, the results obtained for coupon TAR-09 are considered representative for all virgin specimens.

Experimental strain gauge records depicted in figure 5.8 point to a non-uniform strain field. The highest strains are found establishing at the specimen center (sampling position 2), while the lowest install close to the lateral free edges (positions 4 and 5). This distribution is attributed to the clamped condition, enforced at the tabs. Due to the specimen's symmetry, identical strains are measured at sampling positions 1 and 3, and at positions 4 and 5. The close agreement between top and bottom readings suggests the absence of any out-of-plane bending phenomena. No evidence is given of any relevant discrete events occurring before failure, as indicated by the curves' linearity. The strength of this particular specimen is 11 525 µm/m, which is 4 % below the experimentally determined average of 11 949 µm/m.

Figure 5.9 depicts the specimen's damage pattern after tensile loading up to failure. As highlighted by the red arrow, damage initiated first in the tabs' vicinity due to stress concentrations, caused by the clamped boundary condition. After spreading perpendicularly to the loading axis, the crack propagates along the fiber direction of the top- and bottom-most stacks.

Regarding the simulated local strains at approximately the same sampling positions listed in table 5.2, similar results are obtained. As shown in figure 5.10, the linear relation between local and nominal strains is not disturbed by any particular events along the entire loading history. Although the exact strains, measured during the experiment, are slightly underestimated by the model, strain distribution is qualitatively identical. Highest strains are also predicted at sampling point 2. As expected, strains at the bottom surface are coincident with those monitored at the top, thus indicating pure in-plane displacements. Failure is finally predicted at 11 569 µm/m nominal

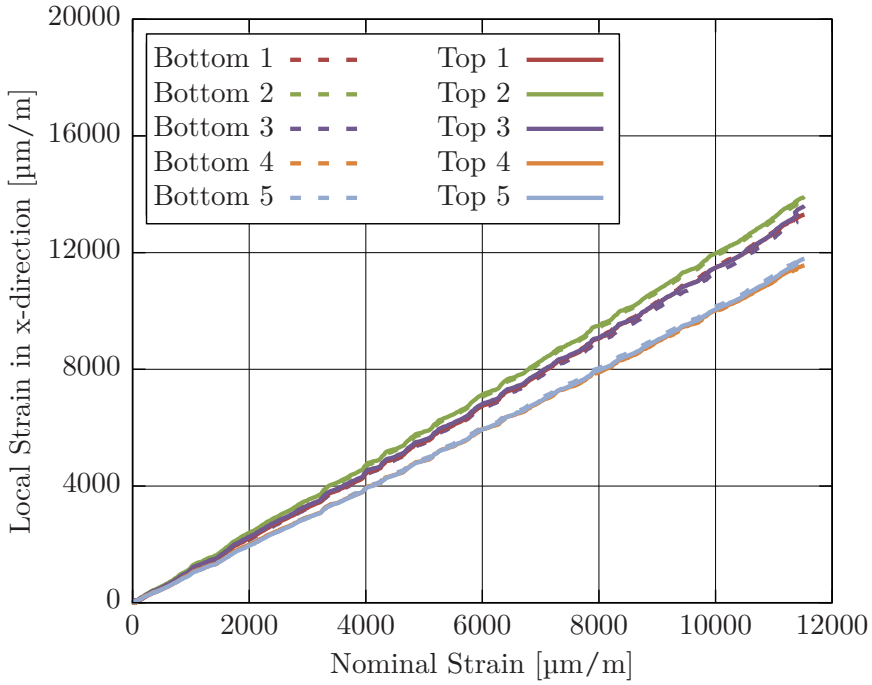

Figure 5.8.: Experimentally determined strains at distinct back-to-back sampling positions for coupon TAR-09. Strain field non-uniformity due to clamped tabs.

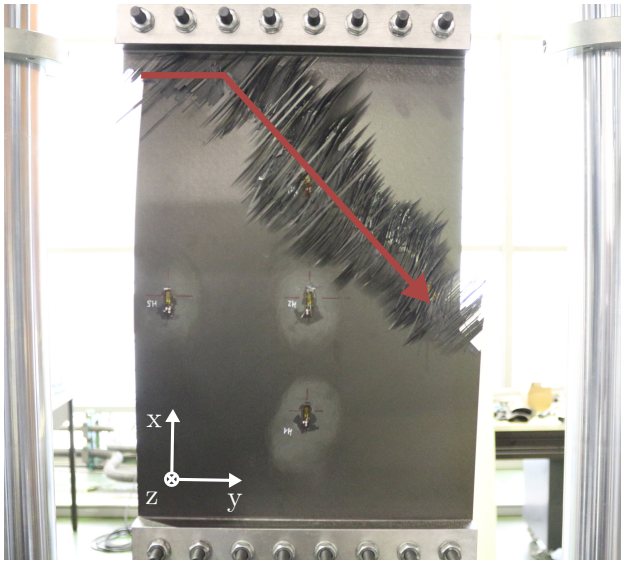

Figure 5.9.: Damage pattern of virgin specimen TAR-09 after tension test. Crack initiation at the transition zone between tab and gauge region; propagation along the red path.

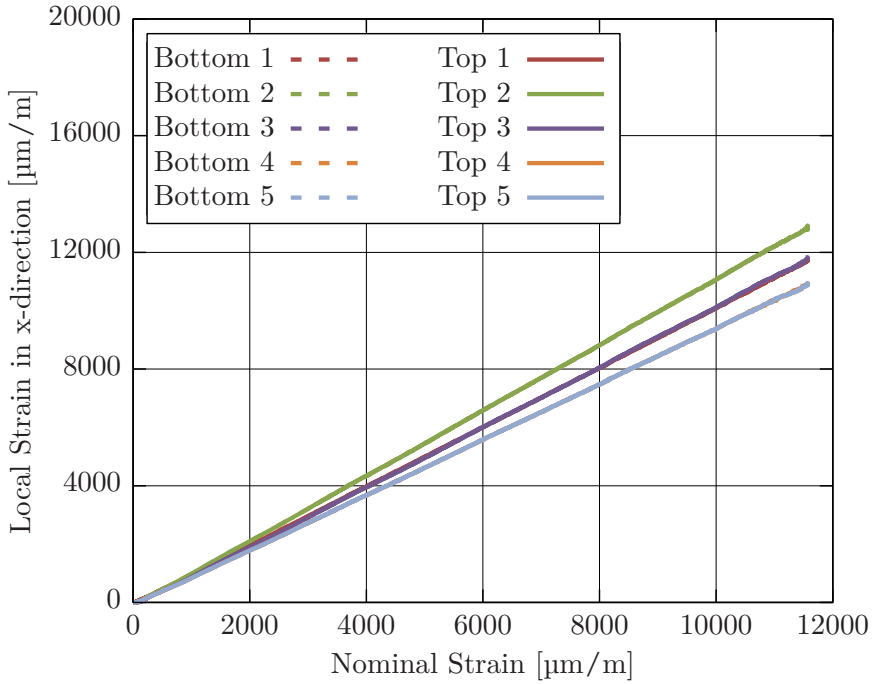

Figure 5.10.: Simulated local strains at specific sampling points for specimen TAR-09. Non-uniform strain distribution due to resistance to lateral contraction at the clamped tabs.

strain, which is an excellent approximation of the experimentally obtained result.

Simulation results point to the strain concentrations at the transition zone from tab to gauge region being responsible for damage initiation. At roughly 6000 µm/m, intralaminar matrix failure establishes in the top- and bottom-most stacks at the gauge region's corners. This damage mode is accompanied by delaminations in the adjacent interfaces. As the load increases, these inter- and intralaminar matrix cracks propagate towards the specimen center. Around 11 000 µm/m, wide-spread inter- and intralaminar matrix failure is found in the outer layers and their interfaces. At a nominal strain of 11 300 µm/m, which is just prior to failure (11 569 µm/m), fiber stiffness at the 0°-plies starts degrading, at the same hot-spots. The experimentally determined and the simulated damage patterns establishing at failure are in good agreement. Although the crack path is not fully developed in the model, due to premature analysis termination, the resemblance is yet visible. Figure 5.11 depicts the ultimate damage pattern, predicted by simulation. It shows intralaminar matrix cracks in the bottom-most stack, delamination in the first interface, and fiber fracture in the second stack of 0° ply orientation, at ultimate failure. Failure initiation loci and propagation direction are well predicted (c.f. figure 5.9).

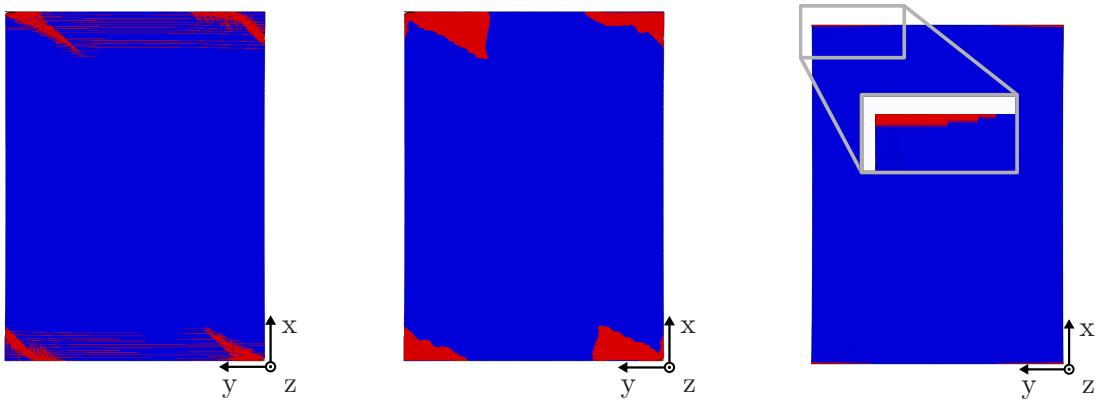

(a) Matrix failure (b) Delamination (c) Fiber fracture

Figure 5.11.: Ultimate damage pattern on virgin specimen (red color denotes full degradation): (a) matrix cracks in the first 45°-stack, (b) delaminations in interface 1, and (c) fiber fracture at the edges of stack 2 with a fiber orientation of 0°. Damage initiates from the gauge region's corners. Load introduction tabs are not displayed.

5.5.2. Repaired Coupons

Results obtained from the seven repaired large tested coupons are summarized in appendix F, table F.2. For the discussion below, the focus is drawn on specimens TAR-01 and TAR-05. Given the test samples' similarity and the moderate repair strength scatter of 3.7 %, these two are regarded as representatives.

Experimentally determined strains, recorded at the top and bottom surfaces, are depicted in figure 5.12. These curves also suggest strain field symmetry about the longitudinal and transversal mid-planes, i.e. equivalent strains at sampling points 1 and 3, and 4 and 5. The curves' linearity indicates no major incidents occurring before failure at 10 854 µm/m. Congruence between local top and bottom strains at positions 1, 3, 4, and 5 implies mostly in-plane deformations. Strains at positions 1 and 3 are equivalent to the top cover readings at position 2, and higher than those measured at the equivalent positions on the pristine specimen (c.f. figure 5.8). This points to stress concentrations occurring in the repair vicinity. However, strains are distinctly lower at the bottom cover.

Figure 5.13 shows that, in fact, all repaired specimens consistently exhibit lower strains running through the bottom cover ply, than those measured at the equivalent position on the virgin specimens. This is attributed to the weak butt-joint at the bottom surface, between parent and patch layers. The lower strains running through these adherents determine the load transfer through the bottom doubler. Comparison of the strains establishing at the bottom cover plies through all specimens, reveals significant scatter. In spite of the alleged reproducibility, considerable variation regarding load transfer at the bottom surface establishes, whose cause is narrowed down to the manufacturing process. Yet, no correlation between the load carrying contribution exerted by the bottom cover ply and the ultimate failure loads is found. This suggests that by design, only insignificant loads are bypassed through the bottom doubler.

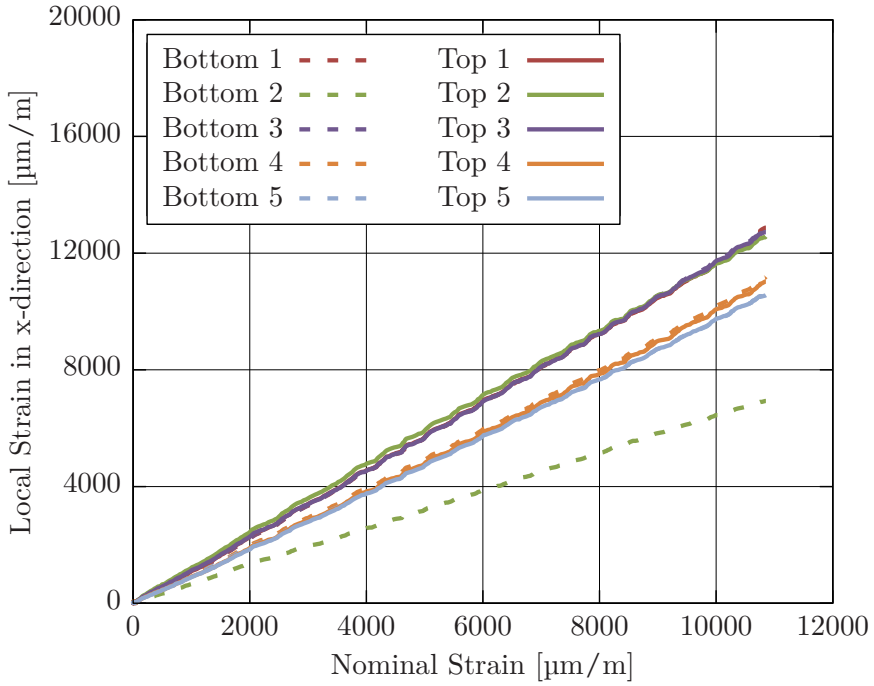

Figure 5.12.: Experimentally determined strains at distinct back-to-back sampling positions for coupon TAR-05. Considerable strain divergence at the top and bottom surfaces at sampling position 2 implies weaker load bypass at the bottom.

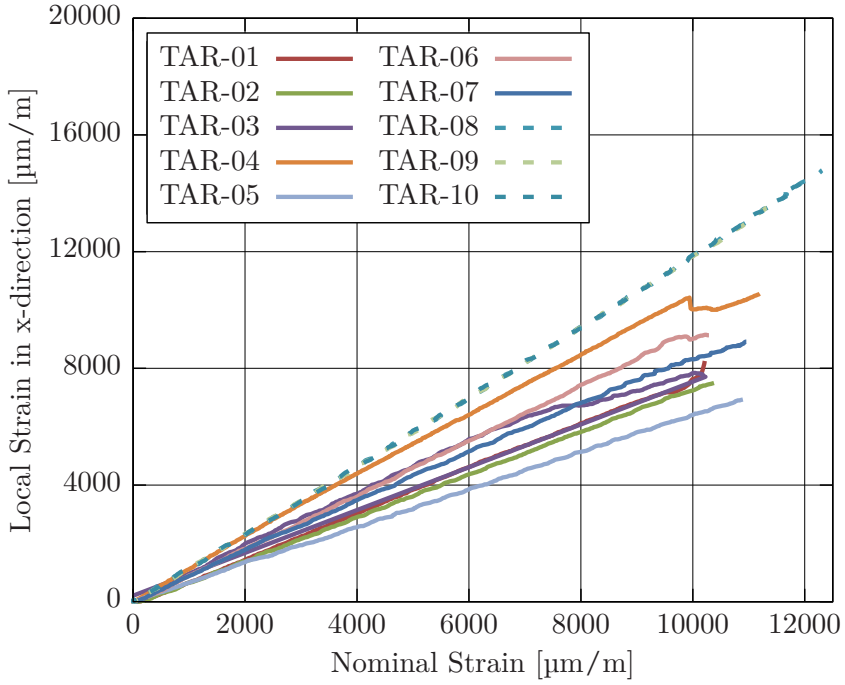

Figure 5.13.: Bottom cover strains (position 2) of all tested specimens. Solid lines: repaired specimens; dashed line: virgin specimens. Strains establishing at the bottom position 2 for repaired specimens are lower than those found in virgin coupons at the same position. Significant strain scatter in repaired specimens suggests manufacturing quality variation.

In contrast, top cover strains are similar to those establishing in virgin specimens at the same position, thus implying good load transfer between parent and patch, and considerable load bypass through the top cover ply (figure 5.14).

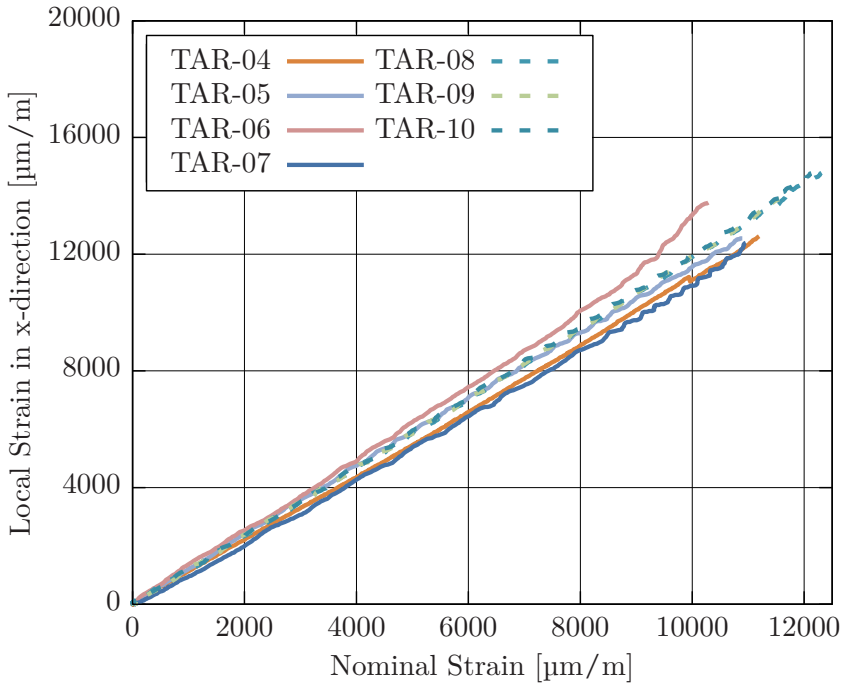

Figure 5.14.: Strains at the top sampling position 2. Solid lines: repaired specimens; dashed line: virgin specimens. Good agreement between repaired and virgin strains attests good load-transfer.

Further details regarding the response of repaired specimens is revealed by the DIC output, acquired from the top surface of coupon TAR-01. Figure 5.15 depicts the top surface strain field, in loading direction, at a nominal strain of approximately 6300 µm/m. Strains are evidently non-uniformly distributed, presenting increased strains at the diagonal paths (yellow-colored), crossing at the specimen's center. This particular strain pattern establishes in virtue of the constrained lateral contraction, at the clamped tabs.

The top cover ply also undergoes considerable strain, approximately at the circumference with D_{out} diameter (c.f. figure 5.3). Regarding the top surface, a substantial amount of sound material is removed for repair. Thus, load is not only bypassed through the parent structure's flanks (i.e. around the repair area), but especially through the top-side doubler. Given the higher adhesive compliance, large separations establish at the scarf bond-line between parent and patch, which are found responsible for severe strain concentrations in this particular region. More specifically, strain hot-spots install rather in the cover ply above the patch, i.e. within the D_{out}-circumference, than above the parent adherent.

It is worth mentioning, that the specimen center region also undergoes moderate displacement along the z-axis. As illustrated by figure 5.16, the center region experiences roughly 1 mm transversal motion right at the beginning. With increasing load, the transversal displacement rate converges towards a moderate value. The cause for this deflection is chiefly attributed to initial

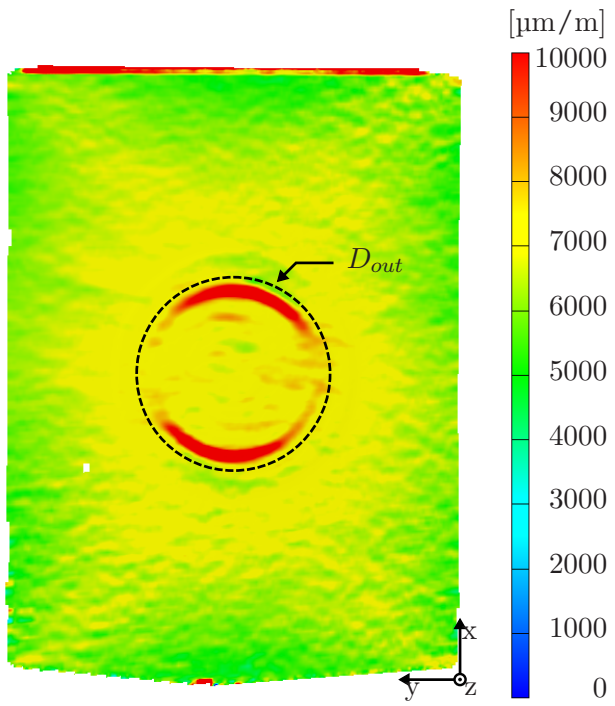

Figure 5.15.: Strain field in x-direction (ε_x) at the top side of coupon TAR-01, at 6300 µm/m nominal strain. High strains establish at the gauge region center and corners. Hot-spots install in the repair region (D_{out}). Spurious strains are measured at the top- and bottom-most coupon edges.

manufacturing-related deformation. As the asymmetrical repair plies cure in a co-bonding process, they cause the initially flat parent structure to warp. In-plane tensile loading is found counteracting these out-of-plane deformations. Moreover, given the repair asymmetry, eccentric load paths may also contribute to this result.

The experimentally determined repair strength of coupon TAR-01 is 10 233 µm/m. Although the failure is sudden, the damage pattern depicted in figure 5.17 suggest its initiation either at one of the strain hot-spots in the repair region, or at the gauge region's corner, or even both. The crack path is found connecting these critical regions and propagating along the 135° direction.

Simulated strains at the specified sampling points are depicted in figure 5.18. Local strains at positions 1, 2, and 3 are fairly identical, while lower strains establish towards the free edges. Although the simulated absolute values are consistently lower than the test strains, good qualitative agreement is achieved. At approximately 8000 µm/m (arrow 1), the bottom cover strain curve assumes a different slope. This load transfer reduction is caused by adhesive failure in the butt-joint, mainly induced by peel stresses. This supports the assumption that the bottom cover ply strains, measured during the experiment (figure 5.13), are caused by poor adhesion in the butt region. However, experimental results imply this being the condition over the entire loading history, which in turn points to inadequate repair manufacturing.

A more comprehensive overview of the establishing strain hot-spots is provided by figure 5.19, which depicts the simulated strain fields, in loading direction, at the top and bottom surfaces,

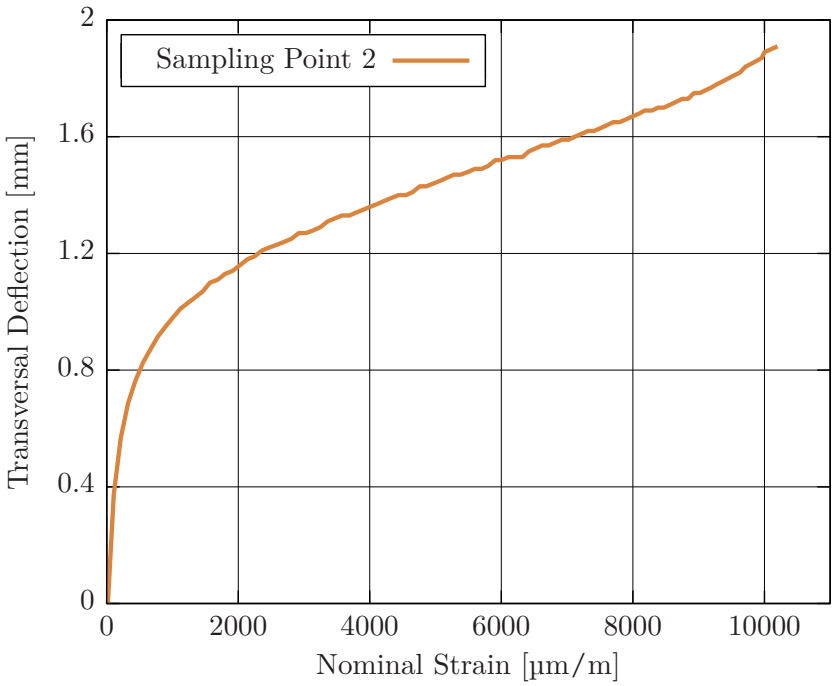

Figure 5.16.: Transversal deflection acquired through DIC at the top cover ply center point (sampling point 2). Displacement is attributed to manufacturing-related distortion and load path eccentricity.

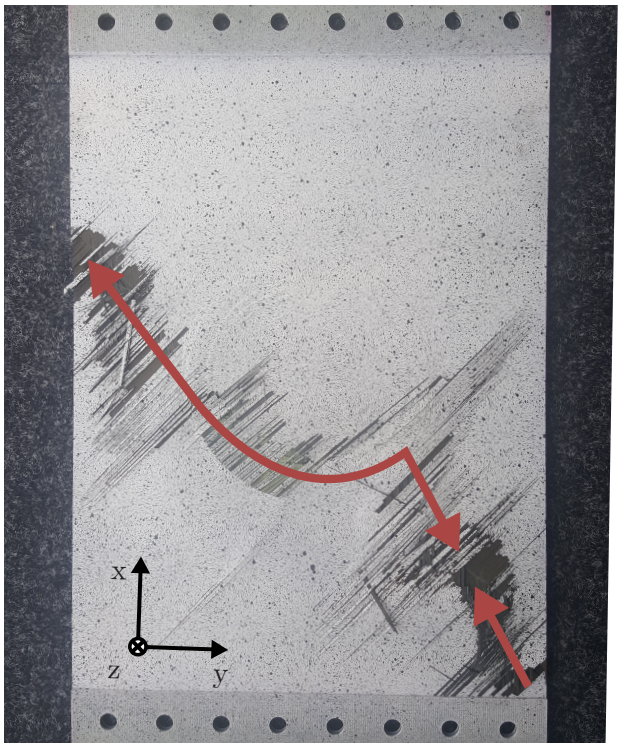

Figure 5.17.: Repaired specimen TAR-01 after tension test. Crack initiation at the strain hot-spots and propagation along the red arrows.

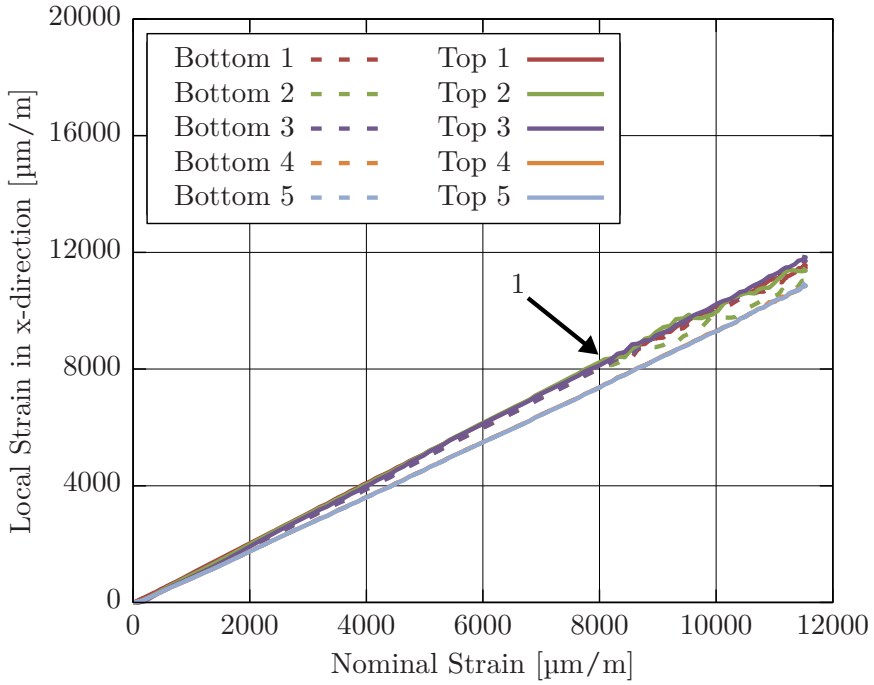

Figure 5.18.: Simulated strains at distinct back-to-back sampling positions for coupon TAR-05. Similar strains at top and bottom surfaces. Strain divergence at sampling position 2 initiates at 8000 µm/m (arrow 1) due to adhesive damage onset at the butt-joint.

at roughly 6700 µm/m. Like the DIC result (figure 5.15), strain concentrations are found along diagonal paths and at the coupon center. At the corners, strains are over-estimated due to over-restrictive boundary conditions. At the top surface (figure 5.19a), hot-spots are less pronounced and they extend over a wider area, when compared to the DIC result, establishing at both, parent and patch adherents. Strain concentrations also install at the doubler run-out (D_T). This result evidences good load transfer between the involved adherents. Judging by the strain level, considerable loads are effectively bypassed through the bottom cover ply (figure 5.19b). Strain hot-spots establish at the butt bond-line, D_{in}, and also at the doubler run-out, D_B.

Evaluating the through-the-thickness deflection at the center points (figure 5.20), the predicted motion is very modest, when compared to the DIC result. This is ascribed solely to the load path eccentricity, since the model disregards any initial warpage.

The simulation result plausibility is further discussed by stress analysis at the three bond-lines: top cover, butt and scarf, and bottom cover adhesives. Figure 5.21 depicts the cross-section of the repair region. The relative control variables ξ_i, with $i = \{T, SA, B\}$, for each bond-line, are indicated along with distinct stress concentration loci.

In figure 5.22, the cohesive tractions[6] and the degradation variables establishing at the xz-symmetry plane, are plotted for the three bond-lines, at a nominal strain of 6700 µm/m. Cohesive

[6]Given the traction-separation description assigned to the cohesive elements, three stress components are calculated, which are equivalent to the tractions at the adhesive surfaces. Thus, in this context, stresses and tractions are used interchangeably.

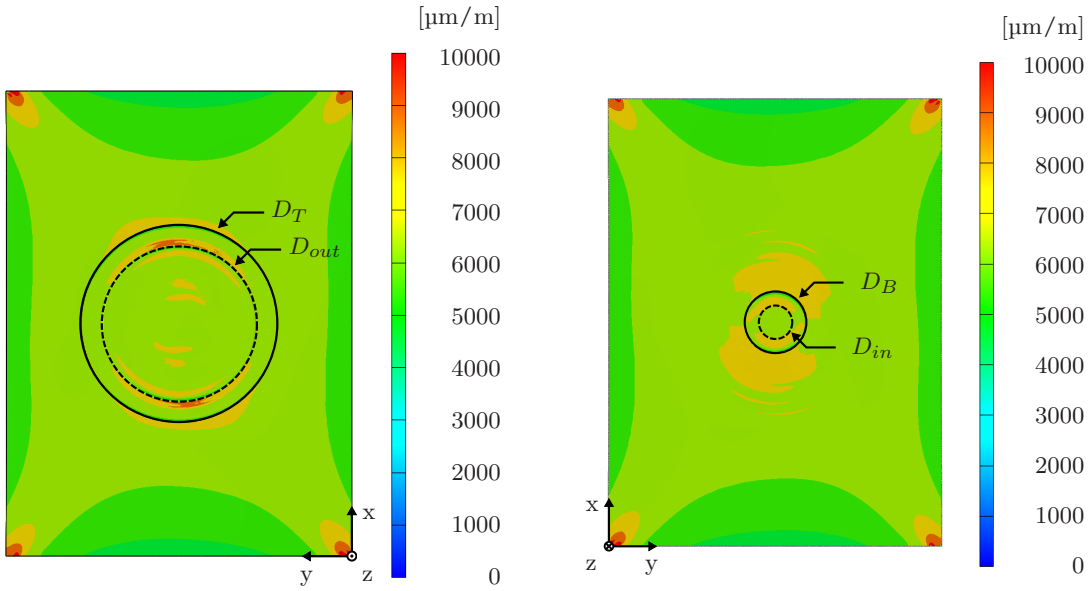

(a) Top surface

(b) Bottom surface

Figure 5.19.: Simulated strain fields in x-direction (ε_x) at the top (a) and bottom (b) surfaces, at 6700 µm/m nominal strain. High strains establish in the repair vicinity and at the gauge region corners. Hot-spots at the bond-lines (D_{in} and D_{out}) and at the doubler run-outs (D_T and D_B) are found establishing in loading direction.

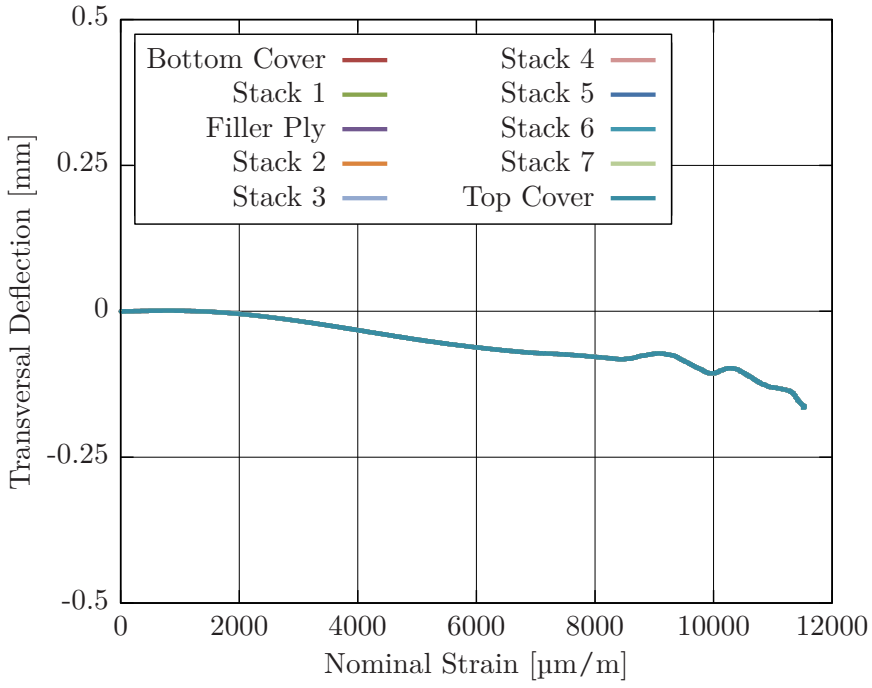

Figure 5.20.: Transversal deflection of the all stacks' center points (sampling position 2), obtained by simulation. Moderate deflection is attributed to eccentric load paths.

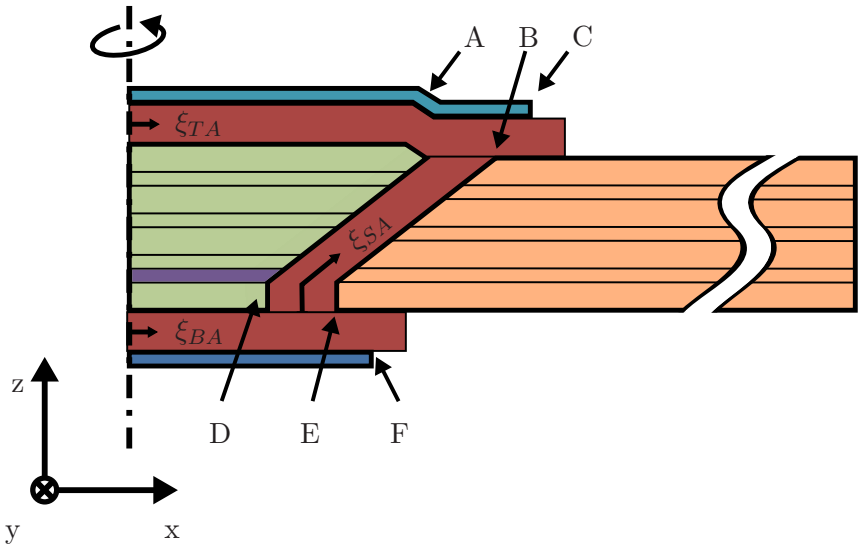

Figure 5.21.: Schematic cross-section of the repair region. Paths along the bond-lines for stress analysis (highlighted in red). Distinct positions A - F denote stress concentration loci.

tractions at the top cover adhesive are largely negligible. However, moderate tractions establish at the regions denoted by the arrows A, B, and C. At the adhesive joggle (A), which results from the inclusion of a filler ply in the patch stacking sequence, increased tractions in all three modes establish (c.f. figure 5.21). Further stress concentrations are found installing at the scarf bond-line run-out (B), due to the high adhesive's compliance and the resulting pronounced separation between parent and patch adherents. Yet, the highest tractions are shown at the top cover ply run-out, where degradation has already initiated at the considered load state.

The second plot of figure 5.22 indicates high adhesive stiffness degradation occurring at the butt joint (D). This is attributed to the high peel stresses, establishing due to this particular bond-line geometry. It is also noted, that the highest mode II shear tractions install at the 0° ply run-outs, thus leading to local adhesive degradation in the scarf region.

Stress distributions at the bottom and top cover adhesives are fairly similar. Pronounced tractions establish at the main adherent's discontinuity, caused by the butt bond-line (E). Even higher strains install at the bottom cover ply run-out (F). However, the adhesive is found not yet degrading, which is ultimately because of lesser loads being conducted through the bottom part of the structure.

Due to the rotational symmetry associated to the present repair design, figure 5.21 also represents the cross-section in the yz-symmetry plane. The respective traction distributions are depicted in figure 5.23. Stress concentrations are found establishing at precisely the same features. However, they are less pronounced here, due to the installing strain profile, which is found decreasing towards the free edges (i.e. in y-direction). Degradation is also found initiating at the butt joint. Yet, due to the moderate tractions, degradation in the scarf region is only expected at higher loads. It is noted that in this direction, mode III tractions are most significant, which install at the 90° ply run-outs.

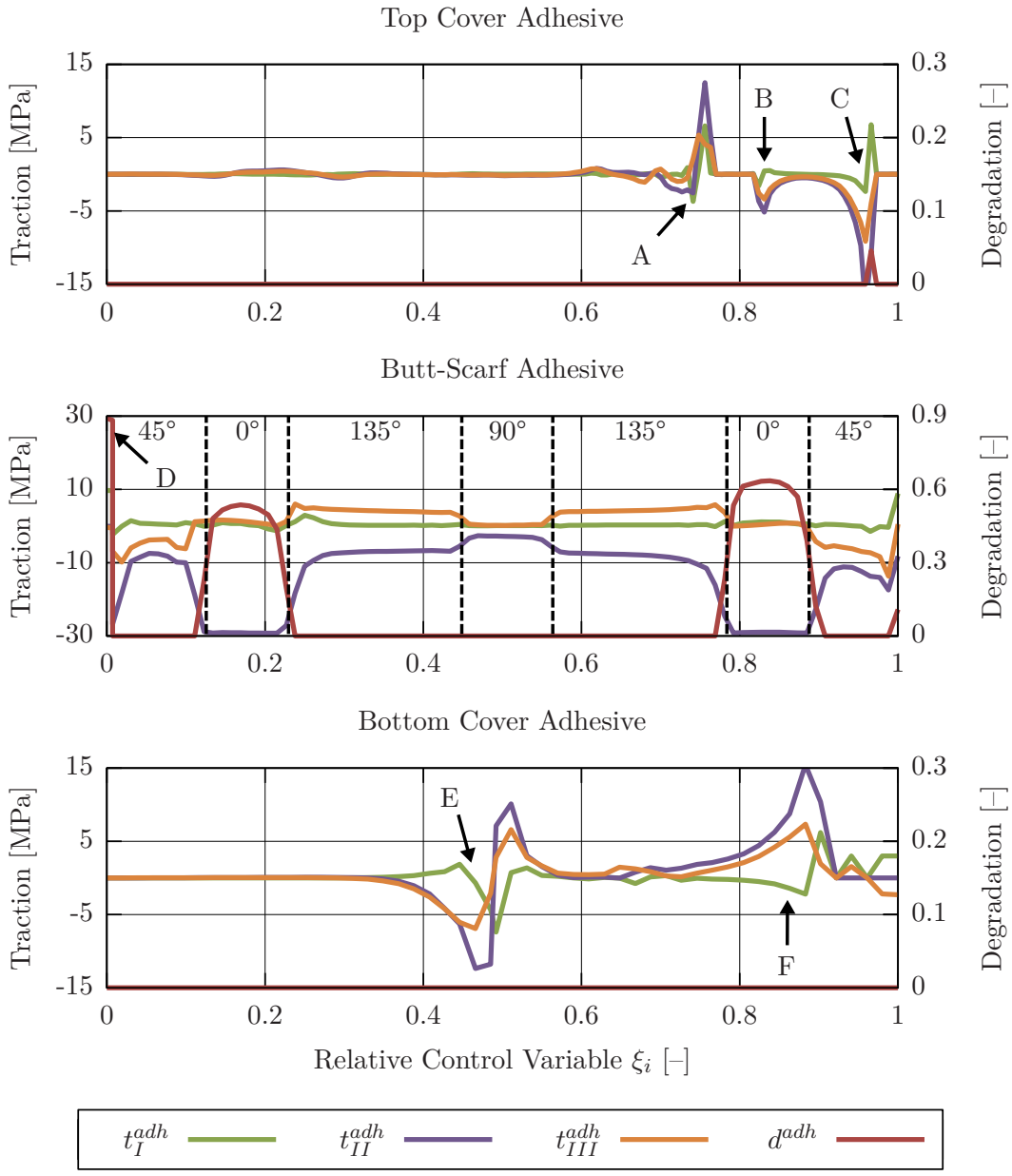

Figure 5.22.: Adhesive tractions and degradation establishing at the xz-symmetry plane, at 6700 µm/m nominal strain. Adherent run-outs (C and F), joggles (A), and distinct compliances in the joining parts (B and E) lead to stress concentrations. Degradation initiates at the butt joint (D) and in the scarf region at the 0° layers (c.f. figure 5.21).

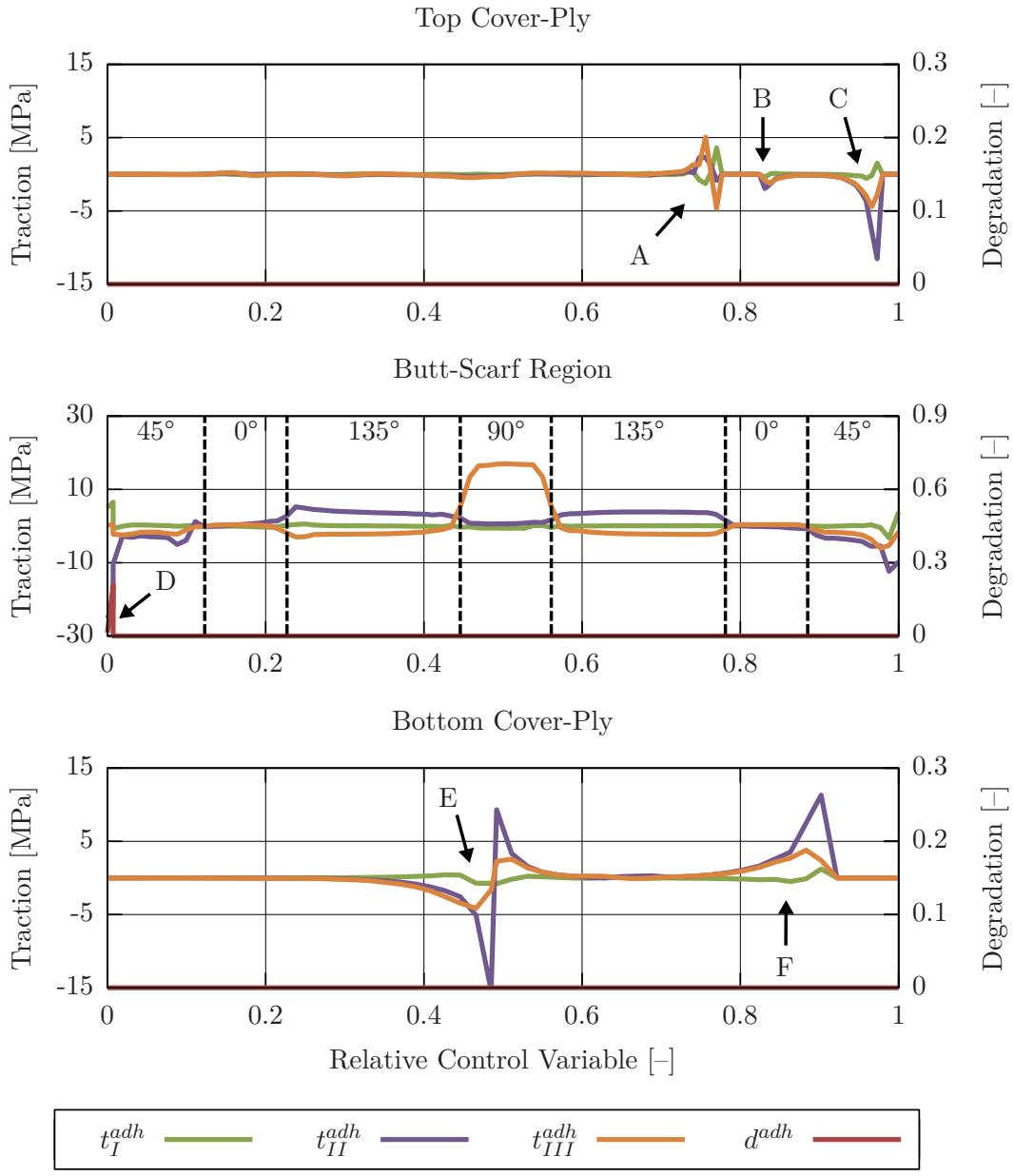

Figure 5.23.: Adhesive tractions and degradation establishing at the yz-symmetry plane, at 6700 µm/m nominal strain. Adherent run-outs (C and F), joggles (A), and distinct compliances in the joining parts (B and E) lead to stress concentrations. At this load level, degradation is only found in the butt-joint (D) (c.f. figure 5.21).

These observations regarding stress distribution and failure mechanisms in the adhesives are found in harmony with conclusions drawn from earlier studies, as presented for instance by Hart-Smith [150], Soutis et al. [153, 154], Campilho et al. [156, 157, 159], and Xiaoquan et al. [162].

Concerning the predicted failure mechanisms, they are best explained by analyzing the damage state in the various model components, immediately before failure (11 440 µm/m). Similarly to what has been discussed regarding the experimental result, the present model also identifies two independent loci of failure initiation. Damage initiates and propagates at the gauge region's corners. These are actually four independent loci, however, regarded as one, due to their similarity. At the same time, damage is found originating and growing in the repair region.

The damage mechanisms occurring at the corners are identical to those described with respect to the virgin specimen. In summary, intralaminar matrix failure is the first emerging mode at a nominal strain of roughly 6300 µm/m, which establishes due to partially constrained lateral contraction, induced by the load introduction tabs. As this damage mode propagates in the top- and bottom-most stacks, delaminations install in the adjacent interfaces. Owing to the increasing load, these defects propagate from the corners towards the xz-symmetry plane, and extend to all parent laminate plies, except for the 0° plies. Due to the decreasing load carrying capability of the degrading 45° and 135° stacks, fiber failure initiates eventually in the 0° plies at the same corners and also propagates towards the center (c.f. figure 5.11).

Severe peel stresses induced at the butt-joint between patch and parent laminate are responsible for its early degradation, as implied by figure 5.22. Due to high loads running through the 0° plies, severe stress concentrations establish at their run-outs in the scarf region. As illustrated by figure 5.24a, they lead to degradation onset and growth in circumferential direction. At the top doubler adhesive, wide-spread failure is predicted in the joggle and scarf bond-line regions, just before failure (figure 5.24b). This leads to an interruption of the load path through the top cover. At the bottom cover, degradation is less pronounced and is rather confined to the butt bond-line and cover ply run-out regions. Owing to the failing cover ply adhesives (especially at the top), load transfer is now left solely to the main structure. As a result, intralaminar matrix cracks install in the transversal radial direction (i.e. in y-direction), due to stress concentrations at the hole edges, and in circumferential direction, at the 0° ply run-out associated stress hot-spots (figure 5.24c).

The ultimately establishing damage pattern is thus a combination of intralaminar fiber and matrix failure at the corners, and adhesive and intralaminar matrix failure in the repair vicinity. Delamination damage is consistently found at intralaminar cracks. In spite of its complexity, good agreement between experimental (figure 5.17) and the simulated damage distribution is attained.

Regarding repair strength, the simulation result (11 506 µm/m) exceeds the experimentally determined load capacity by roughly 9 %. Given the model's complexity and the many interacting phenomena, this is still a remarkable result. However, three potential causes for the over-estimation are identified. Firstly, initial warpage of the test specimens is disregarded by the FE models. Upon loading, the initial deformation is counteracted, thus leading to local stresses. These may favor failure earlier than predicted. Secondly, material parameters assigned to the adhesive might be too optimistic. As described in appendix C.2 and depicted in figure C.5, the mode II fracture

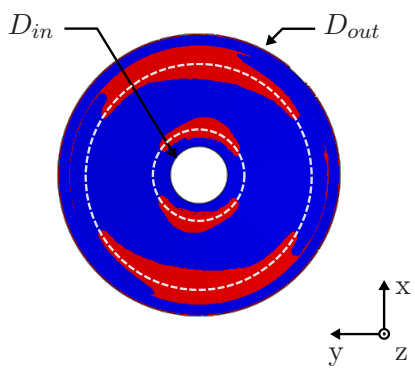

(a) Adhesive failure in scarf bond-line

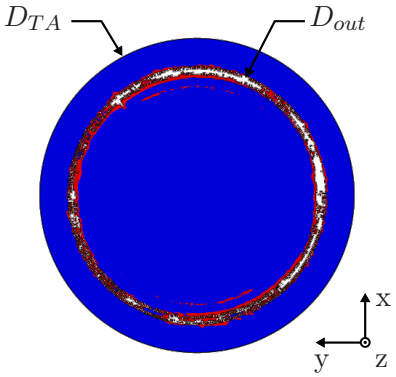

(b) Adhesive failure in top cover adhesive

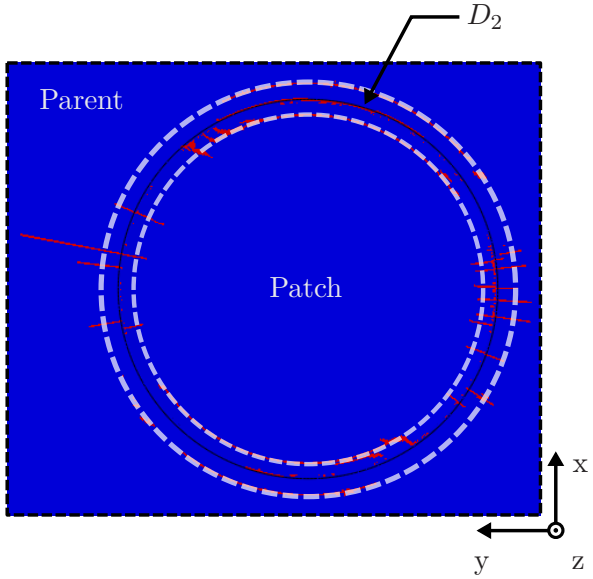

(c) Intralaminar matrix cracks in top-most parent and patch layers

Figure 5.24.: Damage pattern in repair vicinity just prior to failure, at 11 440 µm/m (red color denotes stiffness degradation beyond 75 %): (a) adhesive failure establishes in the scarf region at the 0° ply run-outs denoted by the dashed circumferences; (b) top cover adhesive failure at the joggle and above the scarf bond-line (D_{out}); (c) intralaminar matrix cracks propagating in transversal radial direction, and throughout the circumference of 0° ply run-outs (dashed circumference) in both, parent and patch top-most layers.

toughness, $\mathcal{G}_{IIc}^{adh}$, is derived by extrapolation of the best-fit curve, which in turn is obtained from MMB tests at three different mode-mixtures. Given the considerable data scatter, the fitted curve may be inappropriate for extrapolation. Instead, determining the mode II properties through the End-notched Flexure (ENF) test is expected rendering more trustworthy results and should be considered in future studies. Thirdly, scatter with respect to the establishing strains at the bottom cover (c.f. figure 5.13) suggests inconsistency regarding the repair manufacturing quality. Strategies for assuring repair quality must be developed and adopted, and proper means of accounting for manufacturing variances are required.

5.6. Reparability Verification

For the sake of argument, it be supposed that a given structural damage can be removed and repaired according to the design, introduced in this chapter. It requires a proper reparability criterion to assess, whether or not the proposed repair configuration is appropriate for restoring airworthiness. Since the tension specimen discussed so far is merely a generic structure, a simple criterion is adopted for the purpose of demonstration. This consists in requiring the repaired structure to attain at least DUL. As introduced in sub-section 5.4.3, this reparability threshold is set to 5900 µm/m. Before this background and as implied by figure 5.25, both, experimental and simulation results, attest the specimen's reparability, by adopting the proposed repair configuration. The experimental results attest an average strength recovery of 89 %. In contrast, the simulated results suggest strength restoration to 99 % of the predicted virgin load capability.

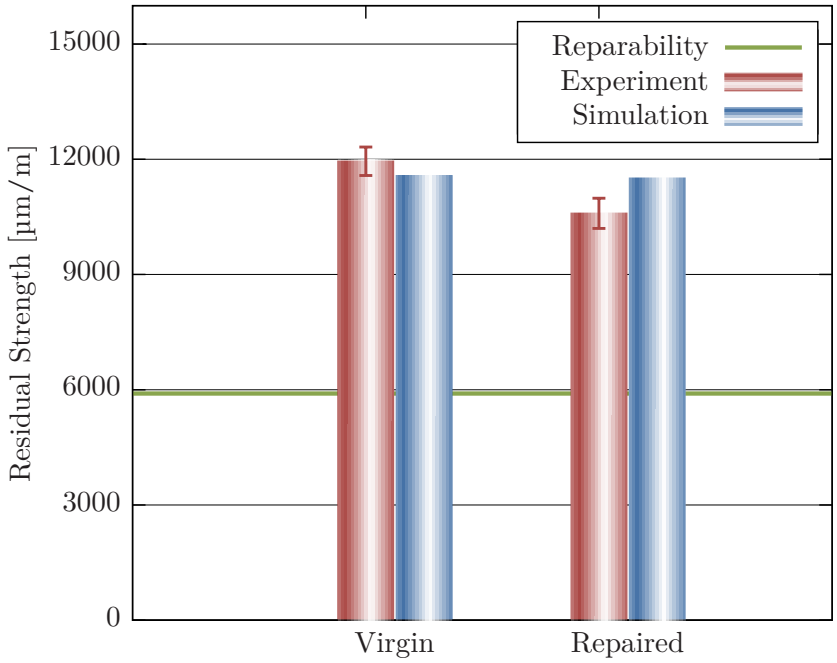

Figure 5.25.: Virgin and repaired strengths determined by experiments and simulation. Repair configuration exceeds the reparability threshold by far and the respective strength is close to the pristine load capability.

5.7. Conclusion

A method for predicting the strength of scarf-bonded repairs is presented and discussed. For that purpose, a parametric FE model is developed, which supports the simulation of the principal phenomena governing the response of repaired composite structures. As such, this behavior prediction capability exceeds that of most proposed models, which focus solely on adhesive-related failure mechanisms. The method's validity is discussed by comparing results obtained by simulation and experimental testing on virgin and repaired large tension coupons. Although measurement capabilities adopted during the experiments are limited, they altogether highlight the consistency between experimental and simulation results. This agreement is demonstrated concerning strain distribution, failure mechanisms, ultimate strength, and final damage pattern. While the adopted instruments are unable to monitor phenomena occurring at the bond-lines inside the specimen, predicted stress concentrations and crack paths are found consistent with findings reported in the literature.

Regarding reparability verification, experimental and numerical analyses, conducted under consideration of the adopted repair design, imply strength restoration beyond the as-designed DUL threshold. Yet, the predicted repair strength is found slightly over-estimating the experimental result by less than 9 %. This still represents a good estimate, when considering the model's complexity. Referring to the third hypothesis postulated on page 3, it is in deed shown, that high repair strength prediction accuracy is attainable by the proposed method. However, better results are considered attainable, when considering more realistic adhesive properties, less deformed specimens, and increased and reproducible repair manufacturing quality.

In the future, other loading conditions and structures should be considered for further validation of the presented method. Extending this approach to also cover for fatigue phenomena is a crucial step towards certification. The repair specification process can also be endorsed by integration of the presented parametric model in an optimization framework. This supports the identification of more efficient repairs. Regarding the tension test discussed above, waisted specimens of varying width should be considered, to prevent failure from initiating at the transition zone between tabs and gauge region. In doing so, phenomena, establishing in the repair vicinity, can be highlighted. With respect to the proposed model, computation efficiency could be increased, for instance, by the reduction of the number of finite elements through-the-thickness, especially in areas, afar from the immediate repair region. To still account for the main failure mechanisms, more sophisticated damage models, accounting for inter- and intralaminar failure can be adopted.

6 Summary

The present thesis targets the issue of over-conservatism, associated to the decision-making process for damage assessment and repair, as currently adopted for managing impact damage in composite airframe structures. Restrictive handling specifications are the consequence of an empirical approach, which requires the employment of heavy knock-down factors, to cover for uncertainties and worst-case scenarios. To overcome the limitations resulting thereof, a novel decision-making process is proposed, consisting of individual damage assessment, based on residual strength predictions. Instead of evaluating the residual load carrying capability based on damage size only, it is advocated to include all relevant structure properties in an appropriate model of the part under investigation. For that purpose, special attention is given to detailed impact damage characterization, where the most relevant damage features are returned from NDI images. For realistic damaged structure representation, defects are classified according to the individual layup architecture, and reconstruction algorithms are employed to derive empirically consisted defect shapes from generally fragmented images. These are further considered in a detailed parametric model of the individual damaged part, thus enabling accurate structural behavior predictions. The comparison of the simulated residual strength with the applicable design allowables, provides a solid basis for condition-based airworthiness assessments. As part of the decision-making process, repair is also addressed. In contrast to the currently adopted reparability thresholds based on the damage extent, the proposed method suggests the reparability of a particular damaged part to be verified by individual estimation of the attainable repair strength, and comparison to the respective design allowables. For that purpose, a detailed parametric model for scarf bonded repair representation is proposed, which is shown to effectively cover for the most relevant failure mechanisms.

Confidence in this novel decision-making process is drawn from different experimental tests. Defect shapes, derived from conventional NDI images by the proposed damage characterization module are found consistent with the effective damage morphology. The behavior of coupons with different artificial and impact damage, tested under compression load, is also well predicted by the adopted modeling strategy. Not only are the estimated residual strengths found in excellent agreement with experimental results, but also the simulated mechanisms leading up to failure are well predicted. This applies also to the simulation of repaired structures. Experimentally observed behavior and especially the attained repair strength are well predicted by the adopted models. In spite of the good agreement between the results obtained at each process module with the respective validation basis, further experimental substantiation at different structural levels is required, to prove the proposed method's robustness. To certify the proposed method and to increase its acceptance, static and fatigue test evidence must be provided, and strategies must be developed, for excluding (or at least minimizing) the possibility of human error during the decision-making process [9].

Extending the presented method beyond monolithic design, impact-induced damage, scarf bonded repair, and uni-axial loading conditions is surely associated to many new challenges. However,

such extensions are indispensable contributions to the goal of efficient and demand-oriented maintenance, repair, and overhaul of airframe structures.

A Defect Verification

A.1. Delamination Characterization Verification

Figures A.1 and A.2 present the delamination characterization results for specimens CAI-TC1-04 and CAI-TC1-07, impacted at 40 J (c.f. table D.4). They depict a comparison between delamination shapes, derived from ultrasonic image analysis, and interlaminar defect patterns, obtained by µCT image processing.

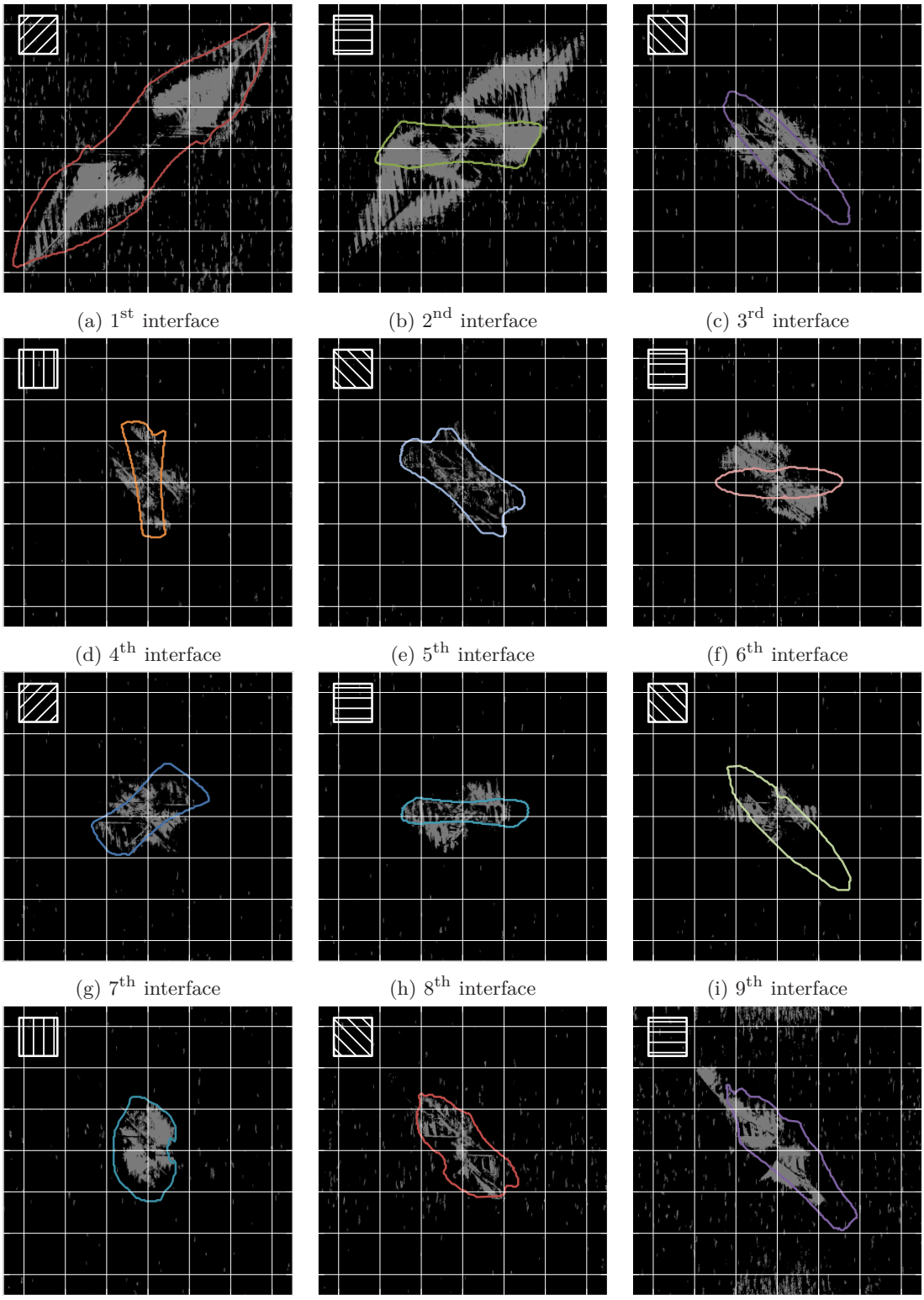

(a) 1st interface (b) 2nd interface (c) 3rd interface

(d) 4th interface (e) 5th interface (f) 6th interface

(g) 7th interface (h) 8th interface (i) 9th interface

(j) 10th interface (k) 11th interface (l) 12th interface

Figure A.1.: Superposition of delamination contours from ultrasonic image analysis (polygons), with interlaminar damage images from µCT image processing (gray-scale figure), for specimen CAI-TC1-04. Grid line spacing is 10 mm. Adopted thresholds cause inappropriate voxel segmentation. Considering the images of adjacent interfaces provides a good perception of the delamination extent.

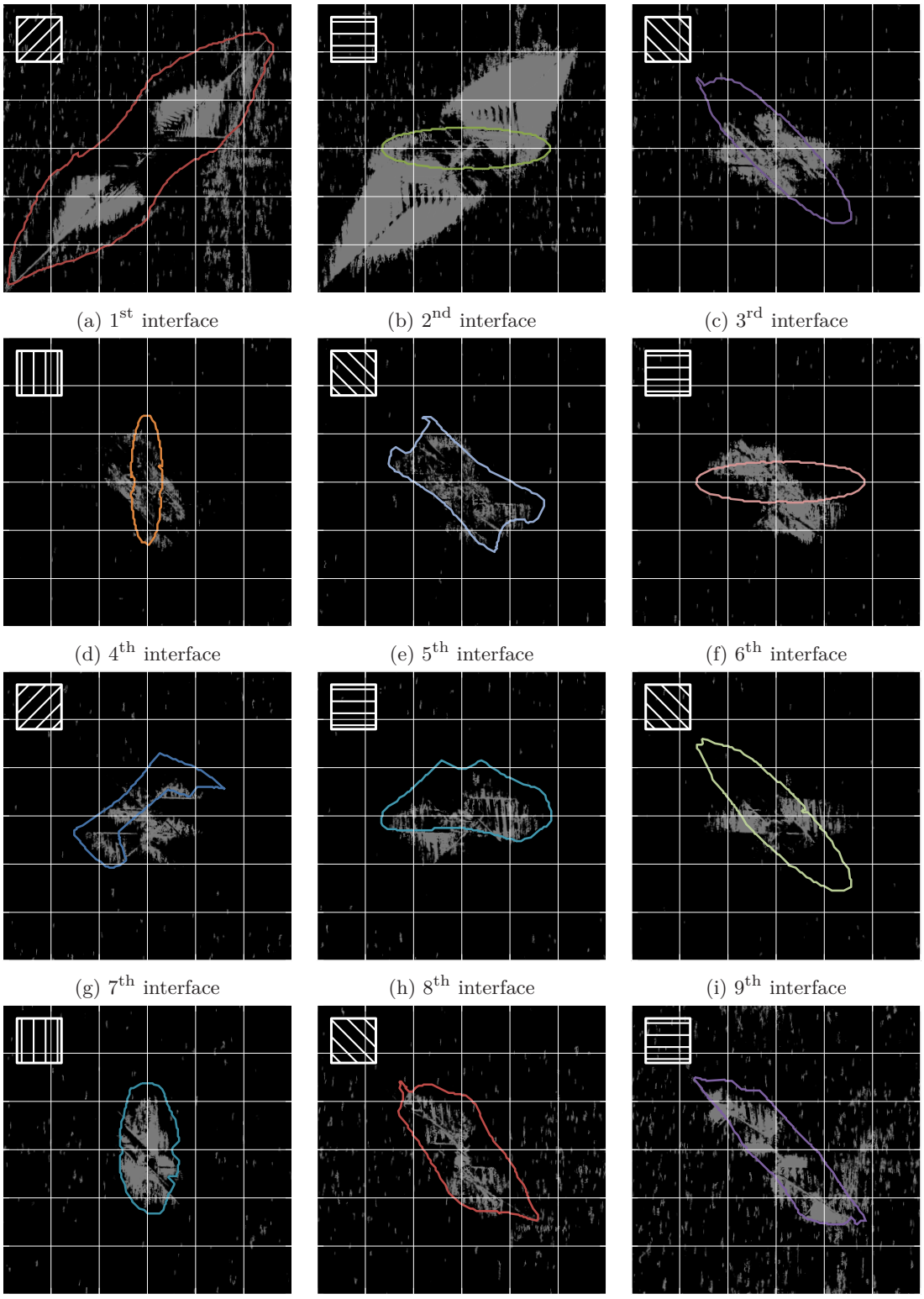

(a) 1st interface (b) 2nd interface (c) 3rd interface

(d) 4th interface (e) 5th interface (f) 6th interface

(g) 7th interface (h) 8th interface (i) 9th interface

(j) 10th interface (k) 11th interface (l) 12th interface

Figure A.2.: Superposition of delamination contours from ultrasonic image analysis (polygons), with interlaminar damage images from µCT image processing (gray-scale figure), for specimen CAI-TC1-07. Grid line spacing is 10 mm. Adopted thresholds cause inappropriate voxel segmentation. Considering the images of adjacent interfaces provides a good perception of the delamination extent.

A.2. Experimental Fiber Fracture Characterization

By means of the de-ply technique, fiber fractures are analyzed in each stack. The results for all three de-plied CAI specimens are presented in tables A.1 to A.3. Coordinates and orientations refer to the coordinate system presented in figure 3.6 and are expressed in millimeters and degrees, respectively. Crack lengths are presented by the effectively measured fracture segment length (measured), and by the extension of its projection onto the ply orientation's orthogonal axis (projected). These values are also presented graphically, along with the results obtained from image analysis, for comparison.

Stack	Stack orientation	Crack orientation	Crack length [mm]	
			measured	projected
1 (bottom)	45°	0°	0	0
2	0°	90°	3	3
3	135°	41°	11	11
4	90°	150°	14	12
5	135°	72°	9	8
6	0°	79°	5	5
7	45°	0°	10	7
8	0°	107°	10	10
9	135°	141°	6	1
10	90°	13°	9	9
11	135°	40°	8	8
12	0°	127°	36	29
13 (top)	45°	133°	52	52

Table A.1.: Fiber crack geometry in specimen CAI-4.

Measured and projected fiber crack lengths for specimen CAI-TC1-04 are presented in figures 3.22 and 3.24. Fiber crack orientation is depicted in figure 3.23.

Stack	Stack orientation	Crack orientation	Crack length [mm]	
			measured	projected
1 (bottom)	45°	0°	0	0
2	0°	82°	7	7
3	135°	56°	11	11
4	90°	143°	15	12
5	135°	42°	12	12
6	0°	96°	20	20
7	45°	0°	8	6
8	0°	99°	6	6
9	135°	71°	18	16
10	90°	18°	6	6
11	135°	9°	6	5
12	0°	129°	45	35
13 (top)	45°	133°	52	52

Table A.2.: Fiber crack geometry in specimen CAI-5.

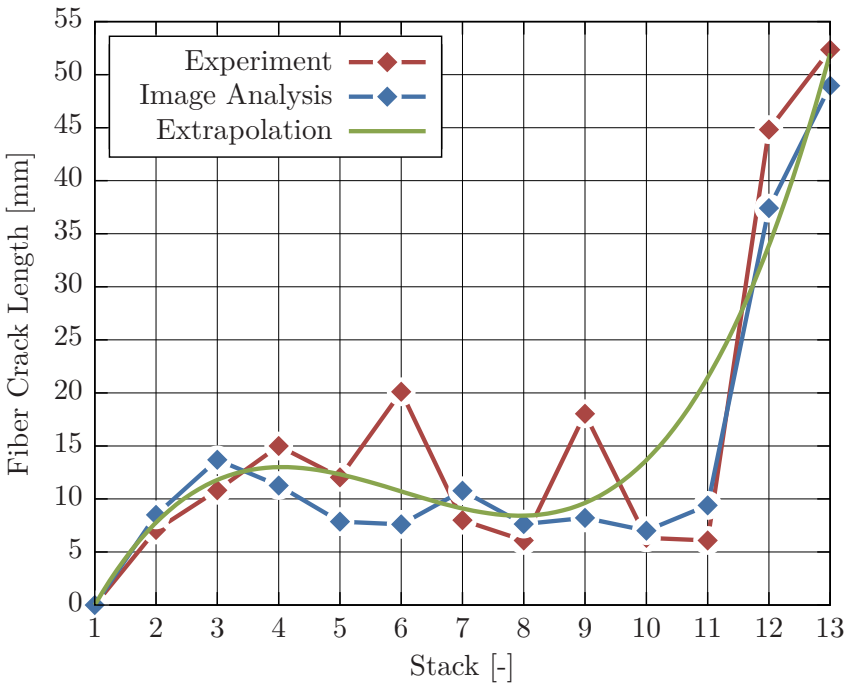

Figure A.3.: True crack lengths derived from de-ply test, image analysis, and from the cubic extrapolation ($c_2 = 2.3$, $c_3 = -6.5$), for coupon CAI-TC1-05. Good agreement among the applied methods.

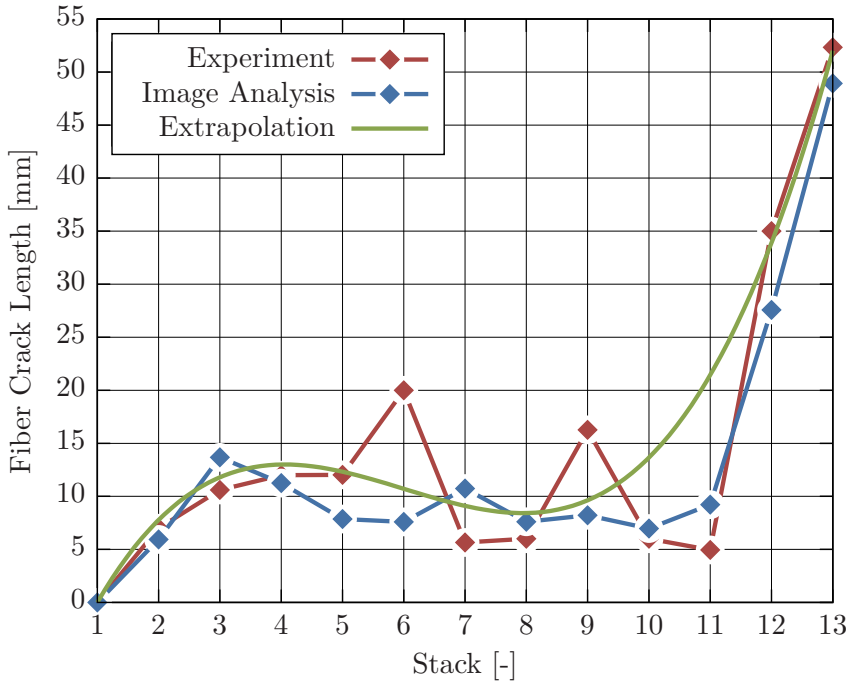

Figure A.4.: Projected crack lengths derived from de-ply test, image analysis, and from the cubic extrapolation ($c_2 = 2.3$, $c_3 = -6.5$), for coupon CAI-TC1-05. Good agreement among the applied methods.

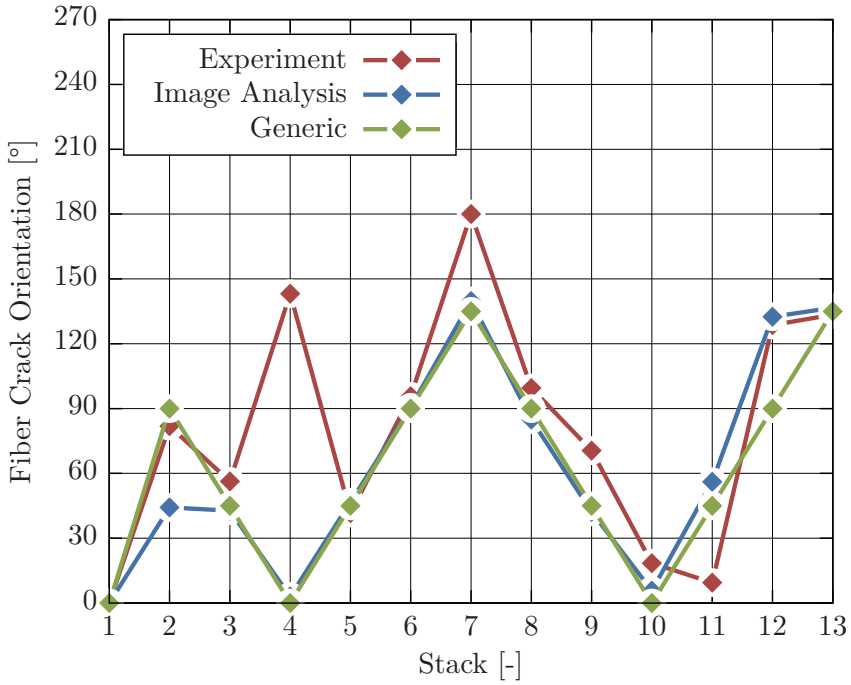

Figure A.5.: Fiber crack orientations derived from de-ply test, image analysis, and from the generic method, for coupon CAI-TC1-05.

Stack	Stack orientation	Crack orientation	Crack length [mm]	
			measured	projected
1 (bottom)	45°	0°	0	0
2	0°	96°	9	9
3	135°	39°	6	6
4	90°	150°	16	14
5	135°	39°	6	6
6	0°	73°	10	10
7	45°	171°	6	5
8	0°	83°	8	8
9	135°	34°	7	7
10	90°	172°	7	7
11	135°	51°	6	6
12	0°	127°	34	27
13 (top)	45°	138°	51	51

Table A.3.: Fiber crack geometry in specimen CAI-7.

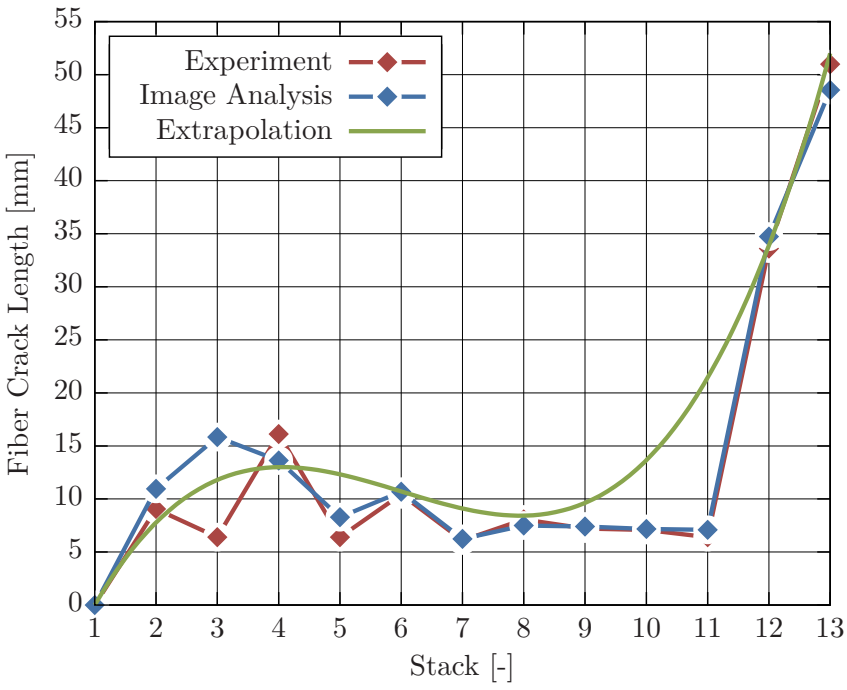

Figure A.6.: True crack lengths derived from de-ply test, image analysis, and from the cubic extrapolation ($c_2 = 2.3$, $c_3 = -6.5$), for coupon CAI-TC1-07. Good agreement among the applied methods.

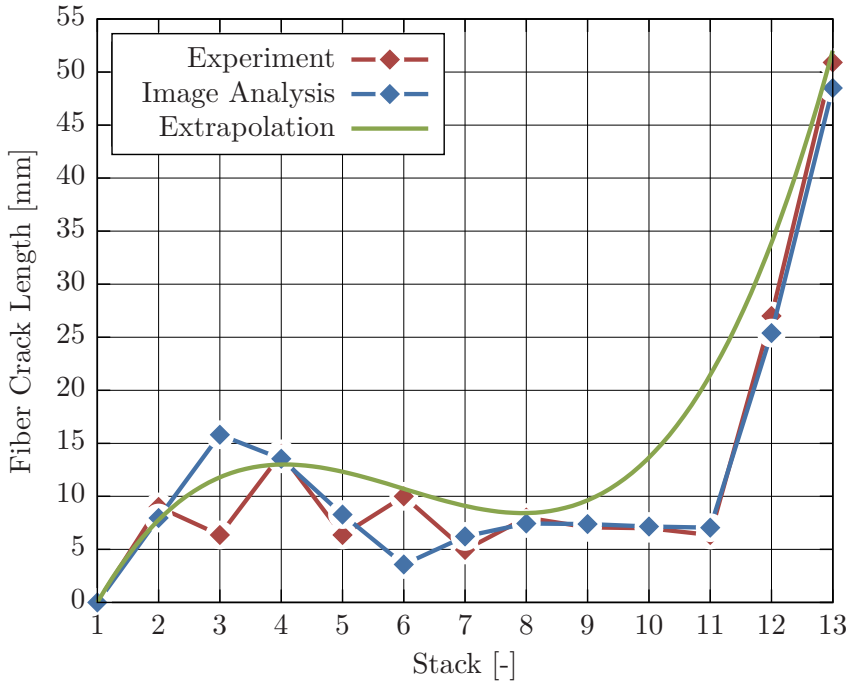

Figure A.7.: Projected crack lengths derived from de-ply test, image analysis, and from the cubic extrapolation ($c_2 = 2.3$, $c_3 = -6.5$), for coupon CAI-TC1-07. Good agreement among the applied methods.

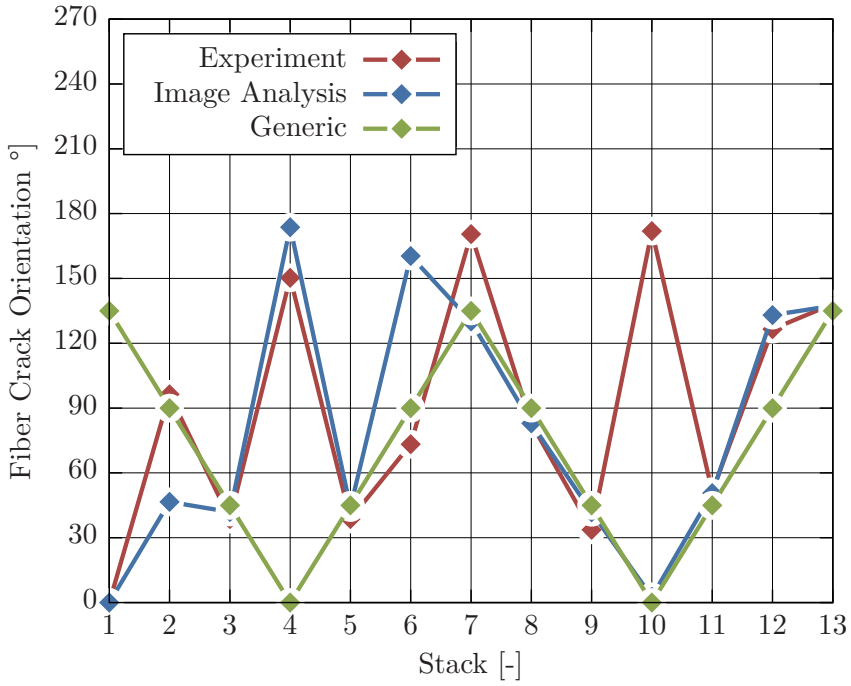

Figure A.8.: Fiber crack orientations derived from de-ply test, image analysis, and from the generic method, for coupon CAI-TC1-07.

B Interlaminar Matrix Properties

B.1. DCB Test

A total of 5 specimens is tested according to the test standard ASTM 5528 [125]. Results are summarized in table B.1 and plotted in figure B.1.

The average specimen geometry and material parameters from table B.1 are considered in the analytical load-displacement curve depicted in figure B.1. Before damage onset, the cross-beam displacement, Δ, is defined as a function of the applied load, F, and the system's compliance, C_{DCB}, (equation (B.1)) [140]. The parameters w and E_{11} represent the specimen's width an lamina Young modulus in length direction.

$$\Delta = \frac{8a_I^3}{wE_{11}h^3} \cdot F = C_{DCB} \cdot F \tag{B.1}$$

In the CBT, deflections and rotations at the crack tip are accounted by considering an increased crack length [164]. The initial corrected crack length is thus defined as $a_I = a_{ini} + \chi_I h$, with a_{ini} being the effective initial crack length and $h = {}^{t}/_{2}$ the laminate half-thickness. The correction parameter, χ_I, is defined by

$$\chi_I = \sqrt{\frac{E_{11}}{11G_{13}}\left[3 - 2\left(\frac{\Gamma}{1+\Gamma}\right)^2\right]}, \tag{B.2}$$

with

$$\Gamma = 1.18\frac{\sqrt{E_{11}E_{22}}}{G_{13}}. \tag{B.3}$$

E_{22} and G_{13} are the elasticity modules in transverse and in longitudinal shear directions, respectively.

Considering that crack propagation occurs once the SERR, $\mathcal{G}$, equates the fracture toughness, $\mathcal{G}_{Ic}$, equation (B.4) applies.

$$\mathcal{G}_{Ic} = \mathcal{G} = \frac{F^2}{2w}\frac{\partial C_{DCB}}{\partial a} \tag{B.4}$$

Solving equation (B.4) for the evolving crack length, a_I, and substituting it in equation (B.1) yields the load-displacement relation in the crack propagation domain (equation (B.5)). The

intersection point of both analytical curve segments denotes the transition from the linear-elastic to the crack-growth regime. Geometrical moment of inertia is denoted by I.

$$\Delta = \frac{2}{3}\frac{\sqrt{\left(\mathcal{G}_{Ic} w\right)^3 E_{11} I}}{F^2} \tag{B.5}$$

Specimen Label	Dimensions			Results	
	t [mm]	w [mm]	a_0 [mm]	$\mathcal{G}_{Ic}$ [N/mm]	F_{max} [N]
TC2-DCB-02	3.04	25.08	56.5	0.44	60.5
TC2-DCB-03	3.03	25.11	57.0	0.43	59.8
TC2-DCB-04	3.03	25.08	57.5	0.45	58.5
TC2-DCB-07	3.05	25.06	57.5	0.46	63.1
TC2-DCB-08	3.04	25.08	57.0	0.45	60.2
Average	3.04	25.08	57.10	0.44	60.4
CoV [%]	0.3	0.1	0.7	1.9	2.8

Table B.1.: DCB tests on Hexcel®M91/IM7: Geometrical parameters and experimental results.

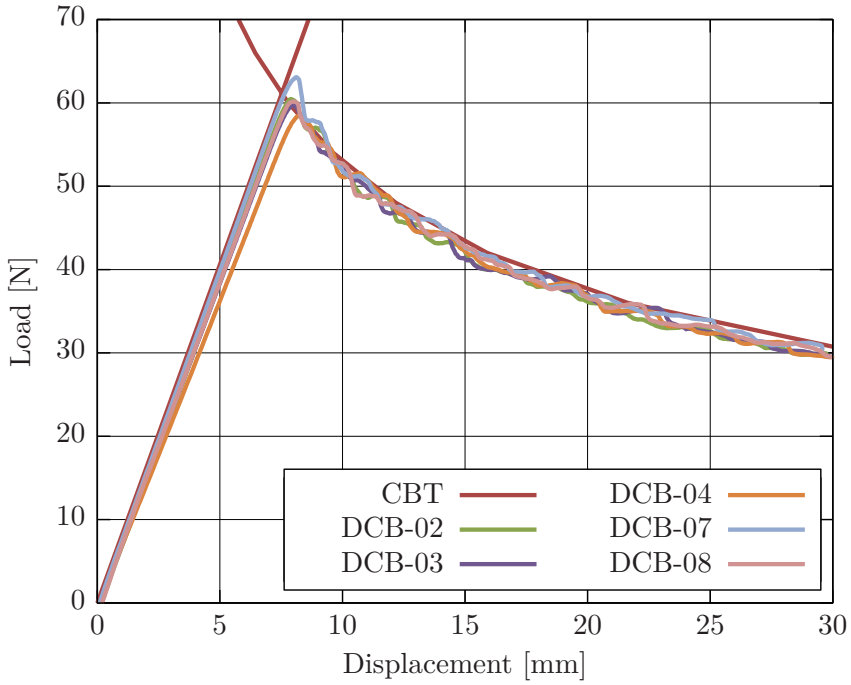

Figure B.1.: DCB tests on Hexcel®M91/IM7: Analytical (CBT) and experimental load-displacement curves.

B.2. MMB Tests

Three different specimen batches are tested in compliance to test standard ASTM 6671 [126] for three different mixed-mode ratios, $\beta \in \{0.23, 0.49, 0.92\}$, with $\beta = \mathcal{G}_I/\mathcal{G}_{II}$. Results are summarized in tables B.2 to B.4 and plotted in figures B.3 to B.5.

Like the analytical load-displacement relation describing the DCB response, the MMB test curve is also described by two domains: one exhibiting linear-elastic behavior, and a second domain covering the specimen's global response under crack propagation conditions. A detailed derivation of the equations governing the MMB specimen behavior is, for instance, given by Bennati et al. [164]. The CBT is also adopted here.

The MMB test setup can be viewed as the superposition of the DCB and ENF tests for pure mode I and mode II conditions, respectively. Thus, the global load-displacement behavior (D vs. Δ) is given by the relation $\Delta = C_{MMB} \cdot F$, where C_{MMB} denotes the compliance of the MMB setup. This is given by equation (B.6).

$$C_{MMB} = A^2 \cdot C_{DCB} + B^2 \cdot C_{ENF} \tag{B.6}$$

Considering the test setup depicted in figure B.2, compliances for pure mode I and II loading are given by equations B.1 and B.7. Hereby, the corrected crack length for mode II is defined as $a_{II} = 0.42 a_I$.

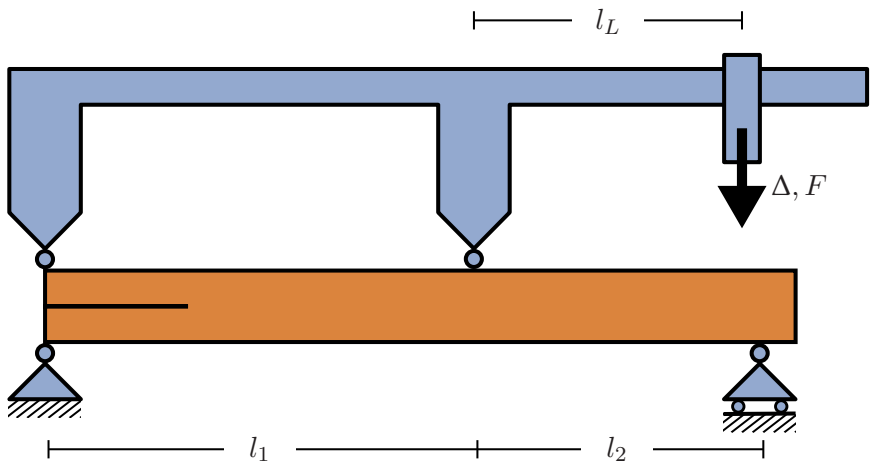

Figure B.2.: Schematic of the MMB test setup. Mixed-mode ratio is set by adjusting the test apparatus lengths l_L, l_1, and l_2.

$$C_{ENF} = \frac{3a_{II}^3 + 2l_2^3}{8wE_{11}h^3} \tag{B.7}$$

The coefficients A and B result from the test setup (figure B.2) and are defined by equations B.8 and B.9, respectively.

$$A = \frac{1}{2}\left(\frac{l_L + l_1}{l_1 + l_2} + \frac{l_L}{l_1} - 1\right) \tag{B.8}$$

$$B = \left(1 + \frac{l_L}{l_1}\right) \tag{B.9}$$

As shown for the DCB solution, the evolving crack length is obtained from equation (B.4), however now considering the MMB compliance (equation (B.6)). Solving the resulting equation for a_0, and substituting this expression in the original equation $\Delta = C_{MMB} \cdot F$, yields the load-displacement relation in the growing crack domain.

The results of a coupon batch tested at a mixed-mode ratio of $\beta = 0.23$ are presented in table B.2. The respective experimental setup parameters are specified as follows: $l_1 = 66\,\text{mm}$, $l_2 = 34\,\text{mm}$, and $l_L = 80\,\text{mm}$ (c.f. figure B.2). The corresponding load-displacement curves are plotted in figure B.3, considering the test batch average parameters.

Specimen Label	Dimensions			Results	
	t [mm]	w [mm]	a_0 [mm]	$\mathcal{G}_c$ [N/mm]	F_{max} [N]
TC2-MMB-01	3.00	25.08	30.0	0.93	171.9
TC2-MMB-02	3.01	25.08	30.0	0.76	166.6
TC2-MMB-03	3.01	25.07	30.0	0.93	181.5
TC2-MMB-04	3.01	25.09	30.0	0.94	173.8
TC2-MMB-06	3.05	25.08	30.0	0.91	179.4
TC2-MMB-07	3.05	25.08	30.0	0.92	176.7
Average	3.02	25.08	30.0	0.90	176.7
CoV [%]	0.7	0.0	0.0	7.6	4.1

Table B.2.: MMB tests on Hexcel®M91/IM7: Geometrical parameters and experimental results (mixed-mode ratio: $\beta = 0.23$).

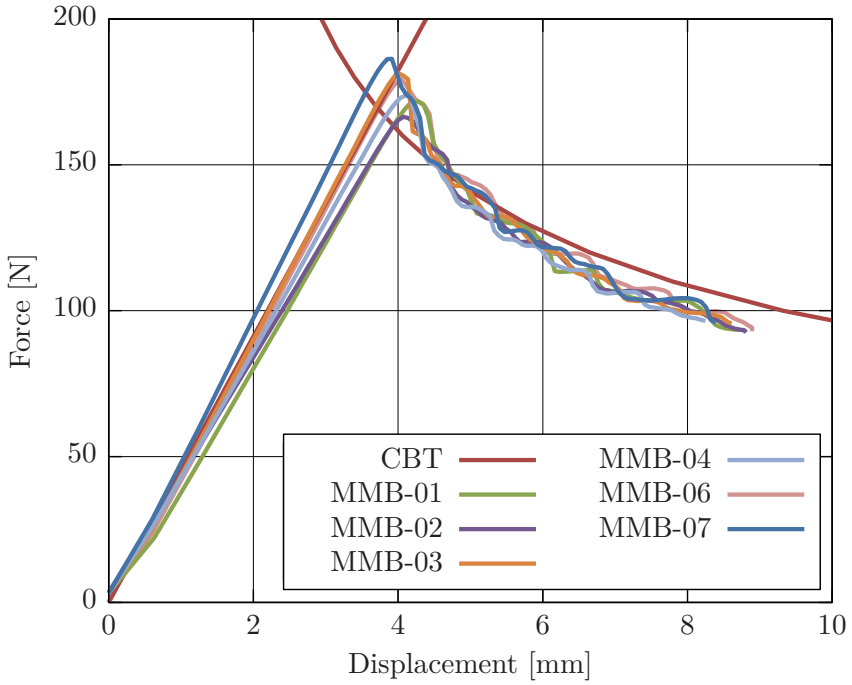

Figure B.3.: MMB tests on Hexcel®M91/IM7: Analytical (CBT) and experimental load-displacement curves (mixed-mode ratio: $\beta = 0.23$).

A second coupon batch is tested at a mixed-mode ratio of $\beta = 0.49$. Experimental setup parameters are set to: $l_1 = 50\,\text{mm}$, $l_2 = 50\,\text{mm}$, and $l_L = 42.5\,\text{mm}$. Geometrical parameters and test results are presented in table B.3 and in figure B.4.

Specimen Label	Dimensions			Results	
	t [mm]	w [mm]	a_0 [mm]	$\mathcal{G}_c$ [N/mm]	F_{max} [N]
TC2-MMB-10	3.01	25.09	30.0	2.11	429.0
TC2-MMB-11	3.01	25.08	30.0	2.08	436.3
TC2-MMB-12	3.00	25.07	30.0	2.03	413.1
TC2-MMB-13	3.01	25.07	31.0	2.16	413.3
TC2-MMB-14	3.01	25.08	31.0	2.00	407.6
Average	3.01	25.08	30.0	2.08	419.9
CoV [%]	0.1	0.0	1.7	3.0	2.9

Table B.3.: MMB tests on Hexcel®M91/IM7: Geometrical parameters and experimental results (mixed-mode ratio: $\beta = 0.49$).

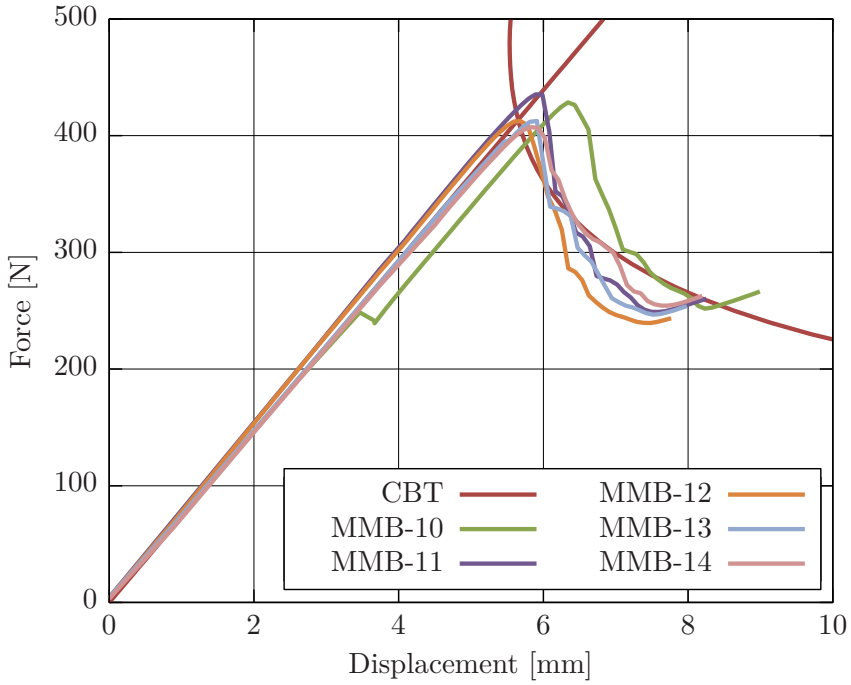

Figure B.4.: MMB tests on Hexcel®M91/IM7: Analytical (CBT) and experimental load-displacement curves (mixed-mode ratio: $\beta = 0.49$).

Finally, a third coupon set is tested at a mixed-mode ratio of $\beta = 0.92$. Experimental setup parameters are described by: $l_1 = 50\,\text{mm}$, $l_2 = 50\,\text{mm}$, and $l_L = 22.5\,\text{mm}$. Geometrical parameters and test results are presented in table B.4 and in figure B.5.

Specimen Label	Dimensions			Results	
	t [mm]	w [mm]	a_0 [mm]	$\mathcal{G}_c$ [N/mm]	F_{max} [N]
TC2-MMB-16	3.02	25.08	31.0	3.46	873.9
TC2-MMB-17	3.04	25.08	31.0	3.84	894.1
TC2-MMB-18	3.05	25.07	31.0	3.92	899.5
TC2-MMB-19	3.06	25.07	31.0	3.44	893.2
TC2-MMB-20	3.03	25.07	31.0	3.86	895.4
Average	3.04	25.08	31.0	3.70	887.9
CoV [%]	0.6	0.0	0.0	6.3	1.4

Table B.4.: MMB tests on Hexcel®M91/IM7: Geometrical parameters and experimental results (mixed-mode ratio: $\beta = 0.92$).

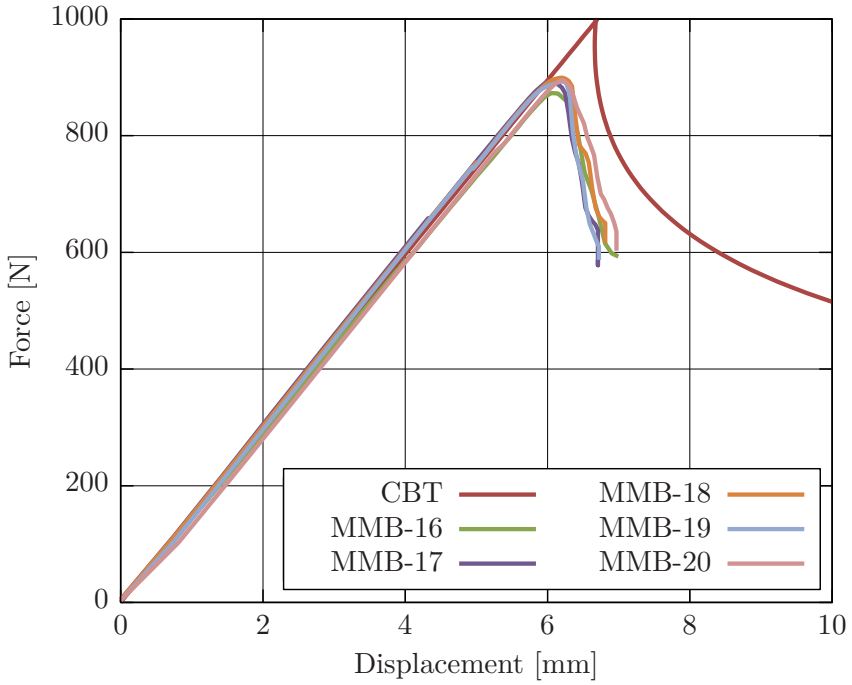

Figure B.5.: MMB tests on Hexcel®M91/IM7: Analytical (CBT) and experimental load-displacement curves (mixed-mode ratio: $\beta = 0.92$).

The mixed-mode interaction parameter η^m is obtained by fitting a BK-law curve (equation (4.28)) through the experimentally obtained data, such as to minimize the Residual Sum of Squares (RSS). Then, the effective mode II fracture toughness $\mathcal{G}_{IIc}$ is determined by extrapolating the best-fit curve to $\beta = 1.0$.

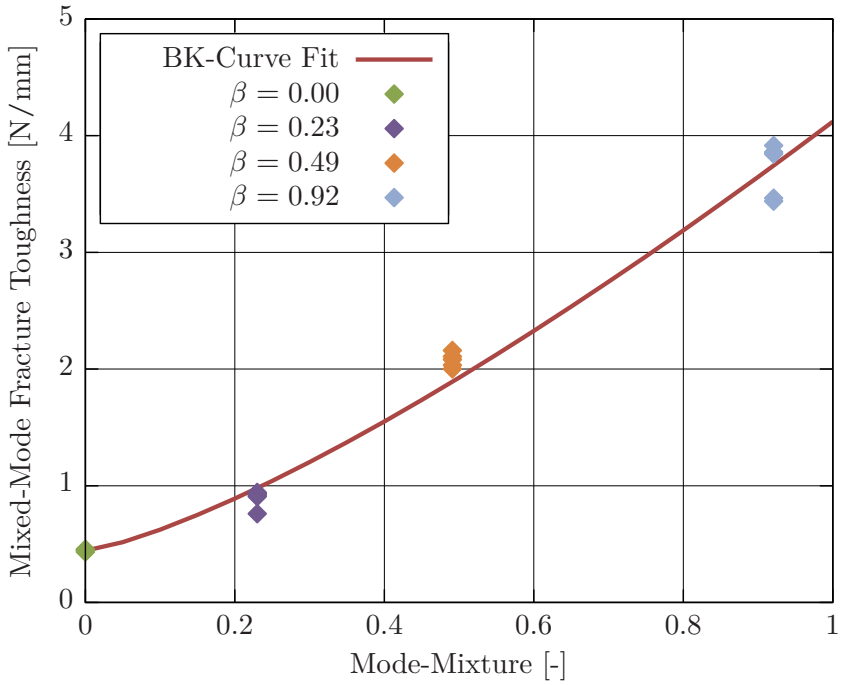

Figure B.6.: MMB tests on Hexcel®M91/IM7: Mixed-mode interaction parameter determined by curve fitting.

C Adhesive Properties

C.1. DCB Test

A total of 5 specimens is tested according to the test standard ASTM 5528 [125]. Although this is designed for determining interlaminar properties of unidirectional laminates, it is extended here to the acquisition of adhesive properties. The obtained results are summarized in table C.1 and plotted in figure C.1. An analytical load-displacement curve is included in figure C.1, according to the considerations introduced in appendix B.1. Hereby, the average values regarding specimen geometry and material parameters presented in table C.1 are adopted. The strong scatter among the load-displacement curves is due to dissimilar initial crack lengths, which result from a pre-loading step.

Specimen Label	Dimensions			Results	
	t [mm]	w [mm]	a_0 [mm]	$\mathcal{G}_c$ [N/mm]	F_{max} [N]
TC2-DCB-CO-02	3.17	25.08	58.5	1.12	92.4
TC2-DCB-CO-03	3.16	25.10	61.5	1.28	86.4
TC2-DCB-CO-05	3.22	24.98	59.0	1.35	97.9
TC2-DCB-CO-06	3.21	25.05	54.0	1.23	103.0
TC2-DCB-CO-08	3.21	25.07	55.5	1.42	109.5
Average	3.19	25.06	57.70	1.28	97.8
CoV [%]	0.8	0.2	5.1	8.3	9.2

Table C.1.: DCB tests on Cytec FM®300: Geometrical parameters and experimental results.

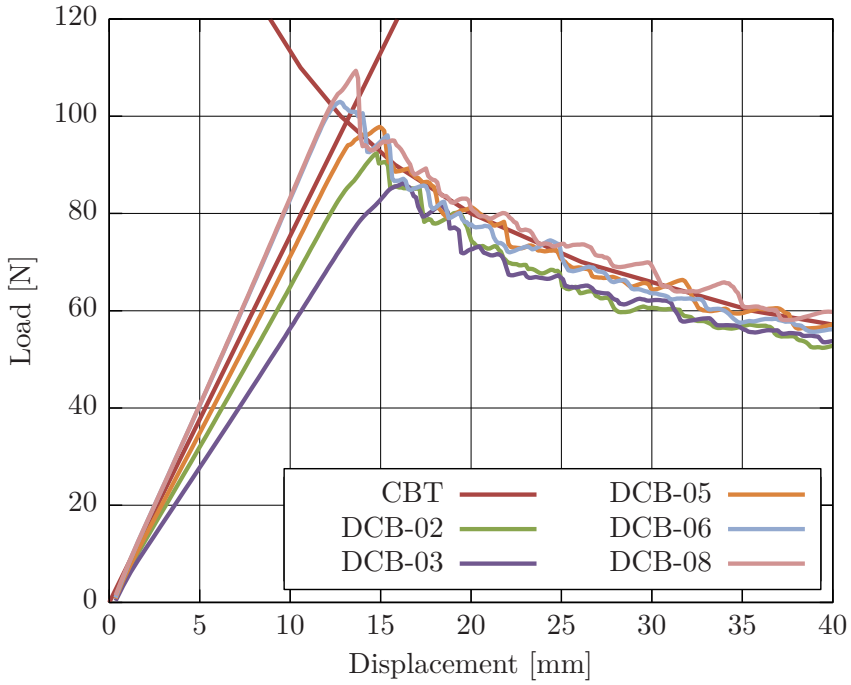

Figure C.1.: DCB tests on Cytec FM®300: Analytical (CBT) and experimental load-displacement curves. Strong scatter due to dissimilar initial crack length, which result from pre-loading.

C.2. MMB Tests

Again, three different specimen batches are tested according to test standard ASTM 6671 [126] under mixed-mode conditions. This test procedure is designed for interlaminar property characterization and is extended in the present context to adhesive tests. The same mixed-mode ratios considered for the matrix characterization are now adopted to the adhesive tests.

The results obtained from a coupon batch tested at a mixed-mode ratio of $\beta = 0.23$ are presented in table C.2. Referring to figure B.2, the test rig parameters are specified as follows: $l_1 = 66\,\text{mm}$, $l_2 = 34\,\text{mm}$, and $l_L = 80\,\text{mm}$. Load-displacement curves obtained for each specimen are plotted in figure C.2. The very dissimilar initial crack lengths, establishing due to pre-loading, are the cause for the significant scatter. Especially towards higher mixed-mode ratios, determining the crack length after pre-loading becomes increasingly challenging and thus error-prone. Consequently, pre-loading is dispensed in the subsequent MMB tests at mixed-mode ratios 0.49 and 0.92.

Specimen Label	Dimensions			Results	
	t [mm]	w [mm]	a_0 [mm]	$\mathcal{G}_c$ [N/mm]	F_{max} [N]
TC2-MMB-CO-02	3.16	25.08	33.5	1.63	239.2
TC2-MMB-CO-03	3.15	25.09	31.5	1.35	237.4
TC2-MMB-CO-04	3.20	25.07	32.0	1.42	239.9
TC2-MMB-CO-05	3.22	25.07	44.0	1.63	179.9
TC2-MMB-CO-06	3.20	25.06	34.0	1.56	237.5
Average	3.19	25.07	35.0	1.52	226.8
CoV [%]	0.9	0.1	14.7	8.3	11.6

Table C.2.: MMB tests on Cytec FM®300: Geometrical parameters and experimental results (mixed-mode ratio: $\beta = 0.23$).

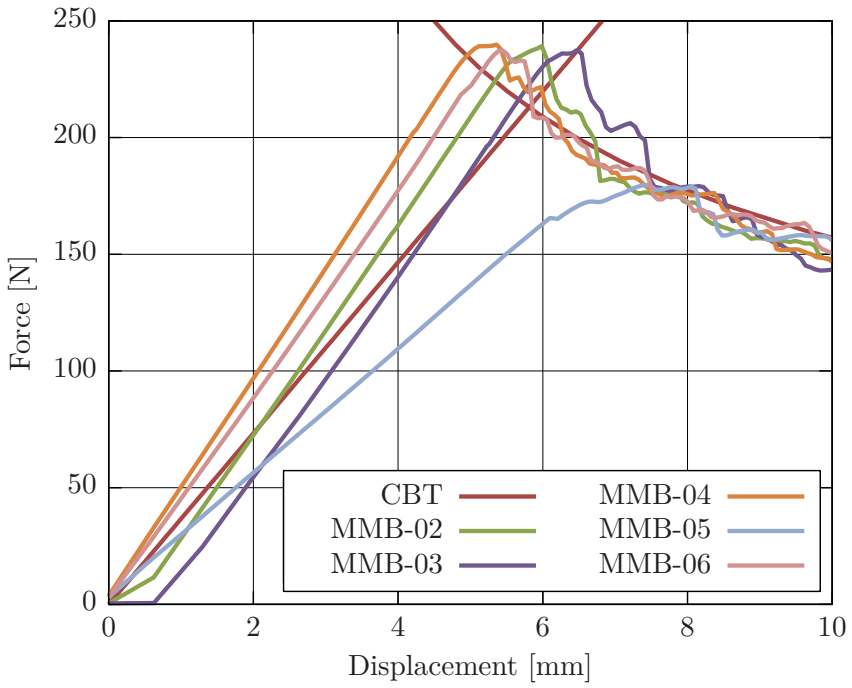

Figure C.2.: MMB tests on Cytec FM®300: Analytical (CBT) and experimental load-displacement curves (mixed-mode ratio: $\beta = 0.23$).

Under mixed-mode ratio $\beta = 0.49$ ($l_1 = 50\,\text{mm}$, $l_2 = 50\,\text{mm}$, and $l_L = 42.5\,\text{mm}$), a total of five specimens is tested. The corresponding results are presented in table C.3 and figure C.3. It is noted that the crack propagation segment is significantly underestimated by the CBT. This is attributed to the pessimistic derivation of the fracture toughness in pure mode II, which is obtained through extrapolation (c.f. figure C.5).

Specimen Label	Dimensions			Results	
	t [mm]	w [mm]	a_0 [mm]	$\mathcal{G}_c$ [N/mm]	F_{max} [N]
TC2-MMB-CO-07	3.20	25.06	30.0	4.05	659.8
TC2-MMB-CO-08	3.20	25.06	30.0	3.88	626.8
TC2-MMB-CO-09	3.19	25.08	30.0	3.67	625.7
TC2-MMB-CO-22	3.18	25.07	31.0	3.62	610.9
TC2-MMB-CO-23	3.16	25.07	31.0	3.34	604.9
Average	3.19	25.07	30.4	3.71	625.6
CoV [%]	0.5	0.0	1.8	7.3	3.4

Table C.3.: MMB tests on Cytec FM®300: Geometrical parameters and experimental results (mixed-mode ratio: $\beta = 0.49$).

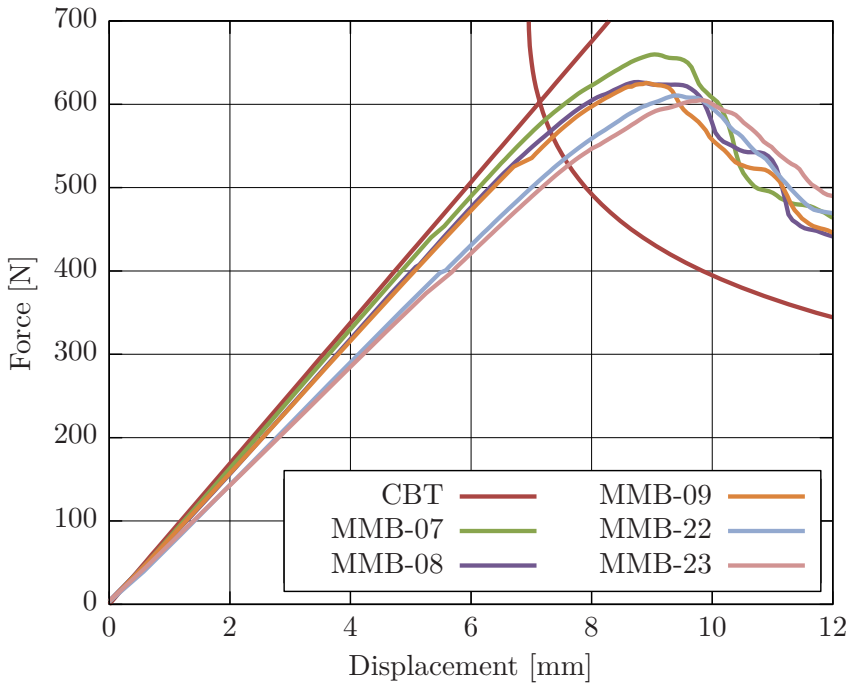

Figure C.3.: MMB tests on Cytec FM®300: Analytical (CBT) and experimental load-displacement curves (mixed-mode ratio: $\beta = 0.49$).

A third coupon batch is subjected to experimental testing at a mixed-mode ratio of $\beta = 0.92$. The respective test rig parameters are: $l_1 = 50\,\text{mm}$, $l_2 = 50\,\text{mm}$, and $l_L = 22.5\,\text{mm}$. Geometric parameters and experimental results are given in table C.4 and figure C.4. The depicted results also suggest a too low fracture toughness in mode II. However, the associated underestimation of the crack propagation segment is moderate.

Specimen Label	Dimensions			Results	
	t [mm]	w [mm]	a_0 [mm]	$\mathcal{G}_c$ [N/mm]	F_{max} [N]
TC2-MMB-CO-25	3.22	25.07	31.0	10.18	1318.0
TC2-MMB-CO-26	3.20	25.07	31.0	9.50	1305.4
TC2-MMB-CO-27	3.21	25.07	31.0	9.79	1316.1
TC2-MMB-CO-28	3.20	25.08	31.0	9.29	1297.5
TC2-MMB-CO-29	3.18	25.07	31.0	8.61	1297.2
Average	3.20	25.07	31.0	9.47	1306.9
CoV [%]	0.5	0.0	0.0	6.2	0.8

Table C.4.: MMB tests on Cytec FM®300: Geometrical parameters and experimental results (mixed-mode ratio: $\beta = 0.92$).

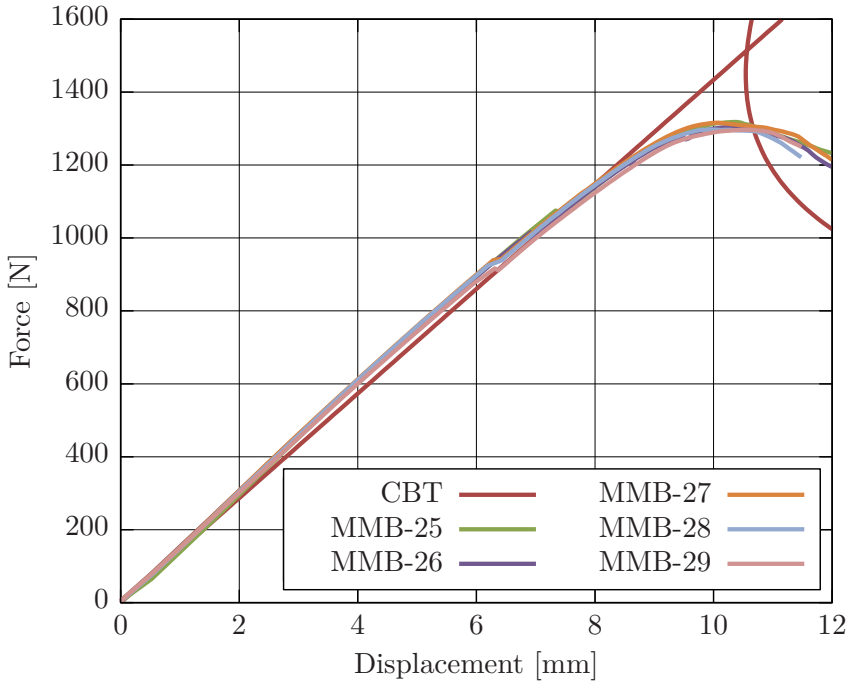

Figure C.4.: MMB tests on Cytec FM®300: Analytical (CBT) and experimental load-displacement curves (mixed-mode ratio: $\beta = 0.92$).

Based on the critical fracture toughnesses experimentally determined at different mixed-mode ratios, the mixed-mode interaction parameter η^{adh} is found by fitting a BK-law curve (equation (4.28)) through the data points (figure C.5). Then, the mode II fracture toughness $\mathcal{G}_{IIc}$ is determined by extrapolating the newly found BK curve to $\beta = 1.0$.

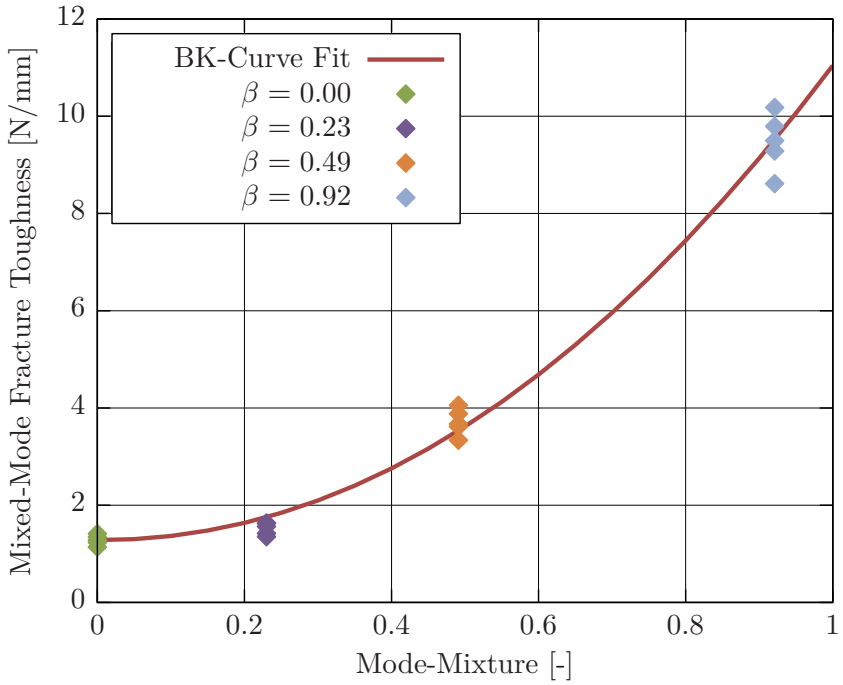

Figure C.5.: MMB tests on Hexcel®M91/IM7: Mixed-mode interaction parameter determined by curve fitting.

D Impact and Residual Strength Test Results

In the following subsections, experimental and simulation results obtained from impact-damaged CAI coupons are presented. Impact and CAI test results are summarized in the tables below. Each table depicts the specimen details regarding a specific impact energy. A statistic evaluation is added at each table's bottom (average and coefficient of validity). Each coupon test is described by the following parameters: geometric dimensions (length, width, and thickness), impact energy, damage parameters (dent depth, maximum fiber crack length, and projected delamination area), and residual properties (nominal failure stress, nominal failure strain, and failure load). Common to all specimens, except the virgin coupons, is the moderate impact velocity ranging from 3 to 4 m/s and the impactor diameter of 16 mm. Mass and height of the falling weight are adapted in order to achieve the appointed impact energy.

All specimens are inspected using pulse-echo ultrasonics to characterize delamination defects. In addition, coupons CAI-TC1-01 through CAI-TC1-07 (all impacted at 40J) are further submitted to µCT inspection. It is noted however, that the specimens CAI-TC1-04, CAI-TC1-05, and CAI-TC1-07 are subjected to destructive damage inspection after NDI (results are presented in appendix A.2); therefore no CAI test results are available. For these specimens, the fiber crack length is obtained from de-ply tests, while maximum fiber crack length (FC) ascribed to the remaining specimens is measured at the surface, using a caliper. Pixel-accurate delamination areas are quantified using the methods proposed in section 3.4.1, and the dent depth is measured after impact with a caliper.

The structural behavior is recorded using a load cell, and strain gauges or DIC. Specimens monitored by DIC are identified by the symbol †. Regarding the residual properties, only the peak load (force) is effectively measured during the experiment. The referred stress is understood as the nominal stress, which is defined as the peak load divided by the initial specimen cross section (equation D.1). Residual nominal strain is obtained from the nominal stress by applying Hook's law and considering a laminate Young modulus in loading direction E_x, which for the present laminate is 50.39 GPa (equation D.2).

$$\hat{\sigma}_{nom} = \frac{\hat{F}}{w \cdot t} \tag{D.1}$$

$$\hat{\varepsilon}_{nom} = \frac{\hat{\sigma}_{nom}}{\hat{E}_x} \tag{D.2}$$

For each damaged condition, result plots are presented for representative coupons. Graphics

obtained from the experiments present either strain gauge readings or through-the-thickness displacements at both surface center points. The simulation results are presented by strain readings at the sampling points introduced by figure 4.15 and also by transversal deflections at the center points of each stack. It is reminded that stack 1 is located at the coupon bottom surface and stack 13 consequently at the top, while the impact is introduced at the top surface.

D.1. Virgin Coupons

Specimen Label	Dimensions			Impact Energy	Damage Parameters			Residual Properties		
	l	w	t		Dent	FC	Dela	Stress	Strain	Force
	[mm]	[mm]	[mm]	[J]	[mm]	[mm]	[mm^2]	[MPa]	[µε]	[kN]
CAI-TC1-15	150.0	100.0	4.17	0	0	0	0	465.0	9228	193.9
CAI-TC1-16	150.0	100.0	4.19	0	0	0	0	464.2	9212	194.5
CAI-TC1-17	150.0	100.0	4.17	0	0	0	0	454.1	9012	189.3
CAI-TC1-18	150.0	100.0	4.14	0	0	0	0	463.2	9192	191.8
average	150.0	100.0	4.17	0	0	0	0	461.6	9161	192.4
CoV [%]	0.0	0.0	0.5	0.0	0.0	0.0	0.0	1.1	1.1	1.2

Table D.1.: Impact and residual strength parameters for virgin specimens.

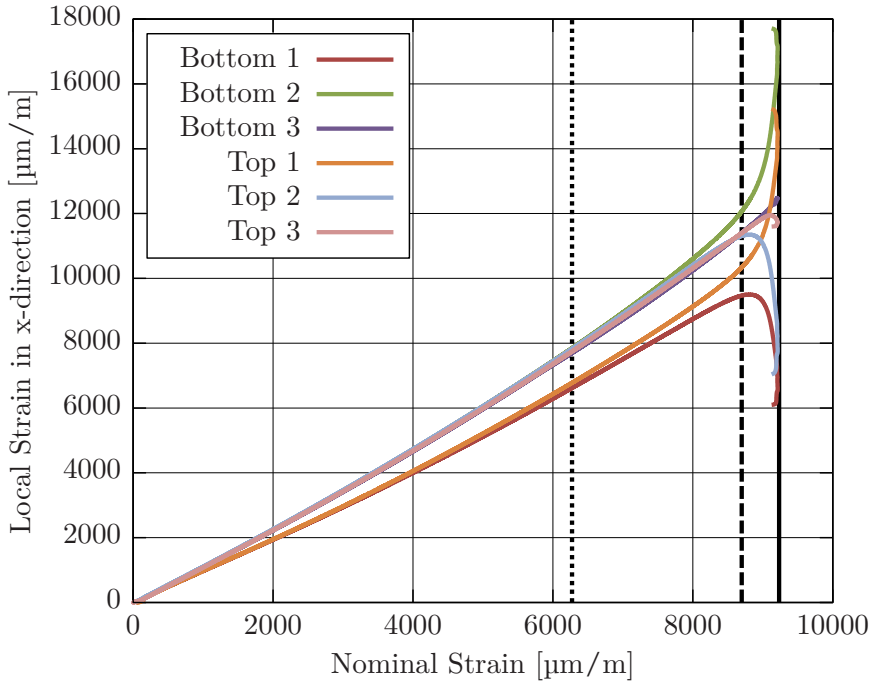

Figure D.1.: Experimental local strains versus nominal strain (TC1-CAI-16). Higher compliance at positions 2 and 3. Local and nominal strains mostly identical at position 1. Dotted line: transversal deflection onset (6300 µm/m); dashed line: buckling onset (8700 µm/m); solid line: ultimate failure (9212 µm/m).

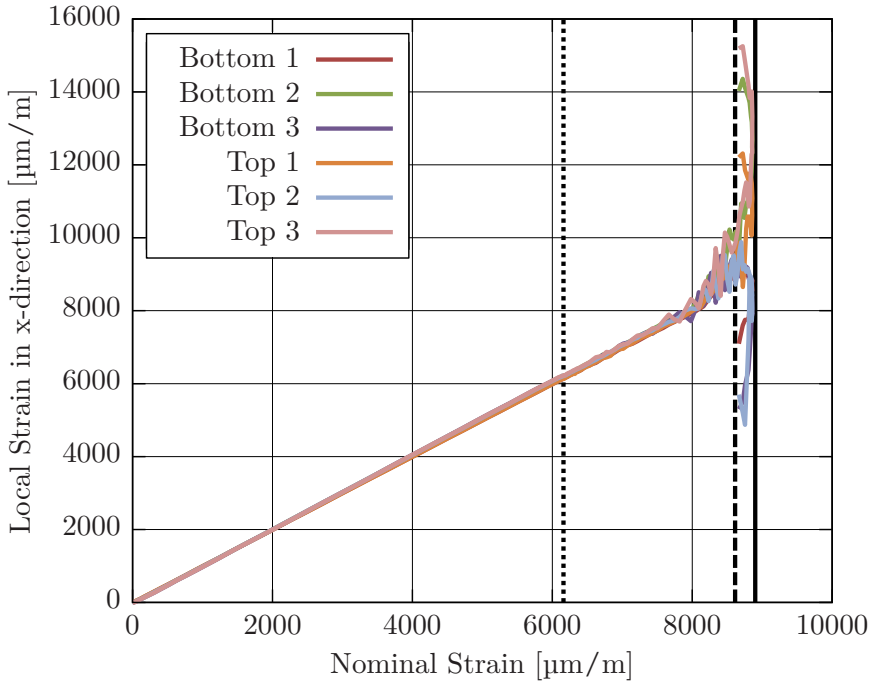

Figure D.2.: Simulated local strains versus nominal strain (TC1-CAI-16). Uniform strain field. Dotted line: transversal deflection onset (6200 µm/m); dashed line: buckling onset (8600 µm/m); solid line: ultimate failure (8860 µm/m).

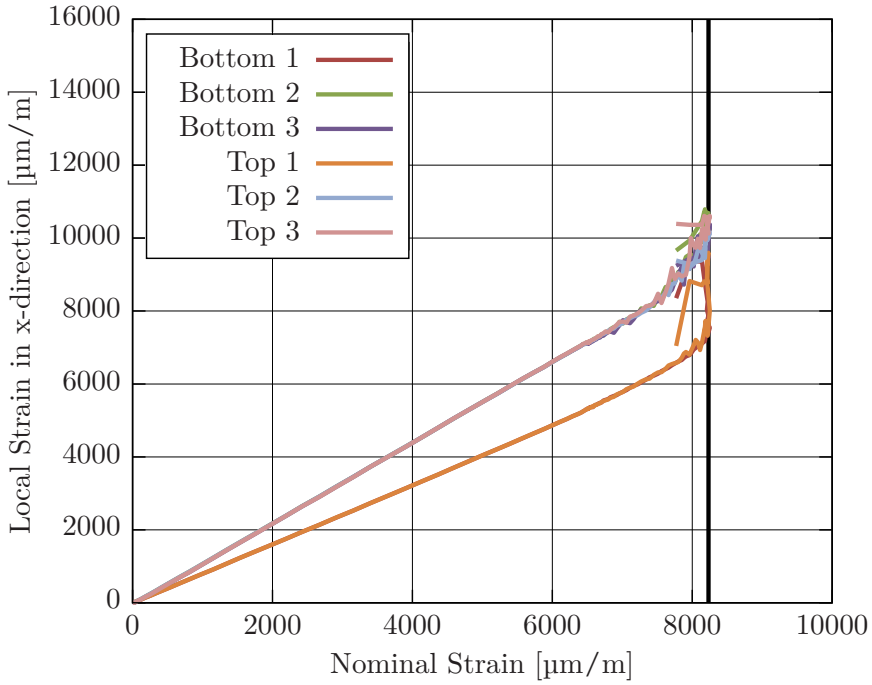

Figure D.3.: Simulated local strains versus nominal strain for ideal friction at the clamped areas (TC1-CAI-16). Significantly lower local strains at position 1 and premature failure due to clamped conditions. Solid line: ultimate failure (8241 µm/m).

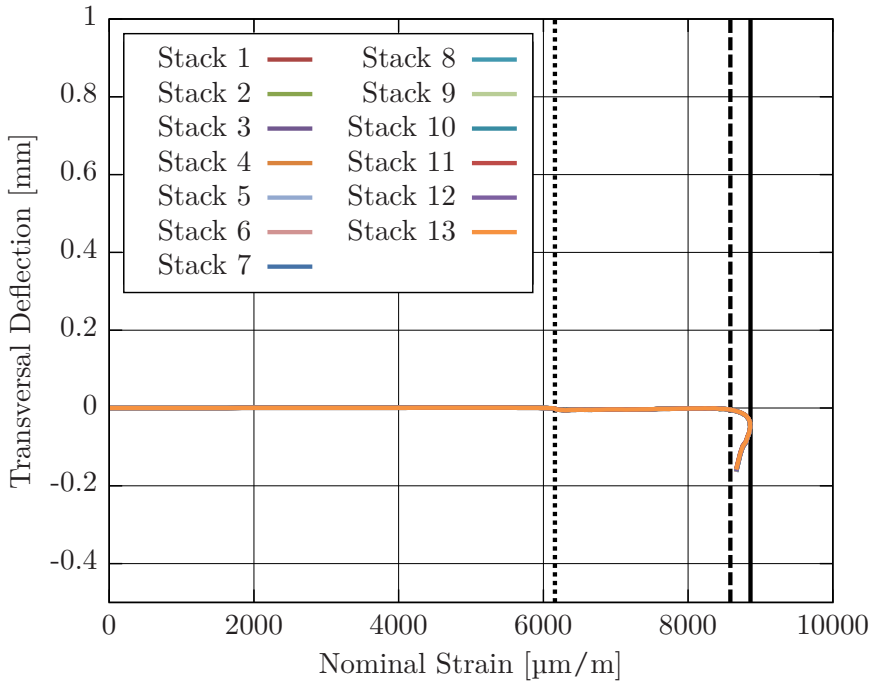

Figure D.4.: Simulated transversal stack deflections at the specimen center versus nominal strain (TC1-CAI-16). Dotted line: transversal deflection onset (6300 µm/m); dashed line: buckling onset (8700 µm/m); solid line: ultimate failure (9212 µm/m).

D.2. Impacted Coupons at 20 J

Specimen Label	Dimensions			Impact Energy	Damage Parameters			Residual Properties		
	l [mm]	w [mm]	t [mm]	[J]	Dent [mm]	FC [mm]	Dela [mm^2]	Stress [MPa]	Strain [µε]	Force [kN]
CAI-TC1-21†	150.0	100.0	4.15	20	0.19	0	360	339.1	6730	140.7
CAI-TC2-02	150.0	100.0	4.15	20	0.21	0	420	334.6	6640	138.9
CAI-TC2-03†	150.0	100.0	4.08	20	0.21	0	420	345.6	6859	141.0
CAI-TC2-04	150.0	100.0	4.15	20	0.22	0	443	332.0	6588	137.8
average	150.0	100.0	4.13	20	0.21	0	411	337.8	6704	139.6
CoV [%]	0.0	0.0	0.8	0.0	6.1	0.0	8.6	1.8	1.8	1.1

Table D.2.: Impact and residual strength parameters for specimens impacted at 20J; † denotes DIC monitored tests.

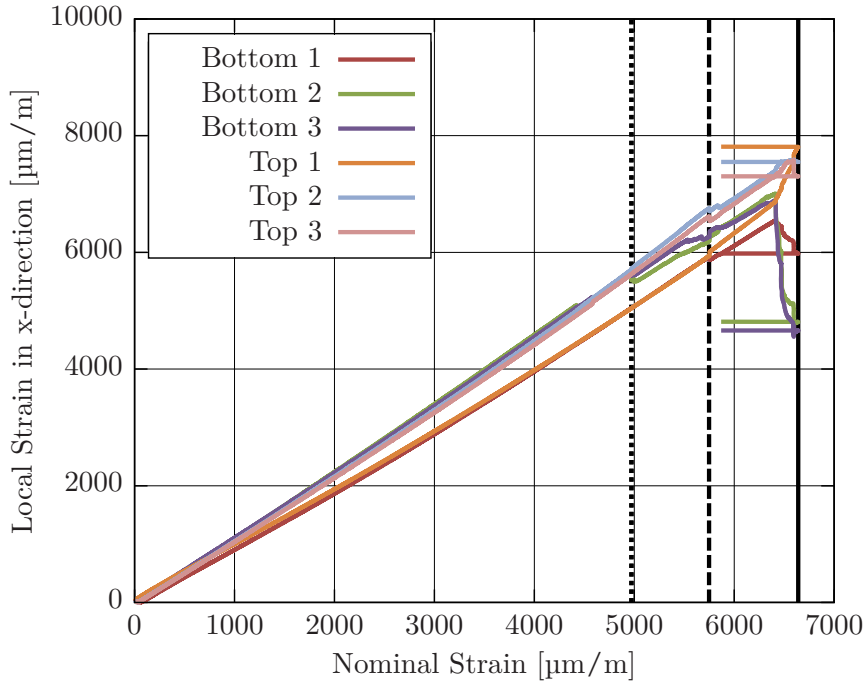

Figure D.5.: Experimental local strains versus nominal strain (TC2-CAI-02). Dotted line: strain at positions 2 and 3 point to sub-laminate buckling at 5000 µm/m; dashed line: all strain gauges accuse transversal deflection, indicating global buckling (5700 µm/m); solid line: ultimate failure (6640 µm/m).

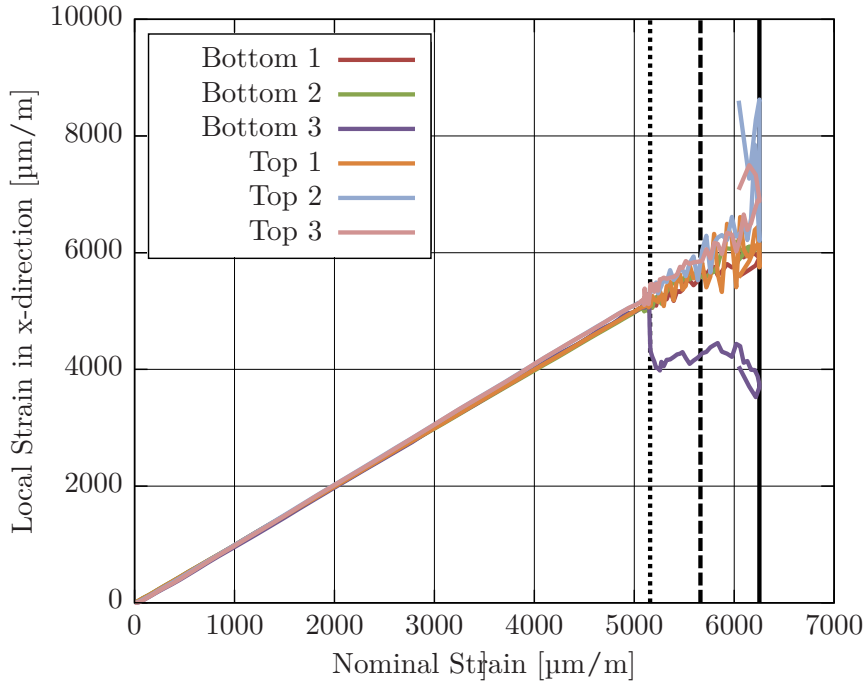

Figure D.6.: Simulated local strains versus nominal strain (TC2-CAI-02). Dotted line: sub-laminate buckling (5200 µm/m); dashed line: global buckling (5500 µm/m); solid line: ultimate failure (6254 µm/m).

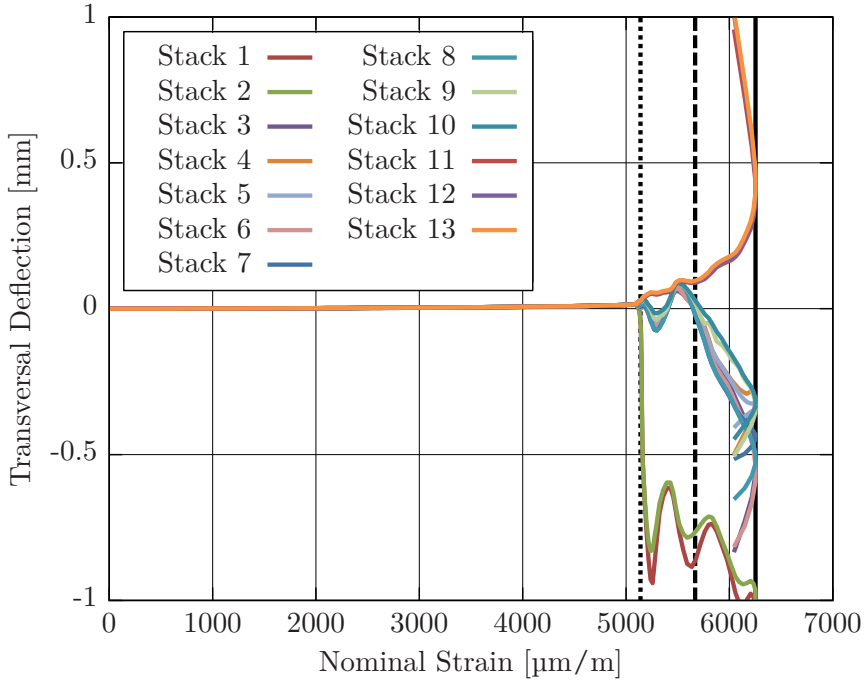

Figure D.7.: Simulated transversal stack deflections at the specimen center versus nominal strain (TC2-CAI-02). Dotted line: buckling of stacks 1 and 2 (5200 µm/m); dashed line: buckling experienced by all stacks (5500 µm/m); solid line: ultimate failure (6254 µm/m).

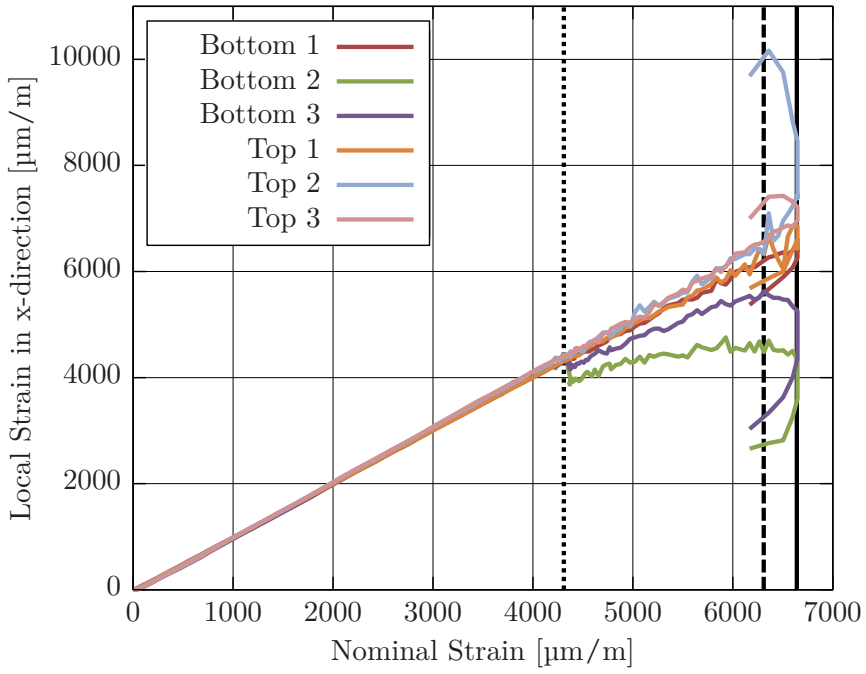

Figure D.8.: Simulated local strains versus nominal strain (TC1-CAI-21). Dotted line: sub-laminate buckling at the bottom stack (4300 µm/m); dashed line: sub-laminate buckling of all stacks (6300 µm/m); solid line: ultimate failure (6651 µm/m).

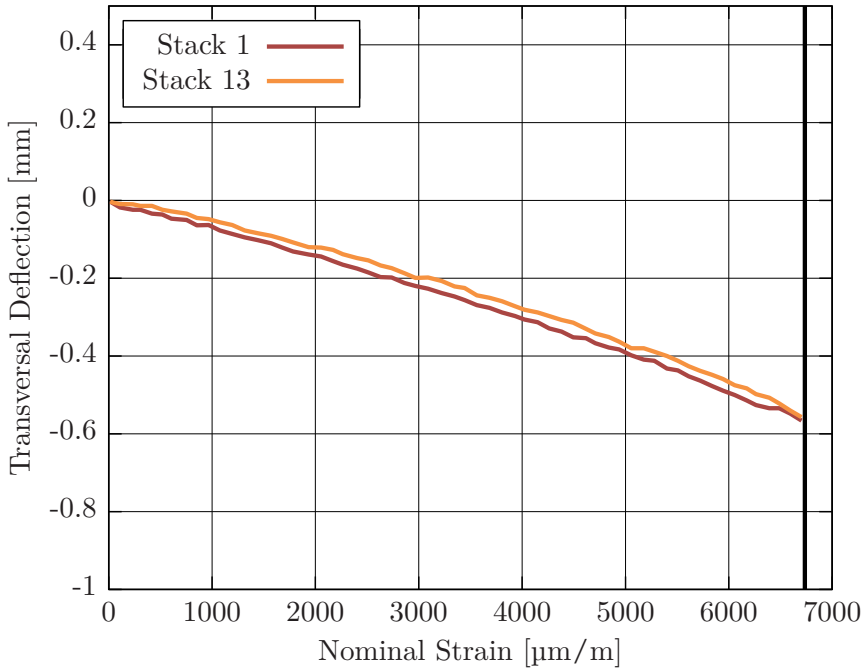

Figure D.9.: Experimental transversal stack deflections at the specimen center versus nominal strain (TC1-CAI-21). Solid line: ultimate failure (6730 µm/m).

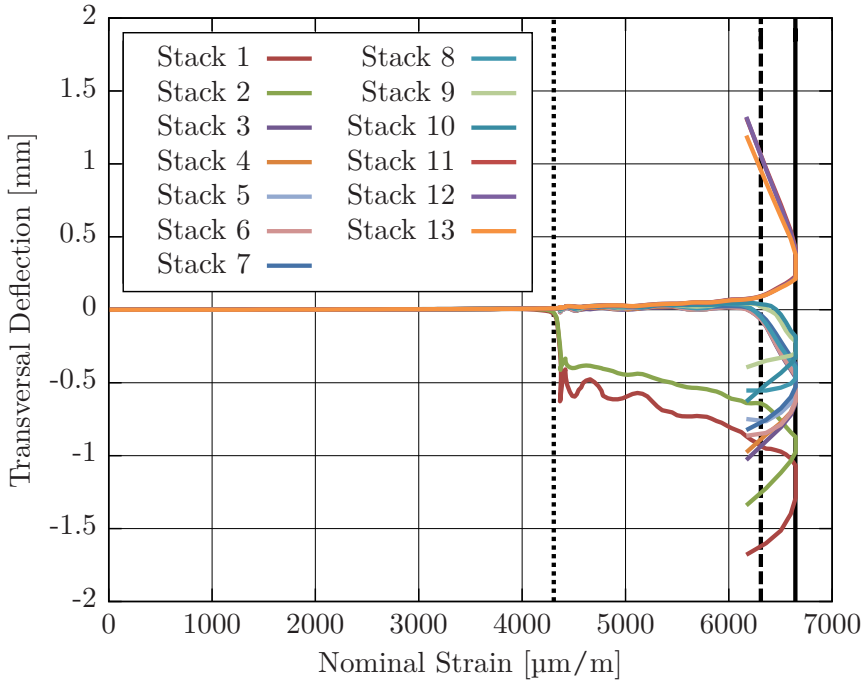

Figure D.10.: Simulated transversal stack deflections at the specimen center versus nominal strain (TC1-CAI-21). Dotted line: sub-laminate buckling of stacks 1 and 2 (4300 µm/m); dashed line: sub-laminate buckling of all stacks (6300 µm/m); solid line: ultimate failure (6651 µm/m).

D.3. Impacted Coupons at 30 J

Specimen Label	Dimensions			Impact Energy	Damage Parameters			Residual Properties		
	l	w	t		Dent	FC	Dela	Stress	Strain	Force
	[mm]	[mm]	[mm]	[J]	[mm]	[mm]	[mm^2]	[MPa]	[με]	[kN]
CAI-TC2-05	150.0	100.0	4.15	30	0.28	7	856	305.5	6063	126.8
CAI-TC2-06	150.0	100.0	4.13	30	0.31	30	753	285.6	5667	117.9
CAI-TC2-07†	150.0	100.0	4.14	30	0.32	30	929	277.1	5499	114.7
CAI-TC2-08†	150.0	100.0	4.10	30	0.29	10	753	319.9	6349	131.2
average	150.0	100.0	4.13	30	0.30	19	823	297.0	5894	122.7
CoV [%]	0.0	0.0	0.5	0.0	6.1	64.5	10.4	6.5	6.5	6.2

Table D.3.: Impact and residual strength parameters for specimens impacted at 30J; † denotes DIC monitored tests.

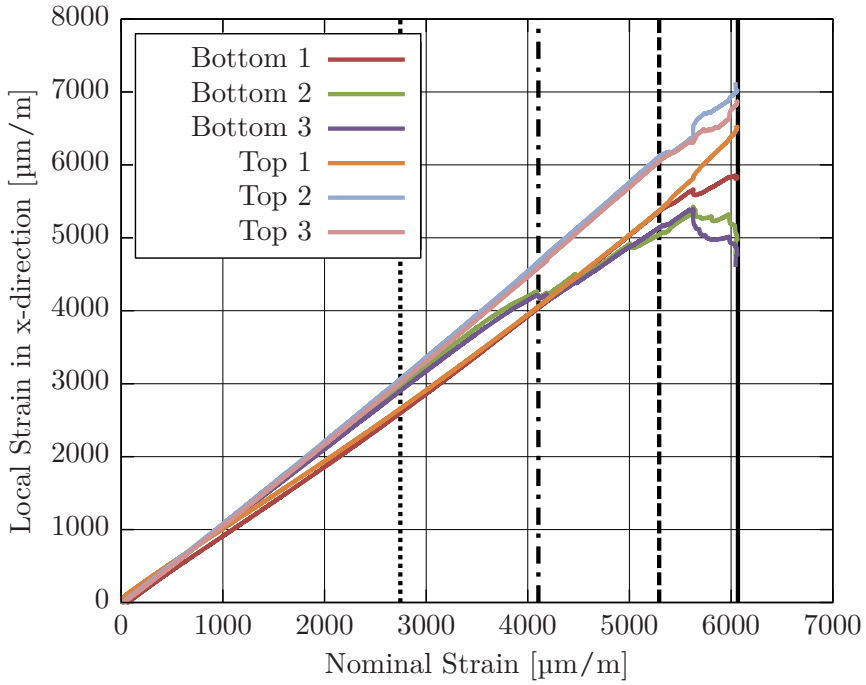

Figure D.11.: Experimental local strains versus nominal strain (TC2-CAI-05). Dotted line: sub-laminate buckling onset at 2700 µm/m; dot-dashed line: strain jumps suggest multiple stacks experiencing buckling (4100 µm/m); dashed line: strain divergence noticed at sampling position 1 indicates global buckling (5300 µm/m); solid line: ultimate failure (6063 µm/m).

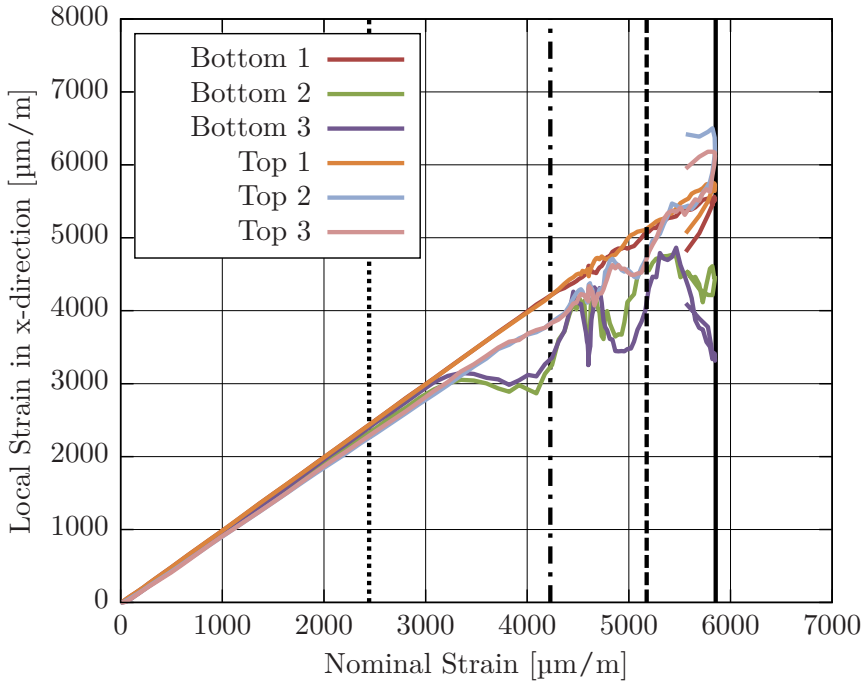

Figure D.12.: Simulated local strains versus nominal strain (TC2-CAI-05). Dotted line: sub-laminate buckling onset at 2400 µm/m; dot-dashed line: slight strain divergence at position 1, possibly associated to multiple stacks experiencing buckling (4100 µm/m); dashed line: denotes buckling onset in all stacks (c.f. figure D.13) (5200 µm/m); solid line: ultimate failure (5849 µm/m).

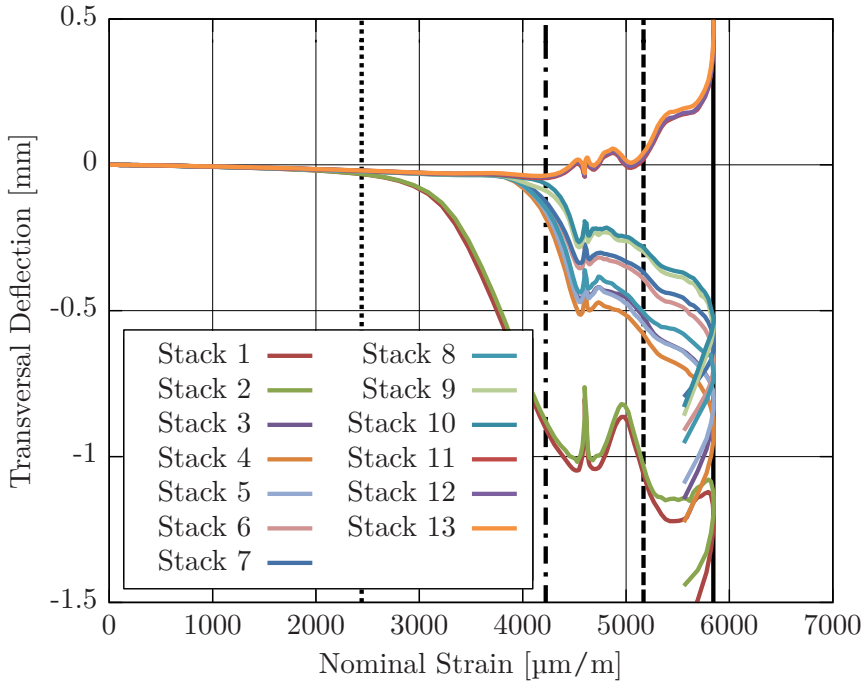

Figure D.13.: Simulated transversal stack deflections at the specimen center versus nominal strain (TC2-CAI-05). Dotted line: sub-laminate buckling onset at 2400 µm/m; dot-dashed line: multiple stack buckling (4100 µm/m); dashed line: all stacks undergoing buckling (5200 µm/m); solid line: ultimate failure (5849 µm/m).

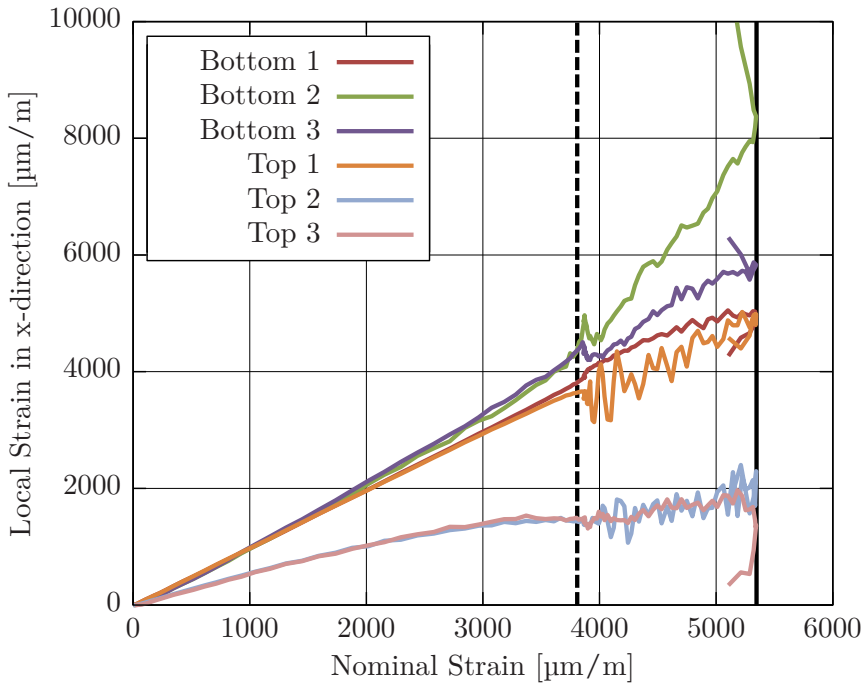

Figure D.14.: Simulated local strains versus nominal strain (TC2-CAI-07). Dashed line: strain divergence suggests buckling in all stacks (3900 µm/m); solid line: ultimate failure (5344 µm/m).

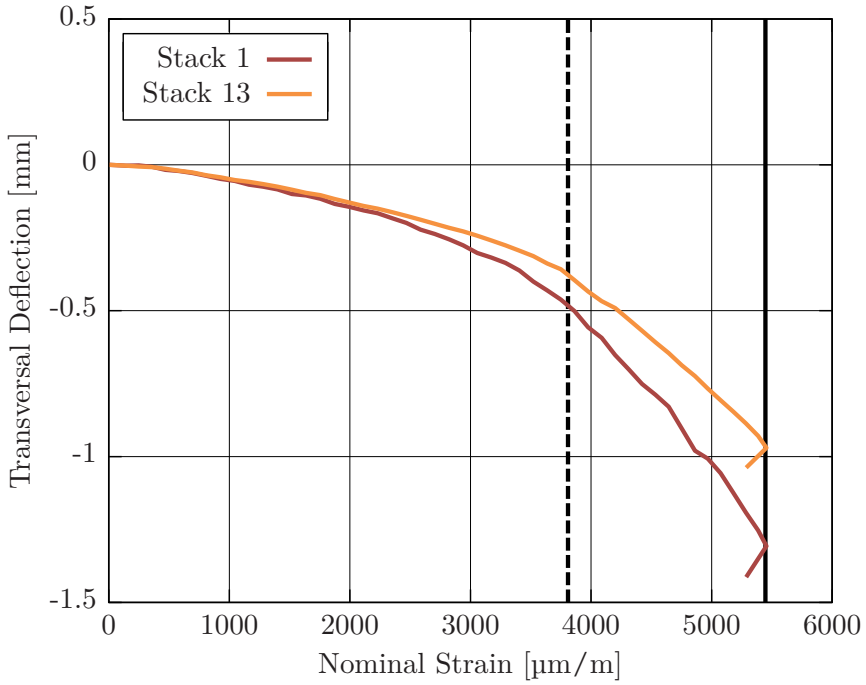

Figure D.15.: Experimental transversal stack deflections at the specimen center versus nominal strain (TC2-CAI-07). Dashed line: deflection rate change hints at buckling in all stacks (3800 µm/m); solid line: ultimate failure (5499 µm/m).

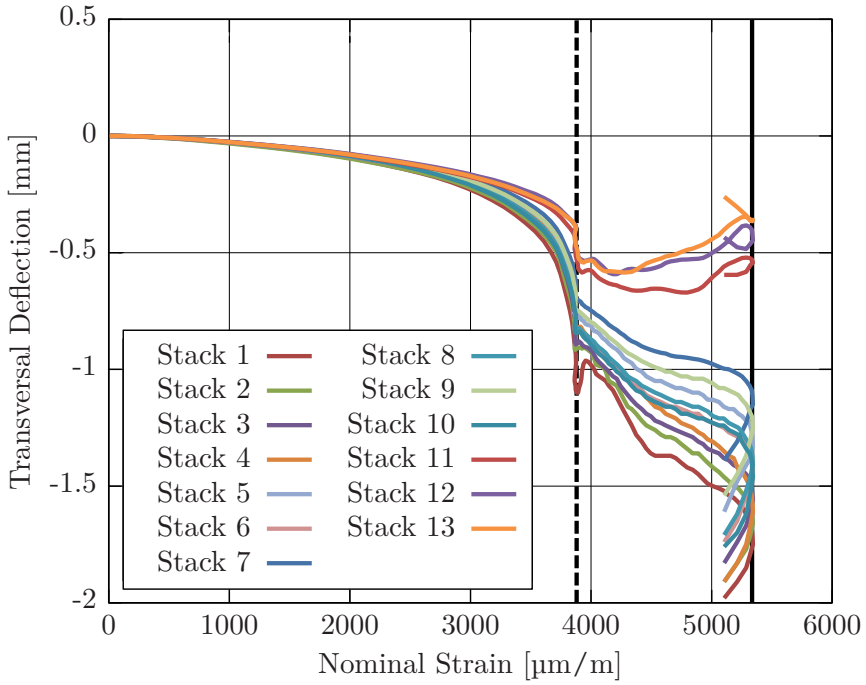

Figure D.16.: Simulated transversal stack deflections at the specimen center versus nominal strain (TC2-CAI-07). Dashed line: buckling in all stacks (3800 µm/m); solid line: ultimate failure (5499 µm/m).

D.4. Impacted Coupons at 40 J

Specimen Label	Dimensions			Impact Energy	Damage Parameters			Residual Properties		
	l	w	t		Dent	FC	Dela	Stress	Strain	Force
	[mm]	[mm]	[mm]	[J]	[mm]	[mm]	[mm^2]	[MPa]	[με]	[kN]
CAI-TC1-01†	150.1	100.1	4.15	40	0.67	53	1317	274.0	5438	113.8
CAI-TC1-02†	150.1	100.1	4.18	40	0.48	52	1219	277.9	5514	116.3
CAI-TC1-03†	150.0	100.0	4.19	40	0.69	47	1397	260.7	5174	109.2
CAI-TC1-04	150.0	100.0	4.15	40	0.68	52	1333	Not available		
CAI-TC1-05	150.0	100.0	4.17	40	0.63	52	1180	Not available		
CAI-TC1-07	150.1	100.0	4.16	40	0.55	51	1212	Not available		
CAI-TC1-08	150.0	100.0	4.16	40	0.42	54	1257	277.3	5503	115.4
CAI-TC1-09	150.0	100.0	4.18	40	0.52	55	1117	265.3	5264	110.9
CAI-TC1-10	150.0	100.0	4.18	40	0.54	55	1211	276.0	5478	115.4
CAI-TC1-12	150.1	100.0	4.16	40	0.66	53	1442	244.9	4860	101.9
CAI-TC1-13	150.0	100.0	4.16	40	0.68	48	1174	266.4	5286	110.8
average	150.0	100.0	4.17	40	0.59	52	1260	267.8	5315	111.7
CoV [%]	0.0	0.0	0.3	0.0	15.9	4.3	8.0	4.2	4.2	4.2

Table D.4.: Impact and residual strength parameters for specimens impacted at 40J; † denotes DIC monitored tests.

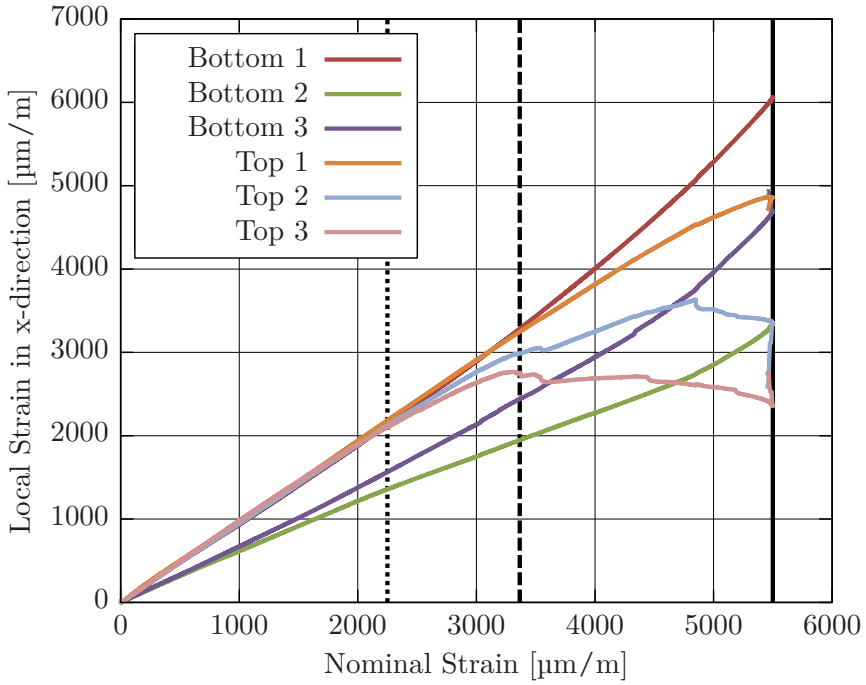

Figure D.17.: Experimental local strains versus nominal strain (TC1-CAI-08). Dotted line: Strain alleviation at the top center region, possibly due to crest formation at the fiber crack (2200 µm/m); dashed line: strain divergence at sampling position 1 indicates significant transversal deflection (3400 µm/m); solid line: ultimate failure (5503 µm/m).

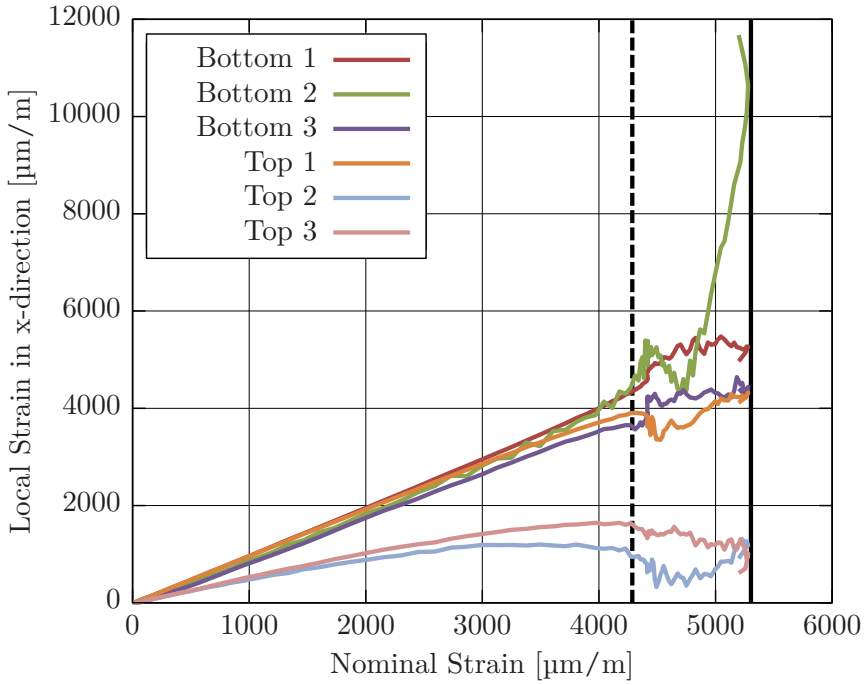

Figure D.18.: Simulated local strains versus nominal strain (TC1-CAI-08). Dashed line: strain jumps at all sampling positions imply global buckling (4300 µm/m); solid line: ultimate failure (5282 µm/m).

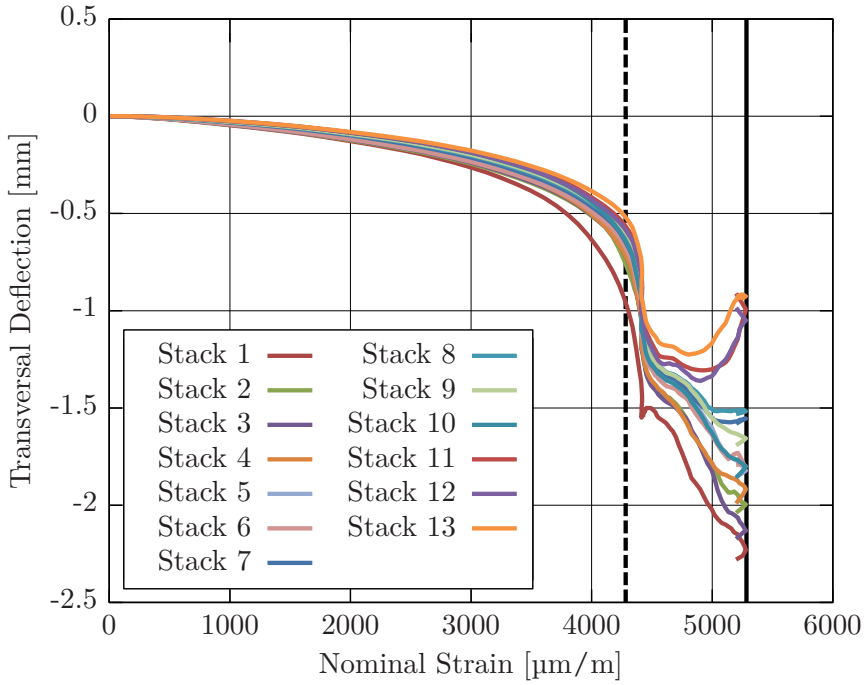

Figure D.19.: Simulated transversal stack deflections at the specimen center versus nominal strain (TC1-CAI-08). Transversal deflection over the entire loading history. Dashed line: buckling of all stacks (4300 µm/m); solid line: ultimate failure (5282 µm/m).

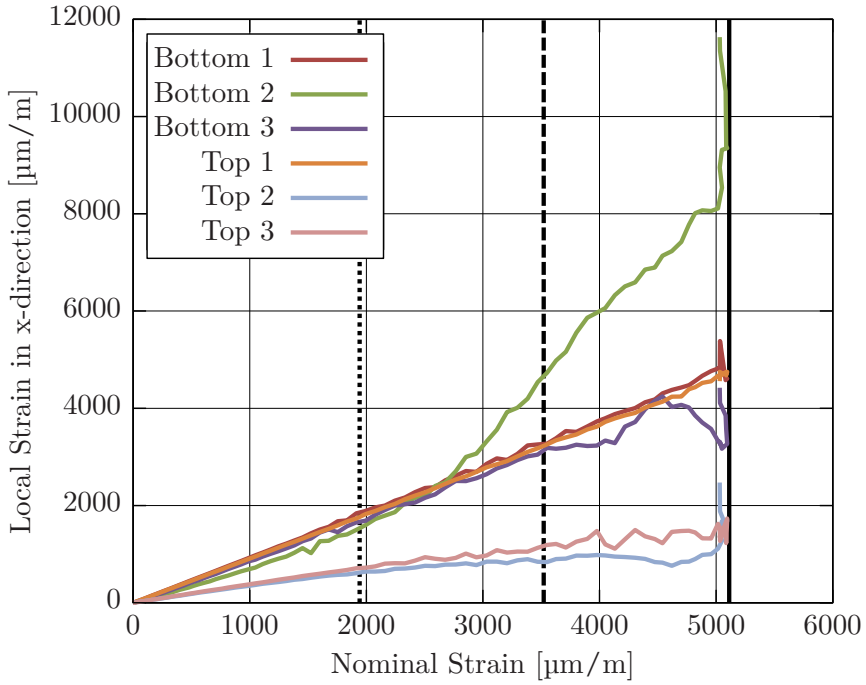

Figure D.20.: Simulated local strains versus nominal strain (TC1-CAI-03). Dotted line: separation of bottom stacks from the main laminate at 1900 µm/m; dashed line: increased deflection rate (3500 µm/m); solid line: ultimate failure (5111 µm/m).

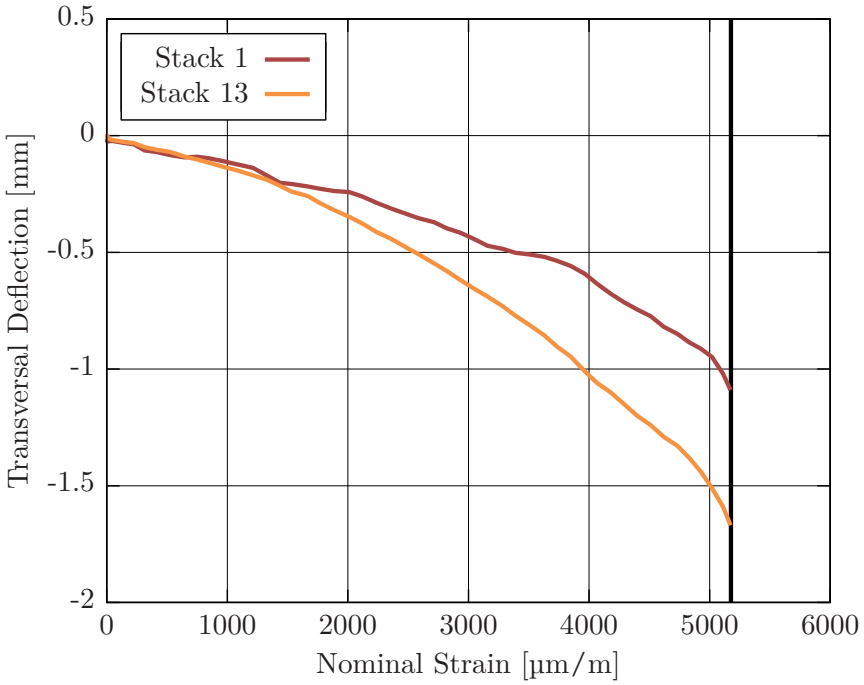

Figure D.21.: Experimental transversal stack deflections at the specimen center versus nominal strain (TC1-CAI-03). Transversal deflection over the entire loading history indicated by the non-linear progression. Solid line: ultimate failure (5174 µm/m).

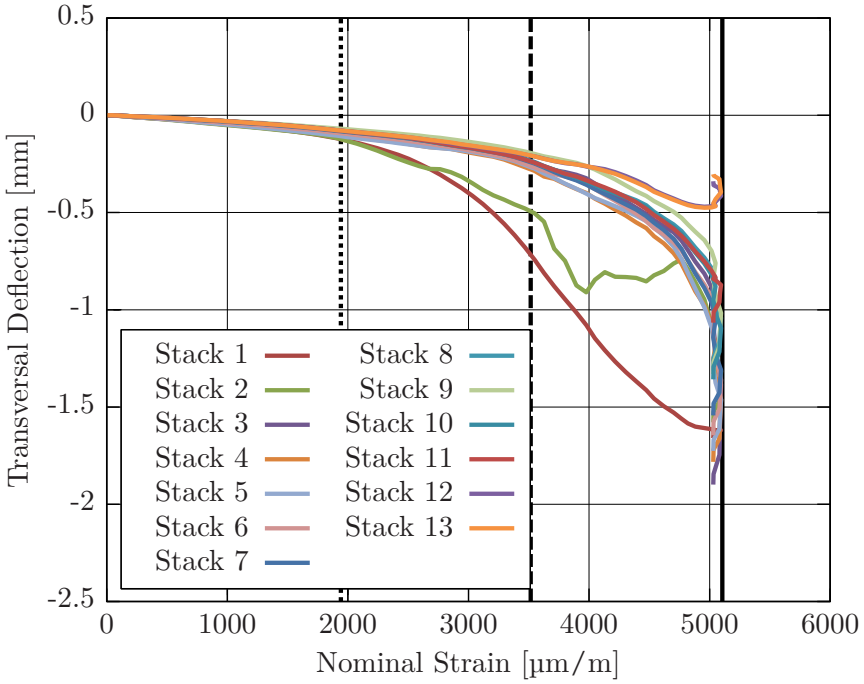

Figure D.22.: Simulated transversal stack deflections at the specimen center versus nominal strain (TC1-CAI-03). Dotted line: separation of bottom stacks from the main laminate at 1900 µm/m; dashed line: increased deflection rate (3500 µm/m); solid line: ultimate failure (5111 µm/m).

D.5. Impacted Coupons at 50 J

Specimen Label	Dimensions			Impact Energy	Damage Parameters			Residual Properties		
	l	w	t		Dent	FC	Dela	Stress	Strain	Force
	[mm]	[mm]	[mm]	[J]	[mm]	[mm]	[mm^2]	[MPa]	[µε]	[kN]
CAI-TC2-09	150.0	100.0	4.13	50	0.98	57	1664	254.3	5046	105.0
CAI-TC2-10	150.0	100.0	4.13	50	0.89	58	1799	257.8	5117	106.5
CAI-TC2-11†	150.0	100.0	4.12	50	0.92	54	1914	245.0	4862	100.9
CAI-TC2-12†	150.0	100.0	4.12	50	0.95	53	1844	242.7	4816	100.0
average	150.0	100.0	4.13	50	0.94	56	1805	250.0	4960	103.1
CoV [%]	0.0	0.0	0.1	0.0	4.1	4.3	5.8	2.9	2.9	3.0

Table D.5.: Impact and residual strength parameters for specimens impacted at 50J; † denotes DIC monitored tests.

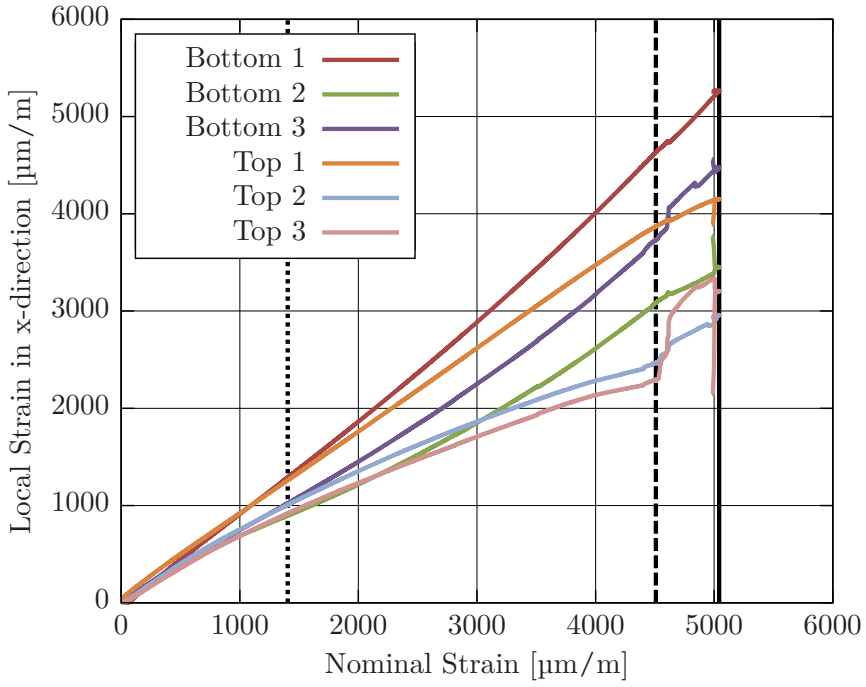

Figure D.23.: Experimental local strains versus nominal strain (TC2-CAI-09). Dotted line: diverging strains hint at increasing transversal deflection rates (1400 µm/m); dashed line: strain jumps point to significant buckling (4500 µm/m); solid line: ultimate failure (5046 µm/m).

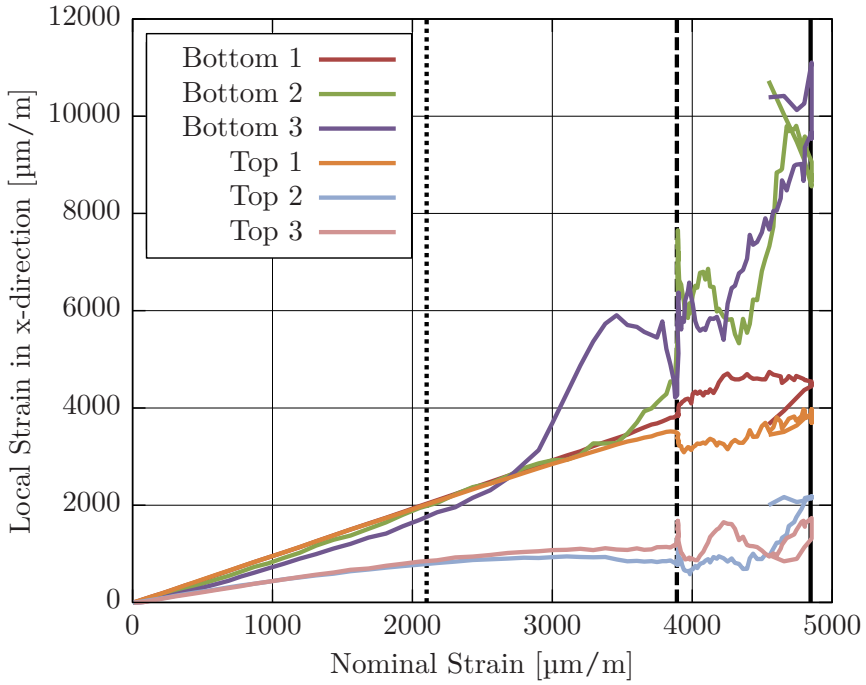

Figure D.24.: Simulated local strains versus nominal strain (TC2-CAI-09). Dotted line: separating sub-laminates signalized by strain divergence at the center (2100 µm/m); dashed line: significant strain jumps point to buckling of all stacks (3900 µm/m); solid line: ultimate failure (4848 µm/m).

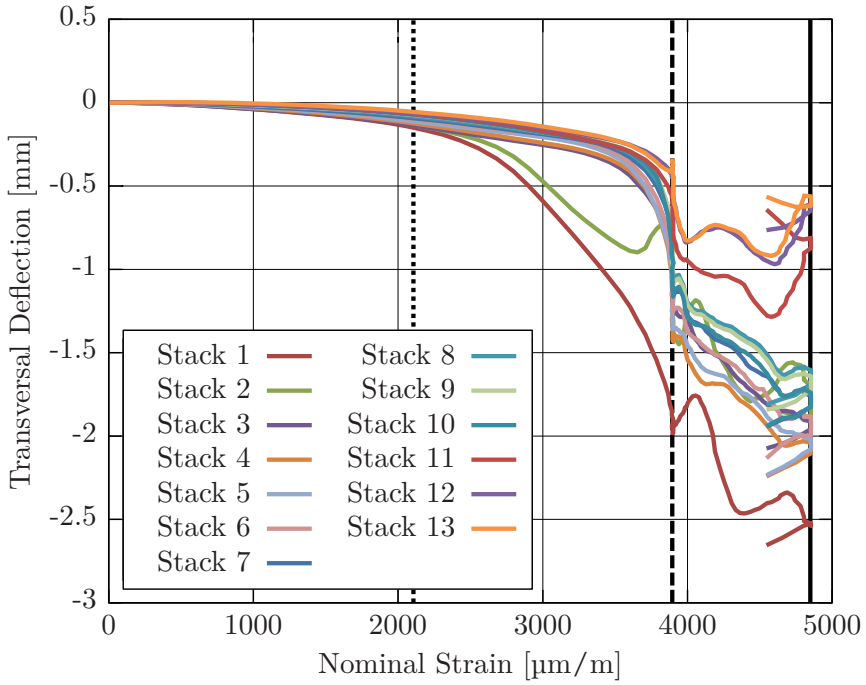

Figure D.25.: Simulated transversal stack deflections at the specimen center versus nominal strain (TC2-CAI-09). Dotted line: sub-laminate separation onset (2100 µm/m); dashed line: buckling of all stacks (3900 µm/m); solid line: ultimate failure (4848 µm/m).

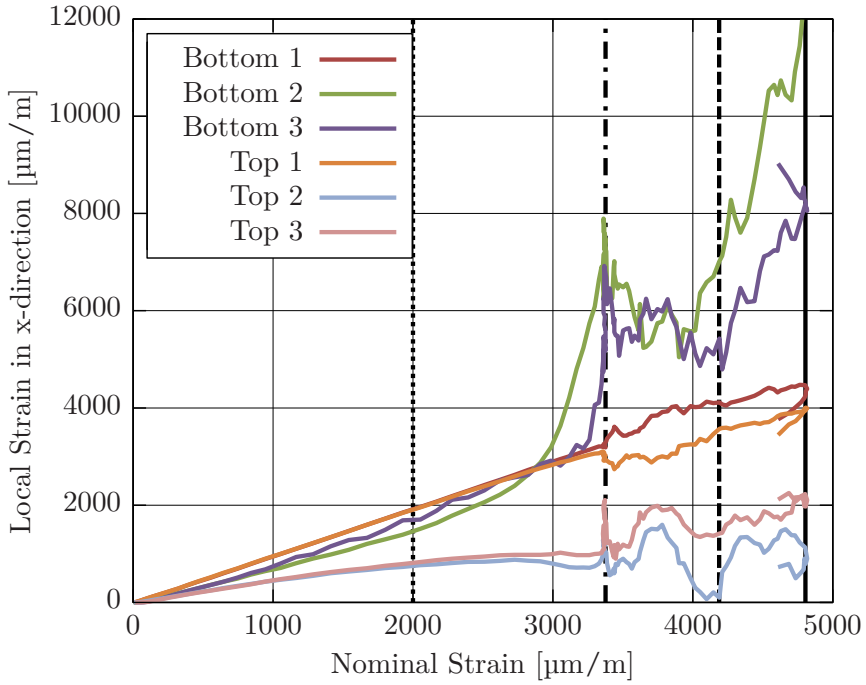

Figure D.26.: Simulated local strains versus nominal strain (TC2-CAI-12). Dotted line: diverging strains hint at separating sub-laminates (2000 µm/m); dot-dashed line: strain jumps point to considerable buckling (3400 µm/m); dashed line: second jump points to buckling mode-shift (4200 µm/m); solid line: ultimate failure (4818 µm/m).

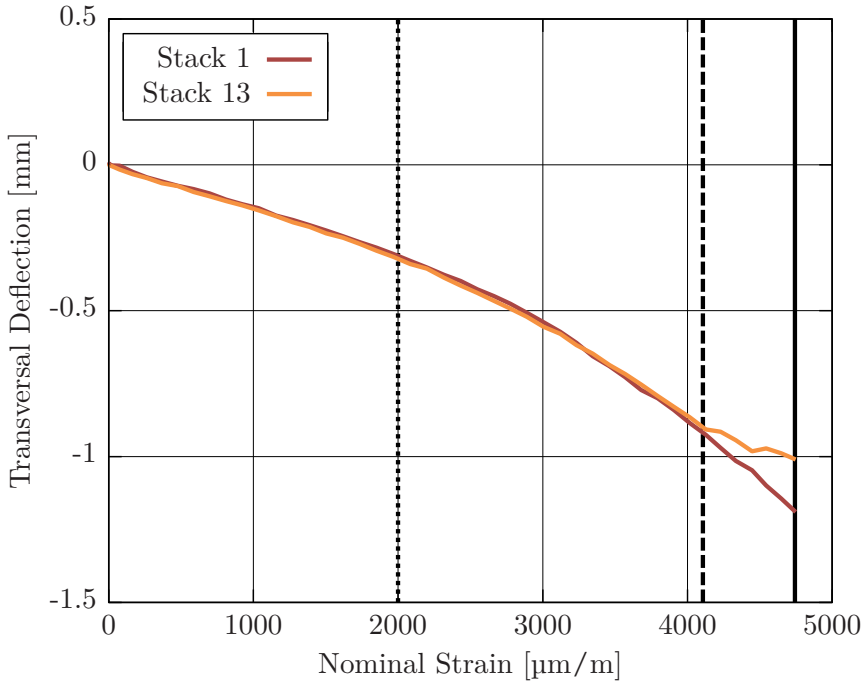

Figure D.27.: Experimental transversal stack deflections at the specimen center versus nominal strain (TC2-CAI-12). Dotted line: increasing non-linearity points to transversal deflection (2000 µm/m); dashed line: sub-laminate buckling (4100 µm/m); solid line: ultimate failure (4816 µm/m).

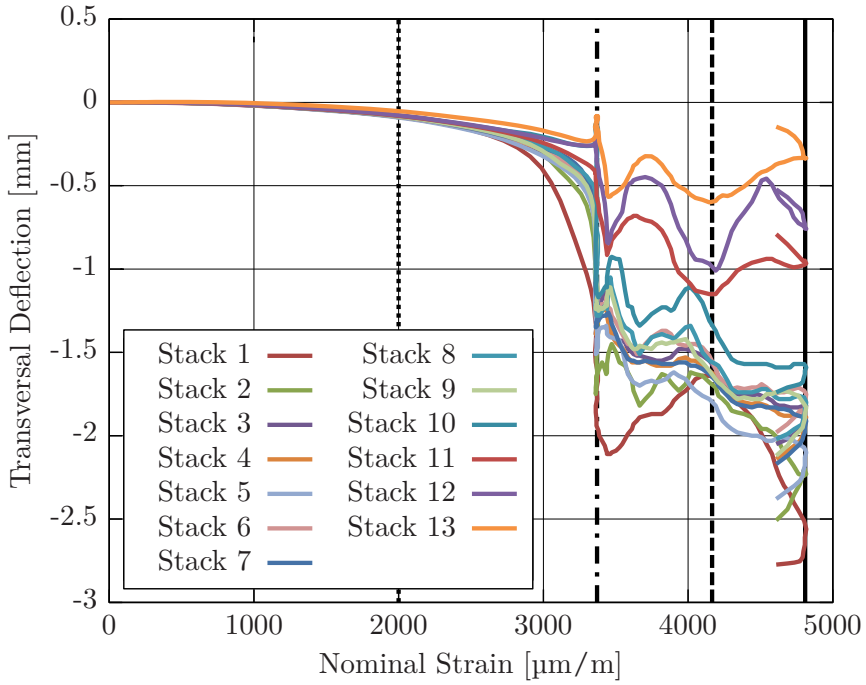

Figure D.28.: Simulated transversal stack deflections at the specimen center versus nominal strain (TC2-CAI-12). Dotted line: separating sub-laminates (2000 µm/m); dot-dashed line: considerable buckling (3400 µm/m); dashed line: buckling mode-shift (4200 µm/m); solid line: ultimate failure (4818 µm/m).

E Artificial Damage and Residual Strength Test Results

In this appendix, experimental and simulation results are presented for artificially damaged specimens. For each damage configuration, the coupons' geometrical, damage, and residual properties are listed. As before, a statistical evaluation is added at the tables' bottom. The coupon describing parameters are its geometric dimensions (length, width, and thickness), damage parameters (maximum fiber crack length and delamination envelope area), and residual properties (nominal failure stress, nominal failure strain, and failure load). The artificially introduced defects are listed in table 3.2.

In consistency with the layup model and the respective coordinate system presented in figure 3.5, the defects included in the following models are located at (or close to) the bottom surface. Similarly to the impacted specimens, the symbol † identifies coupons monitored using DIC.

E.1. Artificially Delaminated Coupons: A-Series

Specimen Label	Dimensions			Damage Parameters		Residual Properties		
	l	w	t	FC	Dela	Stress	Strain	Force
	[mm]	[mm]	[mm]	[mm]	[mm^2]	[MPa]	[µε]	[kN]
CAI-TC2-A1†	150.0	100.0	4.17	0	1965	427.2	8478	178.2
CAI-TC2-A2	150.0	100.0	4.19	0	2000	423.4	8402	177.4
CAI-TC2-A3	150.0	100.0	4.20	0	1975	446.3	8856	187.4
CAI-TC2-A5†	150.0	100.0	4.14	0	N/A	433.0	8593	179.3
average	150.0	100.0	4.17	0	1987	432.5	8583	180.6
CoV [%]	0.0	0.0	0.6	0.0	1.0	2.3	2.3	2.6

Table E.1.: Artificial defect and residual strength parameters for A-type damaged specimens; † denotes DIC monitored tests.

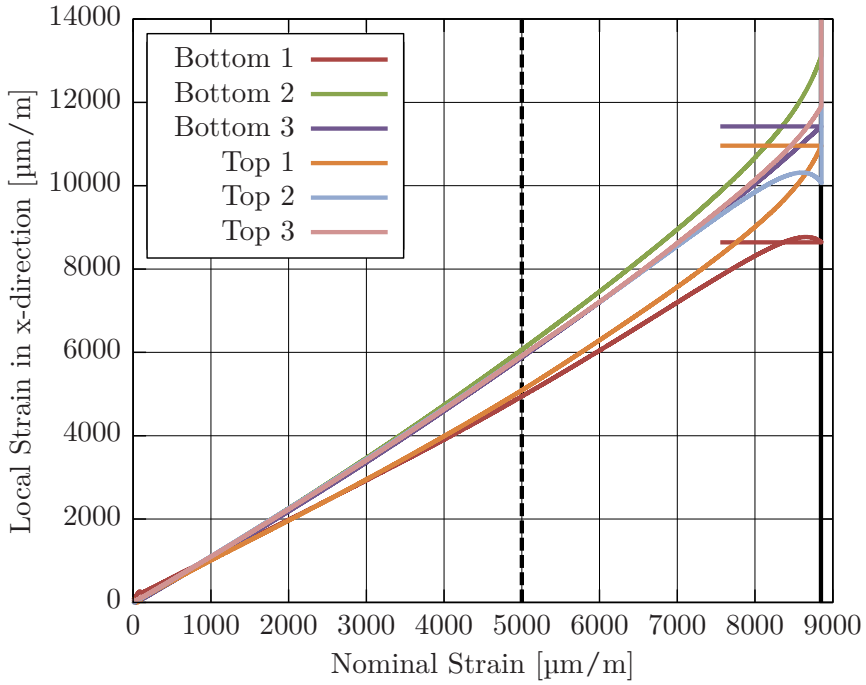

Figure E.1.: Experimental local strains versus nominal strain (TC2-CAI-A3). Dashed line: strain divergence in all positions suggests transversal deflection in both sub-laminates (5000 µm/m); solid line: ultimate failure (8856 µm/m).

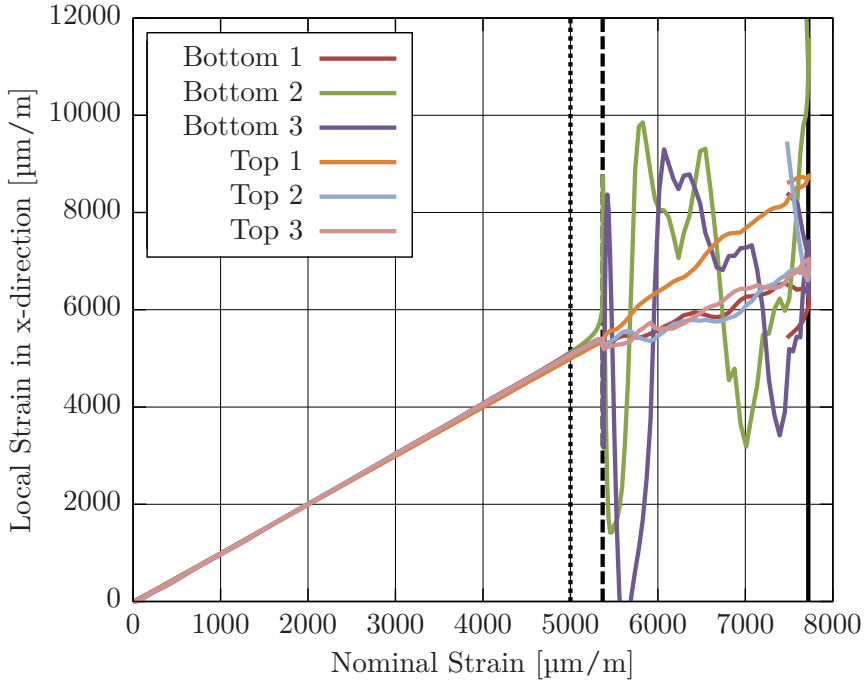

Figure E.2.: Simulated local strains versus nominal strain (TC2-CAI-A3). Dotted line: diverging strains at the center hint at sub-laminate deflection onset (5000 µm/m); dashed line: strain divergence at position 1 suggests buckling in both sub-laminates (5300 µm/m); solid line: ultimate failure (7727 µm/m).

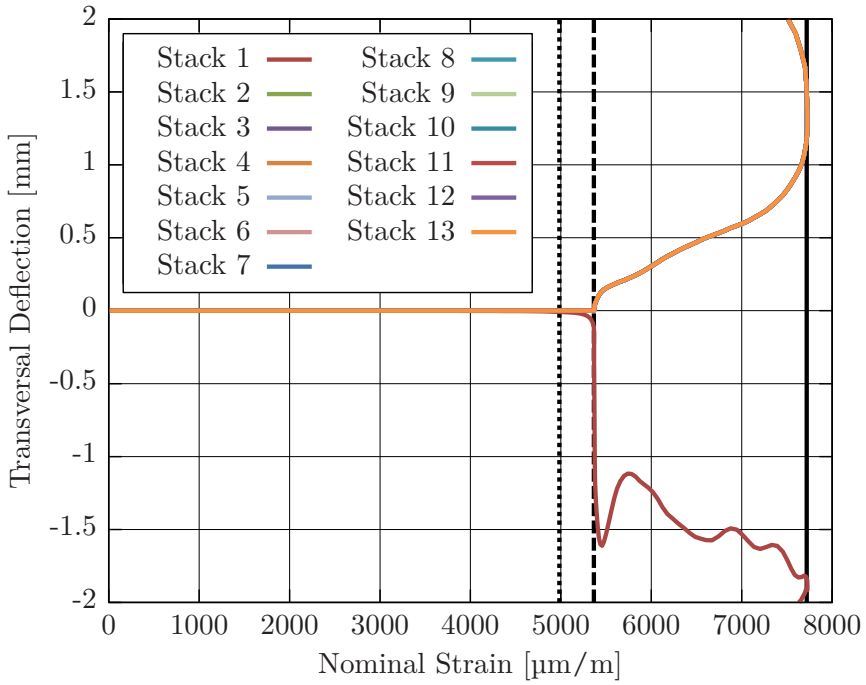

Figure E.3.: Simulated transversal stack deflections at the specimen center versus nominal strain (TC2-CAI-A3). Dotted line: transversal deflection of the bottom sub-laminate (5000 µm/m); dashed line: buckling in both sub-laminates (5300 µm/m); solid line: ultimate failure (7727 µm/m).

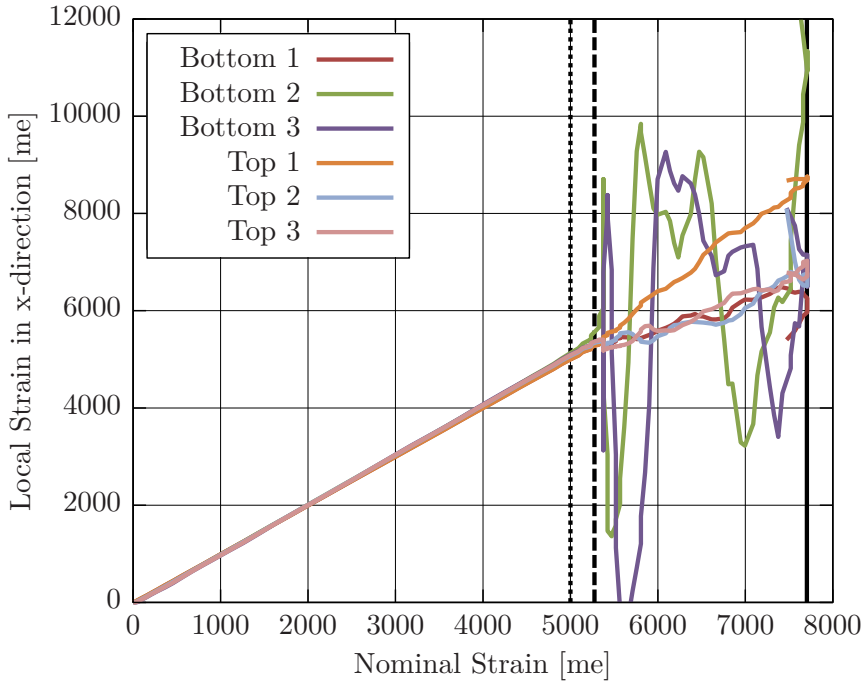

Figure E.4.: Simulated local strains versus nominal strain (TC2-CAI-A1). Dotted line: diverging strains at the center hint at sub-laminate deflection onset (5000 µm/m); dashed line: strain divergence at position 1 suggests buckling in both sub-laminates (5300 µm/m); solid line: ultimate failure (7704 µm/m).

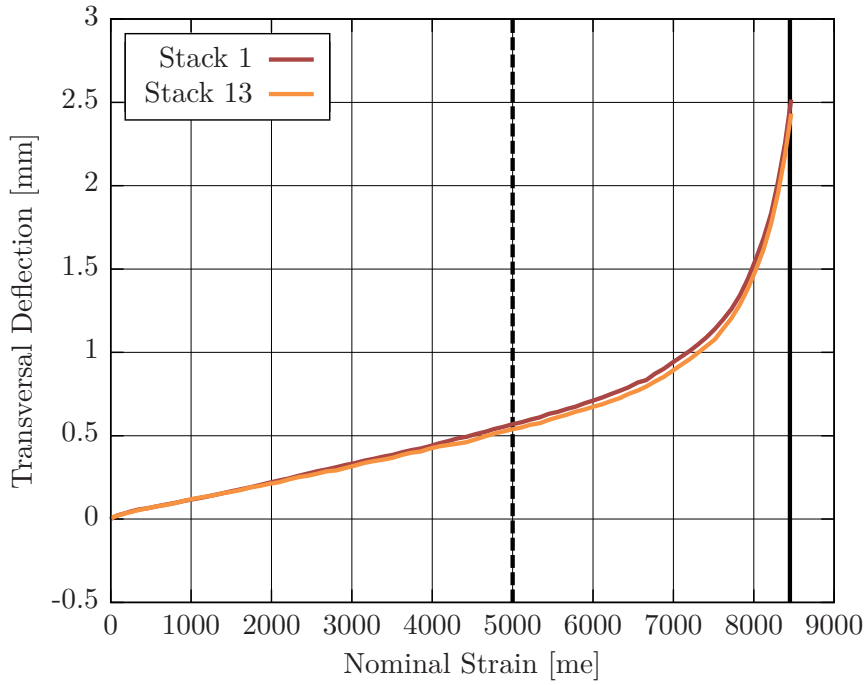

Figure E.5.: Experimental transversal stack deflections at the specimen center versus nominal strain (TC2-CAI-A1). Dashed line: non-linear curve progression in the same direction point to transversal deflections of both sub-laminates (5300 µm/m); solid line: ultimate failure (8478 µm/m).

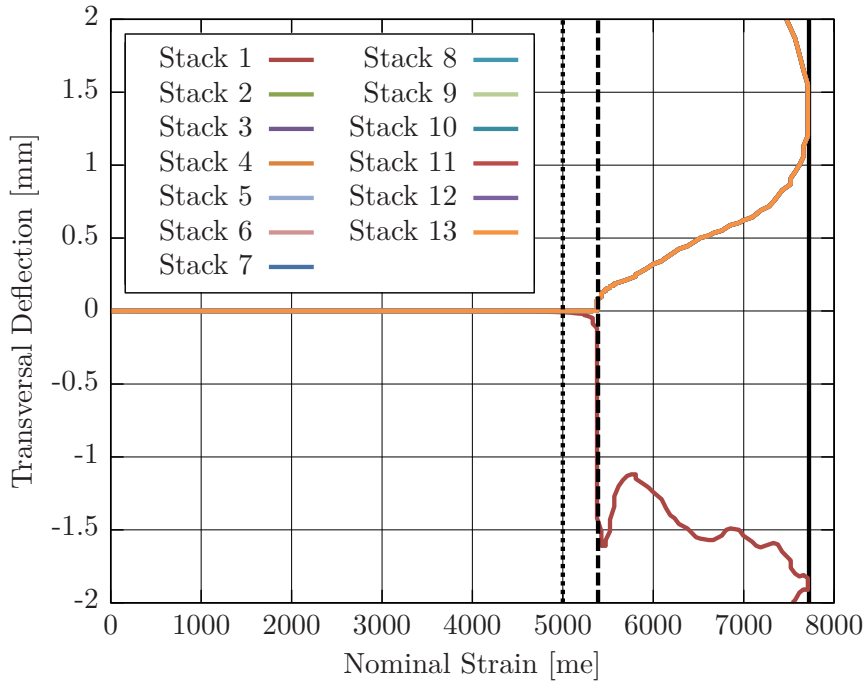

Figure E.6.: Simulated transversal stack deflections at the specimen center versus nominal strain (TC2-CAI-A1). Dotted line: deflection onset of the bottom sub-laminate (5000 µm/m); dashed line: buckling in both sub-laminates (5300 µm/m); solid line: ultimate failure (7704 µm/m).

E.2. Artificially Delaminated Coupons: B-Series

Specimen Label	Dimensions			Damage Parameters		Residual Properties		
	l	w	t	FC	Dela	Stress	Strain	Force
	[mm]	[mm]	[mm]	[mm]	[mm^2]	[MPa]	[µε]	[kN]
CAI-TC2-B1	150.0	100.0	4.17	0	2058	270.9	5377	113.0
CAI-TC2-B2	149.9	100.0	4.17	0	2046	276.6	5489	115.3
CAI-TC2-B4†	149.9	100.0	4.15	0	2059	293.0	5815	121.6
CAI-TC2-B5†	149.9	100.0	4.18	0	2068	291.7	5789	121.9
average	149.9	100.0	4.17	0	2058	283.1	5618	118.0
CoV [%]	0.0	0.0	0.3	0.0	0.4	3.9	3.9	3.8

Table E.2.: Artificial defect and residual strength parameters for B-type damaged specimens; † denotes DIC monitored tests.

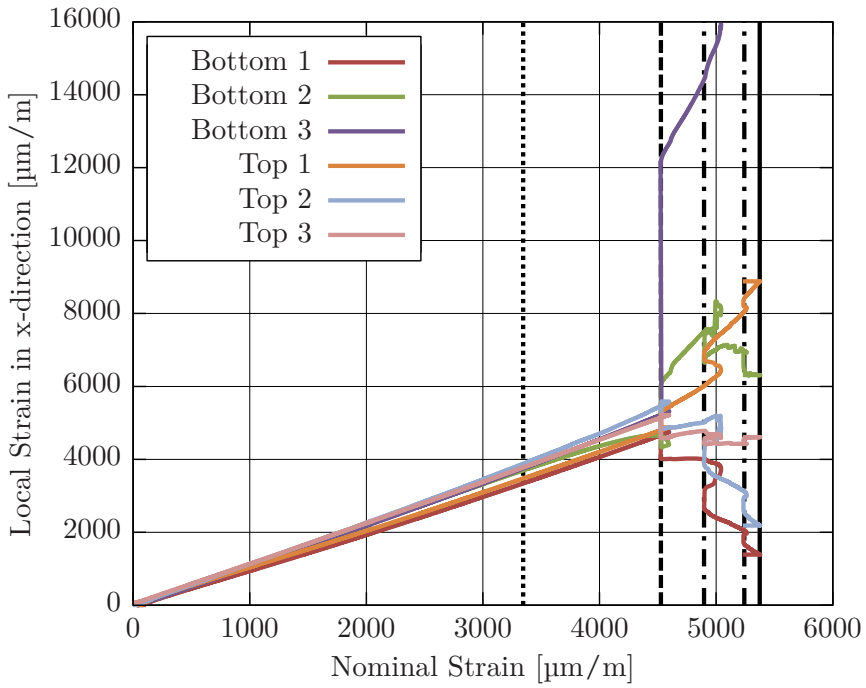

Figure E.7.: Experimental local strains versus nominal strain (TC2-CAI-B1). Dotted line: divergence at positions 2 and 3 indicates slight transversal deflections, beginning at 3300 µm/m; dashed line: strain jumps in all positions suggests buckling in both sub-laminates (4500 µm/m); dot-dashed lines: strain jumps indicating mode-shifts 4900 µm/m and 5200 µm/m; solid line: ultimate failure (5377 µm/m).

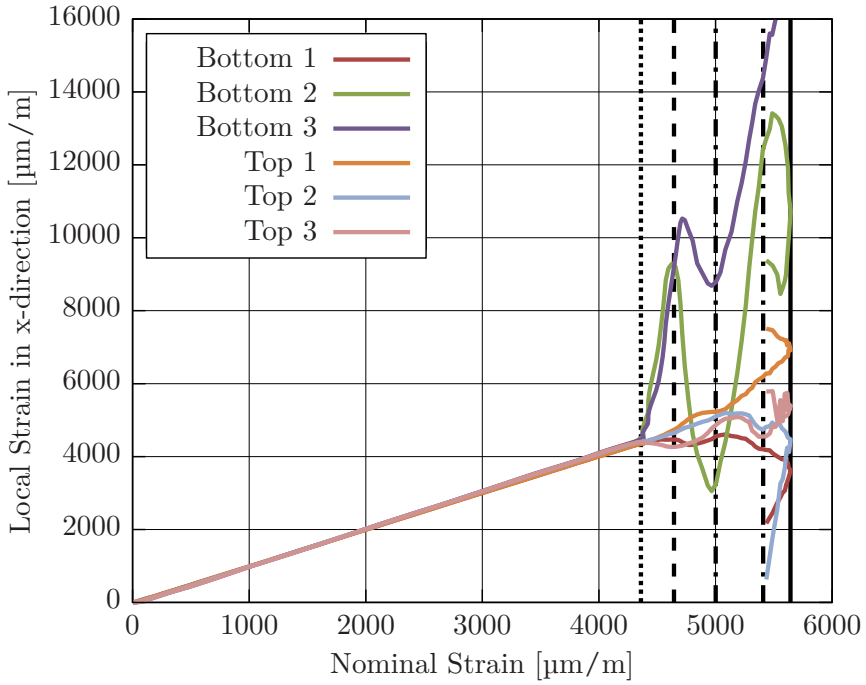

Figure E.8.: Simulated local strains versus nominal strain (TC2-CAI-B1). Dotted line: strong divergence at positions 2 and 3 indicates buckling onset at 4400 µm/m; dashed line: divergence in all positions suggests buckling in both sub-laminates (4600 µm/m); dot-dashed lines: strain jumps indicating mode-shifts 5000 µm/m and 5400 µm/m; solid line: ultimate failure (5644 µm/m).

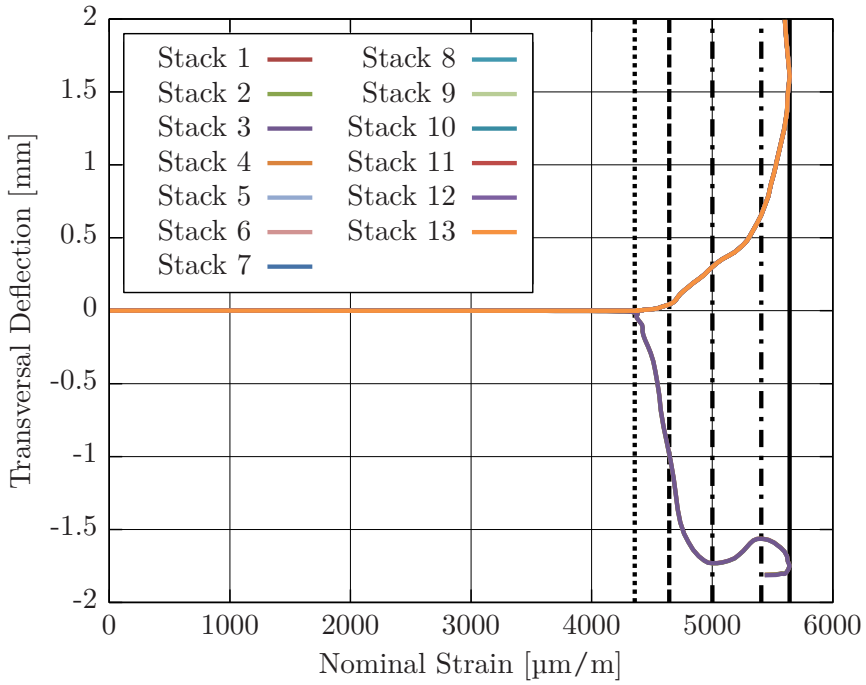

Figure E.9.: Simulated transversal stack deflections at the specimen center versus nominal strain (TC2-CAI-B1). Dotted line: thinner sub-laminate buckles at 4400 µm/m; dashed line: buckling in both sub-laminates (4600 µm/m); dot-dashed lines: mode-shifts 5000 µm/m and 5400 µm/m; solid line: ultimate failure (5644 µm/m).

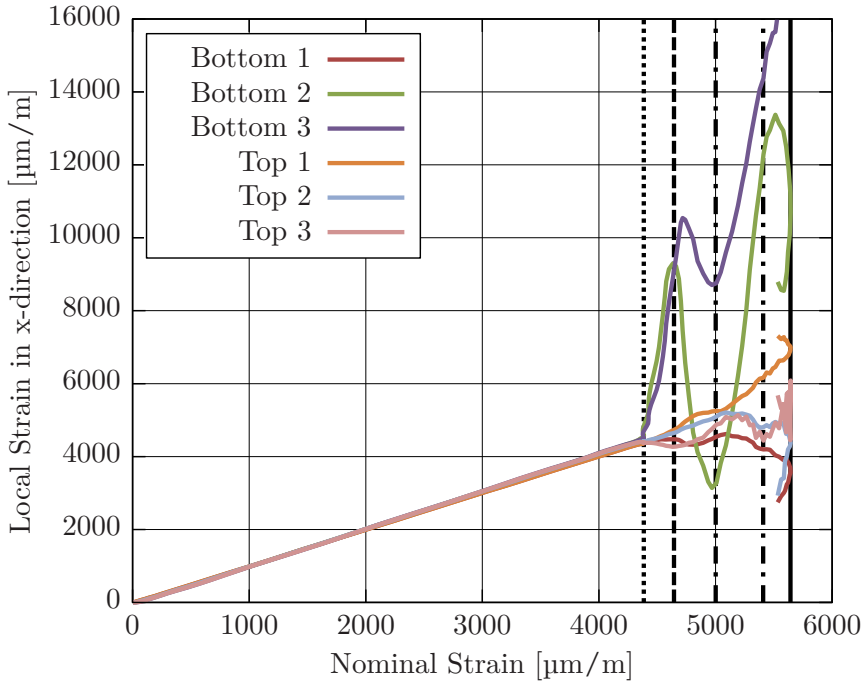

Figure E.10.: Simulated local strains versus nominal strain (TC2-CAI-B5). Dotted line: strong divergence at positions 2 and 3 indicates buckling onset at 4400 µm/m; dashed line: divergence in all positions suggests buckling in both sub-laminates (4600 µm/m); dot-dashed lines: strain jumps indicating mode-shifts 5000 µm/m and 5400 µm/m; solid line: ultimate failure (5647 µm/m).

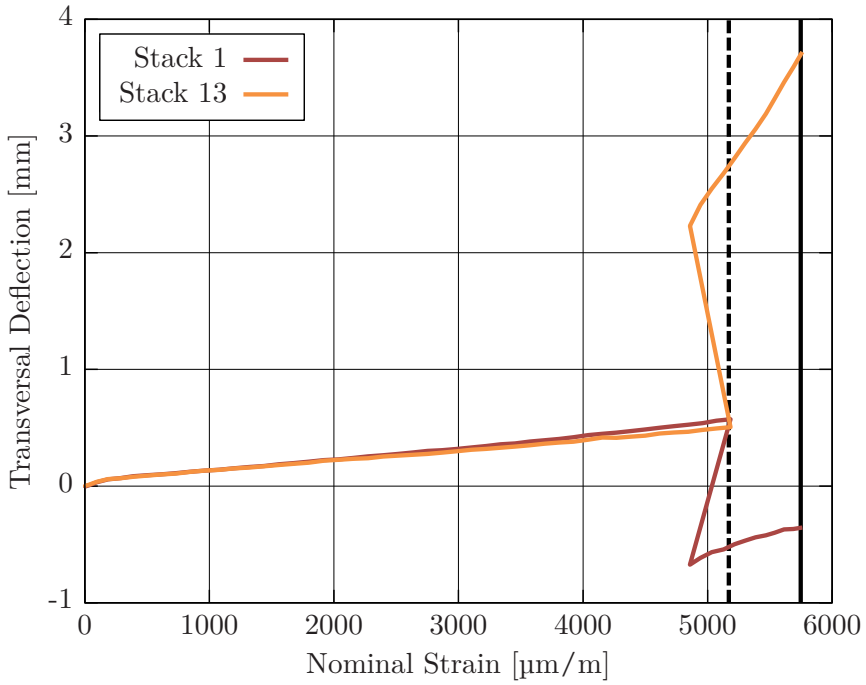

Figure E.11.: Experimental transversal stack deflections at the specimen center versus nominal strain (TC2-CAI-B5). Dashed line: snap-through buckling in both sub-laminates in opposite directions (5200 µm/m); solid line: ultimate failure (5789 µm/m).

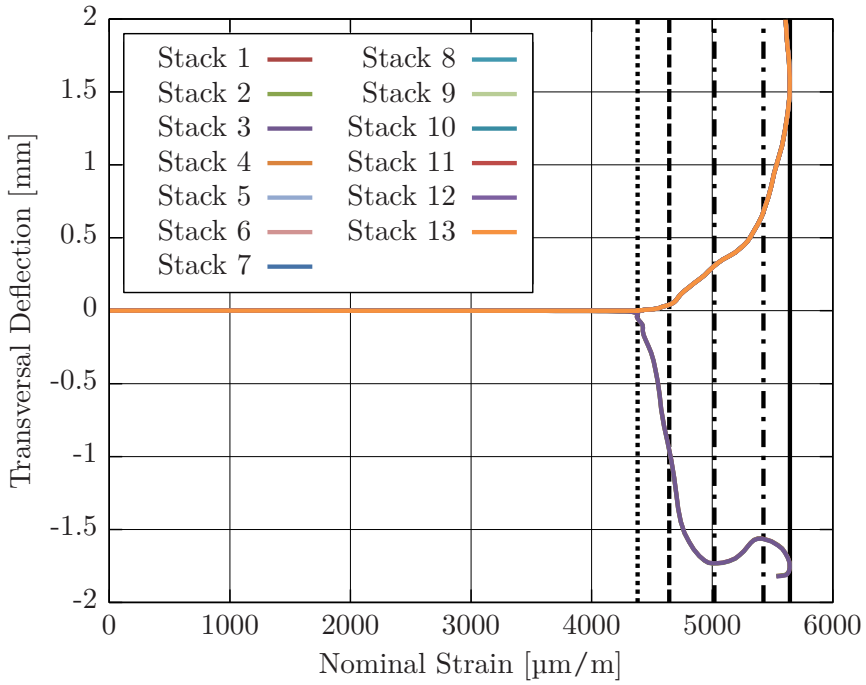

Figure E.12.: Simulated transversal stack deflections at the specimen center versus nominal strain (TC2-CAI-B5). Dotted line: thinner sub-laminate buckles at 4400 µm/m; dashed line: buckling in both sub-laminates (4600 µm/m); dot-dashed lines: mode-shifts 5000 µm/m and 5400 µm/m; solid line: ultimate failure (5647 µm/m).

E.3. Artificially Delaminated Coupons: C-Series

Specimen Label	Dimensions			Damage Parameters		Residual Properties		
	l	w	t	FC	Dela	Stress	Strain	Force
	[mm]	[mm]	[mm]	[mm]	[mm^2]	[MPa]	[µε]	[kN]
CAI-TC2-C1	150.0	100.0	4.15	25	0	374.5	7432	155.4
CAI-TC2-C2	149.9	100.0	4.15	25	0	379.5	7531	157.5
CAI-TC2-C3	149.9	99.9	4.06	25	0	390.7	7754	158.5
CAI-TC2-C4†	149.9	99.9	4.11	25	0	376.0	7462	154.4
CAI-TC2-C5†	149.9	100.0	4.16	25	0	389.7	7734	162.1
average	149.9	100.0	4.13	25	0	382.1	7583	157.6
CoV [%]	0.0	0.0	1.0	0.0	0.0	2.0	2.0	1.9

Table E.3.: Artificial defect and residual strength parameters for C-type damaged specimens; † denotes DIC monitored tests.

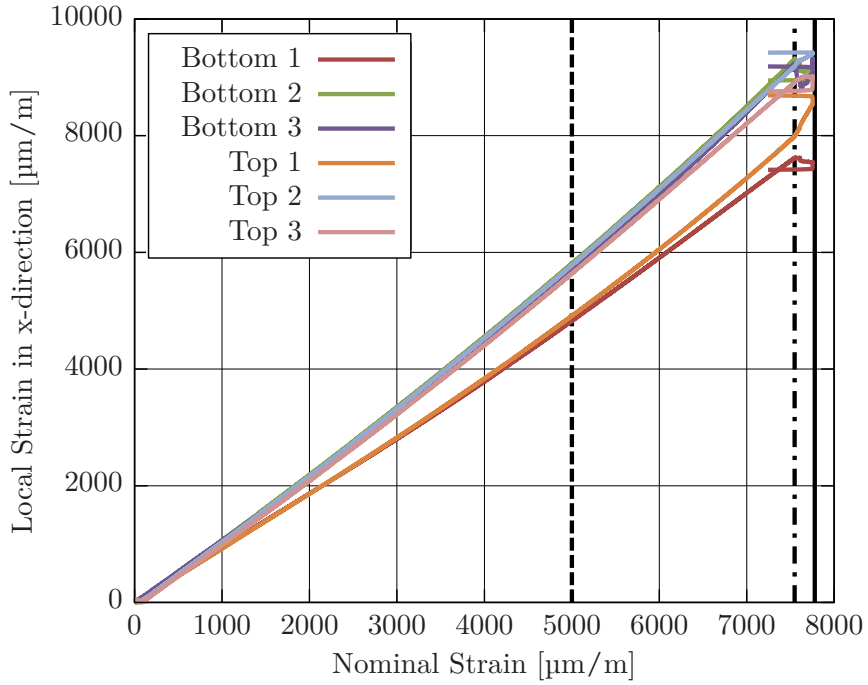

Figure E.13.: Experimental local strains versus nominal strain (TC2-CAI-C3). Dashed line: slight strain divergence points to increasing deflection rate 5000 µm/m; dot-dashed line: strain jumps in all sampling points indicate buckling (7500 µm/m); solid line: ultimate failure (7754 µm/m).

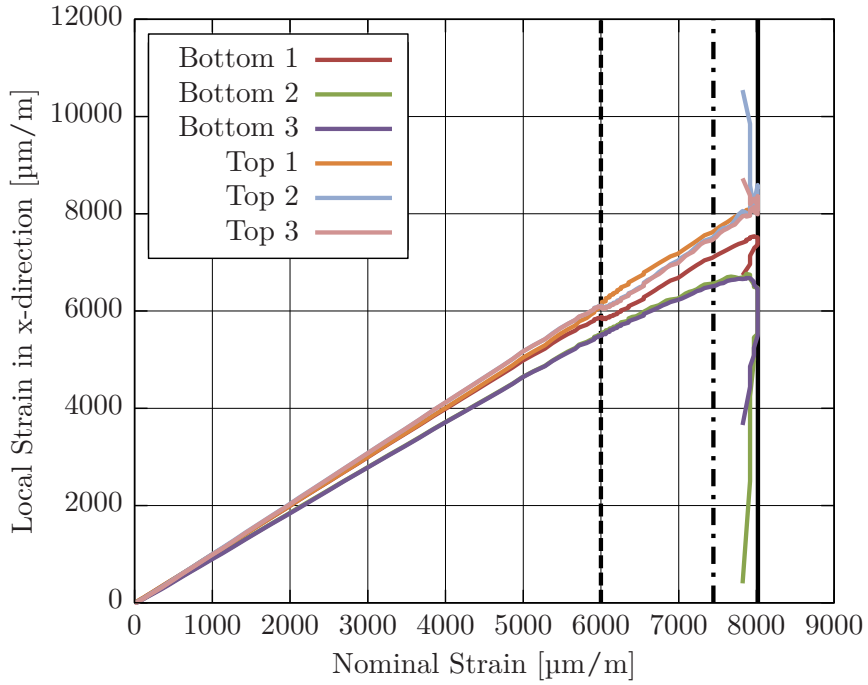

Figure E.14.: Simulated local strains versus nominal strain (TC2-CAI-C3). Dashed line: slight strain jumps imply buckling at 6000 µm/m; dot-dashed line: increasing deflection rate change (7500 µm/m); solid line: ultimate failure (8022 µm/m).

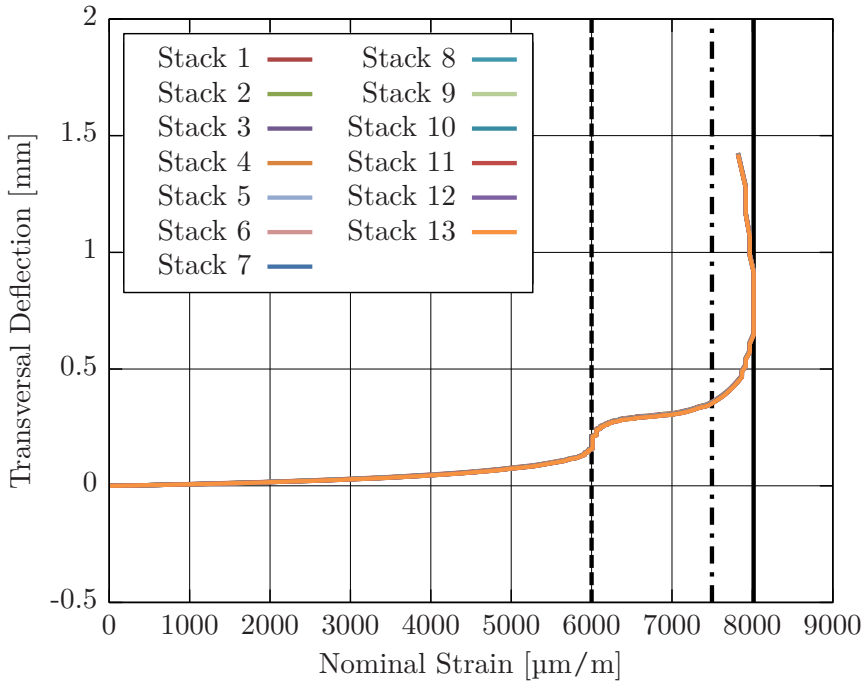

Figure E.15.: Simulated transversal stack deflections at the specimen center versus nominal strain (TC2-CAI-C3). Dashed line: deflection jump implies buckling 6000 µm/m; dot-dashed line: increased deflection rate (7500 µm/m); solid line: ultimate failure (8022 µm/m).

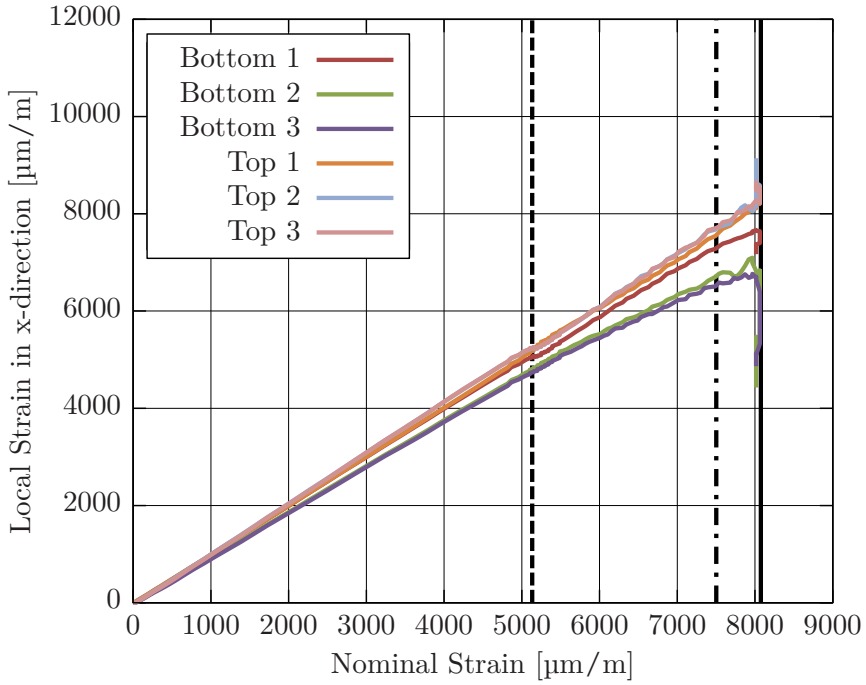

Figure E.16.: Simulated local strains versus nominal strain (TC2-CAI-C5). Dashed line: slight strain jumps imply buckling 5100 µm/m; dot-dashed line: increased deflection rate (7500 µm/m); solid line: ultimate failure (8071 µm/m).

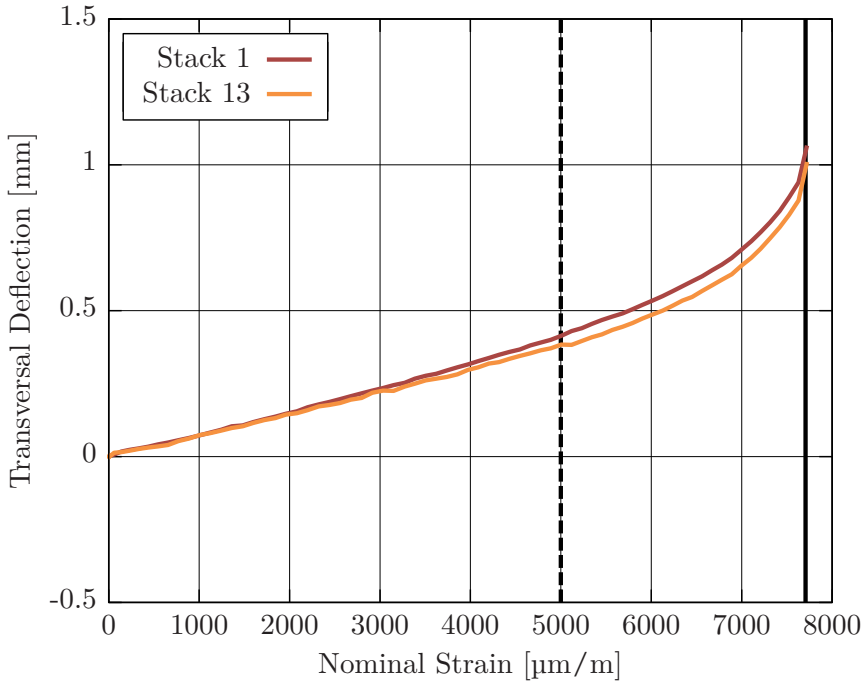

Figure E.17.: Experimental transversal stack deflections at the specimen center versus nominal strain (TC2-CAI-C5). Dashed line: increased deflection rate (5000 µm/m); solid line: ultimate failure (7734 µm/m).

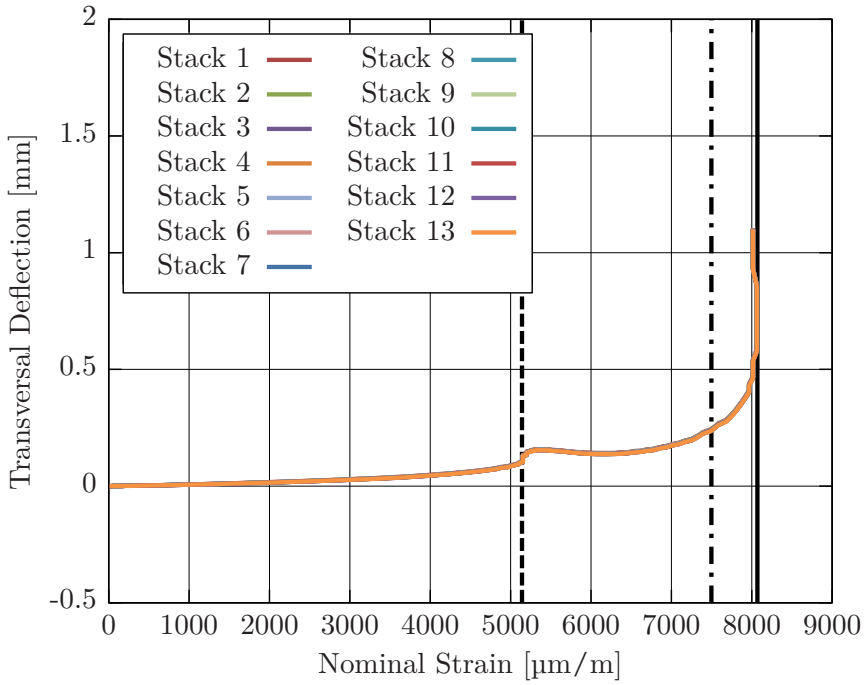

Figure E.18.: Simulated transversal stack deflections at the specimen center versus nominal strain (TC2-CAI-C5). Dashed line: deflection jump implies buckling 5100 µm/m; dot-dashed line: increasing deflection rate (7500 µm/m); solid line: ultimate failure (8071 µm/m).

E.4. Artificially Delaminated Coupons: D-Series

Specimen Label	Dimensions			Damage Parameters		Residual Properties		
	l [mm]	w [mm]	t [mm]	FC [mm]	Dela [mm^2]	Stress [MPa]	Strain [µε]	Force [kN]
CAI-TC2-D1	149.9	100.0	4.10	25	0	382.7	7595	156.9
CAI-TC2-D2	149.9	100.0	4.13	25	0	384.0	7621	158.6
CAI-TC2-D3	149.9	100.0	4.15	25	0	393.6	7811	163.4
CAI-TC2-D4†	149.9	100.0	4.14	25	0	387.9	7698	160.6
CAI-TC2-D5†	149.9	100.0	4.10	25	0	386.3	7666	158.4
average	149.9	100.0	4.12	25	0	386.9	7678	159.6
CoV [%]	0.0	0.0	0.6	0.0	0.0	1.1	1.1	1.6

Table E.4.: Artificial defect and residual strength parameters for D-type damaged specimens; † denotes DIC monitored tests.

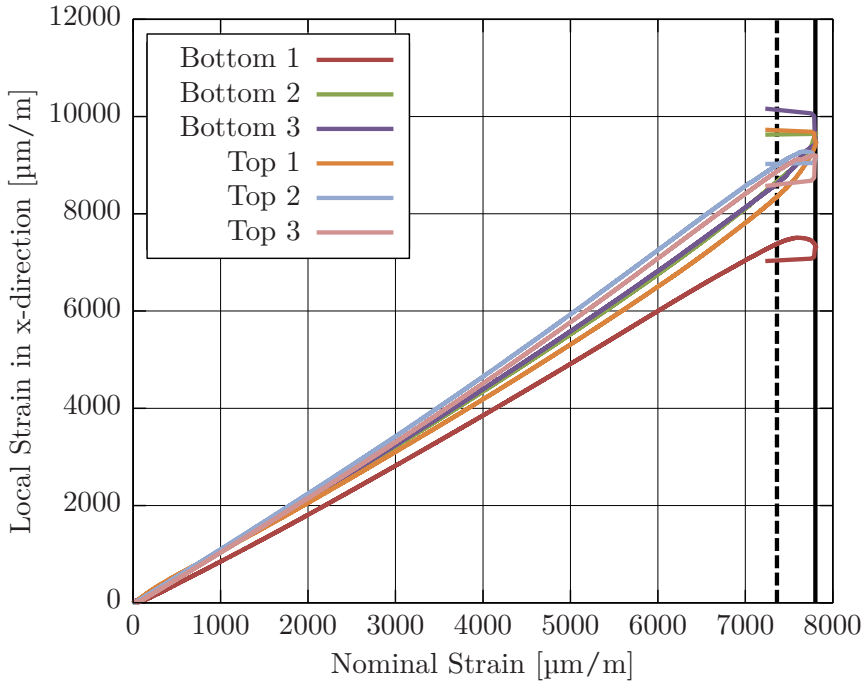

Figure E.19.: Experimental local strains versus nominal strain (TC2-CAI-D3). Dashed line: considerable strain divergence implies increasing deflection rate 7400 µm/m; solid line: ultimate failure (7811 µm/m).

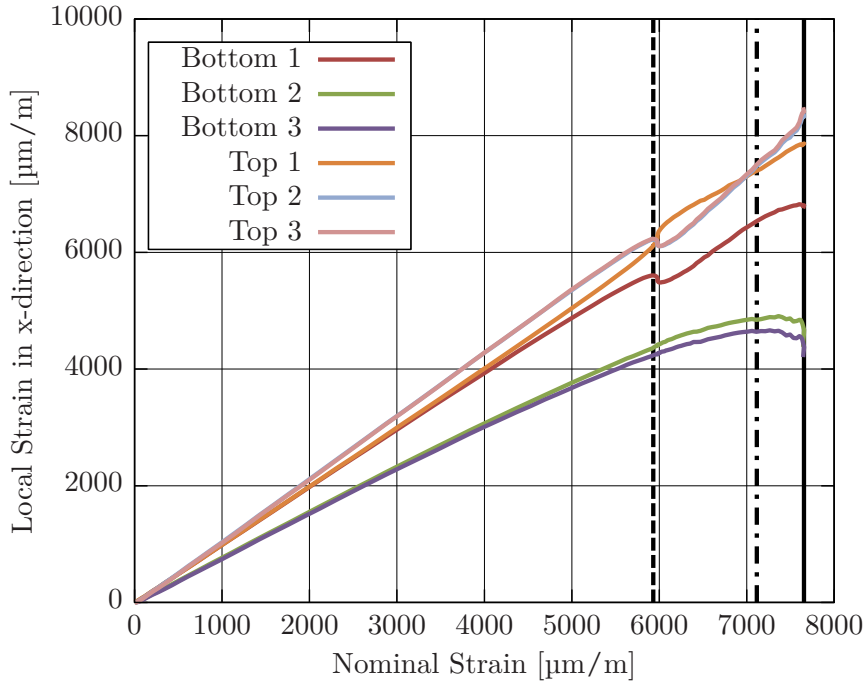

Figure E.20.: Simulated local strains versus nominal strain (TC2-CAI-D3). Dashed line: strain jumps imply buckling at 6000 µm/m; dot-dashed line: increased deflection rate (7100 µm/m); solid line: ultimate failure (7657 µm/m).

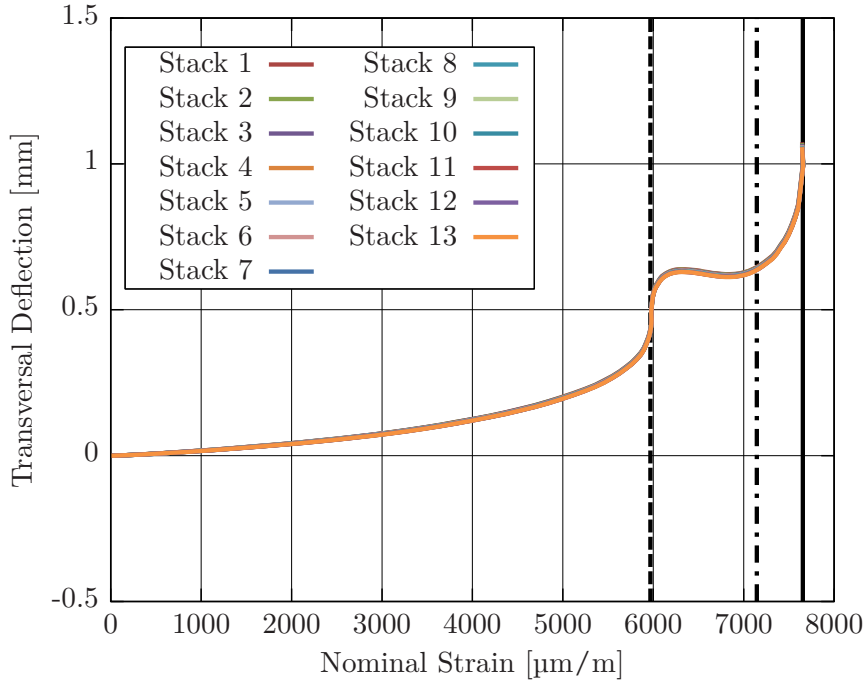

Figure E.21.: Simulated transversal stack deflections at the specimen center versus nominal strain (TC2-CAI-D3). Transversal deflection over the entire loading history. Dashed line: deflection jump implies buckling 6000 µm/m; dot-dashed line: deflection rate change (7100 µm/m); solid line: ultimate failure (7657 µm/m).

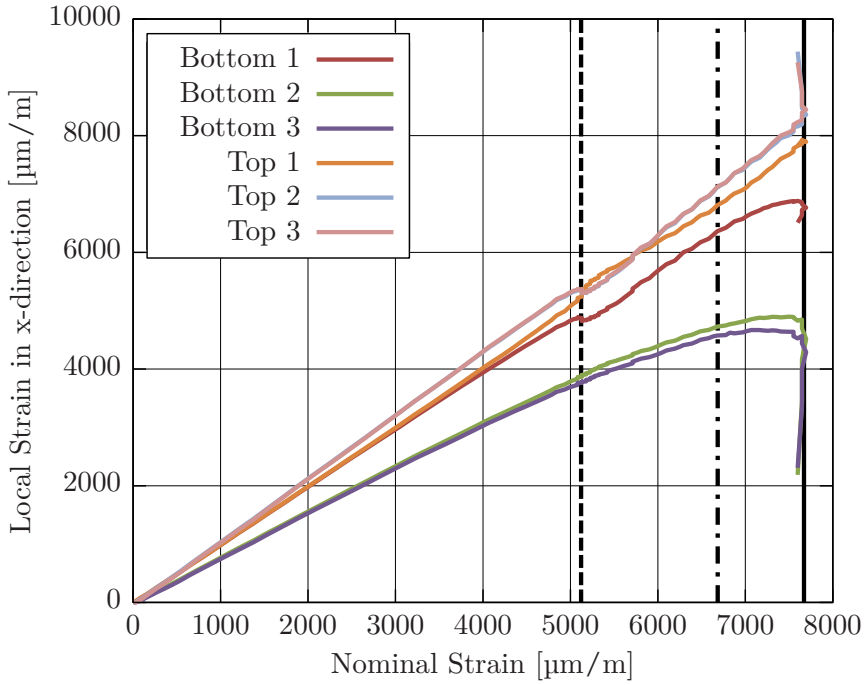

Figure E.22.: Simulated local strains versus nominal strain (TC2-CAI-D5). Dashed line: strain jumps imply buckling at 5100 µm/m; dot-dashed line: increasing deflection rate (6700 µm/m); solid line: ultimate failure (7678 µm/m).

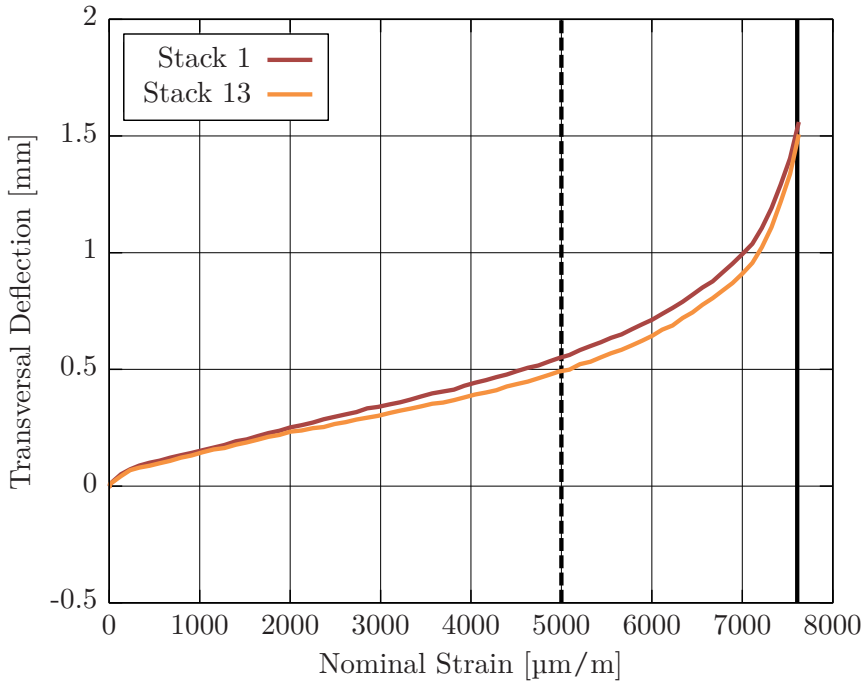

Figure E.23.: Experimental transversal stack deflections at the specimen center versus nominal strain (TC2-CAI-D5). Dashed line: deflection rate change (5000 µm/m); solid line: ultimate failure (7666 µm/m).

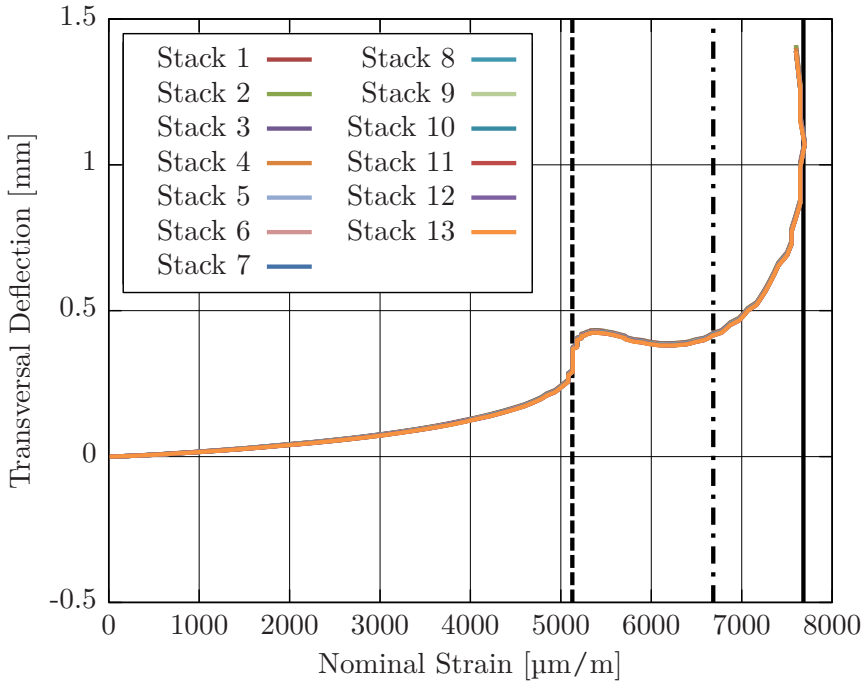

Figure E.24.: Simulated transversal stack deflections at the specimen center versus nominal strain (TC2-CAI-D5). Transversal deflection over the entire loading history. Dashed line: deflection jump implies buckling 5100 µm/m; dot-dashed line: deflection rate change (6700 µm/m); solid line: ultimate failure (7678 µm/m).

E.5. Artificially Delaminated Coupons: AC-Series

Specimen Label	Dimensions			Damage Parameters		Residual Properties		
	l	w	t	FC	Dela	Stress	Strain	Force
	[mm]	[mm]	[mm]	[mm]	[mm^2]	[MPa]	[µε]	[kN]
CAI-TC2-AC1	149.9	100.0	4.12	25	2026	351.7	6980	144.8
CAI-TC2-AC2	150.0	100.0	4.10	25	2031	381.0	7561	156.2
CAI-TC2-AC3	150.0	100.0	4.16	25	2030	385.1	7642	160.2
CAI-TC2-AC4†	149.9	100.0	4.16	25	2030	346.0	6866	144.0
CAI-TC2-AC5†	150.0	100.0	4.10	25	2008	347.5	6896	142.5
average	150.0	100.0	4.13	25	2025	362.3	7189	149.5
CoV [%]	0.0	0.0	0.7	0.0	0.5	5.3	5.3	5.4

Table E.5.: Artificial defect and residual strength parameters for AC-type damaged specimens; † denotes DIC monitored tests.

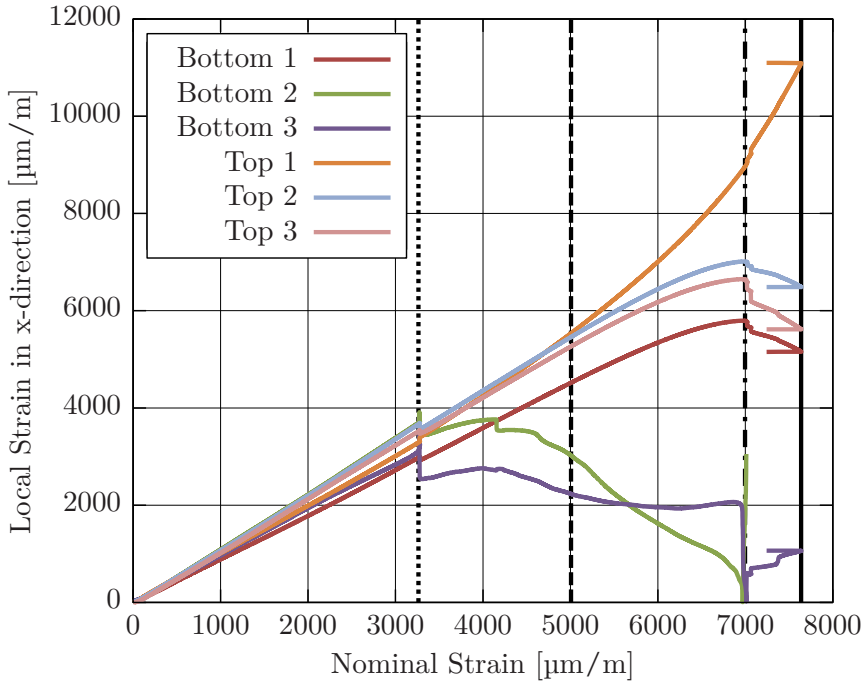

Figure E.25.: Experimental local strains versus nominal strain (TC2-CAI-AC3). Dotted line: strain jumps at all monitored positions point to buckling of both sub-laminates (3300 µm/m); dashed line: increasing strain divergence indicates continuous deflection increase (5000 µm/m); dot-dashed line: strain jumps imply second buckling event (7000 µm/m); solid line: ultimate failure (7642 µm/m).

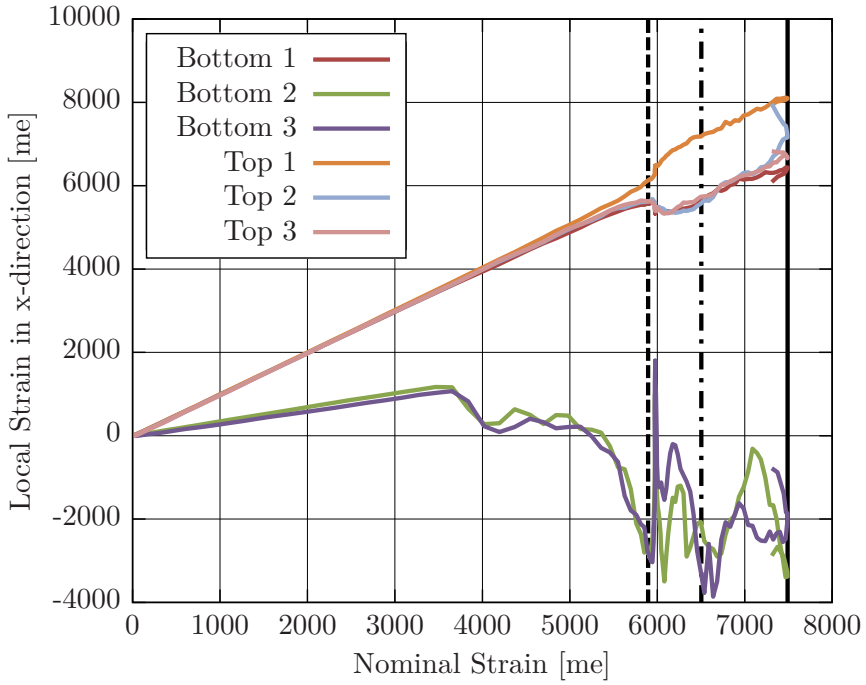

Figure E.26.: Simulated local strains versus nominal strain (TC2-CAI-AC3). Dashed line: strain jumps at all monitored positions points to buckling of both sub-laminates (5900 µm/m); dot-dashed line: strain jumps at the bottom center imply mode-shift (6500 µm/m); solid line: ultimate failure (7489 µm/m).

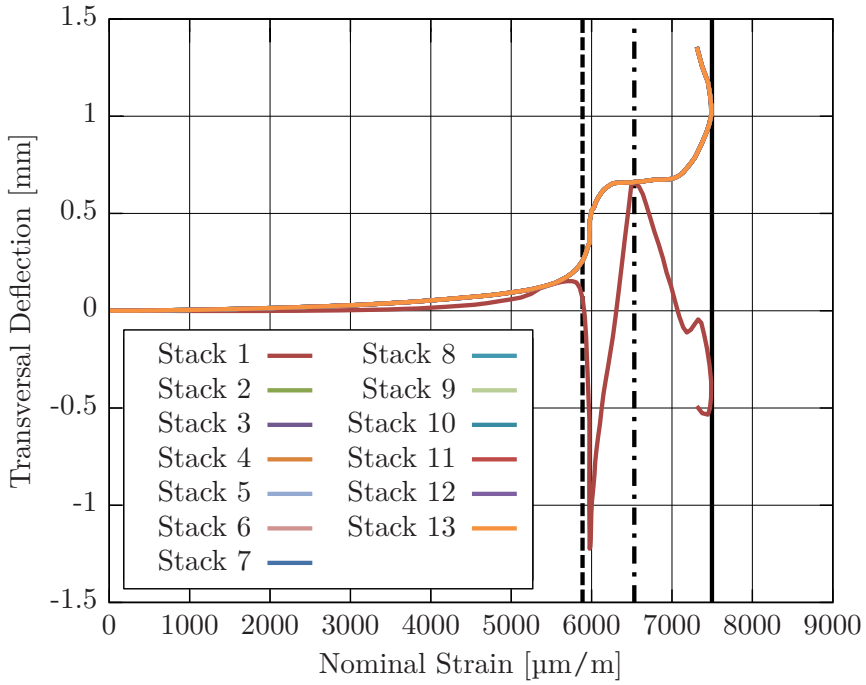

Figure E.27.: Simulated transversal stack deflections at the specimen center versus nominal strain (TC2-CAI-AC3). Dashed line: buckling of both sub-laminates in opposite directions (5900 µm/m); dot-dashed line: mode-shift and snap-back at the bottom stack (6500 µm/m); solid line: ultimate failure (7489 µm/m).

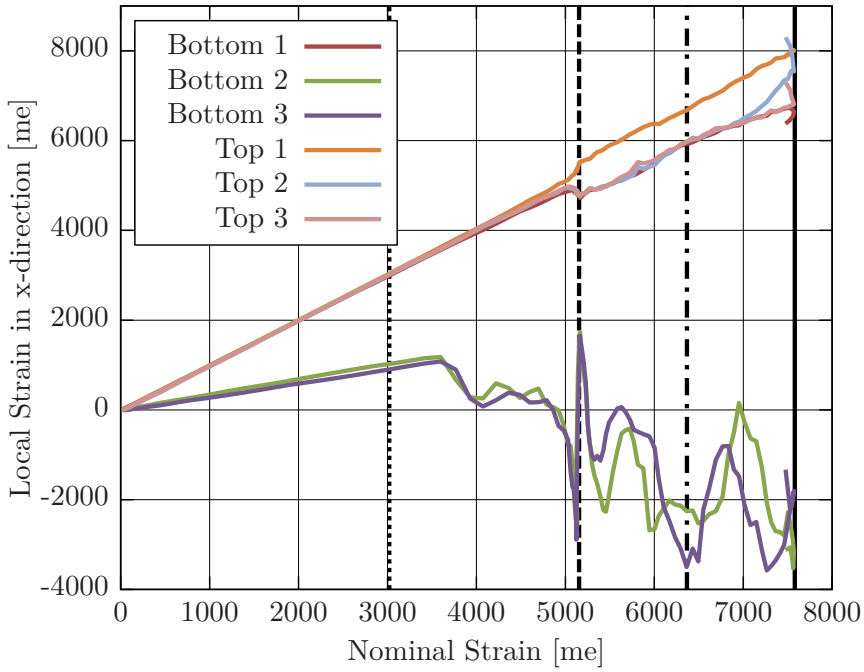

Figure E.28.: Simulated local strains versus nominal strain (TC2-CAI-AC5). Dotted line: slight strain divergence at position 1 implies transversal deflection onset; dashed line: strain jumps at all monitored positions points to buckling of both sub-laminates (5100 µm/m); dot-dashed line: strain jumps at the bottom center imply mode-shift (6300 µm/m); solid line: ultimate failure (7570 µm/m).

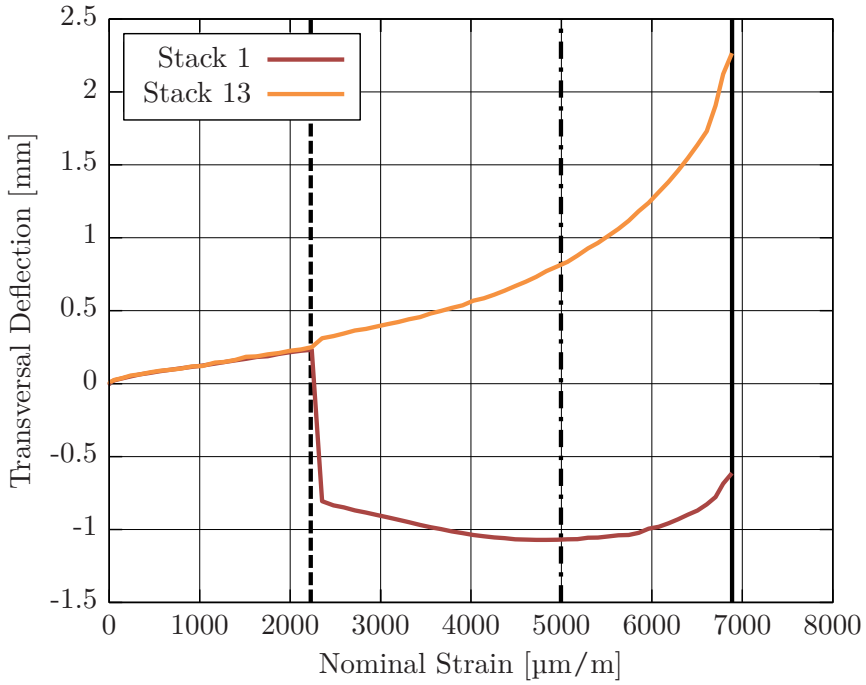

Figure E.29.: Experimental transversal stack deflections at the specimen center versus nominal strain (TC2-CAI-AC5). Dashed line: buckling of both sub-laminates in opposite directions (2200 µm/m); dot-dashed line: mode-shift at the bottom stack (5000 µm/m); solid line: ultimate failure (6896 µm/m).

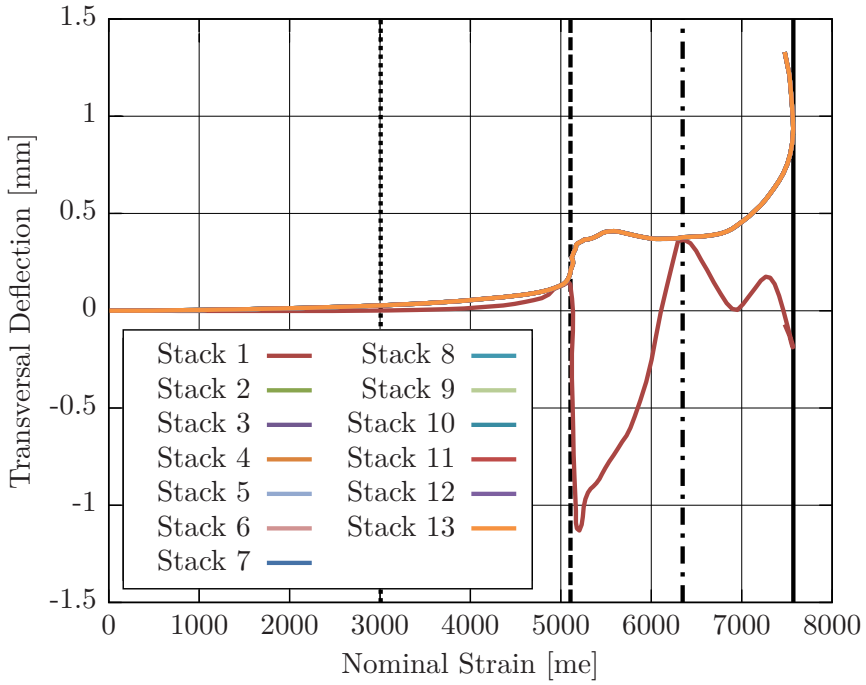

Figure E.30.: Simulated transversal stack deflections at the specimen center versus nominal strain (TC2-CAI-AC5). Dotted line: transversal deflection onset (3000 µm/m); dashed line: buckling of both sub-laminates in opposite directions (5100 µm/m); dot-dashed line: mode-shift and snap-back at the bottom stack (6300 µm/m); solid line: ultimate failure (6896 µm/m).

E.6. Artificially Delaminated Coupons: BD-Series

Specimen Label	Dimensions			Damage Parameters		Residual Properties		
	l	w	t	FC	Dela	Stress	Strain	Force
	[mm]	[mm]	[mm]	[mm]	[mm^2]	[MPa]	[µε]	[kN]
CAI-TC2-BD1	150.0	100.0	4.16	25	2035	284.1	5638	118.2
CAI-TC2-BD2	149.9	100.0	4.18	25	2036	292.3	5801	122.2
CAI-TC2-BD3	149.9	100.0	4.13	25	2042	291.8	5791	120.5
CAI-TC2-BD4†	149.9	100.0	4.12	25	2030	283.8	5632	116.9
CAI-TC2-BD5†	150.0	100.0	4.15	25	2033	283.5	5626	117.7
average	149.9	100.0	4.15	25	2035	287.1	5698	119.1
CoV [%]	0.0	0.0	0.6	0.0	0.2	1.6	1.6	1.8

Table E.6.: Artificial defect and residual strength parameters for BD-type damaged specimens; † denotes DIC monitored tests.

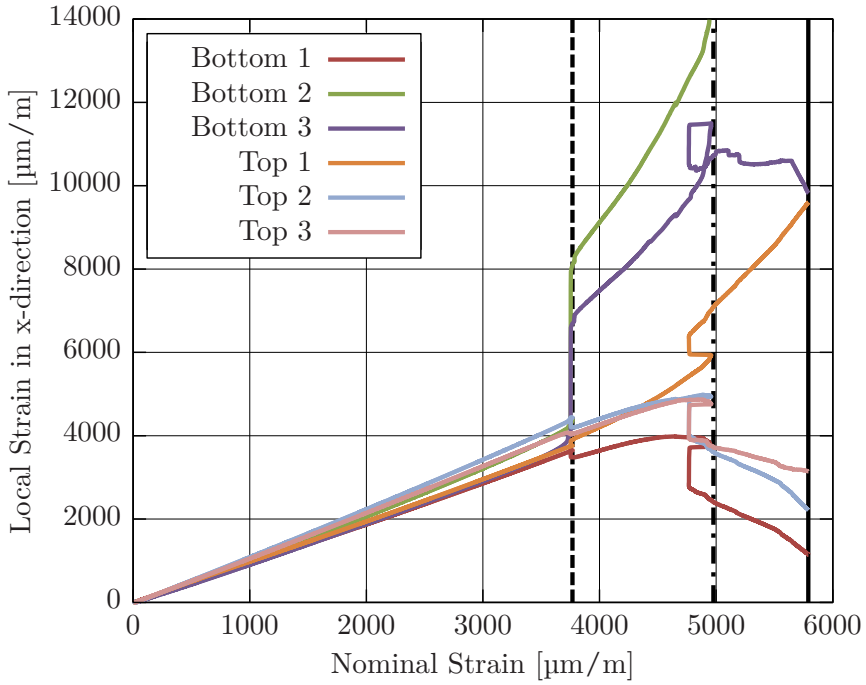

Figure E.31.: Experimental local strains versus nominal strain (TC2-CAI-BD3). Dashed line: strain jumps at all monitored positions point to buckling of both sub-laminates (3800 µm/m); dot-dashed line: strain jumps and nominal strain drop indicate snap-through buckling (5000 µm/m); solid line: ultimate failure (5791 µm/m).

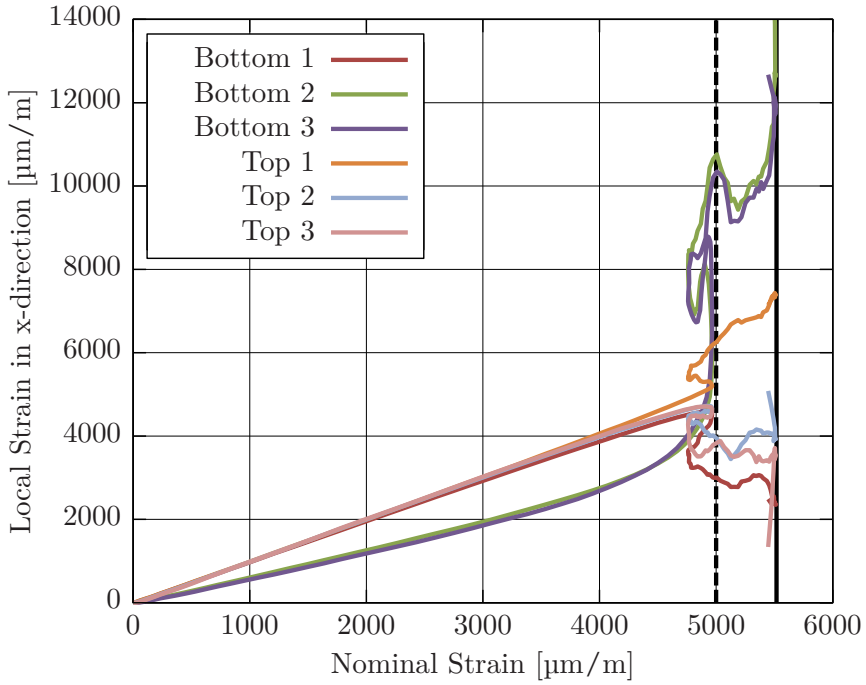

Figure E.32.: Simulated local strains versus nominal strain (TC2-CAI-BD3). Dashed line: strain jumps and nominal strain drop indicate snap-through buckling (5000 µm/m); solid line: ultimate failure (5618 µm/m).

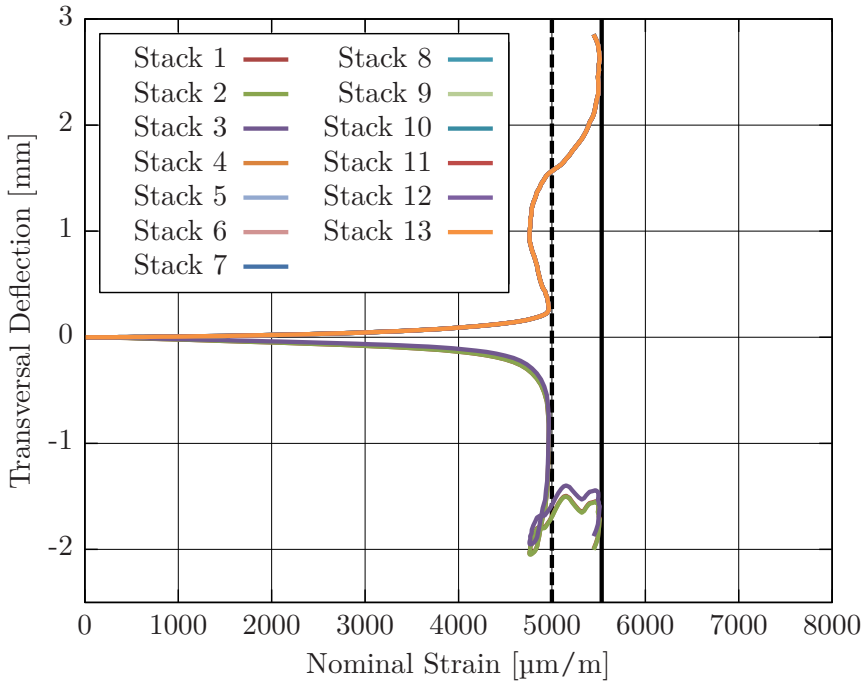

Figure E.33.: Simulated transversal stack deflections at the specimen center versus nominal strain (TC2-CAI-BD3). Dashed line: snap-through buckling in opposite directions (5000 µm/m); solid line: ultimate failure (5618 µm/m).

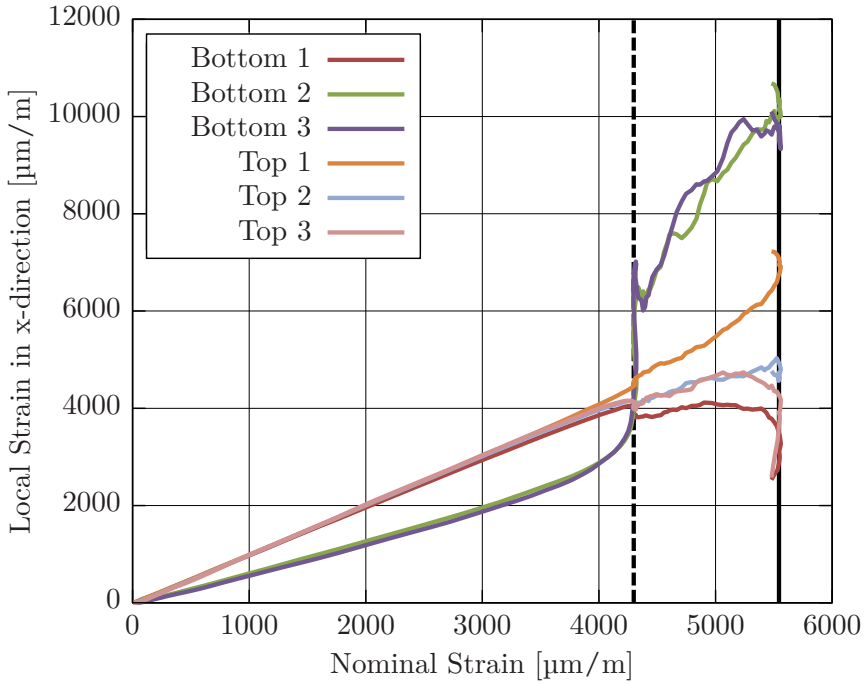

Figure E.34.: Simulated local strains versus nominal strain (TC2-CAI-BD5). Dashed line: strain jumps at all monitored positions points to buckling of both sub-laminates (4300 µm/m); solid line: ultimate failure (5560 µm/m).

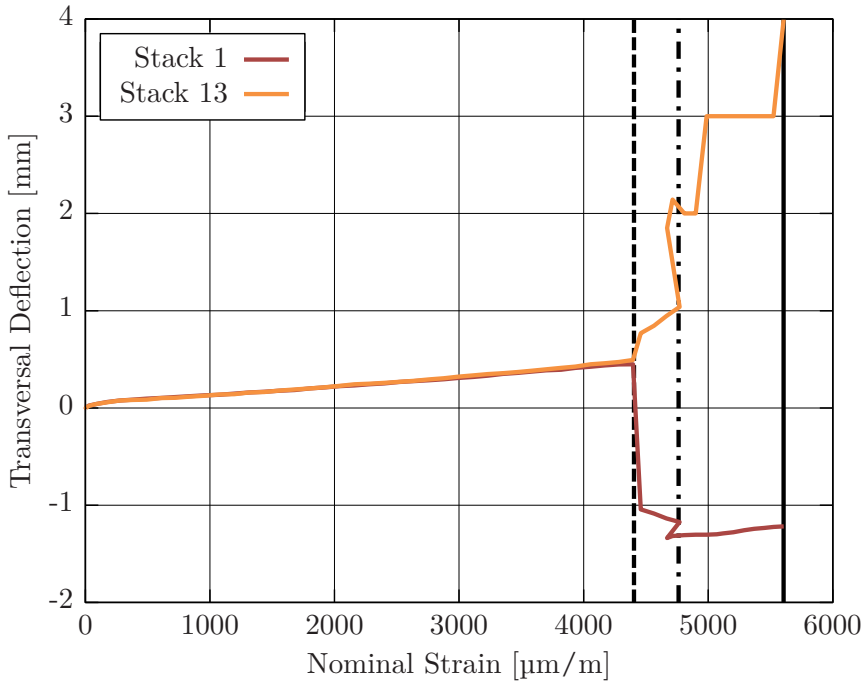

Figure E.35.: Experimental transversal stack deflections at the specimen center versus nominal strain (TC2-CAI-BD5). Dashed line: buckling in opposite directions (4400 µm/m); dot-dashed line: snap-through buckling; solid line: ultimate failure (5626 µm/m).

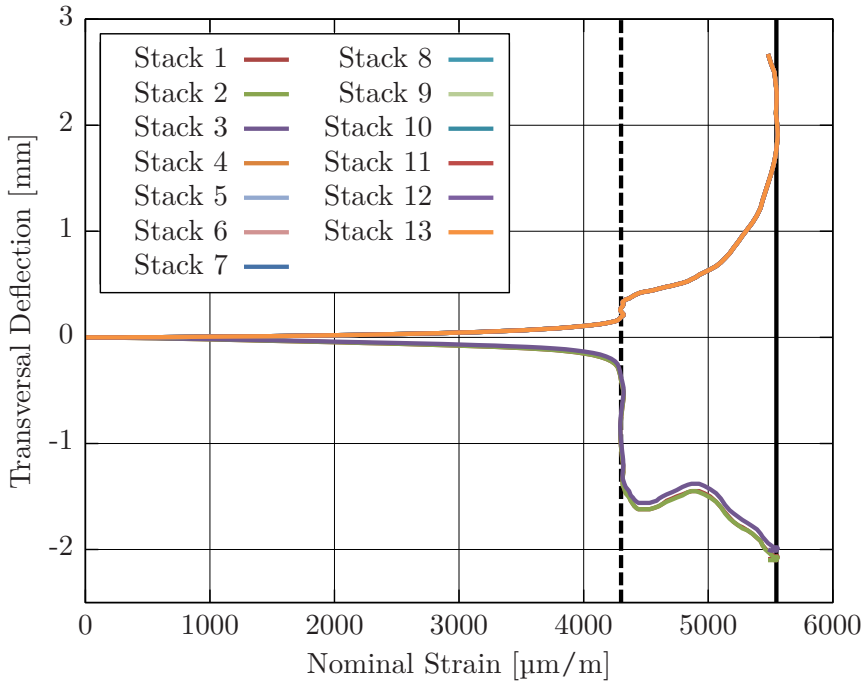

Figure E.36.: Simulated transversal stack deflections at the specimen center versus nominal strain (TC2-CAI-BD5). Dashed line: buckling in opposite directions (4300 µm/m); solid line: ultimate failure (5560 µm/m).

F Tensile Repair Strength Test Results

Experimental results are summarized in the tables below, where a statistic evaluation is added at the table's bottom (average and coefficient of validity). Each coupon test is described by the following parameters: geometric dimensions (gauge length, width, and thickness of the parent laminate and at the repair center) and residual properties (nominal failure stress, nominal failure strain, and failure load).

F.1. Virgin Coupons

Specimen Label	Dimensions			Residual Properties		
	l_g [mm]	w [mm]	t [mm]	Stress [MPa]	Strain [µε]	Force [kN]
TAR-08	400	300	2.13	611.6	12137	390.8
TAR-09	400	300	2.11	580.7	11525	367.6
TAR-10	405	300	2.10	614.0	12185	386.8
average	401.7	300.0	2.11	602.1	11949.0	381.7
CoV [%]	2.9	0.0	0.7	3.1	3.1	3.2

Table F.1.: Geometrical and strength parameters for large virgin tension specimens.

F.2. Repaired Coupons

Specimen Label	Dimensions				Residual Properties		
	l_g [mm]	w [mm]	t [mm]	t_c [mm]	Stress [MPa]	Strain [με]	Force [kN]
TAR-01†	400	300	2.11	3.01	515.7	10233	326.4
TAR-02†	400	300	2.10	2.94	523.8	10395	330.0
TAR-03†	403	300	2.10	2.86	517.2	10263	325.8
TAR-04	400	300	2.10	2.95	564.1	11196	355.4
TAR-05	400	300	2.11	2.97	546.9	10854	346.2
TAR-06	400	300	2.11	2.92	518.5	10290	328.2
TAR-07	405	300	2.12	2.91	550.3	10921	350.0
average	401.1	300.0	2.11	2.94	533.8	10593.3	337.4
CoV [%]	0.5	0.0	0.4	1.6	3.7	3.7	3.7

Table F.2.: Geometrical and residual strength parameters for large repaired tension specimens; † denotes DIC monitored tests.

Bibliography

[1] *IATA Air Passenger Forecast Shows Dip in Long-Term Demand*. Nov. 26, 2015. URL: http://www.iata.org/pressroom/pr/Pages/2015-11-26-01.aspx (visited on 11/17/2016).

[2] *SRIA Executive Summary*. Sept. 2012. URL: http://www.acare4europe.org/sria/exec-summary (visited on 11/17/2016).

[3] V. Faivre and E. Morteau. "Damage tolerant composite fuselage sizing - Characterization of accidental damage threat". In: *FAST 48 Airbus Technical Magazine* 48 (Aug. 2011), pp. 10–16.

[4] C. Soutis. "Carbon fiber reinforced plastics in aircraft construction". In: *Materials Science and Engineering: A*. International Conference on Recent Advances in Composite Materials 412.1 (Dec. 5, 2005), pp. 171–176.

[5] *UPDATED ANALYSIS: Delta Order for A350; A330neo Hinged on Pricing, Availability*. Airways Magazine. Nov. 25, 2014. URL: https://airwaysmag.com/industry/analysis-delta-order-for-a350-a330neo-hinged-on-pricing-availability/ (visited on 09/26/2017).

[6] F.-J. Kirschfink. "Heutige und zukünftige Trends und Herausforderungen in der Flugzeug Maintenance Repair and Overhaul". Presentation. Luftfahrt der Zukunft. Haus der Wissenschaft, Braunschweig, Germany, June 27, 2011.

[7] FAA. *Advisory Circular 25.571-1D*. Jan. 13, 2011.

[8] S. Abrate. *Impact on composite structures*. Cambridge University Press, Apr. 1, 1998. 302 pp.

[9] EASA. *Acceptable Means of Compliance 20-29 / Amendment 6*. July 26, 2010.

[10] K. B. Armstrong, L. G. Bevan, and W. F. Cole II. *Care and repair of advanced composites*. 2nd ed. SAE International, June 30, 2005. 639 pp.

[11] AIRBUS. *A321 Structural Repair Manual*. Manual N SRM 004. Blagnac, France: AIRBUS S.A.S., Feb. 2002.

[12] D. Adams. *Damage tolerance testing of composites*. Composites World. Dec. 30, 2016. URL: https://www.compositesworld.com/articles/damage-tolerance-testing-of-composites(2) (visited on 04/04/2018).

[13] A. Nettles and J. Jackson. "Compression After Impact Testing of Sandwich Composites for Usage on Expendable Launch Vehicles". In: *Journal of Composite Materials* 44.6 (Mar. 1, 2010), pp. 707–738.

[14] D. Hachenberg. "The Role of Advanced Numerical Methods in the Design and Certification of Future Composite Aircraft Structures". In: World congress on computational mechanics. Vol. 1. Vienna, Austria: Vienna University of Technology, 2002, pp. I–490.

[15] F. Romano. “Design of composite stiffened panels by new design criteria and progressive failure analysis”. Dissertation. Napoli, Italy: Universitá Degli Studi di Napoli Federico II, Mar. 22, 2015. 128 pp.

[16] F. Caputo et al. “Numerical study for the structural analysis of composite laminates subjected to low velocity impact”. In: *Composites Part B: Engineering* 67 (Dec. 2014), pp. 296–302.

[17] G. Short, F. Guild, and M. Pavier. “The effect of delamination geometry on the compressive failure of composite laminates”. In: *Composites Science and Technology* 61.14 (Nov. 2001), pp. 2075–2086.

[18] M. Pavier and W. Chester. “Compression failure of carbon fibre-reinforced coupons containing central delaminations”. In: *Composites* 21.1 (Jan. 1990), pp. 23–31.

[19] T. Gottesman and S. Girshovich. “Impact Damage Assessment and Mechanical Degradation of Composites”. In: *Key Engineering Materials* 141-143 (1998), pp. 3–18.

[20] K. Y. Lin and A. V. Styuart. “Probabilistic Approach to Damage Tolerance Design of Aircraft Composite Structures”. In: *Journal of Aircraft* 44.4 (2007), pp. 1309–1317.

[21] M. W. Long and J. D. Narciso. “Probabilistic Design Methodology for Composite Aircraft Structures”. In: (June 1, 1999), p. 138.

[22] P. M. Gary and M. G. Riskalla. *Development of Probabilistic Design Methodology for Composite Structures*. VOUGHT AIRCRAFT CO DALLAS TX, Aug. 1997.

[23] E. V. González et al. “Simulation of drop-weight impact and compression after impact tests on composite laminates”. In: *Composite Structures* 94.11 (Nov. 2012), pp. 3364–3378.

[24] S. Rivallant et al. “Experimental analysis of CFRP laminates subjected to compression after impact: The role of impact-induced cracks in failure”. In: *Composite Structures* 111 (May 1, 2014), pp. 147–157.

[25] R. Borrelli et al. “A Repair Criterion for Impacted Composite Structures based on the Prediction of the Residual Compressive Strength”. In: *Procedia Engineering*. International Symposium on Dynamic Response and Failure of Composite Materials, DRaF2014 88 (Jan. 1, 2014), pp. 117–124.

[26] X. Tang and M. Gaedke. *Study of Strength of Carbon-Fiber Composite Laminates with Rectangular Inserts and Ply Cuts.* 1997.

[27] Tang, Xiaodong et al. “Methodology for Residual Strength of Damaged Laminated Composites”. In: *American Institute of Aeronautics and Astronautics* 97-1220 (1997).

[28] L. Kärger et al. “Evaluation of impact assessment methodologies. Part I: Applied methods”. In: *Composites Part B: Engineering* 40.1 (Jan. 2009), pp. 65–70.

[29] L. Kärger et al. “Evaluation of impact assessment methodologies. Part II: Experimental validation”. In: *Composites Part B: Engineering* 40.1 (Jan. 2009), pp. 71–76.

[30] Baaran, Jens, Kärger, Luise, and Wetzel, Anja. *CODAC Version 1.6 Manual*. Interner DLR Bericht IB 131-2005/38. Braunschweig: Deutsches Zentrum für Luft- und Raumfahrt, Aug. 2005.

[31] W. Tan et al. “Predicting low velocity impact damage and Compression-after-impact (CAI) behaviour of composite laminates”. In: *Composites Part A: Applied Science and Manufacturing* 71 (Apr. 2015), pp. 212–226.

[32] T. Nyman, A. Bredberg, and J. Schon. “Equivalent Damage and Residual Strength for Impact Damaged Composite Structures”. In: *Journal of Reinforced Plastics and Composites* 19.6 (Apr. 1, 2000), pp. 428–448.

[33] Y. Yang, X. Sun, and S. Li. “Residual Compressive Strength Assessment of Impacted Laminates based on C-Scan Data”. In: *International Conference on Composite Materials - ICCM19*. International Conference on Composite Materials. Montreal, Canada, 2013, p. 8.

[34] M. F. S. F. de Moura et al. “Prediction of compressive strength of carbon–epoxy laminates containing delamination by using a mixed-mode damage model”. In: *Composite Structures* 50.2 (Oct. 1, 2000), pp. 151–157.

[35] A. Ellison and H. Kim. “Computed tomography informed composite damage state model generation”. In: *Journal of Composite Materials* (May 6, 2018).

[36] C. P. Dienel, T. Wille, and J. Guerrero Santafe. “A new Method for Individual Impact Damage and Repair Assessment on Composite Structures based on Residual Strength Analysis”. In: *Greener Aviation 2016*. Greener Aviation 2016. Brussels, Belgium, Nov. 10, 2016.

[37] C. P. Dienel et al. “Estimation of airframe weight reduction by integration of piezoelectric and guided wave–based structural health monitoring”. In: *Structural Health Monitoring* (Nov. 29, 2018), p. 11.

[38] C. P. Dienel. *Katalog für typische Schäden an CFK-Luftfahrtstrukturen*. Interner DLR Bericht IB 131-2014_04. Hamburg: Deutsches Zentrum für Luft- und Raumfahrt, 2014.

[39] W. Cantwell and J. Morton. “The impact resistance of composite materials - a review”. In: *Composites* 22.5 (Sept. 1991), pp. 347–362.

[40] R. Olsson and L. E. Asp. “A review of some key developments in the analysis of the effects of impact upon composite structures”. In: *American society for testing and materials special technical publication*. Symposium on Composite Structures - Theory and Practice. Vol. 1383. Seattle, WA, May 17, 1999, pp. 12–28.

[41] M. Richardson and M. Wisheart. “Review of low-velocity impact properties of composite materials”. In: *Composites Part A: Applied Science and Manufacturing* 27.12 (1996), pp. 1123–1131.

[42] R. Olsson. “Modelling of impact damage zones in composite laminates for strength after impact”. In: *Aeronautical Journal* 116.1186 (Dec. 2012), pp. 1349–1365.

[43] K. Srinivasan et al. “Characterization of Damage Modes in Impacted Thermoset and Thermoplastic Composites”. In: *Journal of Reinforced Plastics and Composites* 11.10 (Oct. 1, 1992), pp. 1111–1126.

[44] V. Obdržálek and J. Vrbka. “On the applicability of simple shapes of delaminations in buckling analyses”. In: *Composites Part B: Engineering* 42.3 (2011), pp. 538–545.

[45] M. de Freitas and L. Reis. “Failure mechanisms on composite specimens subjected to compression after impact”. In: *Composite Structures* 42.4 (Aug. 1998), pp. 365–373.

[46] M. Pavier and M. Clarke. “Experimental techniques for the investigation of the effects of impact damage on carbon-fibre composites”. In: *Composites Science and Technology* 55.2 (1995), pp. 157–169.

[47] S. A. Hitchen and R. M. J. Kemp. “The effect of stacking sequence on impact damage in a carbon fibre/epoxy composite”. In: *Composites* 26.3 (Mar. 1, 1995), pp. 207–214.

[48] S. Gao and J. K. Kim. “Three-Dimensional characterization of impact damage in CFRPs”. In: *Key Engineering Materials* 141-143 (1998), pp. 35–54.

[49] C. Garnier et al. “The detection of aeronautical defects in situ on composite structures using Non Destructive Testing”. In: *Composite Structures* 93.5 (Apr. 2011), pp. 1328–1336.

[50] A. Amaro et al. “Damage detection on laminated composite materials using several NDT techniques”. In: *Insight - Non-Destructive Testing and Condition Monitoring* 54.1 (2012), pp. 14–20.

[51] X. E. Gros. “Review of NDT techniques for detection of low energy impacts in carbon reinforcements”. In: *SAMPE Journal* 31.2 (Apr. 1995), pp. 29–34.

[52] K. B. Katnam, L. F. M. Da Silva, and T. M. Young. “Bonded repair of composite aircraft structures: A review of scientific challenges and opportunities”. In: *Progress in Aerospace Sciences* 61 (Aug. 1, 2013), pp. 26–42.

[53] M. Hosur et al. “Estimation of impact-induced damage in CFRP laminates through ultrasonic imaging”. In: *NDT & E International* 31.5 (1998), pp. 359–374.

[54] F. Aymerich and S. Meili. “Ultrasonic evaluation of matrix damage in impacted composite laminates”. In: *Composites Part B: Engineering* 31.1 (Jan. 2000), pp. 1–6.

[55] D. D. Symons. “Characterisation of indentation damage in 0/90 lay-up T300/914 CFRP”. In: *Composites Science and Technology* 60.3 (Feb. 2000), pp. 391–401.

[56] P. J. Schilling et al. “X-ray computed microtomography of internal damage in fiber reinforced polymer matrix composites”. In: *Composites Science and Technology* 65.14 (Nov. 2005), pp. 2071–2078.

[57] R. Stoessel et al. “Analysis of inner fracture surfaces in CFRP based on µ-CT image data”. In: 4th Conference on Industrial Computed Tomography (iCT). Wels, Austria, Dec. 2012.

[58] O. Bullinger et al. “Laminographic Inspection of Large Carbon Fibre Composite Aircraft-Structures at Airbus”. In: *Proceedings of the 19th World Congress on Non-Destructive Testing 2016*. 19th World Congress on Non-Destructive Testing 2016. Munich, Germany, July 2016, p. 10.

[59] C. Wood et al. “Computed laminography of CFRP using an X-ray cone beam and robotic sample manipulator systems”. In: *NDT & E International* (Nov. 13, 2017). In collab. with C. Wood et al.

[60] W. Yin et al. “Noncontact Characterization of Carbon-Fiber-Reinforced Plastics Using Multifrequency Eddy Current Sensors”. In: *IEEE Transactions on Instrumentation and Measurement* 58.3 (Mar. 2009), pp. 738–743.

[61] X. E. Gros. "An eddy current approach to the detection of damage caused by low-energy impacts on carbon fibre reinforced materials". In: *Materials & Design* 16.3 (1995), pp. 167–173.

[62] S. Freeman. "Characterization of Lamina and Interlaminar Damage in Graphite/Epoxy Composites by the Deply Technique". In: *ASTM Special Technical Publication*. 1982, pp. 50–62.

[63] R. Szeliski. *Computer Vision: Algorithms and Applications*. Texts in Computer Science. London: Springer-Verlag, 2011.

[64] H. Spontón and J. Cardelino. "A Review of Classic Edge Detectors". In: *Image Processing On Line* 5 (June 7, 2015), pp. 90–123.

[65] C. Yang, H. Ma, and M. Fu. *Advanced Technologies in Modern Robotic Applications*. Springer, May 18, 2016. 428 pp.

[66] A. F. Frangi et al. "Multiscale vessel enhancement filtering". In: *Medical Image Computing and Computer-Assisted Intervention — MICCAI'98*. International Conference on Medical Image Computing and Computer-Assisted Intervention. Springer Berlin Heidelberg, Oct. 11, 1998, pp. 130–137.

[67] L. Antiga. "Generalizing vesselness with respect to dimensionality and shape". In: *The Insight Journal* (Aug. 3, 2007), p. 175.

[68] G. N. Srinivasan and G. Shobha. "Segmentation Techniques for Target Recognition". In: *W. Trans. on Comp.* 7.10 (Oct. 2008), pp. 1555–1563.

[69] J. Canny. "A Computational Approach to Edge Detection". In: *IEEE Transactions on Pattern Analysis and Machine Intelligence* PAMI-8.6 (Nov. 1986), pp. 679–698.

[70] G. P. McCombe et al. "X-ray damage characterisation in self-healing fibre reinforced polymers". In: *Composites Part A: Applied Science and Manufacturing* 43.4 (Apr. 1, 2012), pp. 613–620.

[71] F. Léonard et al. "The quantification of impact damage distribution in composite laminates by analysis of X-ray computed tomograms". In: *Composites Science and Technology* 152 (Nov. 10, 2017), pp. 139–148.

[72] Hexcel, ed. *HexPly M91 Product Data Sheet*. 2016.

[73] AITM 1-0010. *Determination of Compression Strength After Impact*. AIRBUS S.A.S., Blagnac, France, Oct. 2005.

[74] ASTM D7136. *Standard Test Method for Measuring the Damage Resistance of a Fiber-Reinforced Polymer Matrix Composite to a Drop-Weight Impact Event*. ASTM, 2007.

[75] ASTM D7137. *Standard Test Method for Compressive Residual Strength Properties of Damaged Polymer Matrix Composite Plates*. ASTM, Nov. 15, 2007.

[76] S. Suzuki and K. Abe. "Topological Structural Analysis of Digitized Binary Images by Border Following". In: *Computer Vision, Graphics, and Image Processing* 30.1 (Apr. 1, 1985), pp. 32–46.

[77] Y. Xiong et al. “A prediction method for the compressive strength of impact damaged composite laminates”. In: *Composite Structures* 30.4 (1995), pp. 357–367.

[78] H. Sekine, N. Hu, and M. A. Kouchakzadeh. “Buckling Analysis of Elliptically Delaminated Composite Laminates with Consideration of Partial Closure of Delamination”. In: *Journal of Composite Materials* 34.7 (Apr. 1, 2000), pp. 551–574.

[79] T. P. Philippidis and V. A. Passipoularidis. “Residual strength after fatigue in composites: Theory vs. experiment”. In: *International Journal of Fatigue* 29.12 (Dec. 1, 2007), pp. 2104–2116.

[80] H. T. Han and S. W. Choi. *The Effect of Loading Parameters on Fatigue of Composite Laminates: Part V*. DOT/FAA/AR-01/24. Washington DC, USA: Office of Aviation Research, Jan. 13, 2011.

[81] A. Nettles, A. Hodge, and J. Jackson. “An Examination of the Compressive Cyclic Loading Aspects of Damage Tolerance for Polymer Matrix Launch Vehicle Hardware”. In: *Journal of Composite Materials* 45.4 (Feb. 1, 2011), pp. 437–458.

[82] R. Butler et al. “Compressive fatigue limit of impact damaged composite laminates”. In: *Composites Part A: Applied Science and Manufacturing*. Selected Papers from the Joint 8th International Conference on Deformation and Fracture of Composites (DFC-8) and Experimental Techniques and Design in Composite Materials (ETDCM-7) held at the University of Sheffield, UK 38.4 (Apr. 1, 2007), pp. 1211–1215.

[83] A. T. Rhead, R. Butler, and G. W. Hunt. “Post-buckled propagation model for compressive fatigue of impact damaged laminates”. In: *International Journal of Solids and Structures* 45.16 (Aug. 1, 2008), pp. 4349–4361.

[84] A. T. Rhead and R. Butler. “Compressive static strength model for impact damaged laminates”. In: *Composites Science and Technology* 69.14 (Nov. 2009), pp. 2301–2307.

[85] J. Baaran, L. Kärger, and A. Wetzel. “Efficient prediction of damage resistance and tolerance of composite aerospace structures”. In: *Proceedings of the Institution of Mechanical Engineers, Part G: Journal of Aerospace Engineering* 222.2 (Feb. 1, 2008), pp. 179–188.

[86] C. Xiaoquan, A. Al-Mansour, and L. Zhengneng. “Residual Strength of Stitched Laminates After Low Velocity Impact”. In: *Journal of Reinforced Plastics and Composites* 28.14 (July 1, 2009), pp. 1679–1688.

[87] R. Olsson et al. “Experiments and analysis of laminates with artificial damage”. In: *Composites Science and Technology* 63.2 (Feb. 2003), pp. 199–209.

[88] P. Sztefek and R. Olsson. “Tensile stiffness distribution in impacted composite laminates determined by an inverse method”. In: *Composites Part A: Applied Science and Manufacturing* 39.8 (Aug. 2008), pp. 1282–1293.

[89] R. Craven, P. Sztefek, and R. Olsson. “Investigation of impact damage in multi-directional tape laminates and its effect on local tensile stiffness”. In: *Composites Science and Technology* 68.12 (Sept. 2008), pp. 2518–2525.

[90] R. Craven, L. Iannucci, and R. Olsson. “Homogenised non-linear soft inclusion for simulation of impact damage in composite structures”. In: *Composite Structures* 93.2 (2011), pp. 952–960.

[91] V. J. Hawyes, P. T. Curtis, and C. Soutis. “Effect of impact damage on the compressive response of composite laminates”. In: *Composites Part A: Applied Science and Manufacturing* 32.9 (Sept. 2001), pp. 1263–1270.

[92] V. K. Kannan, A. Rajadurai, and B. N. Rao. “Residual strength of laminated composites after impact”. In: *Journal of Composite Materials* 45.9 (May 1, 2011), pp. 1031–1043.

[93] F. Shen, K. H. Lee, and T. E. Tay. “Modeling delamination growth in laminated composites”. In: *Composites Science and Technology* 61.9 (July 1, 2001), pp. 1239–1251.

[94] X. Wang et al. “Compressive failure of composite laminates containing multiple delaminations”. In: *Composites Science and Technology* 65.2 (Feb. 2005), pp. 191–200.

[95] H. Yan et al. “Compression-after-impact response of woven fiber-reinforced composites”. In: *Composites Science and Technology* 70.14 (Nov. 30, 2010), pp. 2128–2136.

[96] C. Bouvet, S. Rivallant, and J. J. Barrau. “Low velocity impact modeling in composite laminates capturing permanent indentation”. In: *Composites Science and Technology* 72.16 (Nov. 16, 2012), pp. 1977–1988.

[97] S. Rivallant, C. Bouvet, and N. Hongkarnjanakul. “Failure analysis of CFRP laminates subjected to compression after impact: FE simulation using discrete interface elements”. In: *Composites Part A: Applied Science and Manufacturing* 55 (2013), pp. 83–93.

[98] F. Caputo, A. De Luca, and R. Sepe. “Numerical study of the structural behaviour of impacted composite laminates subjected to compression load”. In: *Composites Part B: Engineering* 79 (Sept. 15, 2015), pp. 456–465.

[99] K.-J. Bathe. *Finite-Elemente-Methoden*. Trans. by P. Zimmermann. 1. Aufl. 1986. Ber. Nachdruck. Berlin: Springer, 1989. 820 pp.

[100] *Abaqus Analysis User’s Guide*. USA: Dassault Systèmes, May 7, 2015.

[101] L. Nasdala. *FEM-Formelsammlung Statik und Dynamik: Hintergrundinformationen, Tipps und Tricks*. Springer-Verlag, Mar. 2012. 264 pp.

[102] C. P. Dienel. “Modeling the behavior of impact induced multiple delaminations under compressive load”. In: *Proceedings of the American Society for Composites 2014-Twenty-ninth Technical Conference on Composite Materials*. American Society for Composites 2014. San Diego, USA: DEStech Publications, Inc, 2014.

[103] G. Gdalewitsch. *Finite element modeling and residual performance prediction of impacted composite structures*. Interner DLR Bericht IB 131-2013_100. Hamburg: Deutsches Zentrum für Luft- und Raumfahrt, 2013.

[104] A. M. Girão Coelho, J. Toby Mottram, and K. A. Harries. “Finite element guidelines for simulation of fibre-tension dominated failures in composite materials validated by case studies”. In: *Composite Structures* 126 (Aug. 1, 2015), pp. 299–313.

[105] H. Schürmann. *Konstruieren mit Faser-Kunststoff-Verbunden*. 1st Edition. Berlin, Heidelberg, Germany: Springer Verlag, 2005.

[106] DIN EN 2561. *Tensile test parallel to the fibre direction*. DIN, Berlin, Germany, Nov. 1995.

[107] DIN EN ISO 14126. *Determination of compressive properties in the in-plane direction*. DIN, Berlin, Germany, Dec. 2000.

[108] DIN EN 2597. *Tensile test perpendicular to the fibre direction*. DIN, Berlin, Germany, Aug. 1998.

[109] ASTM D5379. *Standard Test Method for Shear Properties of Composite Materials by the V-Notched Beam Method*. ASTM, Jan. 3, 2005.

[110] A. Kaddour et al. "The background to the third world-wide failure exercise". In: *Journal of Composite Materials* 47.20 (Sept. 1, 2013), pp. 2417–2426.

[111] Z. Hashin and A. Rotem. "A Fatigue Failure Criterion for Fiber Reinforced Materials". In: *Journal of Composite Materials* 7.4 (Oct. 1, 1973), pp. 448–464.

[112] Z. Hashin. "Failure Criteria for Unidirectional Fiber Composites". In: *Journal of Applied Mechanics* 47.2 (June 1, 1980), pp. 329–334.

[113] C. Davila, N. Jaunky, and S. Goswami. "Failure Criteria for FRP Laminates in Plane Stress". In: *44th AIAA/ASME/ASCE/AHS/ASC Structures, Structural Dynamics, and Materials Conference*. Structures, Structural Dynamics, and Materials and Co-located Conferences. American Institute of Aeronautics and Astronautics, Apr. 7, 2003.

[114] I. Lapczyk and J. A. Hurtado. "Progressive damage modeling in fiber-reinforced materials". In: *Composites Part A: Applied Science and Manufacturing*. CompTest 2006 38.11 (Nov. 1, 2007), pp. 2333–2341.

[115] A. Parvizi, K. W. Garrett, and J. E. Bailey. "Constrained cracking in glass fibre-reinforced epoxy cross-ply laminates". In: *Journal of Materials Science* 13.1 (1978), pp. 195–201.

[116] G. J. Dvorak and N. Laws. "Analysis of Progressive Matrix Cracking In Composite Laminates II. First Ply Failure". In: *Journal of Composite Materials* 21.4 (Apr. 1, 1987), pp. 309–329.

[117] C. G. Davila and P. P. Camanho. "Physically Based Failure Criteria for Transverse Matrix Cracking". In: 9th Portuguese Conference on Fracture. 2004.

[118] P. P. Camanho et al. "Prediction of in situ strengths and matrix cracking in composites under transverse tension and in-plane shear". In: *Composites Part A: Applied Science and Manufacturing*. CompTest 2004 37.2 (Feb. 2006), pp. 165–176.

[119] N. Knight. "Factors Influencing Progressive Failure Analysis Predictions for Laminated Composite Structures". In: *49th AIAA/ASME/ASCE/AHS/ASC Structures, Structural Dynamics, and Materials Conference, 16th AIAA/ASME/AHS Adaptive Structures Conference,10th AIAA Non-Deterministic Approaches Conference, 9th AIAA Gossamer Spacecraft Forum, 4th AIAA Multidisciplinary Design Optimization Specialists Conference*. American Institute of Aeronautics and Astronautics, 2008.

[120] S. Murakami. *Continuum Damage Mechanics*. Vol. 185. Solid Mechanics and Its Applications. Dordrecht: Springer Netherlands, 2012.

[121] Z. P. Bažant and B. H. Oh. "Crack band theory for fracture of concrete". In: *Matériaux et Construction* 16.3 (May 1983), pp. 155–177.

[122] A. Matzenmiller, J. Lubliner, and R. L. Taylor. "A constitutive model for anisotropic damage in fiber-composites". In: *Mechanics of Materials* 20.2 (Apr. 1, 1995), pp. 125–152.

[123] P. P. Camanho, P. Maimí, and C. G. Dávila. "Prediction of size effects in notched laminates using continuum damage mechanics". In: *Composites Science and Technology* 67.13 (2007), pp. 2715–2727.

[124] P. Maimí et al. *A Thermodynamically Consistent Damage Model for Advanced Composites*. NASA Technical Memorandum NASA/TM-2006-214282. National Aeronautics and Space Administration, Mar. 2006, p. 47.

[125] ASTM D5528. *Standard Test Method for Mode I Interlaminar Fracture Toughness of Unidirectional Fiber-Reinforced Polymer Matrix Composites*. ASTM, Oct. 11, 2001.

[126] ASTM D6671. *Standard Test Method for Mixed Mode I -Mode II Interlaminar Fracture Toughness of Unidirectional Fiber Reinforced Polymer Matrix Composites*. ASTM, Jan. 3, 2006.

[127] S. T. Pinho, L. Iannucci, and P. Robinson. "Physically based failure models and criteria for laminated fibre-reinforced composites with emphasis on fibre kinking. Part II: FE implementation". In: *Composites Part A: Applied Science and Manufacturing* 37.5 (2006), pp. 766–777.

[128] K. Song, Y. Li, and C. Rose. "Continuum Damage Mechanics Models for the Analysis of Progressive Failure in Open-Hole Tension Laminates". In: *52nd AIAA/ASME/ASCE/AHS/ASC Structures, Structural Dynamics and Materials Conference* (2011).

[129] D. Bienek and C. P. Dienel. *Faserbruch-Modellierung zur Berechnung der strukturellen Resttragfähigkeit an einschlag-geschädigten CFK-Strukturen*. Interner Bericht DLR-IB-FA-HH-2016-96. Hamburg: Deutsches Zentrum für Luft- und Raumfahrt, Apr. 2016.

[130] P. P. Camanho, C. G. Dávila, and D. R. Ambur. *Numerical simulation of delamination growth in composite materials*. NASA Technical Memorandum NASA/TP-2001-211041. National Aeronautics and Space Administration, Aug. 2001.

[131] Q. Yang and B. Cox. "Cohesive models for damage evolution in laminated composites". In: *International Journal of Fracture* 133.2 (May 1, 2005), pp. 107–137.

[132] P. Camanho and C. G. Davila. *Mixed-Mode Decohesion Finite Elements for the Simulation of Delamination in Composite Materials*. NASA Technical Memorandum NASA/TM-2002-211737. National Aeronautics and Space Administration, June 2002.

[133] H. Li and N. Chandra. "Analysis of crack growth and crack-tip plasticity in ductile materials using cohesive zone models". In: *International Journal of Plasticity* 19.6 (June 1, 2003), pp. 849–882.

[134] Lin Ye. "Role of matrix resin in delamination onset and growth in composite laminates". In: *Composites Science and Technology* 33.4 (Jan. 1, 1988), pp. 257–277.

[135] M. L. Benzeggagh and M. Kenane. "Measurement of mixed-mode delamination fracture toughness of unidirectional glass/epoxy composites with mixed-mode bending apparatus". In: *Composites Science and Technology* 56.4 (1996), pp. 439–449.

[136] E. González et al. “Simulation of delamination by means of cohesive elements using an explicit finite element code”. In: *Computers, Materials and Continua* 9.1 (2009), pp. 51–92.

[137] A. Turon et al. “An engineering solution for mesh size effects in the simulation of delamination using cohesive zone models”. In: *Engineering Fracture Mechanics* 74.10 (2007), pp. 1665–1682.

[138] S. T. de Freitas and J. Sinke. “Test method to assess interface adhesion in composite bonding”. In: *Applied Adhesion Science* 3.1 (Mar. 24, 2015), p. 9.

[139] A. Turon et al. “Analytical and Numerical Investigation of the Length of the Cohesive Zone in Delaminated Composite Materials”. In: *Mechanical Response of Composites*. Computational Methods in Applied Sciences 10. Springer Netherlands, 2008, pp. 77–97.

[140] P. W. Harper and S. R. Hallett. “Cohesive zone length in numerical simulations of composite delamination”. In: *Engineering Fracture Mechanics* 75.16 (Nov. 2008), pp. 4774–4792.

[141] A. Turon et al. “Accurate simulation of delamination growth under mixed-mode loading using cohesive elements: Definition of interlaminar strengths and elastic stiffness”. In: *Composite Structures* 92.8 (2010), pp. 1857–1864.

[142] Hui C.-Y. et al. “Crack blunting and the strength of soft elastic solids”. In: *Proceedings of the Royal Society of London. Series A: Mathematical, Physical and Engineering Sciences* 459.2034 (June 8, 2003), pp. 1489–1516.

[143] A. Hillerborg, M. Modéer, and P. .-.-E. Petersson. “Analysis of crack formation and crack growth in concrete by means of fracture mechanics and finite elements”. In: *Cement and Concrete Research* 6.6 (Nov. 1, 1976), pp. 773–781.

[144] A. S. Argon. “Fracture: Strength and Toughness Mechanisms”. In: *Comprehensive Composite Materials*. Ed. by A. Kelly and C. Zweben. Oxford: Pergamon, Jan. 1, 2000, pp. 763–802.

[145] C. H. Wang and C. N. Duong. “Chapter 4 - Design of scarf and doubler-scarf joints”. In: *Bonded Joints and Repairs to Composite Airframe Structures*. Ed. by C. H. Wang and C. N. Duong. Oxford: Academic Press, Jan. 1, 2016, pp. 83–112.

[146] J. S. Jones and S. R. Graves. *Repair Techniques for Celion/LARC-160 Graphite/Polyimide Composite Structures*. STS-81-0352-12. NASA, June 1984.

[147] V. Kradinov et al. “Bolted patch repair of composite panels with a cutout”. In: *Composite Structures* 56.4 (June 1, 2002), pp. 423–444.

[148] L. J. Hart-Smith. “Advances in the analysis and design of adhesive-bonded joints in composite aerospace structures”. In: (1974).

[149] L. J. Hart-Smith. “Adhesive-Bonded Joints for Composites - Phenomenological Considerations”. In: Technology Conferences Associates Conference on Advanced Composites Technology. El Segundo, CA, USA, Mar. 1978.

[150] L. J. Hart-Smith. “Further developments in the design and analysis of adhesive-bonded structural joints”. In: *ASTM special technical publication* 749 (1981), pp. 3–31.

[151] L. J. Hart-Smith. *Design Methodology for Bonded-Bolted Composite Joints. Volume I. Analysis Derivations and Illustrative Solutions*. MCDONNELL DOUGLAS CORP LONG BEACH CA, Feb. 1982.

[152] L. J. Hart-Smith. *The design of repairable advanced composite structures*. 851830. Warrendale, PA: SAE International, Dec. 1985.

[153] C. Soutis and F. Z. Hu. "Design and performance of bonded patch repairs of composite structures". In: *Proceedings of the Institution of Mechanical Engineers, Part G: Journal of Aerospace Engineering* 211.4 (Apr. 1, 1997), pp. 263–271.

[154] C. Soutis and F. Z. Hu. "Failure Analysis of Scarf-Patch-Repaired Carbon Fiber/Epoxy Laminates Under Compression". In: *AIAA Journal* 38.4 (Apr. 2000), pp. 737–740.

[155] C. H. Wang and A. J. Gunnion. "On the design methodology of scarf repairs to composite laminates". In: *Composites Science and Technology* 68.1 (Jan. 1, 2008), pp. 35–46.

[156] R. D. S. G. Campilho, M. F. S. F. d. Moura, and J. J. M. S. Domingues. "Stress and failure analyses of scarf repaired CFRP laminates using a cohesive damage model". In: *Journal of Adhesion Science and Technology* 21.9 (Jan. 1, 2007), pp. 855–870.

[157] R. D. S. G. Campilho, M. F. S. F. de Moura, and J. J. M. S. Domingues. "Using a cohesive damage model to predict the tensile behaviour of CFRP single-strap repairs". In: *International Journal of Solids and Structures* 45.5 (Mar. 1, 2008), pp. 1497–1512.

[158] R. D. S. G. Campilho et al. "Computational Modelling of the Residual Strength of Repaired Composite Laminates Using a Cohesive Damage Model". In: *Journal of Adhesion Science and Technology* 22.13 (Jan. 1, 2008), pp. 1565–1591.

[159] R. D. S. G. Campilho et al. "Modelling the tensile fracture behaviour of CFRP scarf repairs". In: *Composites Part B: Engineering* 40.2 (Mar. 1, 2009), pp. 149–157.

[160] A. M. G. Pinto et al. "Numerical evaluation of three-dimensional scarf repairs in carbon-epoxy structures". In: *International Journal of Adhesion and Adhesives*. Special Issue on Joint Design 30.5 (July 1, 2010), pp. 329–337.

[161] P. Cheng et al. "Tensile behaviour of patch-repaired CFRP laminates". In: *Composite Structures* 93.2 (Jan. 2011), pp. 582–589.

[162] C. Xiaoquan et al. "Study of tensile failure mechanisms in scarf repaired CFRP laminates". In: *International Journal of Adhesion and Adhesives* 41 (Mar. 1, 2013), pp. 177–185.

[163] C. E. Materials, ed. *Cytec FM300 Epoxy Adhesive Film Technical Data Sheet*. Dec. 8, 2011.

[164] S. Bennati, P. Fisicaro, and P. Valvo. "An enhanced beam-theory model of the mixed-mode bending (MMB) test - Part II: Applications and results". In: *Meccanica* 48.2 (2013), pp. 465–484.